2021

HIGH INJECTION PRESSURE IMPINGING DIESEL SPRAY CHARACTERISTICS AND SUBSEQUENT SOOT FORMATION IN REACTING CONDITIONS

Zhihao Zhao
Michigan Technological University, zhizhao@mtu.edu

HIGH INJECTION PRESSURE IMPINGING DIESEL SPRAY CHARACTERISTICS AND SUBSEQUENT SOOT FORMATION IN REACTING CONDITIONS

By

Zhihao Zhao

A DISSERTATION

Submitted in partial fulfillment of the requirements for the degree of

DOCTOR OF PHILOSOPHY

In Mechanical Engineering - Engineering Mechanics

MICHIGAN TECHNOLOGICAL UNIVERSITY

2021

This dissertation has been approved in partial fulfillment of the requirements for the Degree of DOCTOR OF PHILOSOPHY in Mechanical Engineering - Engineering Mechanics.

Department of Mechanical Engineering - Engineering Mechanics

Dissertation Advisor:	*Dr. Seong-Young Lee*
Committee Member:	*Dr. Mahdi Shahbakhti*
Committee Member:	*Dr. Sajjad Bigham*
Committee Member:	*Dr. Lei Pan*
Department Chair:	*Dr. William W. Predebon*

Table of Contents

List of figures

List of tables

Preface

The materials in this dissertation (Chapter 2 on the part of literature review, Chapter 3 to 5 on the description on experimental and numerical test conditions, post-processing method, as well as Chapter 6 to 10 on the results and discussion for impinging spray characteristics, thermal characteristics of an impinging spray, soot formation in an impinging spray and the film contribution to soot formation) come from 5 of my publications from SAE International, ASME Internal Combustion Engine Division Fall Technical Conference, and International Journal of Engine Research. I was named as the first author of 5 publications. As the first author, I was responsible for conducting the experiments and simulations, data analysis, plotting the figures, and writing the manuscript. My co-authors at MTU have helped me in setting up the experimental equipment, designing the test conditions, running the simulations, and analyzing the numerical results. My advisor, Dr. Seong-Young Lee helped me review all my publications.

Acknowledgments

It is a precise journey for the five years after reaching the United States. First of all, during the last five years, I want to thank Dr. Seong-Young Lee for his support and guidance for the last five years since 2016. As an amateur 5 years ago, Dr. Lee gave me valuable opportunities to involve the academic research and met external experts in my area. Without his help, I could not have the achievements today. Besides, I not only gained academic knowledge but also personal experience from him. Although we had tough arguments sometimes, his advice, experience and knowledge benefit my personality and academic abilities. To me, he is a kind advisor as well as a friend. I enjoy talking with him not only about the research but also the life. I had five valuable, unforgettable and precise years working with Dr. Lee and I want to maintain the relationship with him further.

Secondly, I want to thank my committee members, Dr. Mahdi Shahbakhti, Dr. Sajjad Bigham, and Dr. Lei Pan. They helped me to extend my current research scope to a new level. Especially, they raised lots of valuable questions during my Ph.D. proposal and I have learned a lot from them.

Thirdly, I want to thank my colleagues, Dr. Xiucheng Zhu, Dr. Le Zhao, Nitisha Ahuja, Jiachen Zhai for their help during the last five years. I want to especially thank Dr. Zhu and Dr. Zhao who helped me with experimental and numerical works. I could say that without them I would experience a tougher time. Also, I appreciate the help of the research staff, Henry Schmidt and William Atkinson. Most of my research was done in the AERB lab at MTU. Henry and Bill helped me set up the experimental devices and conduct the experiments.

Then, I missed my friends at MTU. We had a happy time working, studying, playing, and enjoying the lift at MTU. They gave me help both in life and academic area which I really appreciated.

Last, I want to thank my family. My parents, Wei Zhao and Lu Bai always supported me since the date when I came to this world. Their spirits inspired me to achieve a higher standard for my career. That's the reason why I want to pursue my Ph.D. degree. In 2017, I met my current wife, Xinyu Wang and we got married in 2019. Before and after the marriage, we have been separated by the nations and COVID pandemic by 4 years. The last two years were the toughest time for me, the pandemic came when we scheduled to meet in the US. I nearly gave up, but my wife gave me the strength to fight back. Therefore, this thesis is not only my work, but she has contributed as well.

Definitions

I_o	Incident light intensity
n	Refractive index
$\Delta Trans$	Transmissivity
$\dot{\omega}_i$	Production rate
v	Net stoichiometric coefficient
R	Total number of reactions
M	Total number of species
k_{rw}	Forward rate coefficients
k_{rv}	Reverse rate coefficients
A	Pre-exponential factor
E	Activation energy
R_u	Universal gas constant
MW_c	Molecular weight of carbon
D	Distance between the impinging point to the examined pixel
x_{imp}	Location of impinging point in X-axis

y_{imp}	Location of impinging point in Y-axis
N_{pixel}	Number of pixels
t	Time
θ	Angle in polar coordinate
ED	Expansion rate
I_{int_i}	Integrated intensity
I_{local}	Local intensity
$I_{int\_ave\_i}$	Area-averaged integrated intensity
K	Curvature
TV	Tangent vector
s	Distance on the curve
m	Third parameter for curve fitting
m_{left}	Relative distance between the left neighbor pixel and target pixel
m_{right}	Relative distance between the right neighbor pixel and target pixel
k	Thermal conductivity
T	Temperature

d	Distance between surface and embedded thermocouples
Q	Heat release rate
γ	Constant for gas mixture
Vol	Volume of the combustion vessel
P	Pressure
$I(x,y)_{CFD}$	Intensity obtained from CFD simulations
T_{amb}	Ambient temperature
ρ_{amb}	Ambient density
P_{inj}	Injection pressure
t_{vimp}	Timing of vapor fuel impingement
t_{fimp}	Timing of flame impingement
q''	Heat flux
Nu	Nusselt number
Re	Reynolds number
Sh	Sherwood number
Sc	Schmidt number

$\boldsymbol{Pr}$	Prandtl number
$\boldsymbol{\phi}$	Equivalence ratio
$\boldsymbol{m_{film}}$	Mass of film

List of abbreviations

IRT	Intensity Radial Time
CFD	Computational fluid dynamics
UHC	Unburned hydrocarbon
PM	Particulate matter
ICE	Internal combustion engines
EGR	Exhaust gas recirculation
LTC	Low-temperature combustion
PAH	Polycyclic aromatic hydrocarbon
LIF	Laser-induced fluorescence
TEM	Transmission electron microscope
DI	Direct injection
RIM	Refractive index matching
DNS	Direct numerical simulation
CV	Combustion vessel
FEA	Finite element analysis

DAQ	Data acquisition system
LED	Light-emitting diode
RANS	Reynolds-averaged-Navier-Stokes
LES	Large-eddy-simulation
AMR	Adaptive mesh refinement
CHT	Conjugate heat transfer
NSC	Nagle and Strickland-Constable
KH/RT	Kelvin Helmholtz- Rayleigh Taylor
ASOI	After the start of injection
aHRR	Apparent heat release rate
FFT	Fast Fourier transform
SOI	Start of injection
ASI	After start of impingement
SMD	Sauter Mean Diameter
PDF	Probability density function
FFD	Flame front distance

FER	Flame expansion rate
AID	After the ignition delay

Abstract

The spray impingement in diesel engines attracts the attention of engine researchers in recent decades as the physical size of the engine is reduced. Due to the spray impingement, the atomization, vaporizing and air-fuel mixing quality is altered compared to a free spray. For emission control, soot is one of the major particulate emissions from diesel combustion and its formation in an impinged spray is worthy to be investigated.

Firstly, to understand the impinged spray characteristics, the experiments for both non-vaporizing and reacting conditions were conducted in a constant volume combustion vessel. The impinged spray was captured by a high-speed camera and the instantaneous spray propagation distance and rate were obtained. For a better understanding, the microscopic behavior of the spray propagation, the curvature of the impinged spray was calculated and a relationship between local fuel distribution and soot formation was found. After that, the apparent heat release rate from an impinge spray combustion and the heat flux through the impingement were analyzed. The apparent heat release rate was obtained by the internal chamber pressure and the heat flux was measured by heat flux probes embedded in the impinging plate.

Then, the soot formation of an impinged spray was both studied from experiments and simulations. In the experiments, the natural luminosity mainly due to the incandescence of soot particles was captured by the high-speed camera. A computational fluid dynamics (CFD) approach was adopted to quantitatively study the soot formation in terms of absolute soot mass and soot mass fractions in the vicinity of the wall. In the last, the film formation under different ambient temperatures, impinging distances, and oxygen concentration was investigated in terms of film area and thickness. The impact of film formation on the soot outcomes was then investigated by comparing the rate of film vaporization and soot formation.

To summarize, the main goal of this dissertation is going to benefit the understanding of the impinged spray in reacting diesel-relevant engine conditions. From experiments, a

global view of soot formation in an impinged spray was analyzed and the mechanism of soot formation was further revealed by the CFD simulations.

1 Introductions

1.1 Motivations

In recent decades, even the percentage of green energy such as solar, wind, and nuclear energy is increasing, fossil fuel is still used as the main power supply for the automotive industry. In the United States, near 80% of US energy is provided by fossil [1]. Since internal combustion engines still dominates the power supply area for transportation services, it is necessary to improve the efficiency of the combustion devices to reduce the wasted power as well as the emissions such as NOx, UHC (unburned hydrocarbon), CO_2, and soot which will lead to global warming but mostly human health issue.

Diesel engines, compared with gasoline engines, have potential higher thermal efficiency [2]. At the same time, the conventional diesel combustion will produce particulate matter (PM) and NOx because of the ambient high-temperature and rich fuel-air mixture. Several advanced diesel combustion strategies such as low-temperature combustion have been applied to reduce the soot formation and NOx since the soot and NOx are formed at high-temperature and fuel-rich zones [3–5]. The conventional diesel combustion process is mainly controlled by the air-fuel mixing process which is affected by turbulence [6]. As the engine size becomes more compact, the diesel spray with high injection pressure would lead to the spray impingement hitting on the piston head or the sidewall of the combustion chamber. The spray impingement introduces additional turbulence into the fuel vaporization, air entrainment, and flame propagation [7,8]. The induced turbulence may benefit the air-fuel mixing and reduces the possibility of incomplete combustion. However, the heat loss from the spray through the wall may lead to lower thermal efficiency and quenching effect in the near-wall region. Hence, the mechanism of spray impingement is necessary to be fully understood the concept of low-temperature diesel impinged spray combustion.

Besides the heat loss through the wall, the deposition of fuel on the piston head by the liquid spray impingement especially under the cold-start conditions when the liquid length is longer than the travel distance is another concern for the emission control and thermal efficiency [9]. The deposition of fuel on the hard surface, called wall-wetting or film formation, will affect the fuel vaporization and fuel-air mixing process in the near-wall region. Fuel film has been known as a source of emission outcomes as it is hard to achieve complete combustion in the peripheral area of the film. Although the global properties such as film mass, area, and thickness are quantified by the previous research [9–13], the film-flame interaction under the diesel case is barely studied. In the real engine cycle, if the fuel film from one cycle could not be burned, the unburned fuel will accumulate and affect the heat load in the next cycle [14]. Therefore, it is necessary to investigate the film formation and its correlation with soot formation in a diesel impinging spray under various test conditions such as different ambient temperatures and oxygen concentrations.

1.2 Goals and objectives

The goal of this thesis is to provide a thorough understanding of the diesel impinging spray regarding the spray and flame development, film formation in both non-vaporizing and reacting conditions, thermal characteristics such as heat release rate, and heat transfer through the wall and soot outcomes under different operating conditions. In order to achieve the goal, this research consists of four objectives which are broken into different chapters including the findings from both experiments and simulations to support the goal.

The first objective is to extend the characteristics of impinged spray such as local expansion distance, expansion rate, and local fuel distribution from a non-vaporizing spray to a reacting spray. The findings from the comparison of the non-vaporizing and reaction spray contribute to the understanding of the effect of reactions on the global spray momentum, spray shape, and local spray morphology with different ambient temperatures.

Heat loss from the spray through the wall would lead to a lower heat release rate (lower thermal efficiency) and delayed ignition. Therefore, the second objective is to investigate

the heat transfer between the spray and the impinging surface. The apparent heat release rate is firstly investigated for test conditions under different ambient temperatures. The heat flux is measured by three embedded heat flux probes in the impinging surface and the results are analyzed for reacting conditions. The heat flux measurements are conducted with different ambient temperatures and different locations with respect to the impinging point.

The soot formation in an impinging spray is complex compared to a free spray. The soot outcome is not consistent with the involvement of spray impingement but depends on the various factors such as impinging distance, wall and charge gas temperature, and whether there is a film formed. Therefore, the third objective is to study the soot formation in an impinging spray under different operating conditions. Not only the effect of impingement on the location of soot formation but also the quantitative analysis is evaluated from both experiments and simulations. The location of soot formation is analyzed by using the IRT method under different ambient temperatures. The qualitative information of soot formation is then extracted from the Intensity-Radial-Time (IRT) plots. From simulations, the quantitative soot formation in terms of soot mass fraction and its relationship with local temperature and equivalence ratio is obtained. The findings from this goal give a detailed insight into how soot is produced for an impinging spray both qualitatively and quantitatively.

The liquid film is a special phenomenon for spray impingement when the liquid portion of the spray contacts the hard surface. The film is found to be one of the sources which contribute to the soot formation. Therefore, the last objective of this dissertation is to investigate the film formation in a reacting environment and its impact on the soot production for an impinging spray. As it is hard to accomplish the measurement of film, soot formation simultaneously with combustion which involves the optical signals contributed by the soot incandescence, CFD simulations are performed to visualize the liquid film formation under different ambient temperatures, impinging distances, and oxygen concentrations. Meanwhile, the rate of soot formation and film formation is then

correlated to quantitatively explain the influence of liquid film on instantaneous soot production.

1.3 Thesis organization

With the listed objectives, the thesis is organized into twelve chapters. The first chapter describes the introduction to the spray impingement phenomenon, the goals, and the objectives of the current thesis.

Chapter 2 provides detailed literature regarding the impinged spray characteristics from both non-vaporizing and reacting conditions, soot formation in diesel spray combustion, the film formation in non-vaporizing and vaporizing conditions, and its role in reacting conditions.

Chapters 3 to 4 give a summary of the experimental and numerical approaches utilized in the current study. Chapter 3 provides an overview of the experimental facilities, test conditions, and experimental diagnostics. The setup of optics, combustion vessel, data acquisition system will be provided. The test conditions in the current thesis are summarized and the diagnostics are briefly introduced. Chapter 4 explain the numerical platforms, the configurations of the CFD simulations, spray, turbulence, film, combustion and soot models.

In Chapter 5, all of the methods of post-processing are introduced as follows: firstly, the boundary tracking for the impinged spray and flame. Then, the IRT method and the curvature calculation for the spray boundary. Followed by the histogram of the intensity distributions and the heat flux calculation. Next, the calculation of the apparent heat release rate and the signal filtering and processing for the temperature profiles. Lastly, the validation of simulations regarding the spray penetration, ignition delay, and macroscopic characteristics is also depicted in this chapter.

Chapter 6 starts to discuss the results obtained from the high-speed images by Mie scattering and natural luminosity from non-vaporizing and reacting conditions,

respectively. In this Chapter, the macroscopic characteristics of spray impingement such as instantaneous impinged spray distance and the expansion rate, the IRT plots, and the histogram of the intensities are provided.

Chapter 7 reports the microscopic characteristics of spray impingement including the curvatures of the boundary of the impinged spray, the local fuel distribution, and soot formation along the spray boundary. The state-relationships of the curvatures and the fuel distribution and soot formation are correlated. The microscopic characteristics are also validated for simulations to make sure that the simulations could predict the transient behavior of the impinged spray properly.

In Chapter 8, the apparent heat release rate from the reacting conditions and the heat flux of an impinging diesel spray is discussed. The heat flux are calculated to explain the temporal heat loss at various locations on the wall under different ambient temperatures.

Chapter 9 discusses the soot formation in an impinged spray from both experiments and simulations. A detailed schematic of the chemical species formed in an impinging spray is provided. The flame development under different ambient temperatures is explained using the data visualization tool. The soot quantity, local temperature, and local equivalence ratio are obtained from simulations and their relationships are statistically investigated.

Chapter 10 depicts the film formation on a roughened hard surface and its contribution to the subsequent soot formation in the combustion process. Firstly, the film formation consisted of film thickness, area, and mass, as well as its evaporation process are examined in non-reacting conditions. Then, the film formation is investigated in reacting conditions incorporating with the flame through simulations.

Chapter 11 summarize the main conclusions and findings of this thesis and the recommendations for future studies.

The references are listed in Chapter 12 and the in-house post-processing codes are included in Appendix A. The copyright permission from three publishers, SAE international, the

American Society of Mechanical Engineers, and the International Journal of Engine Research are provided in Appendix B.

2 Literature reviews[1]

2.1 Diesel spray characteristics

Diesel engines are widely used in automotive industries because of their high thermal efficiency and low load advantages over spark-ignition engines. However, NOx and soot particles are often produced in diesel engine combustion due to the dominant mixing-controlled incomplete combustion [2]. The pollutant issue becomes important in recent years because of the environmental protection impact. Therefore, several advanced

---

[1] Reprinted with permission from SAE papers 2019-01-0067 and 2019-01-0267 ©2019 SAE International and 2021-01-0543 ©2021 SAE International. Reprinted with permission from International Journal of Engine Research (IJER) and the American Society of Mechanical Engineers (ASME). The materials in this chapter were published in the following papers:

- Zhao, Z., Zhu, X., Zhao, L., Naber, J. et al., "Spray-Wall Dynamics of High-Pressure Impinging Combustion," SAE Technical Paper 2019-01-0067, 2019, https://doi.org/10.4271/2019-01-0067.
- Zhao, Z., Zhu, X., Naber, J., and Lee, S., "Impinged Diesel Spray Combustion Evaluation for Indirect Air-Fuel Mixing Processes and Its Comparison with Non-Vaporing Impinging Spray Under Diesel Engine Conditions," SAE Technical Paper 2019-01-0267, 2019, https://doi.org/10.4271/2019-01-0267.
- Zhao, Z., Zhu, X., Zhao, L., Tang, M. et al., "A Numerical Study for the Effect of Liquid Film on Soot Formation of Impinged Spray Combustion," SAE Technical Paper 2021-01-0543, 2021, https://doi.org/10.4271/2021-01-0543.
- Zhao, Z, Zhao, L, & Lee, S. "Evaluation of Soot Production Near a Cold Surface for an Impinged Diesel Spray Combustion." Proceedings of the ASME 2020 Internal Combustion Engine Division Fall Technical Conference. ASME 2020 Internal Combustion Engine Division Fall Technical Conference. Virtual, Online. November 4–6, 2020. V001T05A002. ASME. https://doi.org/10.1115/ICEF2020-2938
- Zhao Z, Zhu X, Naber J, Lee S-Y. Assessment of impinged flame structure in high-pressure direct diesel injection. International Journal of Engine Research. 2020;21(2):391-405. doi:10.1177/1468087419859788

combustion strategies and designs of engines have been developed and applied to diesel engines to reduce the formation of NOx and soot further.

Since the thermal NOx is mainly formed in relatively high-temperature combustion, a low-temperature combustion strategy has been developed to reduce the formation of NOx significantly [15]. The design of engine combustion devices, especially the shape of the piston head, has also been evaluated via the engine performance, emission levels, and heat losses [16]. The swirl ratio could be optimized by modifying the shape of the piston head to reduce the formation of NOx. However, it has been reported that spray impingement takes place when using the irregular shape of the piston head to improve the air-fuel mixing through the swirl. Recently, spray impingement has received significant attention for the pollution generated during the cold-start-up and affected engine performance when increasing the compression ratio.

The spray process, especially in diesel engines, is one of the keys in terms of optimizing the in-cylinder combustion process. Lots of experiments were conducted to evaluate the spray behavior of either non-reacting or reacting cases [17–22]. To understand the mechanism of fuel vaporization, the liquid fuel penetration was measured under a wide range of four aspects: 1) The injection pressure, 2) The orifice diameter, 3) The ambient gas temperature, 4) The fuel volatility, and temperature. It turns out that the liquid length will change linearly with the orifice diameter, but the length is independent of the injection pressure. If the fuel is a mixture of high volatility and low volatility fuel, the liquid length mainly depends on the properties of low volatility fraction [6]. The nozzle geometry fuel blend effects were investigated under experiments that were conducted in a constant volume combustion chamber [23]. Four different nozzle geometries include: 1) Divergent, 2) Straight, 3) Straight-rounded, 4) Convergent-rounded were used to quantify the spray characteristics. At the same time, different combinations of fuel mixture were also investigated under the auto-ignition process. Several conclusions were addressed based on the experimental results: The discharge coefficient is varied at different nozzle geometry while the convergent nozzle has a higher coefficient and divergent has a smaller one. The

spray liquid penetration would decrease due to the increases of the ambient pressure and temperature which shows the same trend as the previous study [6].

The spray impingement will re-distribute the velocity field and introduce the turbulence into the fuel expansion. The behavior of normal and oblique impingement is varied due to the momentum change after the impingement. Several types of research were based on normal injections [8,24,25]. Yoshio et al. measured the velocity distribution of the diesel spray after the impingement through the Particle image velocimetry technique [26]. They tested different injection angles and found that the normal impingement will lead to lower velocity compared with a tilted injection. And the surface properties and fuel adhesion on the plate will affect the velocity distribution. The radial thickness growth of the impacted fuel which is also called rebound height is reported under different injection pressure, vessel density, and wall temperature. After comparing the numerical and experimental results, the current CFD spray models show the uncertainties for high injection cases due to complex spray-wall interaction [8]. Due to the non-uniform combustion chamber of the piston head, the diesel spray won't impinge on the wall normally instead of having an incident angle [24,27,28]. Even though the incident angle effect on the velocity distribution is investigated by [26], the behavior of the fuel expansion which has non-symmetric velocity is not fully understood. To quantify the fuel expansion pattern on the plate, Zhu et al. defined the expansion properties by tracing the impinging point and outer boundary of an oblique injection [29].

Several parameters such as rebound height impinged spray distance and expansion rate are chosen as the main measurable index of the non-vaporizing impinged spray. Yu et al. evaluated the effect of fuel blend ratio, ambient temperature, ambient density on the behavior of impinged spray [30]. They found that there are three factors having the dominant influences on the behavior of impinged spray: 1) the mass and momentum of the impinged spray; 2) the spreading or splashing resistance on the surface; 3) the strength of the air entrainment. They argued the impinged spray radius is mainly affected by the momentum of the impacting spray while the impinged spray leading edge height is mainly

affected by the surface tension and viscosity of the fuel. Especially, the impinged spray radius increases and the height decreases with the raised level of air entrainment.

A conceptual model of non-vaporizing impinged spray was described in Zhao et al [31]. In this model, the spray experiences the initial penetration, mixing process before the impingement and expansion on the plate. It is noted that there is a stagnation region on the top of the leading edge. The air-fuel mixing process becomes poor in this region and this could further lead to soot production in reacting cases. Ma et al. investigated the spray and evaporation of a certain diesel blend without the impingement [32]. With the air entrainment analysis, the spray volume increases as the injection pressure increases. The increased spray volume could enhance the air-fuel mixing process. A high injection pressure could penetrate farther and break the larger droplets into smaller ones to enhance the air-fuel mixing process.

The spray impingement with combustion becomes more complex. The flame impingement involves the chemical reactions and heat release from reactions that may contribute to the total wall heat flux. Therefore, the heat flux attributed by the flow is better to be firstly evaluated in non-reacting conditions to exclude the influence of combustion. Torregrosa et al. measured the heat flux in engine motoring conditions [33]. They found that the temporal heat flux is mainly affected by the temperature of ambient gas instead of inner plate temperature. Wang et al. conducted the spray impingement tests in an open area with different injection pressures, impinging distances, and wall temperatures [34]. The impinging and peripheral regions were defined based on the radial temperature profiles. The temperature drop is the maximum at the impinging point and recovering in the peripheral regions. As the flow velocity is increased or impinging distance is reduced, the temperature drop in the impinging region is increased. The temperature drop is the maximum when the temperature of the wall is close to the Leidenfrost temperature of the fuel. Hou et al. also investigated the effect of mass flux and temperature of the wall on the local heat flux and heat transfer coefficients [35].

As the heat flux from the spray to the wall is fuel sensitive, Zhou et al. used n-pentane as the fuel to investigate the relationship between heat flux and film formation under different injection pressure and surface temperature [36]. They found that the peak heat flux is linearly correlated with injection pressure and surface temperature. The film residence time is reduced with a higher surface temperature and injection pressure. Further, Zhou et al. extended their studies adopting different fuels. It was revealed that fuel with a lower boiling point and higher enthalpy of vaporization would result in a stronger cooling effect in non-flash boiling conditions [37].

2.2 Reacting spray-wall interaction at diesel operating conditions

Advanced injection and combustion phasing strategies have been widely adopted in internal combustion engines (ICEs) to improve thermal efficiency and reduce pollutant emissions [26]. Although diesel engines have a higher thermal efficiency than gasoline engines, they produce more NOx and soot particles.

A great number of researchers have focused on the spray combustion processes in diesel engines in the past decades [38–42]. As stated in the study [23], the auto-ignition of diesel free-spray combustion often takes place downstream of the vaporized spray jet. Dec provides a detailed and important conceptual model of conventional diesel spray combustion, which is shown in Figure 2.1, based on the laser-sheet images of diesel spray combustion [7].

In this conceptual model, the liquid fuel experiences dispersion, atomization, vaporization process, and a mixing process with air. This schematic also depicts the diesel combustion process in between the auto-ignition and end of injection. In this quasi-steady process, the ambient air penetrates the interface between the high-temperature fuel vapor and ambient gas, leading to the production of diffusion flame. In contrast, the oxygen penetrates the low-temperature region (brown region after the liquid fuel) and generates a thin, fuel-rich, premixed region. The mixture expands downstream and the temperature is increased into the range of the soot production temperature (1300 K-1600 K). Therefore, the downstream

is occupied by a small amount of soot and combustion products which is shown as a blue region. A high-temperature core where the high soot region is located is formed inside the downstream (red and yellow region).

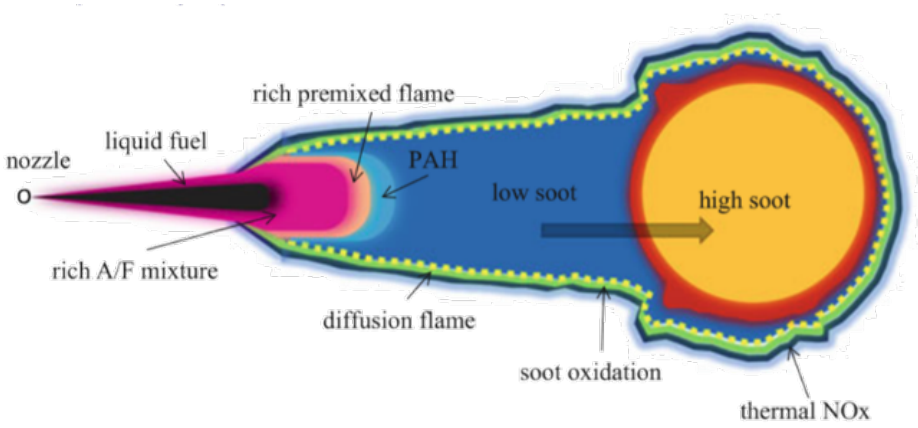

Figure 2.1. A conceptual model of diesel free-spray combustion [7].

A soot-rich core is formed downstream from the conventional diesel combustion. This core potentially leads to pollutant emissions. With tightening government regulations of particulate matter, the priority of reduction in soot particles has been emphasized significantly. Several strategies, such as exhaust gas recirculation (EGR) and partially premixed charge compression ignition, are applied to diesel engines to remove or reduce the formation of soot particles [15,43–45].

Lowering the temperature of the charged gas is one of the ways to minimize thermal NOx in diesel combustion. However, the reduced temperature may lead to incomplete combustion and subsequently generate more soot particles. A low-temperature combustion (LTC) model has been introduced in diesel combustion to assess the low-temperature combustion process [5,15]. Although this LTC conceptual model has not been well verified by all LTC strategies, it provides initial results towards a common description of low-load and single-injection applications. In the LTC model, ignition occurs at the farthest downstream and propagates back toward the nozzle tip. It is reported that soot only forms downstream and the soot occupied region will shrink with the crank angle increases [15].

However, compared with free spray combustion, the impinged fuel jet may lead to liquid film formation due to the short distance between the nozzle and piston head in cold-start conditions, which generates a fuel-rich zone and deteriorates the combustion process. In contrast, the spray impingement on the piston head could also generate finer fuel particles which help the air-fuel mixing process and subsequently optimize combustion. Most of the studies in the spray-wall interaction have focused on the non-vaporizing cases and local film formation [9,12,46], while very few studies have been done to study the detailed spray-wall dynamics and flame propagation of impinging diesel combustion. Several researchers have quantitatively measured the soot concentration in impinged spray combustion. Wang et al. introduced the fuel impingement and nozzle size effects on the soot formation process [42]. The two-color pyrometry was used to quantify the temperature of the soot region. The width, surface area, and height of the normal impinged spray flame were measured through flame luminosity captured by the high-speed camera. They observed that the structure of the impinged flame remained in a quasi-steady state which was comparable with free spray combustion. Du et al. used the natural luminosity technique to quantify the injection pressure impact on ignition and combustion characteristics of impinging diesel spray [47]. With the increased injection pressure, the ignition location is stretched toward the surface of the impinging plate. Increased injection pressure tends to reduce the soot formation due to the optimized air-fuel mixing process because of finer fuel droplets generated by the impingement. However, when introducing a cold impinging plate into the experiments, they suggested using a low injection pressure to elevate the ignition location for normal impingement.

In order to study the inner structure of impinged spray combustion, Bruneaux used laser-induced fluorescence (LIF) with two excitation wavelengths to detect the hydroxyl (OH) radicals and polycyclic aromatic hydrocarbon (PAH) of diesel jet combustion in a constant volume combustion chamber [48]. With simultaneous LIF images, an impinging combustion conceptual model is summarized. In the quasi-steady state of impinging combustion, the diffusion flame is formed at the interface between the ambient air and fuel. The soot is formed near the impinging plate but OH radicals are formed above the soot and

attached with the reaction zone of diffusion flame. After looking at the LIF images, several stages have been defined:

1. Formaldehyde (CH_2O) is formed during the appearance of a cool flame. OH radicals are formed by consuming the formaldehyde with cool flame expansion.

2. During the diffusion portion of combustion, the interface of low and high-temperature is located through the detection of formaldehyde and OH regions, indicating the reaction zone of diffusion flame.

3. Formaldehyde is also observed in the rich premixed zone which is comparable with Dec's conceptual model.

However, Bruneaux's model only shows the normal impingement of fuel spray. With the irregular shapes of piston heads and the arrangement of injectors, the fuel jet will impinge the solid surface with an incident angle. The tilted fuel jet will generate non-symmetric fuel expansion and air-fuel mixing.

The heat loss on the impinging surface due to spray impingement in the combustion process also receives attention because it will affect thermal efficiency and emission levels. Also, the heat loss could lead to terminated combustion near the wall called the quenching effect. Some researchers found the surface temperature could influence the flame structure, ignition delay, as well as ignition location. Under the low surface temperature, the ignition delay is longer while the flame height and width increase as the surface temperature is increased. For reacting conditions, the flame hits the wall instead of a cooling spray and there will be heat loss from the flame to the wall, subsequently leading to termination of combustion near the wall. The heat loss reduces the combustion efficiency as well. From experimental studies, the spatial heat fluxes from reacting conditions were reported. Pillai et al. found that the heat flux is the highest at the stagnation region, i.e., impinging region and decaying with the increase of the radial distance [49]. Kawanabe et al. also found the same behavior with Pillai's research but with a numerical method [50]. After obtaining the heat flux, the local heat transfer coefficients were calculated from the heat flux through the

continuity equation. Moussou et al. investigated the effect of injection pressure and impinging distance on the peak heat transfer coefficients. It was revealed that the peak heat transfer coefficient was increased with a higher injection pressure and lower impinging distance [51]. Similar to the methodology from [51], Mahmud et al. calculated the spatial heat flux and heat transfer coefficient at different radial directions. They found the waveforms of heat flux were correlated with local flamelet speed and the profiles of heat flux had similar shapes even in different radial positions [52]. Some researchers found the surface temperature could influence the flame structure, ignition delay, as well as ignition location [53]. Under the low surface temperature, the ignition delay is longer while the flame height and width increase as the surface temperature is increased. Heat loss from the spray to the cold surface results in delayed ignition and locally flame quenching near the wall, producing more soot particles in the vicinity of the surface [52]. Zhang et al. quantified the relationship between ignition delay, wall temperature, and ignition location with an impinging spray [53]. When the wall temperature was increased, the ignition delay was shortened, and the ignition location was further moved downstream to the wall. The effect of wall temperature on flame development was studied [54]. In their study, a lower wall temperature case showed low-temperature ignition happened in the vortex generated by the impingement and followed by high-temperature ignition kernels at the outer surface of the vortex. At a high wall temperature, the high-temperature ignition kernel was found in the near-wall region without the appearance of low-temperature ignition. For the flame propagation, both lower and higher wall temperature cases showed that the flame propagated from the high-temperature ignition kernel along the stoichiometric iso-surface throughout the whole spray, but the directions varied. They also concluded that the maximum area-averaged heat flux is multiple times higher for a low wall-temperature case than a high wall temperature case. Zhao et al. measured the heat flux during the spray impingement by using a heat flux probe [55]. It was found that the heat flux was the highest near to the impinging point where the spray directly hit on the wall which agrees with the results from a recent work [49].

2.3 Soot formation in diesel spray combustion

Due to the recently tightened emission regulations in the automobile industry, soot formation is one of the main concerns for the emission control of diesel engines. Two factors that globally affect the soot formation in diesel sprays are local temperature and equivalence ratio. The relationships among soot, equivalence ratio, and temperature were well described in the chart from Kitamura et al. [56]. In Figure.10 from ref [56], soot is mostly formed in the range of temperature from ~1500 to 2500 K and equivalence ratio above 2.

The spray impingement in reacting cases is hard to capture since most fuel is vaporized before the impingement and the vapor phase is transparent. The results showed that there will be more soot if the impingement is involved in the combustion process [57]. Increased injection pressures could reduce soot emissions in a non-linear fashion. In contrast, Fattah et al. found that soot temperature and content were reduced by the spray impingement [58]. Shorter impinging distances further reduced soot temperature and content because of an enhanced mixing process. Such a conflict makes the soot formation in spray impingement more complex. Liu et al. also investigated the effect of wall distance to the injector tip and wall temperature on the combustion characteristics [59]. Short wall distance and high wall temperature lead to shorter ignition delay and stable flame development. Li et al. compared free sprays with impinging sprays and the impinging spray was into two types: no-liquid contact and liquid contact impingement [57]. The combustion was enhanced under no liquid contact but deteriorated under liquid contact impingement. Liquid-contact impingement leads to pool flame generation near the wall and unburnt fuel in the spray.

For an impinged diesel spray combustion, although the soot production is reduced with the help of enhanced mixing due to spray impingement [58,60], there is still noticeable soot production in an impinging flame. They concluded that a reduced impinging distance could reduce soot production but the relationship between impinging distance and soot production is non-linear. It is further revealed that the mixing mechanism is different with different impinging distances [60]. The mixing of an impinging spray includes

impingement-enhanced mixing and entrainment wave mixing. With a shorter impinging distance, the impingement-enhanced mixing becomes stronger and boosts the overall mixing rate, showing a peak in the entrainment rate profile. While with a longer impinging distance, the impingement-enhanced mixing and entrainment wave mixing act serially to maintain a constant mixing rate.

To study the soot formation, the characteristics of soot particles such as the diameter of a particle was obtained through transmission electron microscope (TEM) images. The soot aggregates formation and breakup process for a free spray were described in ref [61]. A large number of smaller size primary particles were formed on the surface of the large soot particles upstream. As the axial distance is increased, the aggregates carbonized and then break into smaller compact particles. However, for an impinging spray, several factors, e.g., swirl flow direction, injection pressure, and jet-jet interaction, are considered related to the size of soot particles [62–64]. From these studies, soot formed in the impinging region has a relatively small diameter. As the flame propagates along the impinging surface, the small-size soot particles merge to form larger aggregates. The effect of the direction of induced air swirl on the soot morphology was depicted with optical engine tests [64]. Distinct soot primary particles, long-chain soot aggregates, and fractal large soot aggregates were observed in the impinging, down-swirl (counter clock-wise) and up-swirl (clock-wise), respectively. Although the up-swirl location showed the larger soot aggregates, the number of aggregates is smaller than the impinging region and down-swirl location, reflecting lower soot concentration in soot luminosity images. A higher injection pressure generates larger soot aggregates in pool fire but smaller soot aggregates in the exhaust due to the enhanced soot oxidation rate [62]. The spray-wall interaction with a single-hole injector or jet-jet interaction with a multi-hole injector presumably creates a fuel-rich region and the interactions would alter the air entrainment rate and subsequently soot oxidation [65]. The studies for nano soot structure could give us insights into soot formation and oxidation in diesel flames and help explain the soot formation in the near-wall region.

2.4 Film formation in spray impingement

Liquid films formed on the cylinder and piston head are known as one of the main sources of producing unburned UHC and particulate matter emissions. The emissions are attributed to the deteriorating vaporization and mixing process due to a lack of contact between the ambient gas and film surface [66]. When the film is formed, it could lead to fuel-rich zones after vaporization and further develop pool flames when the fuel-rich mixture interacts with the flame front. An increased injection pressure could reduce the amount of fuel mass deposited on the wall because high injection pressure could change the behavior of droplets from sticking on the wall to splashing [67]. At low wall temperatures, the film exhibited a wavy pattern with no voids inside the film. As the wall temperature was increased, the film area was decreased, and voids are found in the film [68]. Luo et al. found that there was a possibility that the rebound or splashed droplets re-deposited on the wall [69]. The possibility of the re-deposited film may contribute to the soot formation after the end of injection.

Liquid contact also leads to the wall-wetting phenomenon which generates a liquid film on the wall after the impingement. A number of researchers investigated film formation under different operating conditions. LIF is an optical method that could capture film. The laser reflection method was employed by Saito et al. to explore the behavior of adhered fuel film on a wall during a small size direct-injection (DI) diesel engine development [70]. They found that the film thickness of the adhered fuel was found to be 10 μm to 50 μm, and the fuel film area on the wall is strongly affected by the wall temperature. Sendai et al. employed a 355 nm LIF technique to measure the film thickness of a spray impinging on a glass plate in a constant volume combustion vessel [71]. The results showed that the ratio of the adhered fuel to the total injected fuel was about 40% at 10 ms after the end of injection and this ratio does not change with the injection duration. Schulz et al. evaluated the effect of injection pressure, ambient density, and charge pressure on the film thickness [72]. High temperature, longer traveling distance, and higher injection pressure lead to thinner wall film. Even though laser diagnostics could achieve an accurate measurement,

the low frequency of the laser sheet posed difficulty for continuous measurement. Besides, the calibration procedure was too complex. Therefore, Drake et al. developed a novel optical method called the Refractive Index Matching method (RIM) [9]. The calibration procedure of RIM is relatively easy to apply, and it could generate a continuous and time-resolved film thickness measurement. Direct measurement of film properties was conducted by Yu et al. using an oil thickness sensor [30]. The sensor was placed under the injector and the measurement was carried out at atmospheric pressure and room temperature.

All the results of film measurements show that the spray momentum mainly governs the film formation, where the momentum is determined by the injection pressure and ambient density. Besides spray momentum, wall surface and fuel properties also affect film deposition. The film area is increased with higher injection pressures on a smooth surface [9]. However, the film area experienced a reduction with higher injection pressure on a roughened surface [12]. With higher volatility fuels like n-heptane, the film area, mass, and film thickness are much smaller compared with lower volatility fuels such as diesel [12]. The magnitude of the film thickness of a diesel spray is generally above 10 μm [73] while that of an n-heptane spray is under 2 μm [12].

LIF is an optical method that could capture film, PAH, a known soot precursor, and soot luminosity simultaneously. Film and soot incandescence in an optical engine were simultaneously visualized in ref [11]. Tracing the soot incandescence originated from the film, it turns out that soot was adjacent but quenched to film. The adjacence was clearer in ref [10] as the appearance of PAH was also reported. Soot, PAH, and film were connected serially, and strong PAH signals were found peripherally to the film, depicting the transformation from film to soot. Although soot formation is still initiated near the film region, it is reported that film does not strongly affect the bulk flame. For film models, there are many numerical models summarized in ref [74] but a 1D direct numerical simulation (DNS) model has been recently developed [75]. Compared to ref [74], the 1D DNS model considers the temperature gradient in the film instead of treating the film

temperature as uniform. Also, the flame quenching near the film surface is taken into account in the DNS model. It turns out that the flame quenching distance is linearly correlated to the thickness of the fuel vapor layer above the film.

Even there existed a number of studies focusing on the film formation and heat transfer for an impinging spray, most of them were conducted either in non-vaporizing or vaporizing conditions [76–79]. The flame-film interaction was investigated mainly in gasoline operating conditions because the ignition happens later than the end of injection [76,77]. At that time, the liquid film is already deposited and there is no spray coming out. Jungst et al. [10] and Stevens et al. [80] investigated the pool fires phenomenon in gasoline applications. However, for diesel cases, it is more difficult to study the flame-film interaction because the spray impingement, film deposition, and auto-ignition happen simultaneously.

3 The experimental facility, test conditions, and methodology

3.1 Combustion vessel and supplying hardware's overview

3.1.1 Combustion vessel overview

This spray-wall impingement experiment was carried out in a high-pressure, high-temperature constant volume combustion vessel (CV). The CV is a 1.1 L cubic chamber with good optical access. The maximum temperature and pressure that the vessel could maintain are ~ 2000 K and ~ 5000 psi, respectively. Three types of port windows were installed on all six surfaces of the cube: 101 mm diameter transparent window (sapphire), blank metal window, and injector window. The windows were sealed by an o-ring and gasket which made the natural gas leakage less than 6 psi at an initial 100 psi and 30 psi at an initial 500 psi in the vessel during 1 min. The unobstructed orthogonal optical access is coupled with high-speed imaging techniques to study spray development. The impinging plate was mounted on the bottom, and the injector was installed on one of the side windows. Three ports on the eight vertices of the chamber are used for the intake/exhaust of chamber ambient gas, and a mounted dynamic pressure transducer. A Kistler 6001 piezo-electric dynamic pressure transducer coupled with a Kistler 5044a charge amplifier was used to measure the CV pressure. A 3D model of the combustion vessel body is shown in Figure 3.1. The model of the combustion vessel in Solidworks.

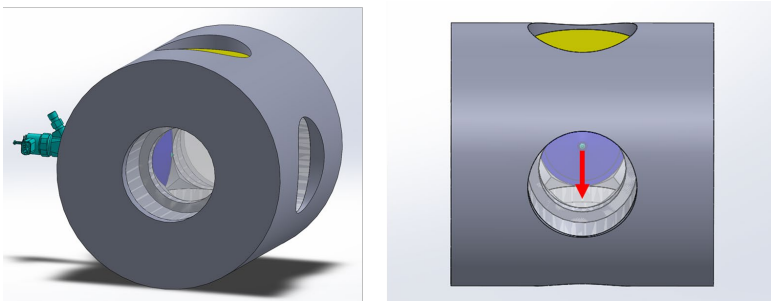

Figure 3.1. The model of the combustion vessel in Solidworks.

Besides the main vessel body, several sub-systems are briefly described here. A high-pressure fuel delivery system was used to provide the target back pressure to a Bosch LBZ solenoid diesel injector. The fuel cart was designed and built by the Alternative Energy Research Lab at Michigan Tech. The fuel cart includes a storage tank, two fuel accumulators, an oil pump, and a front panel to control the valves, monitor the fuel pressure through the gauges. The fuel is initially pressurized by the shop air to ~ 20 psi and then further dramatically pressurized by the oil pump to the target injection pressure. The fuel pressure at the outlet of the fuel cart could reach up to 2500 bar for diesel. A mixing vessel was built to provide the target gas composition to the main combustion vessel. The mixture was made based on the calculation of mixture composition which was provided by the Engine Combustion Network (ECN) [81]. The reactants consisted of acetylene, hydrogen, oxygen, and nitrogen. A spark plug and two fans were mounted on the top window of the vessel. The fans were placed symmetrically to the spark plug to provide a homogeneous environment after the pre-burn process. After the pre-burn, the acetylene and hydrogen were consumed but the unconsumed oxygen was left in the vessel according to the target oxygen volume fraction. A pressure rise in the chamber from the beginning of the filling process is shown in Figure 3.2. After the filling process, a signal is sent to trigger the spark plug to ignite the mixture. The chamber pressure, as well as the bulk temperature, are both increased. Once they reach the target pressure, another signal is sent to the injector to provide the fuel in the vessel. A second pressure rise is also revealed, and it is due to the auto-ignition of the spray.

Based on the different objectives, the impinging plate is switched between quartz transparent window, surface roughened plate, and the metal plate with heat flux probes embedded. The photos of the arrangement of these different impinging surfaces are shown in Figure 3.3.

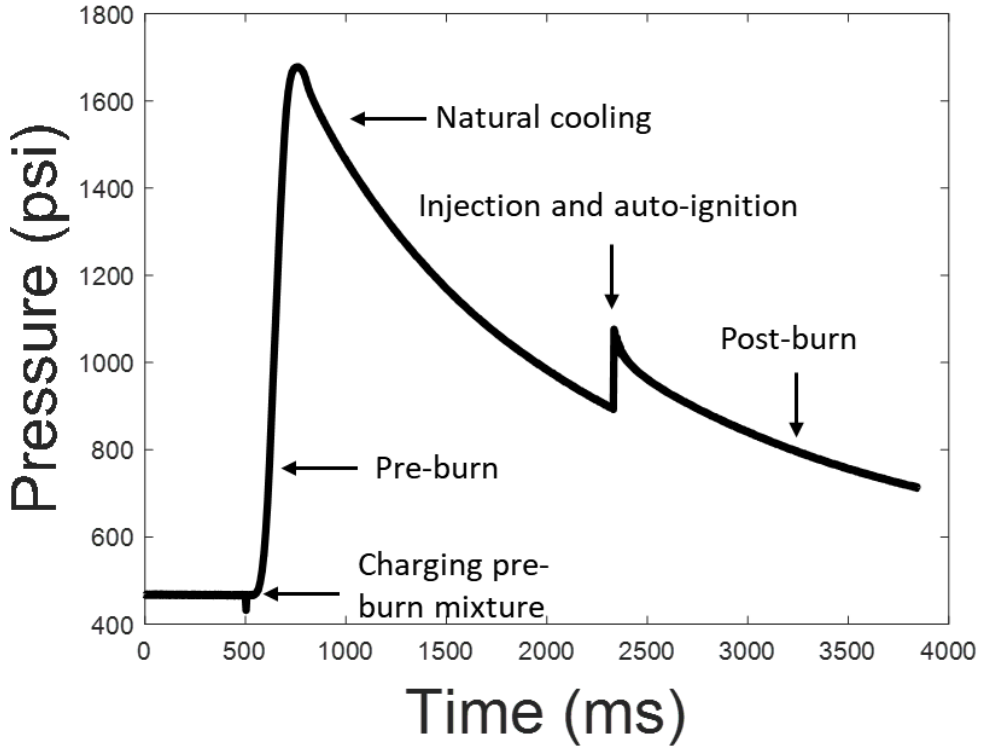

Figure 3.2. The pressure curve on a single combustion event from the start of the test to the end of the combustion.

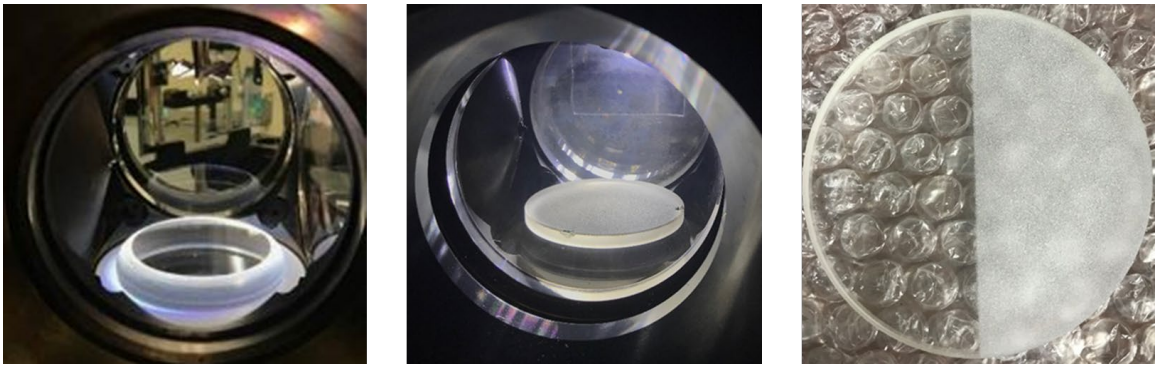

Figure 3.3. From the left to right: transparent quartz impinging window embedded in the combustion vessel, impinging window + additional artificial roughened impinging plate for film thickness measurement, artificial half-smooth-half-roughened impinging plate. The metal impinging plate is not shown here as it shares the identical geometry with the quartz impinging window.

3.1.2 Data acquisition systems and metal impinging window fabrication

The finite element analysis (FEA) analysis has been carried out using ABAQUS/CAE 6.14-3 tool and the best-suited design has been chosen based on stress and temperature distributions on the window plate surface. The window design consists of six heaters, seven thermocouples, and three heat flux transducers.

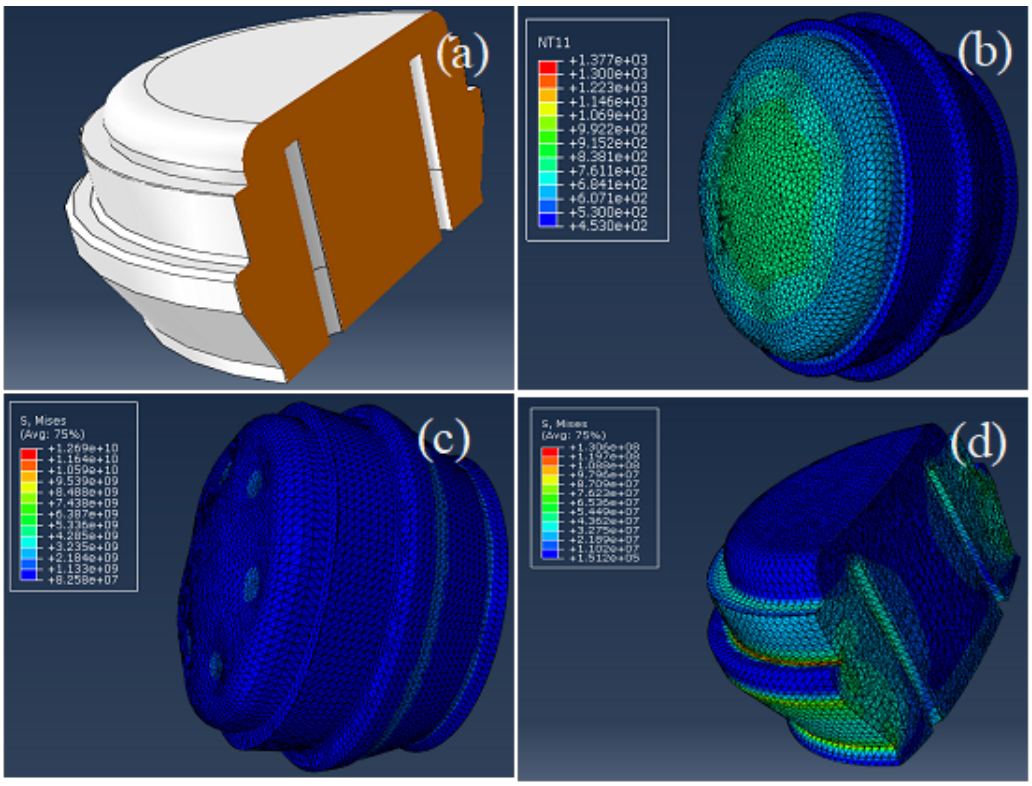

Figure 3.4. Impingement window final design/configuration (a), and FEA results: (b) Temperature distribution; (c) Von-Moises stress distribution; (d) Von-Moises stress distribution with 350 bar load.

From the FEA simulation results based on Figure 3.4(a), the window plate temperature is estimated at 800 K and the Von Moises stresses are around 100 bar (see Figure 3.4(b) and 3.4 (c)). It can be concluded that the window design/configuration can withstand the given pressure and thermal conditions of the combustion vessel and can be achieved a desired uniform temperature of the plate. Further, all six heaters should be positioned 10 mm below

the window plate (top surface), in order to maintain the uniform desired temperature. Further, the analysis for 350 bar load conditions is made to study the material elastic limitations. In this analysis, the only external load is applied in terms of pressure and omitted the thermal loads. From the analysis, the Von-Moises stresses are well below the yield strength of the window material is shown in Figure 3.4(d). Therefore, the current window design/configuration can be used for spray impingement experiments in the combustion vessel.

A single-hole injector nozzle with 120° full-included angle were designed with a fuel injector nominal nozzle outlet diameter: 200 µm.

The data acquisition systems include a National Instruments chassis and two data acquisition system (DAQ) cards. An in-house Labview program is designed to record the temperature signals from either start of the injection or the start of pre-burn ignitions. The trigger level is set to 5 volts as a rising edge and the sampling rate is set to 100 kHz which corresponds to a resolution of 0.01 ms. The resolution could fulfill the requirements of capturing the spray impingement event. The acquisition process is described in Figure 3.5.

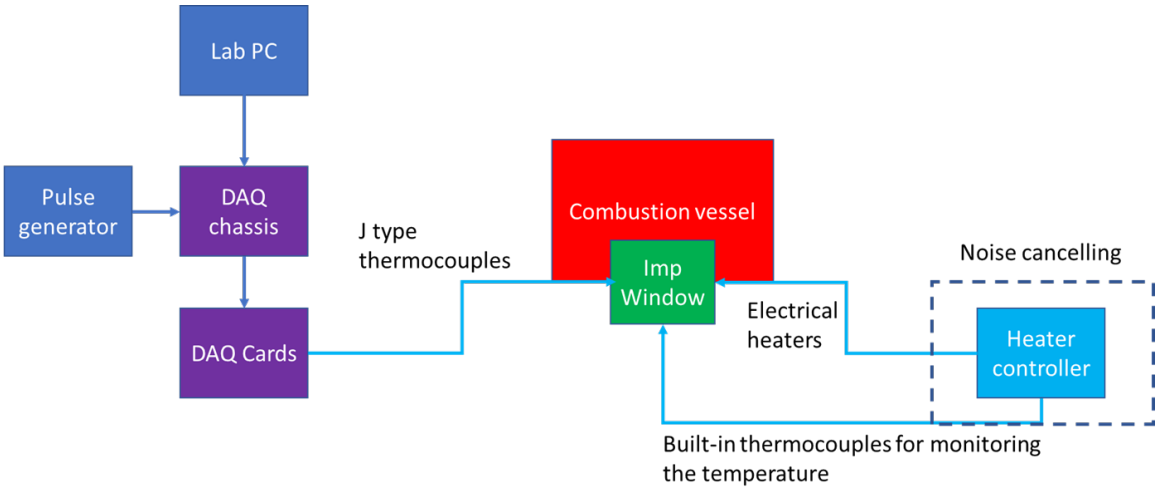

Figure 3.5. Schematic temperature recording during the injection and combustion event.

In addition, the PID heater controller, electrical heaters, and monitor thermocouples are shown in Figure 3.6. And the control logic for the recording program is explained in Figure 3.7.

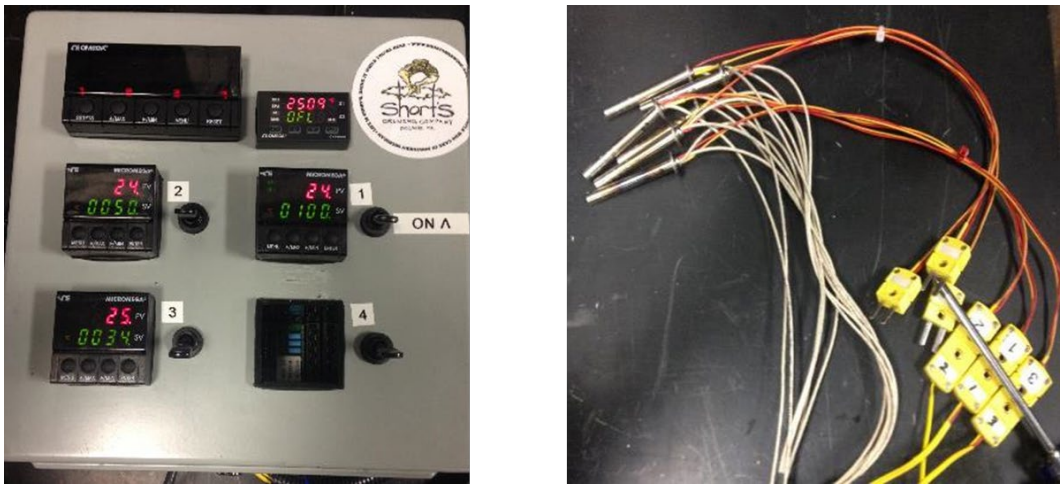

Figure 3.6. Heater controlling box with built-in PID controller, electrical heaters, and monitoring thermocouples.

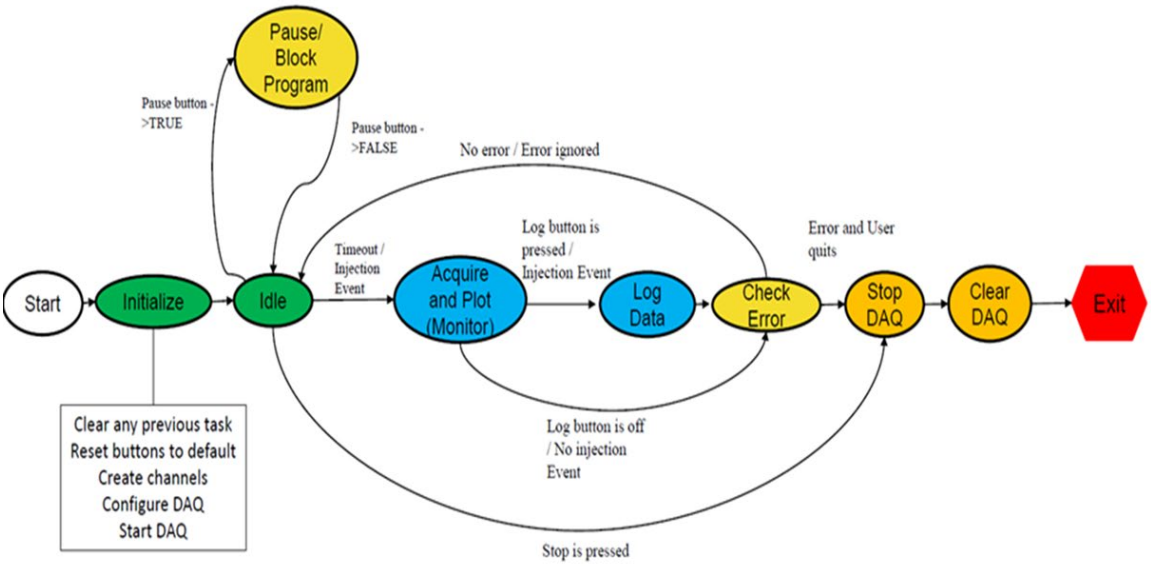

Figure 3.7. Control logic of the temperature recording process in an in-house Labview program.

The J-type thermocouples for the heat flux measurements are calibrated from both the bench test and the combustion vessel test. The response time of the J-type thermocouple is less than 400 μs. The impinging plate is set to the temperature from 100 to 200 °C in the bench test and 100 to 250 °C in the combustion vessel test. The results for the bench and combustion vessel tests are listed in Figure 3.8.

Bench Test								
	Set Temp	Measure Temp Plate	Measure Temp Edge	Middle TC 1	Middle TC 2	Outer TC1	Outer TC2	Outer TC3
Unit	C	C	C	C	C	C	C	C
1	100	88	88					
2	120	107	107					
3	150	135	137					
4	180	164	165	171.72	174.637	171.06	165.8	171.3
5	200	183	184	191.77	194.73	190.77	185.39	191.02
CV Test (CV temp is 100 C)								
	Set Temp	Measure Temp Plate	Measure Temp Edge	Middle TC 1	Middle TC 2	Outer TC1	Outer TC2	Outer TC3
1	100	93						
2	120	112						
3	150	137		146.282	146.021	141.6	141.75	143.056
4	180	163		174.69	175.989	165.621	168.007	167.726
5	200	179		194.723	196.045	181.43	185.003	185.6
6	225	195		217.811	219.779	201.593	206.531	205.249
7	250	222		242.3	244.767	221.587	227.115	226.742

Figure 3.8. Impinging plate temperature calibration in bench and combustion vessel test.

3.2 Test conditions

In this section, the test conditions for spray, combustion, and CFD simulations are summarized. The first section includes the diesel spray tests for the impinged spray characteristics such as impinged spray distance, fuel mass, and soot distribution, etc. The second section includes specific test conditions for film formation. The n-heptane replaced diesel as the target fuel because the thickness of diesel film is out of the range of the RIM method. In the third section, the test conditions for CFD simulations are listed. It is noted the models and detailed configuration of the simulations will be introduced in Chapter 4.

3.2.1 Test conditions for impinging diesel spray

The test conditions for spray tests including both reacting and non-vaporizing conditions are listed in Table 3.1. The test fuel, injection pressures, nozzle diameter, impinging angle, fuel temperature, energizing injection time, injected fuel mass, impinging distance, ambient gas concentration, and ambient temperature are listed. The differences between the non-vaporizing and reacting spray are the injection pressure and ambient gas composition. To maintain the total injected mass in the vessel, the injection pressure was set to 1500 bar for reacting conditions. To investigate the effect of oxygen concentration on the combustion, the oxygen composition after pre-burn was set to 15% and 18%.

Table 3.1. Test conditions for the impinging spray

Parameters	**Value**	**Unit**
Fuel	Ultra-low sulfur diesel	-
Fuel injection pressure (P_{inj})	1200, 1500, 1800	bar
Nominal nozzle outlet diameter	200	μm
Orifice orientation relative to injector axis	60	°
Fuel temperature	363	K
Energizing injection time	2	ms
Injected fuel mass	24 at 1500 bar P_{inj}	mg
Vertical distance between injector tip to impinging distance	40	mm
Oxygen mole fraction	N_2, 0%, 15%, 18%	-
Ambient density (ρ_{amb})	14.8, 22.8, 30.0	kg/m^3
The ambient gas temperature at injection (T_{amb})	423, 800, 900, 1000	K

3.2.2 Test conditions for film measurements

For film measurements, two different optical setups were used for the film measurement: the Refractive Index matching method and the direct backlit method. The RIM method could quantitatively measure the film thickness and area but it has limitations for the film thickness of low-volatile fuel such as diesel. Therefore, for the film measurement, n-heptane replaced diesel as the target fuel. Also, the injection pressure of n-heptane could not reach over 1500 bar. Hence, two lower injection pressures, 600 and 900 bar were added to the test conditions. The test conditions for film measurement are listed in Table 3.2.

Table 3.2. Test conditions for the film measurement

Parameters	**Value**	**Unit**
Fuel	N-heptane	-
Fuel injection pressure	600, 900, 1200, 1500	bar
Nominal nozzle outlet diameter	200	μm
Orifice orientation relative to injector axis	60	°
Fuel temperature	363	K
Energizing injection time	2	ms
Injected fuel mass	24 at 1500 bar P_{inj}	mg
Vertical distance between injector tip to impinging distance	40	mm
Oxygen mole fraction	N_2	-
Ambient density	14.8, 22.8, 30.0	kg/m^3
The ambient gas temperature at injection	423	K

3.2.3 Test conditions for CFD simulations

In this section, the test conditions for CFD simulations are introduced. As diesel is a multi-component fuel, diesel2 was used in the CFD simulations. The reaction mechanism is adopted from [82] with 44 species and 139 reactions. The test conditions for simulations are listed in Table 3.3. To investigate the film formation under different impinging distances, two impinging distances, 30 and 40 mm, were set in the CFD simulations.

Table 3.3. Test conditions for CFD simulations

Parameters	**Value**	**Unit**
Fuel	Diesel2	-
Fuel injection pressure	1500	bar
Nominal nozzle outlet diameter	200	μm
Orifice orientation relative to injector axis	60	°
Fuel temperature	363	K
Energizing injection time	2	ms
Injected fuel mass	24 at 1500 bar P_{inj}	mg
Vertical distance between injector tip to impinging distance	30, 40	mm
Oxygen mole fraction	18%, 21%	-
Ambient density	22.8	kg/m^3
The ambient gas temperature at injection	800, 900, 1000	K

3.3 Methodologies

In this section, the methodologies for the experiments will be introduced. Four different optical diagnostics, Mie scattering, shadowgraph and schlieren, refractive index matching, and natural luminosity are sequentially introduced.

3.3.1 Mie scattering

Mie scattering is a theory based on the elastic scattering of incident light in the droplets, named by Gustav Mie [83]. This typically happened when the droplet/particle size is larger than the wavelength of incident light. On the contrary, Raleigh scattering described a phenomenon when the droplet/particle size is smaller than the wavelength of incident light [84]. In the current study, the droplet size from diesel spray is larger than the wavelength of the backlight which is hundreds of nanometers. The intensity of Mie outcomes from an elastic particle is mainly determined by the incident angle of the light, the intensity of the incident light, I_o, and the power of droplet diameter. Under the identical backlight environment, the droplet diameter will be the dominant factor that affects the intensity outcome. Thus, the Mie scattering signals could be used to qualitatively explain the global spray shape where the liquid droplets occupied and the droplet size in the spray. Sample images from the Mie scattering for the spray test and film measurement are shown in Figure 3.9.

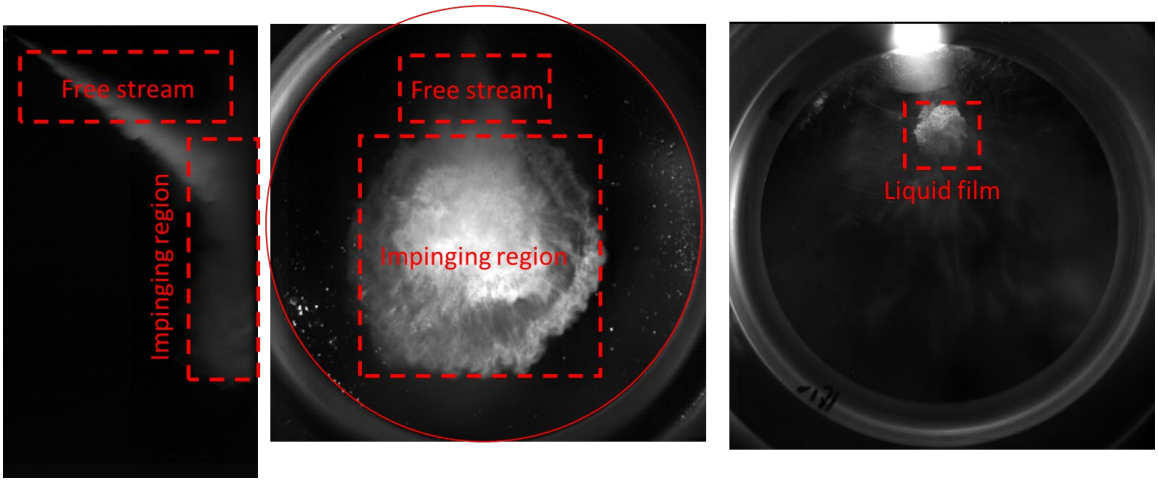

Figure 3.9. From left to right: the side view of an impinging spray, the bottom view of an impinging spray, and the film mark left on the impinging surface. All images were taken by the Mie scattering signals. It is noted that the side and bottom views were taken by diesel spray while the film image was taken by an n-heptane spray.

3.3.2 Shadowgraph and schlieren

As the Mie scattering could only capture the liquid phase of the spray and lack the sensitivity of vapor in a high-temperature environment. Therefore, the shadowgraph and schlieren techniques are adopted mainly to detect the transparent fuel vapor based on the density gradients [85–87]. A Z-shaped schlieren was applied due to the room space limitation of the lab which was also shown in Figure 3.10. The light from a digital mode light-emitting diode (LED) became a point light after passing through a focusing lens. A parabolic mirror was used to expand the point source into a collimated light and this collimated light would be focused back to the camera by using the second parabolic mirror. To visualize the ambient air movement more clearly, a knife-edge was placed in front of the camera lens. Otherwise, the shadow technique was considered without placing the knife edge.

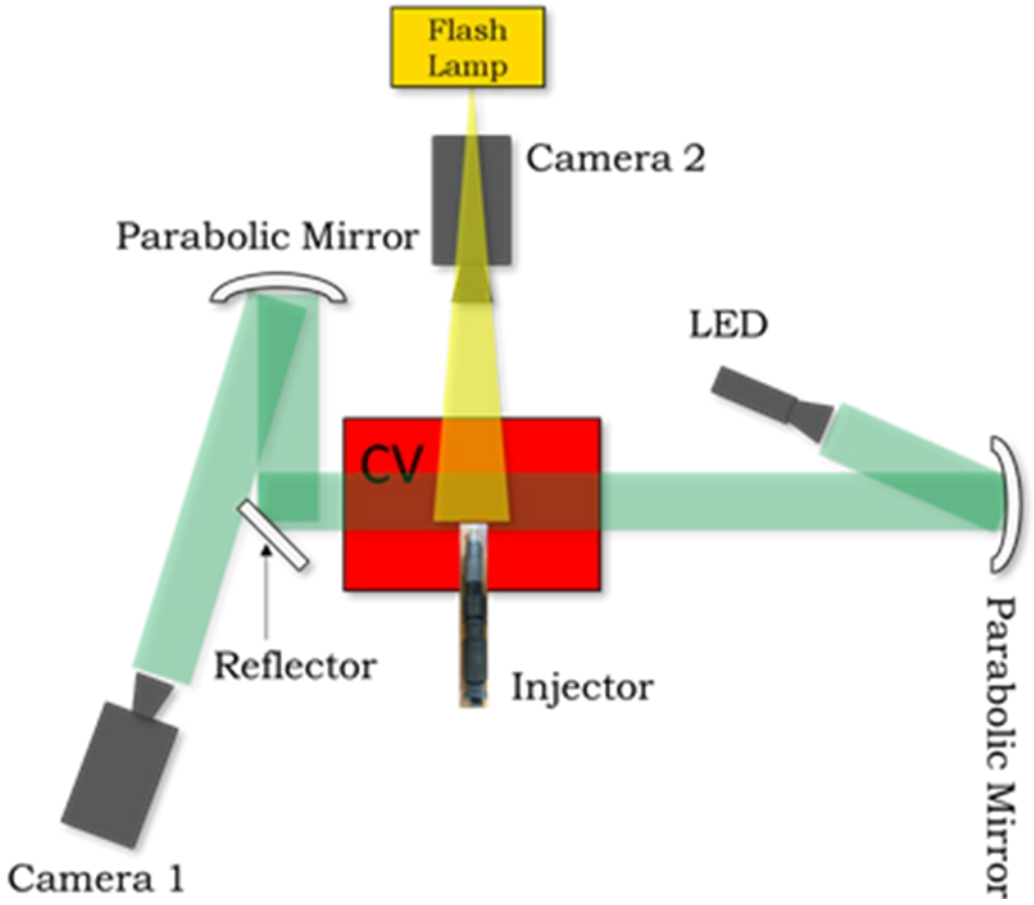

Figure 3.10. The Z-shaped schlieren setup for spray test.

3.3.3 Refractive index matching

RIM is one of the optical techniques that could evaluate the thickness of a liquid film when it is deposited on a roughened impinging surface. The RIM could provide temporal and spatial characteristics of the liquid film through the scattering light ratio from the roughened surface before and after the film deposition. This method requires a similar refractive index between the impinging surface and target fuel. In the current thesis, the refractive indexes for n-heptane and the impinging surface are 1.39 and 1.46, respectively. The relationship between film thickness, surface roughness, and a film-covered area is depicted in Figure 3.11.

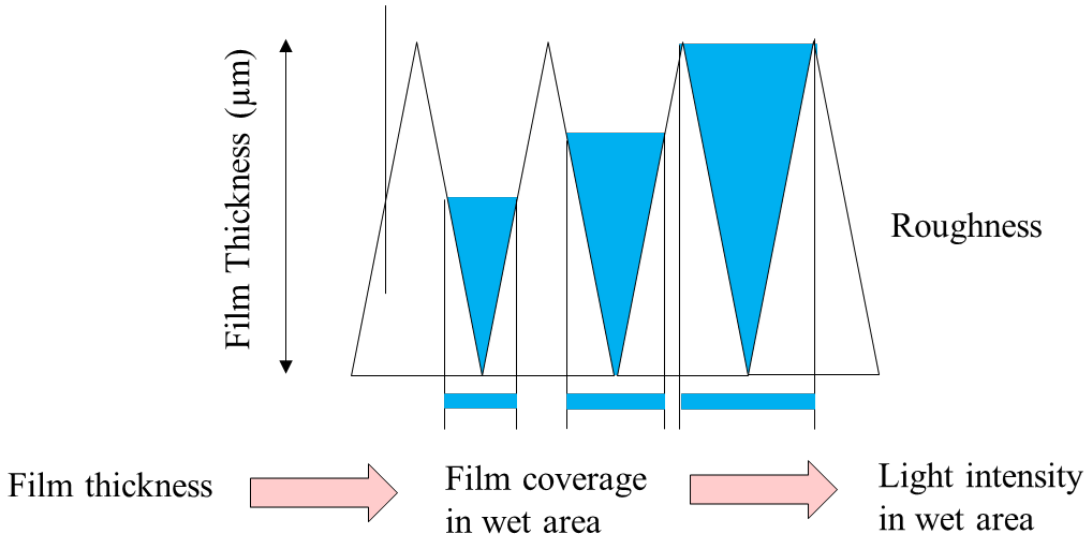

Figure 3.11. Relationship between film thickness, surface roughness, and a film-covered area.

In addition, the schematic of film formation is explained in Figure 3.12. The high-speed camera is looking from the bottom of the impinging surface. Naturally, the roughness of the surface could scatter the incident light on the surface. As the film is deposited on the surface and trapped by the roughness, the incident light from the light source is scattered and diffused on the surface, subsequently changing the intensity in the film region. Therefore, the transmission ratio $\Delta Trans$, which is determined by one minus the ratio of the intensity in a wet area to the intensity of dry area, could be correlated with the film thickness through a calibration process. After that, for the actual spray tests, by finding the local transmission ratio, the film thickness could be calculated.

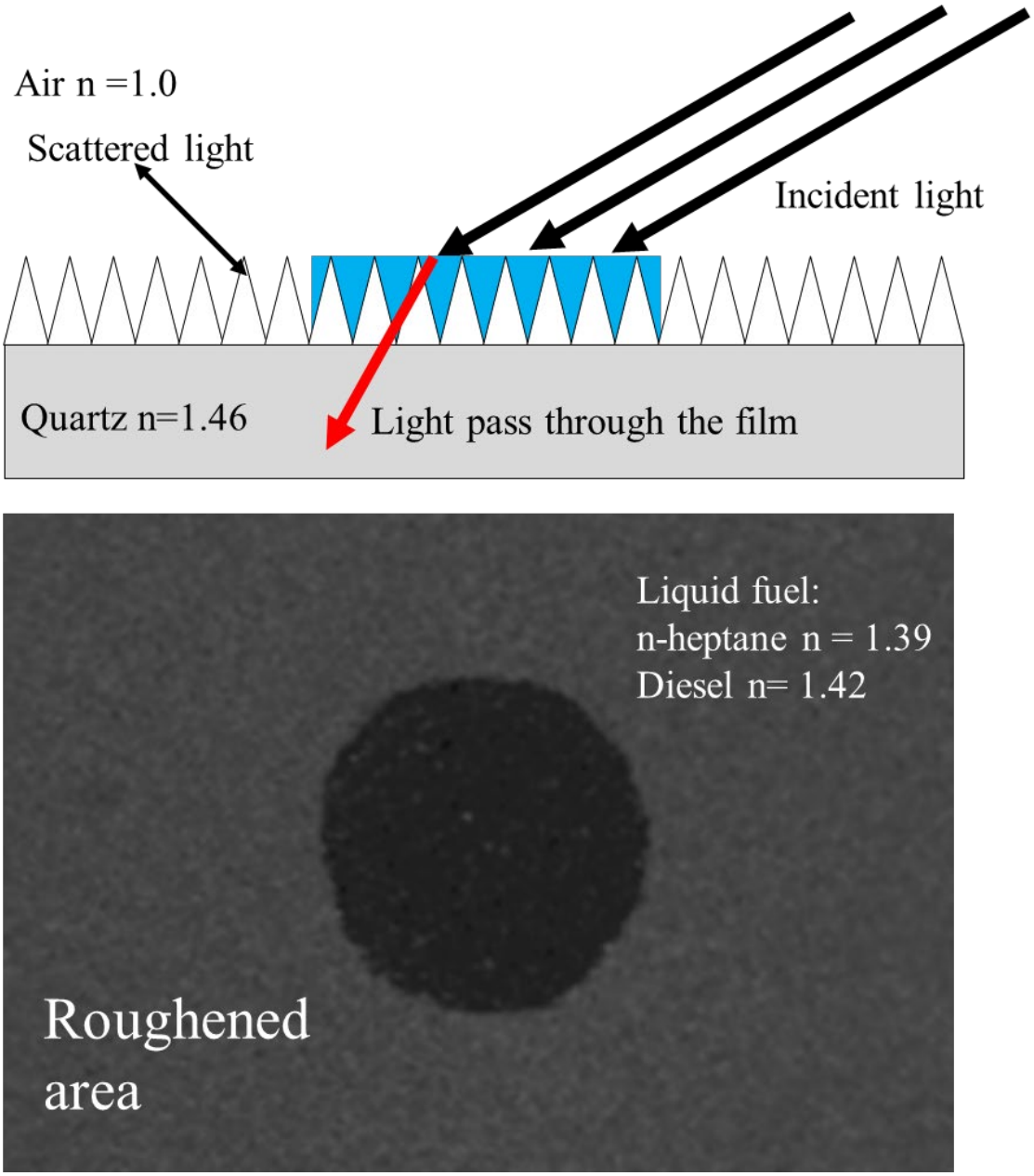

Figure 3.12. The schematic of film formation and the RIM technique fundamentals.

In the calibration, a known volume of the fuel is smoothly deposited on the impinging surface. Divided by the film occupied area, the film thickness could be calculated. Therefore, to avoid the splash from the injection, a precise syringe with the finest resolution of 0.05 mm^3 was used to inject a known volume of fuel on the roughened surface. The injected volume is from 0.5 to 1.5 µL with an increment of 0.1 µL. As n-heptane is a

relatively high-volatile fuel and it may start to evaporate during the deposition, a fuel mixture combining n-heptane and low-volatile fuel dodecane was used for the calibration. The purpose of the dodecane was going to determine the maximum film occupied area. Two compositions were adopted: 90% n-heptane with 10% dodecane, and 95% n-heptane with 5% dodecane. The average transmission ratio and average film thickness in the film region were curve-fitted to obtain the calibration curve. The calibration curve for the current film measurement is shown in Figure 3.13. In addition, the RIM method has a limitation that it could not measure the film thickness higher than surface roughness. Besides, the precision of RIM depends on the contrast of image which is mainly affected by the camera detection range and light intensity.

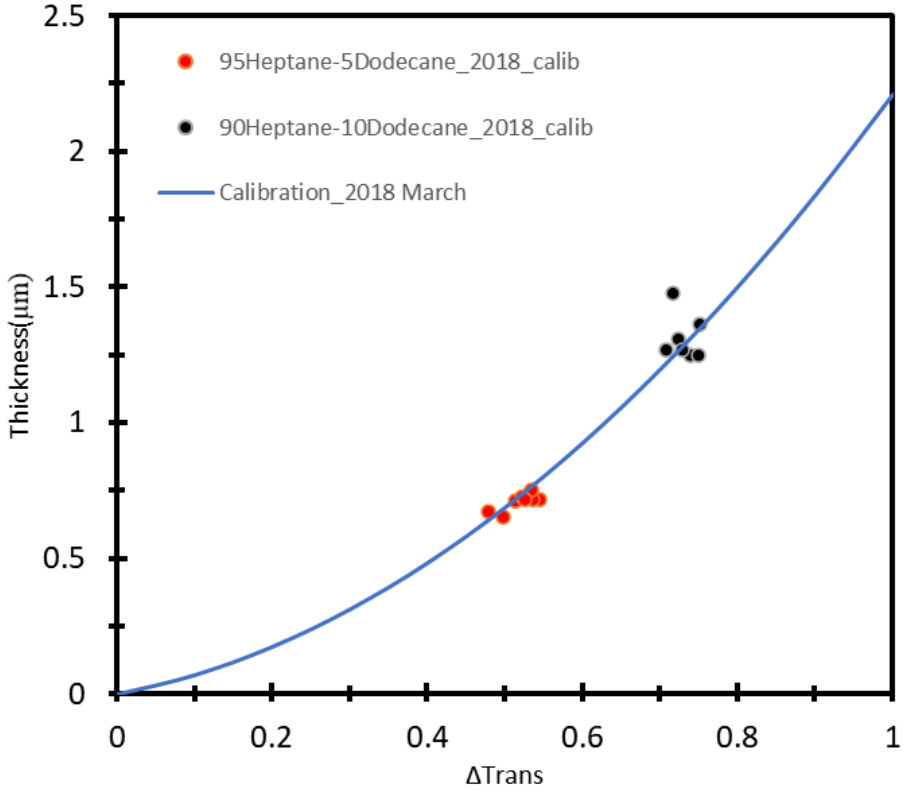

Figure 3.13. The relationship between the transmissivity to the film thickness. Two mixtures were used for the calibration. The equation for the calibration curve is that thickness = $1.667*\Delta Trans^2 + 0.5454*\Delta Trans$.

In addition, the surface roughness profile was measured by a laser profilometer. Four random locations on the roughened surface were examined and the profiles are shown in Figure 3.14.

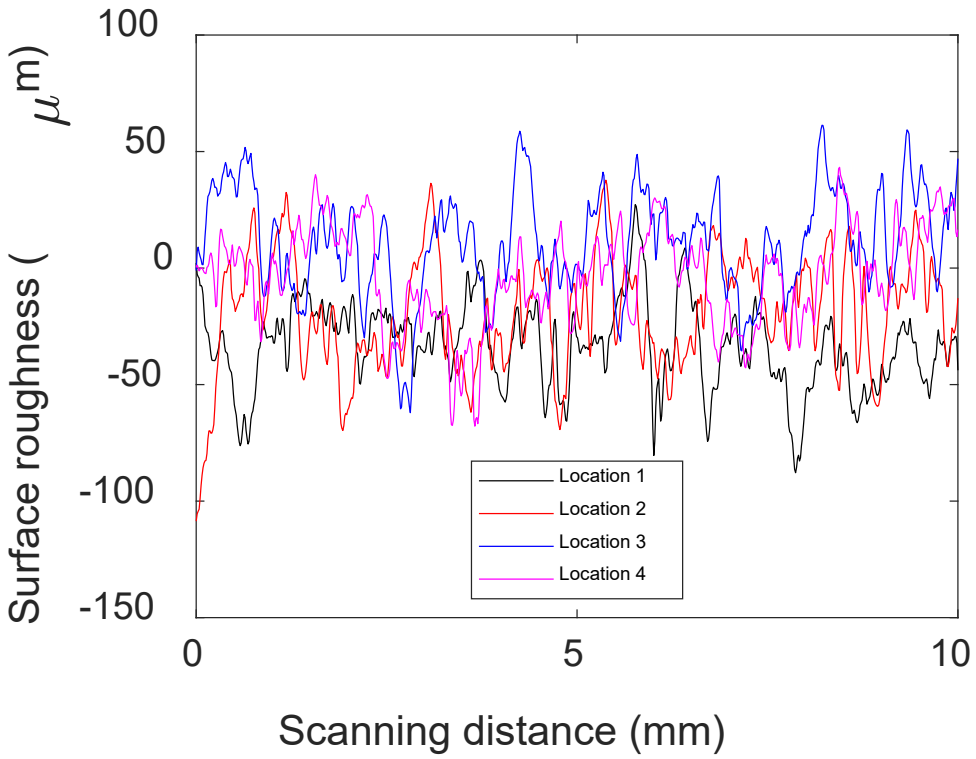

Figure 3.14. Surface roughness on the impinging surface.

3.3.4 Natural luminosity for diesel spray combustion

Natural luminosity is the luminosity generated by the radials' incandescence from the black-body radiation [88–90]. In a diesel spray combustion, the luminosity is dominantly contributed by the radiation from the soot particles. In naked observers such as eyes, the flame is yellow-ish because of the soot incandescence in a high-temperature environment. In addition, the intensity level of soot incandescence is proportional to the soot volume fraction. Therefore, the natural luminosity of a diesel flame is widely used in the engine-related area to qualitatively explain the soot formation. In the experiments, the flame was captured by an 8-bit monochrome high-speed camera and there is no need to supply an

additional light source to light the spray/flame. A sample image from the natural luminosity looking from the bottom is shown in Figure 3.15. The impinging plate is marked by a red circle.

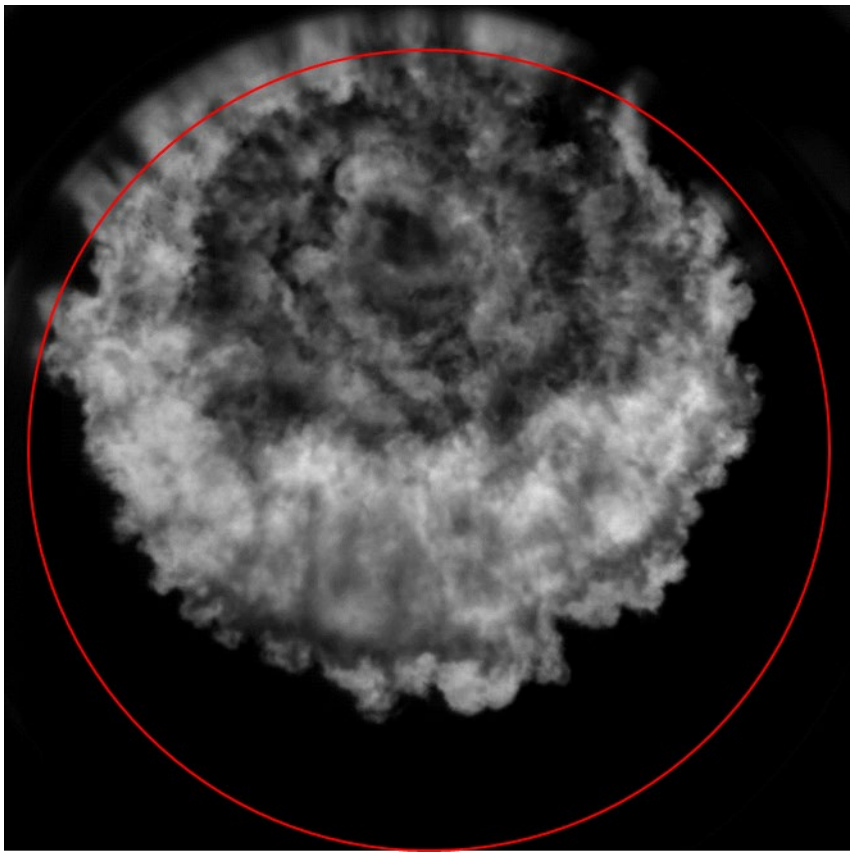

Figure 3.15. Sample natural luminosity image. T_{amb} = 900 K, 18% O_2, P_{inj} = 1500 bar and ρ_{amb} = 22.8/kg/m^3.

3.3.5 Droplet sizing measurements

Malvern Spraytec has been used to measure the droplet size. The working principle of Malvern Spraytec system is: Light from the laser emitter is scattered by the spray droplets. The laser beam is expanded by the collimating optics to provide a wide parallel beam. The scattered light is focused by a focusing lens on a Fourier arrangement and picked up by the detector array. Non-scattered light is focused by the focusing lens so that it passes through the pinhole at the center of the detector array. This is measured by the beam power detector

to give the light transmission. The angle at which a particle diffracts light is inversely proportional to its size. The detector array is made up of over 30 individual detectors, each of which collects the light scattered by a particular range of angles. There is a data channel for each of these. Measuring the angle of diffraction determines the size of the particle, as shown in Figure 3.16.

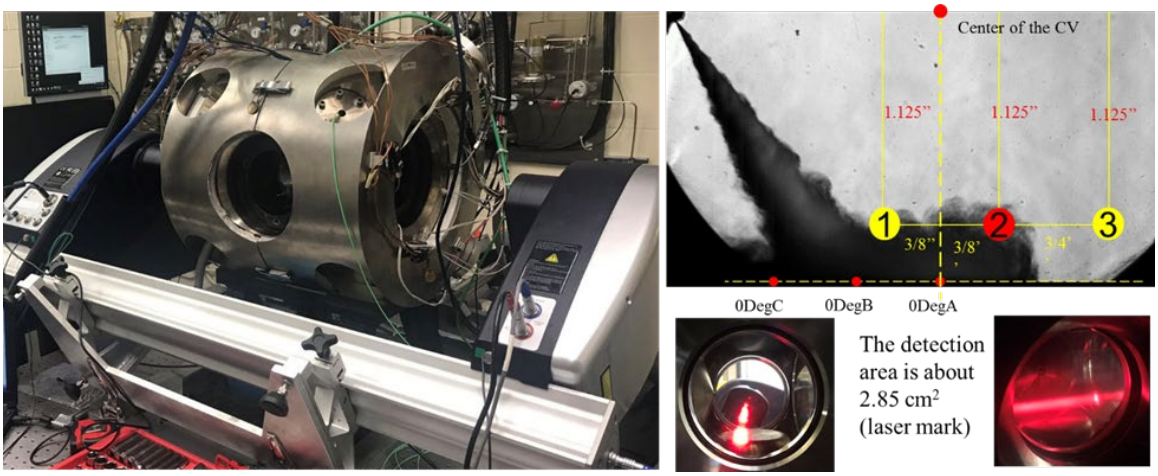

Figure 3.16. Experimental setup and schematic of droplet sizing measurement.

4 Numerical simulation details

In this Chapter, the configurations and main models used in the simulations will be introduced. The Lagrangian-Eulerian approach of coupling the liquid spray with the gaseous phase was employed to describe fuel spray and combustion in a commercial CFD software package CONVERGE©.

4.1 Simulation input configuration

The CV was modeled with a cubic domain. Diesel2 embedded in CONVERGE© package was selected as the fuel. The sub-models for spray, turbulence, liquid drop dynamics, and combustion used in this study are summarized in Table 4.1, with a detailed description provided in [74]. These models have been used extensively in numerical studies and were validated for a wide range of operating conditions, geometries, fuels, and injectors [91–94].

The base mesh size for Reynolds-averaged-Navier-Stokes (RANS) and Large-eddy-simulation (LES) simulations was 4 and 2 mm, respectively. Grid generation was done during runtime along with adaptive mesh refinement (AMR) based upon gradients in velocity, temperature, and species. Fixed embedding of cells was implemented near the nozzle. Mesh size selection was based on published grid convergence studies [95,96]. The minimum grid size is determined by the base grid size divided by the scale level power of 2. In order to investigate the soot formation near the plate due to the heat transfer between the flame and wall, the plate temperature was set to 550 K and the conjugate heat transfer (CHT) model was enabled to predict the wall temperature change during the flame impingement. The CHT is necessary when taking into account the heat transfer in the finite thickness wall [55]. In the current conjugate heat transfer model, the fluid phase, the solid phase, and the interface between solid and fluid are defined. The interface is then virtually separated with front and back surfaces. The heat flux between the fluid and solid was treated as uniform across the interface.

For reacting conditions, a reduced mechanism by Liu et al. [82] including 44 species and 139 reactions was used to calculate autoignition and subsequent combustion by a detailed chemistry combustion model, SAGE. The two-step Hiroyasu-NSC (Nagle and Strickland-Constable) approach was used to simulate the soot formation and oxidation process with acetylene (C_2H_2) as the soot formation precursor [97,98].

The models and inputs parameters for the simulations are summarized in Table 4.1.

Table 4.1. Input parameters and models for CFD simulations.

Models/Parameters	**RANS**	**LES**
Injection model	Blob distribution	
Evaporation model	Frossling correlation	
Collision model	No time counter	
Break-up	KH/RT	
Wall interaction model	O'Rourke and Amsden	
Combustion solver	SAGE detailed	
Chemical mechanism	Liu et al. [82]	
Soot model	Hiroyasu-NSC [97,98]	
Turbulence model	Standard k-ε	Dynamic structure
Base grid size	4 mm	2 mm
AMR level	4	4
Fixed embedding level	4	4
Minimum grid size	0.25 mm	0.125 mm

4.2 Spray/wall interaction models

The spray models are activated once the injection starts. The droplets which have the same thermal properties are combined into a parcel to reduce the computational time. After the injection, the spray experienced primary breakup, secondary breakup, drop drag, collision and coalescence, evaporation, and turbulent dispersion processes [74].

The spray models include: 1) Spray breakup models, 2) Drop Drag models, 3) Collision models, 4) Drop turbulent dispersion models, 5) Drop/wall interaction models, 6) Evaporation models. In this study, spray breakup, drop/wall interaction, and evaporation are discussed because spray penetration, one of the scales that is used to verify the simulation results, is mainly determined by the breakup models. The spray penetration in simulations is determined by the mass fraction of liquid fuel. After the start of injection, if the integrated fuel mass from the injector tip to downstream reaches 0.97 of total injected mass, the distance between the farthest parcel and injector tip will be counted as the spray penetration [74].

The widely used break-up model is Kelvin-Helmholtz and Rayleigh-Taylor instability model [99]. The KH instability takes into account the stability of transferring a cylindrical liquid droplet into the gas phase. RT instability considers the deceleration of drops due to the drag force.

When the droplets impinge on the wall, they may rebound or slide on the surface or lead to liquid wall film deposition. The drop/wall interaction is separated into 4 regimes when considering the effect of non-dimensional temperature which is the ratio of wall temperature and fuel boiling temperature which could be described based on Weber and Laplace number in Kuhnke film splashing model [100].

The other wall film model is provided by O'Rourke and Amsden where the film splash criteria are determined by the Weber number, film thickness, and fuel viscosity [101]. In the current study, the O'Rourke and Amsden model is adopted.

When the liquid fuel is injected into the computational domain, it is converted from a liquid phase to gaseous vapor. The droplet diameter will shrink until the whole droplet becomes fuel vapor. There are two main correlations that describe the rate change of the droplet radius. One is given by Amsden et al. [102] and the other is provided by Chiang [103].

In Frossling correlation, the rate change of the droplet is defined based on the density of liquid and gas phase, the vapor mass fraction, mass diffusivity of liquid vapor in the air,

and Sherwood number (*Sh*) which can be described as a function of Reynolds number (*Re*) and Schmidt number (*Sc*) [102]. Chiang gave a new correlation of Nusselt number (*Nu*) and Sherwood number as an alternative in the equation of droplet radius change [103].

4.3 Turbulence models

Turbulence can significantly increase the mixing rate of species, energy, and momentum. It is important to introduce the turbulence models since the turbulence can significantly enhance air-fuel mixing, especially in diesel combustion because it is a mixing-controlled process. The turbulence methods are divided into three categories in terms of the eddy length scale: 1) RANS, 2) LES, 3) DNS.

RANS simulation is the time-averaged simulation of the motion of the fluid flow. RANS turbulence models available in CONVERGE© are the standard k-ε model and RNG (Renormalization Group) k-ε model. The standard k-ε model assumes that the flow is fully turbulent, and the viscosity of the molecule can be ignored [104]. During the process of averaging the constitutive equations, it is losing fidelity. If the smallest scales of turbulence can be systematically eliminated, the remaining scales of turbulence become more distinguishable. Compared with LES and DNS, the accuracy and computational time of RANS are balanced to obtain reasonable results without having longer computational time. Several RANS models are available in CONVERGE© which are Standard k-ε, Renormalization Group k-ε, Rapid Distortion RNG k-ε which were provided by Han et al. [105] and Realizable k-ε, Standard k-ω which were provided by Wilcox [106].

Besides the RANS model, LES is briefly introduced because it could resolve the large eddies that are affected by the flow field. Based on the large eddy theory, the large-scale eddies are simulated directly while the small-scale eddies are treated isotropic. Therefore, large eddy simulation is conducted through a filtering process to separate the small and large eddies [107,108]. In the current thesis, A one-equation non-viscosity dynamic LES turbulence model known as the dynamic structure model was used to simulate the turbulent sub-grid scale stresses [109]. A sub-grid scale kinetic energy transport equation in this

model was applied to model the energy flow from the resolved scales to the sub-grid scales, based on an energy flow budget between resolved and the sub-grid scales [95].

4.4 Combustion and soot models

The CFD simulations offer several models for diesel combustion models: 1) Detailed SAGE model, 2) Modified Shell Ignition model [110], 3) Characteristics Time Combustion model [111,112], 4) Extended Coherent Flame Model 3 Zones [113].

The SAGE model gives the details of the combustion process that calculates the reaction rates for each elementary reaction while the CFD solver solves the transport equations. SAGE, along with AMR, and an accurate mechanism can be used for modeling many combustion regimes (ignition, premixed, mixing-controlled) [74]. Even though the computational time may be increased, the accuracy of the simulation could be significantly raised up due to the detailed chemistry simulation.

In case of the need for rapid simulations, several simplified combustion models such as Shell, CTC, and ECFM3Z can also be applied individually or combined to describe the combustion process. In the current thesis, a SAGE detailed combustion solver is utilized. The steps of the SAGE solver are briefly described as follows:

For a specific species *i*, the net production rate is given by Equation (4.1):

$$\dot{\omega}_i = \sum_{r}^{R} v_{net} q_r \tag{4.1}$$

where the v is the net stoichiometric coefficient, r is the specific reaction, R is the total number of reactions and M is the total number of species.

The rate of the production q_r is given by Equation (4.2):

$$q_r = k_{fw} \prod_{i=1}^{M} X_i{}^{v_r} - k_{rv} \prod_{i=1}^{M} X_i{}^{v_p} \tag{4.2}$$

In Equation (4.2), the k_{rw} and k_{rv} indicate the forward and reverse rate coefficients where both of them are addressed from Arrhenius form given in Equation (4.3):

$$k_{fw} = AT^b e^{-\frac{E}{R_u T}} \tag{4.3}$$

where the A is the pre-exponential factor, b is the temperature exponent, E is the activation energy and R_u is the universal gas constant.

Then the governing equation for mass in a cell is given by Equation (4.4):

$$\frac{dX_i}{dt} = \dot{\omega}_i \tag{4.4}$$

Soot models are important to predict soot formation and oxidation. Generally, there are four processes including soot inception, soot surface growth, soot coagulation, and soot condensation. Soot inception describes the process when the smallest soot particles are formed from the soot precursors. Soot surface growth explains the competition between the soot growth and the consumption of soot due to the reaction both happening on the soot particle's surface. Soot coagulation indicates the larger soot particles formed by the collision of smaller soot particles. Soot condensation explains the direct formation of large soot particles from the gas-phase soot precursors [74]. In CONVERGE©, the empirical correlation for soot formation and soot oxidation is given by the refs [97,98]. The rate of soot formation is proportional to the Arrhenius pre-exponential factor, and the square root of back pressure, exponential of minus activation energy, and reciprocal of ambient temperature. For soot oxidation, the Nagle and Strickland model is used by using the carbon oxidation mechanism. The soot oxidation rate is determined by the carbon oxidation reaction rate, the surface area of the soot particles, and the molecular weight of carbon [98]. The soot formation from Hiroyasu-NSC mechanism is briefly introduced as follows.

Firstly, the net soot formation rate is given by Equation (4.5):

$$\frac{dm_{soot}}{dt} = \dot{m}_{form} - \dot{m}_{oxi} \tag{4.5}$$

The formation rate $\dot{m}_{form}$ is given by:

$$\dot{m}_{form} = A_{sf} m_{acet} \sqrt{P} e^{-\frac{E_{soot}}{R_u T}} \tag{4.6}$$

Where A_{sf} is the pre-exponential factor, P is the ambient pressure and m_{acet} is the mass of acetylene which is the chosen species for soot precursor. For modelling soot oxidation, the NSC correlation is used considering the carbon oxidation. The soot oxidation is considered to happen on the surface of the soot particles. Therefore, the soot oxidation rate is given by:

$$\dot{m}_{oxi} = SR_{oxi} MW_c \tag{4.7}$$

where the S is the surface area of the soot particles, R is the soot oxidation reaction rate and MW_c is the molecular weight of the carbon.

The soot particle is assumed to be spherical and uniform in size, so that the surface area of the soot particle is given by Equation (4.5):

$$S = n_{soot} \pi {D_s}^2 \tag{4.7}$$

where n_{soot} is the number of soot particles, D_s is the diameter of the soot particle which is 25 nm in this study.

5 Data processing methodologies[2]

Post-processing is one of the most important works in the current thesis. The amount of in-house MATLAB codes for image-processing, signal-processing, and mathematical calculations will be introduced in this section. The detailed programs will be provided in Appendix A.

---

[2] Reprinted with permission from SAE papers 2019-01-0067 and 2019-01-0267 ©2019 SAE International and 2021-01-0543 ©2021 SAE International. Reprinted with permission from International Journal of Engine Research (IJER) and the American Society of Mechanical Engineers (ASME). The materials in this chapter were published in the following papers:

- Zhao, Z., Zhu, X., Zhao, L., Naber, J. et al., "Spray-Wall Dynamics of High-Pressure Impinging Combustion," SAE Technical Paper 2019-01-0067, 2019, https://doi.org/10.4271/2019-01-0067.
- Zhao, Z., Zhu, X., Naber, J., and Lee, S., "Impinged Diesel Spray Combustion Evaluation for Indirect Air-Fuel Mixing Processes and Its Comparison with Non-Vaporing Impinging Spray Under Diesel Engine Conditions," SAE Technical Paper 2019-01-0267, 2019, https://doi.org/10.4271/2019-01-0267.
- Zhao, Z., Zhu, X., Zhao, L., Tang, M. et al., "A Numerical Study for the Effect of Liquid Film on Soot Formation of Impinged Spray Combustion," SAE Technical Paper 2021-01-0543, 2021, https://doi.org/10.4271/2021-01-0543.
- Zhao, Z, Zhao, L, & Lee, S. "Evaluation of Soot Production Near a Cold Surface for an Impinged Diesel Spray Combustion." Proceedings of the ASME 2020 Internal Combustion Engine Division Fall Technical Conference. ASME 2020 Internal Combustion Engine Division Fall Technical Conference. Virtual, Online. November 4–6, 2020. V001T05A002. ASME. https://doi.org/10.1115/ICEF2020-2938
- Zhao Z, Zhu X, Naber J, Lee S-Y. Assessment of impinged flame structure in high-pressure direct diesel injection. International Journal of Engine Research. 2020;21(2):391-405. doi:10.1177/1468087419859788

5.1 Experimental related data processing

5.1.1 Boundary tracking for spray and flame shape

The structure of impinged spray and flame is investigated by using boundary tracking as the main image processing tool. Both general expansion structures for outmost boundaries and film formation area are acquired through using boundary tracking. The global parameters for non-vaporizing conditions (i.e., axial/radial expansion distance at axial direction) were obtained by tracking the boundary of the spray expansion pattern. The procedure of the boundary tracking method is shown in Figure 5.1.

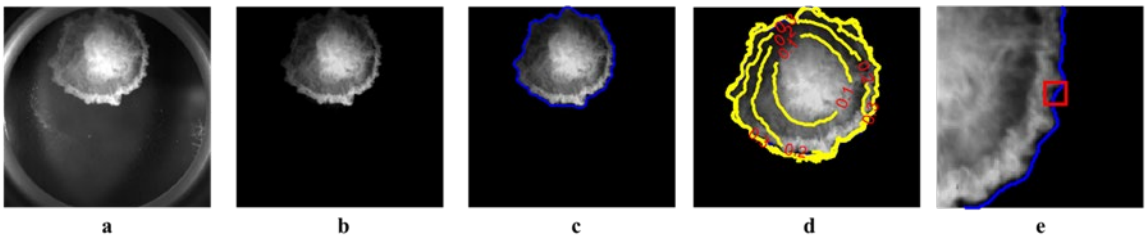

Figure 5.1. Boundary tracking procedure: (a) raw image before background subtraction, (b) gray image after background subtraction, (c) outmost boundary tracking of spray expansion (which is used to obtain spray expansion distance), (d) weight contour of intensity gradient with a zoomed-in spray (which is used to track the shape of liquid film near to the impinging point), and (e) spatial window (red square box) for integration of intensity (which is used to integrate the intensity near boundary pixel).

One sample of the bottom-viewed high-speed image (before background subtraction) is shown in Figure 5.1(a). The background without any spray is subtracted from Figure 5.1(a) and the subtracted gray image is shown in Figure 5.1(b). The boundary of the spray or flame is typically acquired by using the 'bwboundaries' function in MATLAB. The boundary tracking of function 'bwboundaries' is based on the threshold of the absolute magnitude of intensity instead of the gradient of intensity. The threshold can be an arbitrary number based on intensity level or automatically determined by using the 'Otsu' method

[114]. By setting a certain threshold, a visual check is needed to determine whether the threshold is set properly enough to obtain good outcomes. Even though the 'bwboundaries' could find the most connected interested area, there are still some holes and fragments seating in the interested area. The 'fill' function is needed to be adopted to obtain a single, continuous-connected boundary. The single, continuous boundary of spray expansion is shown in Figure 5.1(c), marked by a blue solid line.

There is a liquid film that has been found to be formed near the impinging point after spray impingement. A certain amount of fuel adheres on the plate near the impinging point, showing a very slower expansion rate compared to the expansion rate of the outmost spray boundary. Due to unclear intensity gradient in the film formation region, the original boundary tracking method is no longer applicable. A new method of boundary tracking based on image segmentation is adopted to track the inner structure (liquid film region) of spray expansion. Weighted intensity gradients are acquired based on the local level of intensity and the intensity of the interested seed point. Since the film region is located peripheral to the impinging point, the impinging point is chosen as the seed point. The contour of the weight is shown in Figure 5.1(d). Local weight is inversely correlated to the local intensity gradient, which means the region with a sudden intensity change has a small-weighted gradient. By setting a certain threshold for the weight, the boundary of the film region can be acquired. A visual check is also needed to determine the threshold. In order to investigate the effect of turbulence intensity which can be denoted as the effect of the curvature on the flame luminosity, a spatial window which is shown as a 2 mm long red square in Figure 5.1(e) is used to integrate the intensity near the boundary. The size of this spatial window is determined through sensitivity analysis by varying the size of the square. It is found that larger square-bound leads to overlapped information and smaller square-bound leads to miss information.

One sample of the bottom-viewed high-speed image (after background subtraction) is shown in Figure 5.2(a). After the impingement, the fuel spray expands on the plate radially but with a different expansion rate due to the tilted incident angle. The impinging point is

obtained by the 'Centroid' function and shown as a red dot in Figure 5.2(a). Three directions (left radial, right radial, and axial) are defined to explain the spray expansion behavior. The axial expansion distance is defined as the average distance between the impinging point to the pixels on the local boundary (purple line). There are N_{pixel} numbers of pixels on the boundary. The distance at a given time t can be defined as Equation (5.1)

$$D(t) = \frac{\sum \sqrt{(x - x_{imp})^2 + (y - y_{imp})^2}}{N_{pixel}} \tag{5.1}$$

The x_{imp} and y_{imp} represent the location of the impinging point where the x and y represent the location of the local boundary pixel. Similarly, the radial distance could be obtained. The whole space domain is separated into sectors with respect to the impinging point and the schematic of the space domain is shown in Figure 5.2(b). The local expansion distance at a given time could be represented as $D\ (t, \theta)$ where θ is the radial coordinate. The sector angle α where distance is averaged was determined through the sensitivity analysis and 5° was found to have the best outcome. The three directions (left radial, right radial and axial) in Figure 5.2(a) correspond to the θ of 270°, 90° and 180° in Figure 5.2(b). A sample profile of expansion distance at 2 ms ASOI (after the start of injection) under the non-vaporizing condition is shown in Figure 5.2(c). Three arrows (located at 90°, 180°, and 270°) in Figure 5.2(c) indicate the local expansion distance at right radial, axial, and left radial directions.

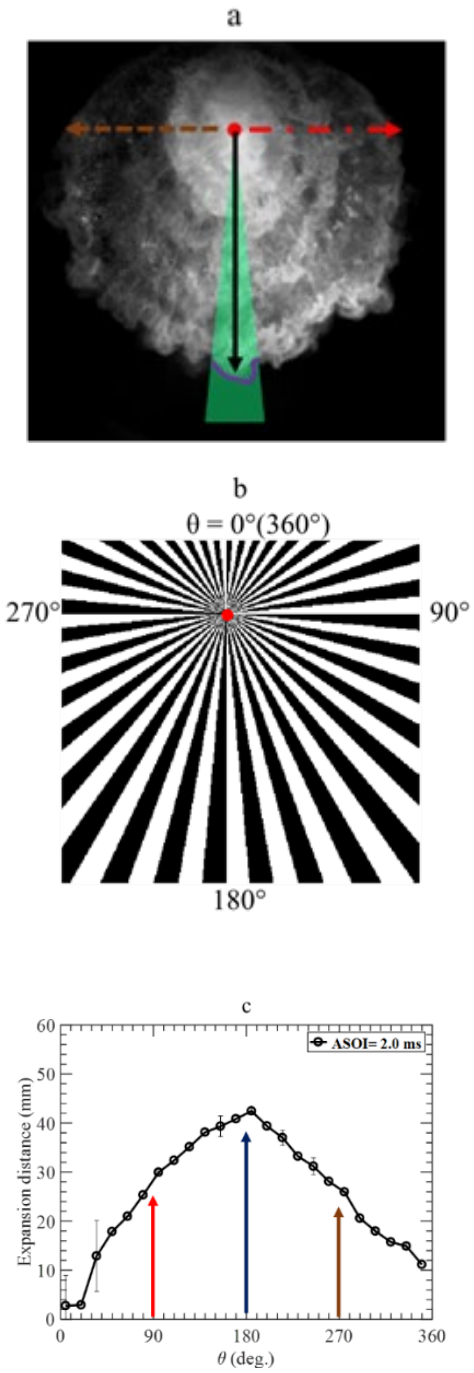

Figure 5.2. The procedure of local boundary tracking method: (a) definitions of the spray expansion directions (dash line: left radial; solid line: axial; dash line with a dot: right radial); (b) space domain of data analysis (θ); (c) profile of expansion distance at 2 ms ASOI under non-vaporizing conditions.

The local expansion rate *ER (t, θ)* could be then defined as Equation (5.2):

$$ER(t,\theta) = \frac{D(t,\theta) - D(t',\theta)}{\Delta t} \tag{5.2}$$

where the *t'* is one frame before *t*. Δt is equal to 1/fps (frame per second). For reacting cases, the flame front distance and expansion rate are obtained by using the same boundary tracking method and space domain.

Besides examining the expansion rate, the density of the spray boundary contour could also be used to qualitatively evaluate the local expansion rate. A sample case is shown in Figure 5.3 including an instantaneous spray image at the end of injection and the temporal contours of the spray boundary from the start of impingement to the end of injection. In the region near the impinging point, the boundary contour is sparser than the leading edge of the spray. Thus, the bulk expansion rate is higher at the impinging region than the leading edge.

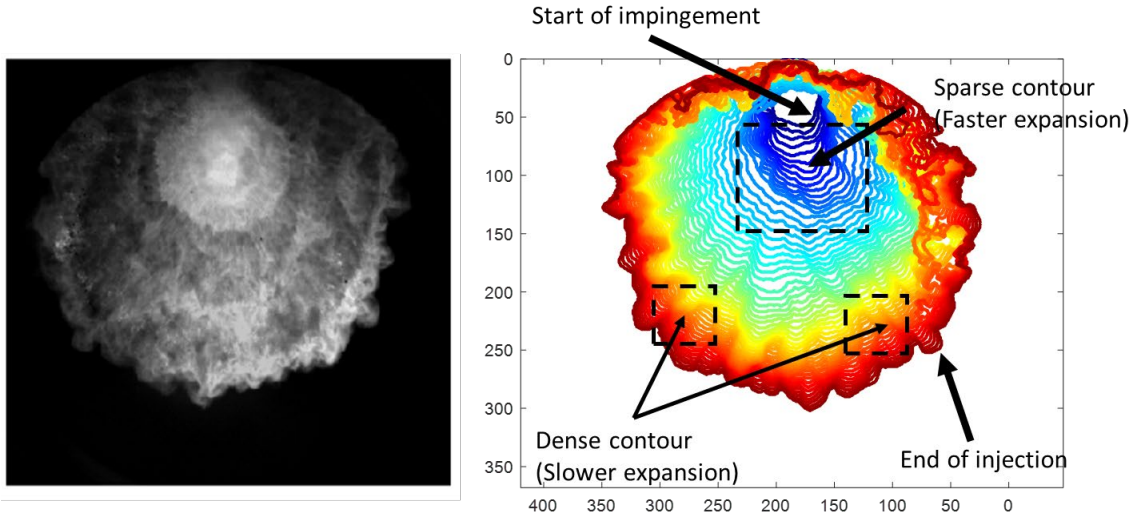

Figure 5.3. Left: the instantaneous image of an impinging spray at the end of the injection. Right: The evolution of the tracked spray boundary from the start of impingement to the end injection.

5.1.2 Intensity-Radial-Time methodology

The soot formation of impinged spray combustion can be indirectly denoted by conducting simultaneous spatial and temporal integration of flame luminosity. The methodology of the integration of flame luminosity has been introduced by previous researchers [18,115,116]. In the free spray case, the flame luminosity is treated radially uniform, and the integration is applied in the axial direction. However, for an impinging case, a polar coordinate system is adopted to explain the integration of luminosity in radial directions. The angle θ of the polar coordinate system represents the inclined angle between the local flame pixel and impinging point. The radius of the coordinate corresponds to the ASOI.

The sample image in Figure 5.4(a) is selected from one combustion event at ambient temperature 900 K and 1.7 ms ASOI. The intense flame luminosity is noted by red in the false-color map. The space domain of the image is separated into sectors with respect to the impinging point. The impinging point is shown as a red dot. In order to determine the best angle sector, the sensitivity analysis is performed by varying sector angles of 20°, 10°, 5°, and 1° and it is found that the best result was from sector angle of 5°. A mask (a red sector in Figure 5.4(b)) scans over the sectors to obtain the integration of flame luminosity. Simply, the integrated intensity in *No.i* sector at a given timestamp is calculated by Equation (5.3):

$$I_{int_i}(t) = \int I_{local}(x, y, t) dA_i(t) \tag{5.3}$$

The $I_{local}\ (x,y,t)$ and $A_i\ (t)$ are the local flame luminosity and the flame occupied area in each sector at a given timestamp. The integrated intensity is converted into a colored arc that sits on the concentric circle in Figure 5.4(c) at a given timestamp. The color of the arc represents the magnitude of the integrated intensity.

The area-averaged integrated flame luminosity replaces the overall integrated flame luminosity to explain the soot formation. Equation (5.3) is then modified to Equation (5.4):

$$I_{int_{ave_i}}(t) = \frac{\int I_{local}(x,y,t)dA_i(t)}{A_i(t)} \tag{5.4}$$

The $I_{int\_ave\_i}$ represents the area-averaged integrated flame luminosity over the flame occupied area of *No.i* sector at a given timestamp. The $I_{int\_ave\_i}$ is then normalized by the maximum range of the camera detection limit (i.e., 255 of intensity). The IRT maps from 0 to 6 ms ASOI are shown in Figure 5.4(d). The overall IRT results are averaged by 5 repeats.

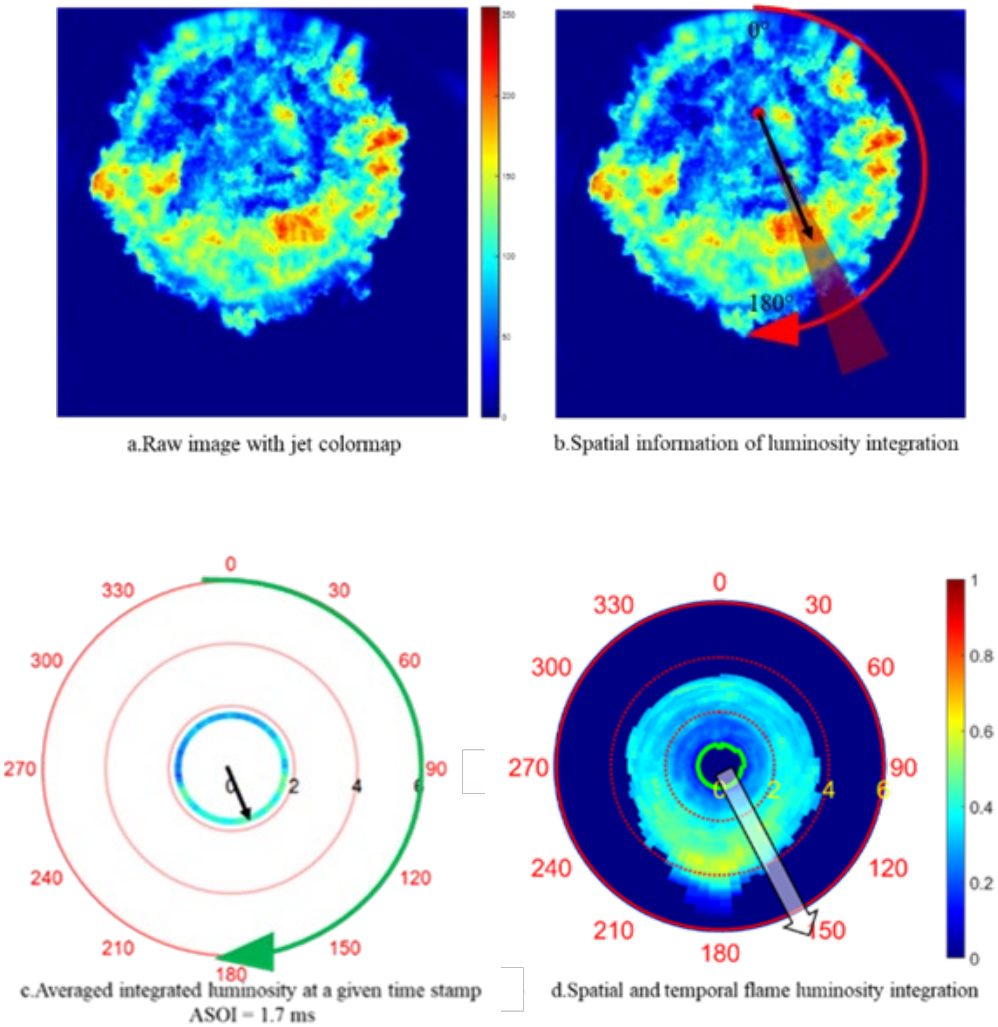

Figure 5.4. A schematic of flame luminosity integration in both space and time domain.

In addition, the time-resolved natural luminosity image and the integrated intensity are shown in Figure 5.5 and Figure 5.6 step by step. They help the audience to understand the temporal integration process.

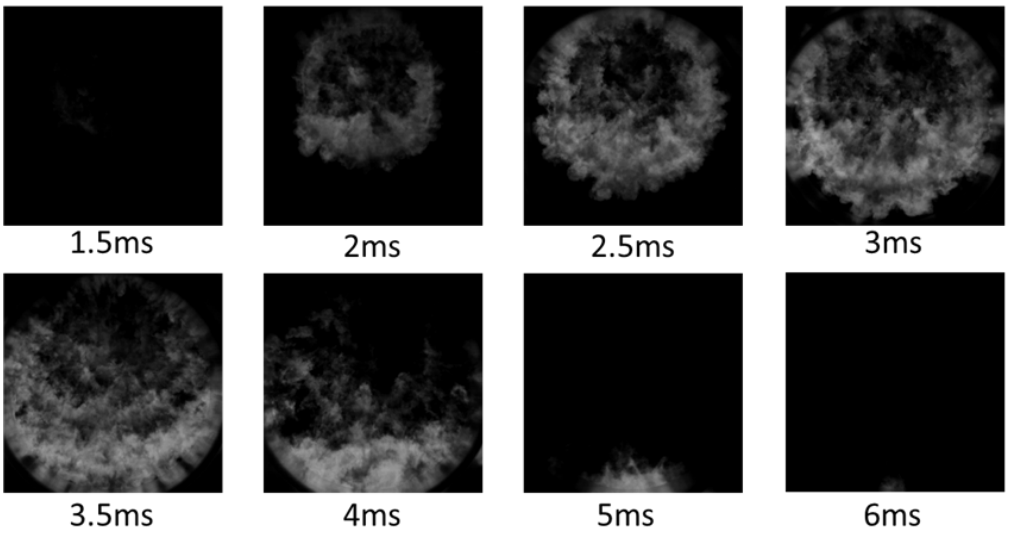

Figure 5.5. Time-resolved natural luminosity images of impinging spray diesel combustion at given ASOIs.

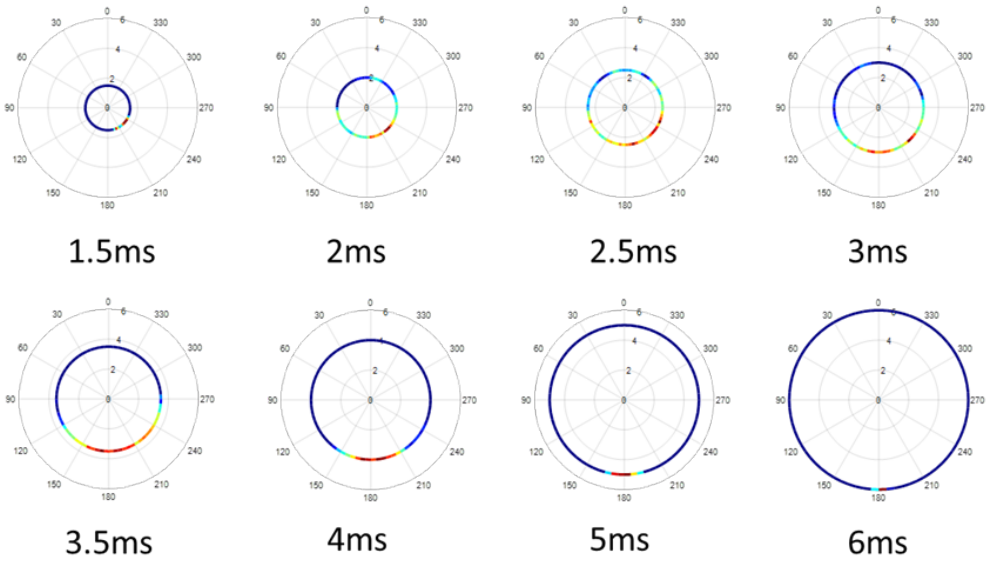

Figure 5.6. Time-resolved integrated flame luminosity at given ASOIs.

5.1.3 Curvature calculation for transient turbulent impinging spray boundary

As the curvature usually has a sign to indicate the orientation, the definition of the curvature needs to be clarified before the curvature calculation. A snapshot of non-vaporizing impinged spray is illustrated in Figure 5.7, looking from the bottom view. During the spray expansion on the plate, the outmost boundary of spray expansion is perturbed by both the surrounding gas and the plate surface friction. It is assumed that the surface drag, which hinders spray boundary expansion, is radially and uniformly distributed, and therefore outmost spray boundary shape is assumed to be both determined by the surrounding gas dynamics (local gas velocity) and initial droplet velocities after the impingement. The captured images illustrate that there exist wrinkled boundaries with a number of convex and concave regions. In concave regions, spray expansion is suppressed by the ambient gas while there is less constraint in the convex regions. The strength of the suppression may affect the strength of the air-fuel mixing process. Note that the definition of the concave and convex shape is with respect to the impinging point. The convex and concave are defined by the positive and negative curvatures, respectively.

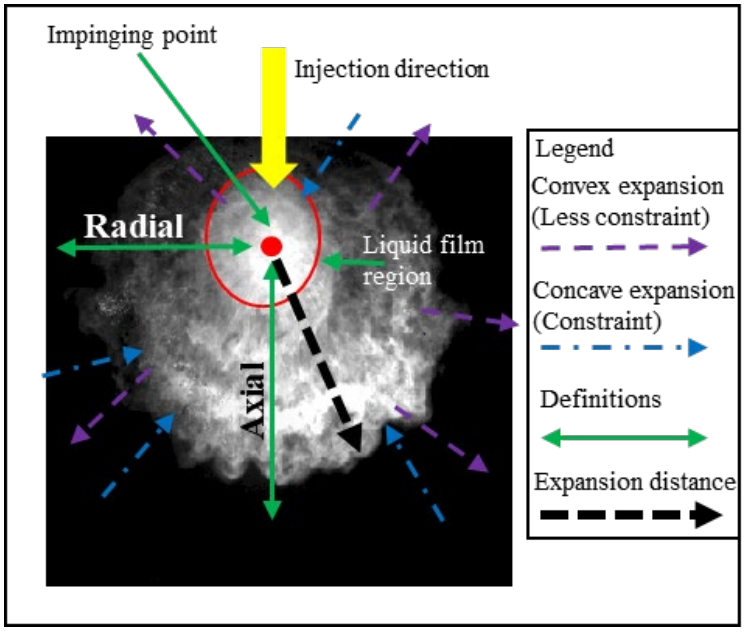

Figure 5.7. A schematic of non-vaporizing impinged spray from the bottom view.

The local curvature of the flame expansion boundary is calculated as an indirect indicator of the local level of air entrainment at the flame boundary region. Mathematically, this curvature is defined as the rate of change of unit tangent vector when a particle is assumed to move on the evaluated curve. This expression can be explained as

$$K = \frac{dTV}{ds} \tag{5.5}$$

where *TV* is the unit tangent vector:

$$TV = \frac{dr}{ds} \tag{5.6}$$

and *s* is the distance on the curve. However, it is hard to directly measure the rate of change of the unit tangent vector. Therefore, the curvature *K* can be expressed as:

$$K = \frac{d^2r}{ds^2} \tag{5.7}$$

If a third parameter *m* is introduced to calculate the tangent vector, then:

$$K = \frac{TV'(m)}{\frac{ds}{dm}} \tag{5.8}$$

$$r'(m) = \frac{ds}{dm} \tag{5.9}$$

K can be then expressed as $r'(m) \text{ ⧸ } r''(m)/r'(m)$. In a 2D image, the *r* can be explained as:

$$r = x\boldsymbol{i} + y\boldsymbol{j} \tag{5.10}$$

where *x* and *y* are corresponding to the dimensions of the image in the Cartesian coordinate. If *y* is considered as a function of *x*, then:

$$\frac{dr}{dx} = \boldsymbol{i} + \frac{dy}{dx}\boldsymbol{j} \tag{5.11}$$

Combining these relations with the previous expression of curvature, the first explicit expression of curvature is revealed as:

$$K = \frac{y''}{(1 + y^2)^{1.5}} \tag{5.12}$$

If local y and x can be explained as $x = f_1(m)$ and $y = f_2(m)$ by using a parameter m, the previous equation is changed to [117,118]:

$$K = \frac{(x'y'' - y'x'')}{(x^2 + y^2)^{1.5}} \tag{5.13}$$

The local curvature at each individual pixel on the boundary can be obtained by curve fitting with a second-order polynomial method. Three pixels, target pixel, its left neighbor pixel, and right neighbor pixel on the boundary, are used to obtain the functions of curve fitting, $x = f_1(m)$ and $y = f_2(m)$. The parameter m is always defined as 0 at the target pixel. At the left neighbor pixel, m_{left} equals the relative distance between the left neighbor pixel and target pixel. Similarly, m_{right} can be obtained. The curvature at each target pixel can be calculated with the definition of K.

Before applying this method in the actual spray images, the verification of the curvature is needed. Therefore, a known size of the circle is generated in MATLAB and its theoretical curvature is the reciprocal of the radius. In Figure 5.8, three circles with the radius of 16, 51, and 101 pixels are generated. The corresponding radiuses in mm are 1.68, 5.36, and 10.61 mm. The local curvature of the circle is calculated starting from the top of the circle along the boundary of the circle. The theoretical and calculated curvatures are shown on the plot next to the corresponding circle. As can be seen in the plot, this method loses the sensitivity near the starting point and end point. As the radius is increased, the percentage

of the length of losing sensitivity is reduced which means that this method has more accurate outcomes from a curve with smaller curvature.

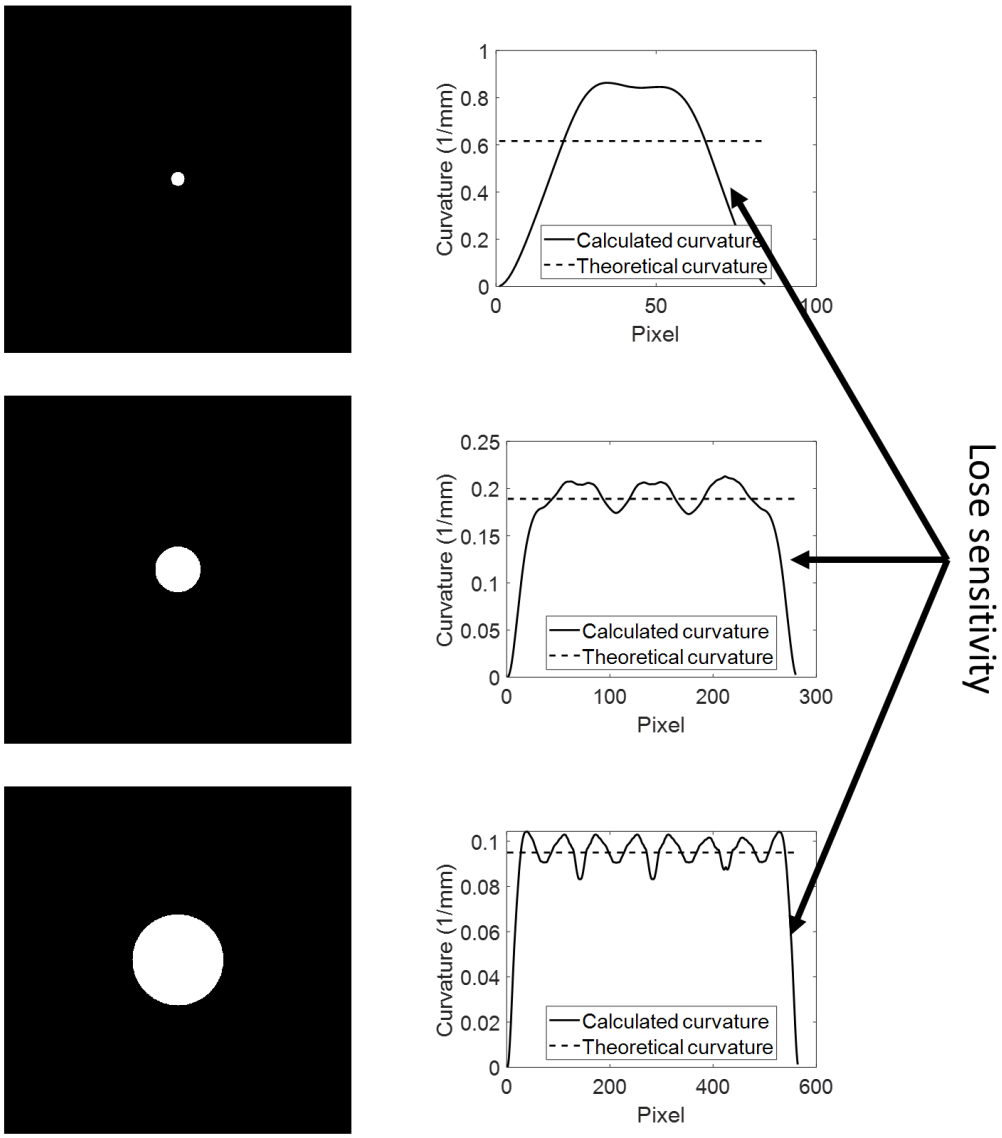

.

Figure 5.8. The verification of the curvature method is introduced in section 5.1.3. Three circles with a radius of 1.68, 5.36, and 10.61 mm are shown from top to the bottom.

Nevertheless, to avoid losing the sensitivity, the vertices instead of all pixels could be used to specifically obtain the bulk curvature on the spray boundary. Therefore, the vertices on the spray were acquired and details are introduced as follows.

From Equation (5.1), the expansion distance is obtained but the plot domain is different when trying to find the vertices. Instead of the radial domain, the pixel-based domain is used to plot the expansion distance. A sample of the expansion distance is shown in Figure 5.9. The red dots in Figure 5.9 represent the location of the vertices. The first derivative of the expansion distance is obtained to find the location of vertices pixels. Similar to the definition of mathematical stagnation points, the vertices lie where the first derivative of the curve is zero and the product of the first derivative of left and right neighbor the pixels is negative. It could be explained as a combination of Equations (5.14) and (5.15):

$$\frac{dD}{dx}|_{x=x_i} = 0 \tag{5.14}$$

$$\frac{dD}{dx}|_{x=x_{i-1}} \frac{dD}{dx}|_{x=x_{i+1}} < 0 \tag{5.15}$$

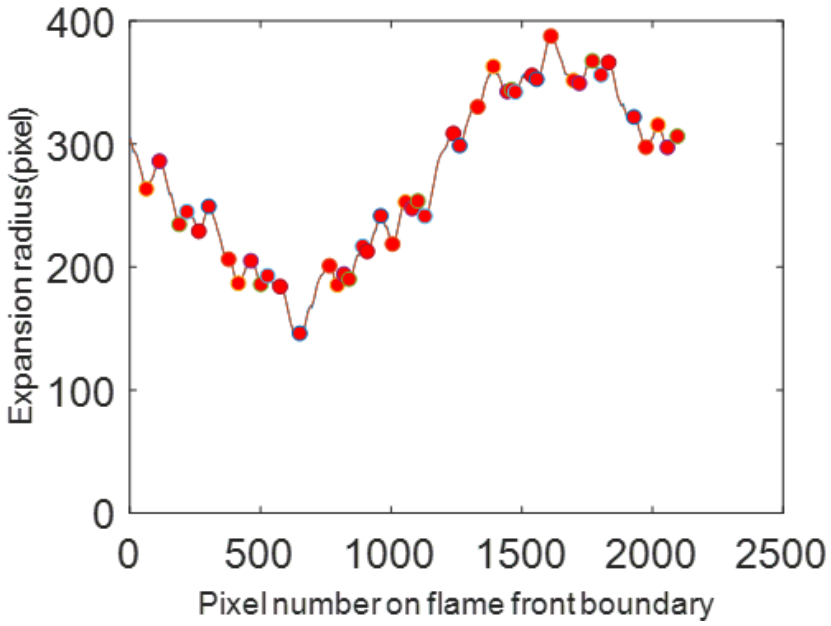

Figure 5.9. Expansion radius at a given timestamp.

After finding the location of the vertices, they are reflected on the spray image. The comparison against the vertices and the spray boundary is shown in Figure 5.10. It is noted that the contrast of the spray is modified.

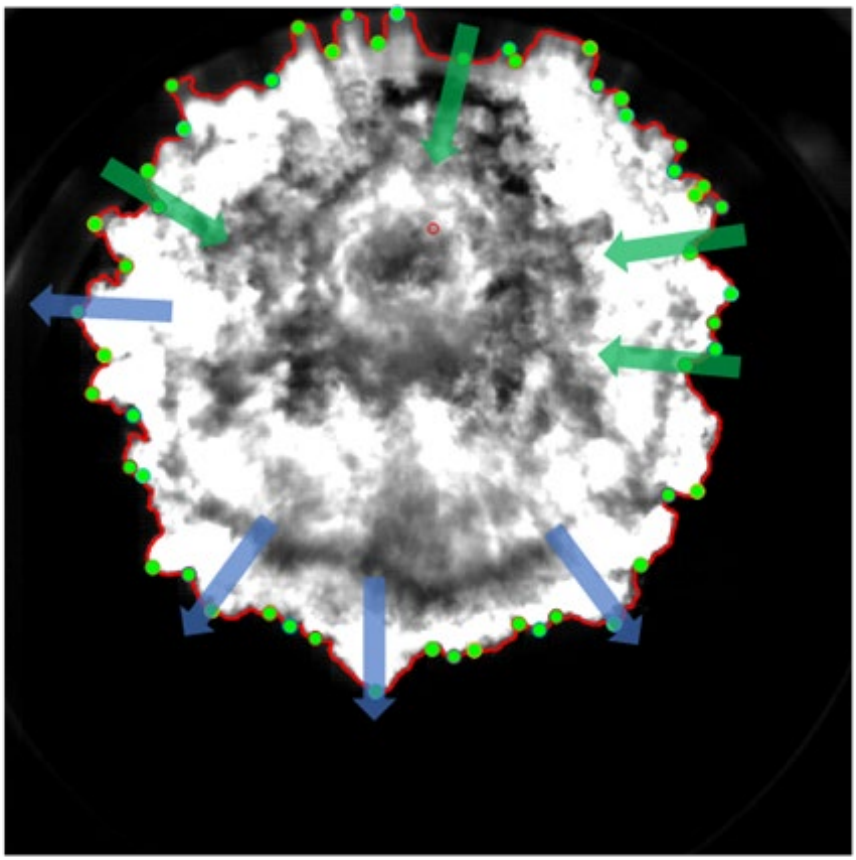

Figure 5.10. Definition of the curvature and the detection of vertices of the flame front boundary. The concave and convex are marked with green and blue arrows, respectively.

5.1.4 Histogram-based distribution

Apart from the normal impingement, the fuel mass distribution could be non-uniform at a tilted incident angle. In reacting cases, the non-uniform mass distribution could form one or several local fuel-rich zones after the impingement, which further deteriorate the air-fuel mixing process and possibly produce the environment for soot formation favor. The intensity level of soot luminosity would be related to the concentration of soot under a similar temperature environment. In the current study, the range of camera detection is separated into 5 groups starting from 0 to 250 (8-bit resolution) with an interval of 50 to

locate the most intensive soot region. The distance between the flame location and the impinging point is calculated. All flame-occupied pixels (without imaging threshold) are counted to obtain enough statistical data. The spatial distribution of the soot luminosity is plotted with the histogram function with a bin width of 1mm.

5.1.5 Heat flux calculation

During the flame expansion on the plate, the temperature difference between the plate and flame leads to heat loss to the cold surface and further lead to soot formation on the plate. A metal plate with three embedded heat flux probes replaces the bottom quartz fixture to measure the surface and inner plate temperatures during the combustion event. The location of heat flux probes is illustrated in Figure 5.11. The location of the ideal impinging point is also marked in Figure 5.11. Its location is calculated based on the CV geometry, arrangement of the injector, and the impinging plate. It is noted that the impinging plate is replaced by a transparent quartz plate in Figure 5.11 for better visualization comparing the location of heat flux probes and the spray pattern. The transparent quartz plate and the metal impinging plate share an identical geometry.

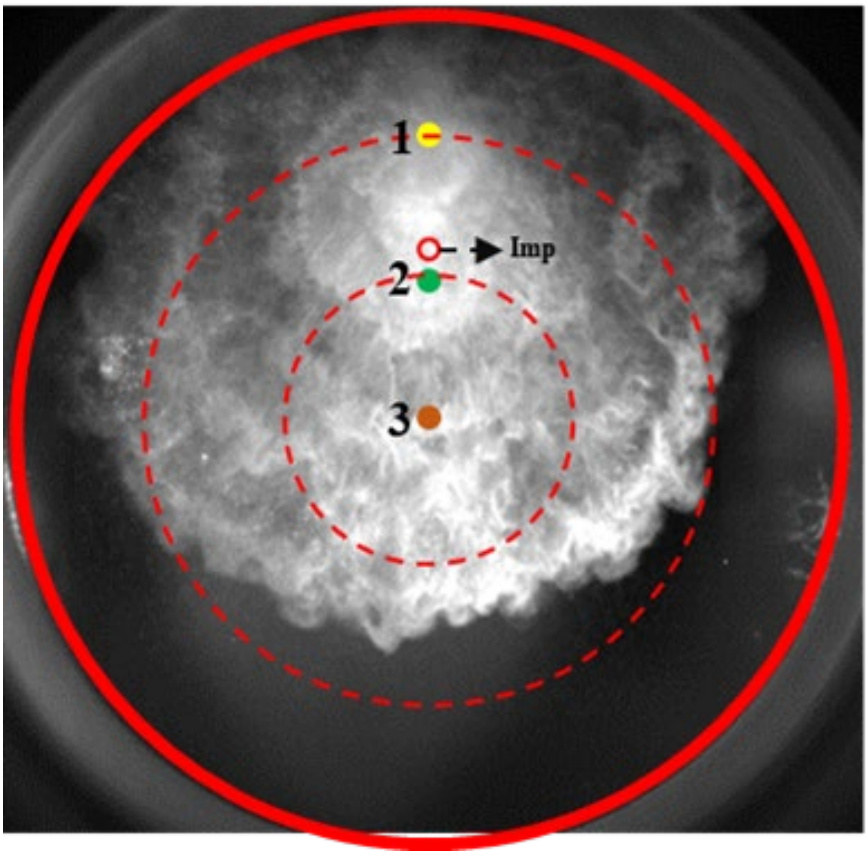

Figure 5.11. Locations of heat flux probes and their relative location with spray. At the initial location, three probes occupied locations 1, 2, and 3. The ideal impinging point is marked in between the location 1 and 2. The ideal impinging point is calculated based on the CV geometry and the arrangement of the injector and impinging plate.

In this test, a DAQ system is triggered to record the temperature profile with a sampling rate of 100 kHz when the pre-burn mode is initiated. However, during the energized injection, there is noise in the temperature profile due to the energizing signals from the injector driver. A 100^{th} order median filter is applied to the original temperature profile and the validation of the filtered temperature is shown in Figure 5.12. These three probes are installed evenly with a radial distance of 25 mm between location A (Location 1 in Figure 5.11) and C (Location 3). The heat flux probe is a 3-wire heat flux probe that consists of a 1.5-mm probe and two welded junctions. The 3-wire probe provides the ability to measure

surface, embedded temperatures. The surface thermocouple is installed exposed to the ambient gas, while the embedded one is installed 2 mm below the surface one.

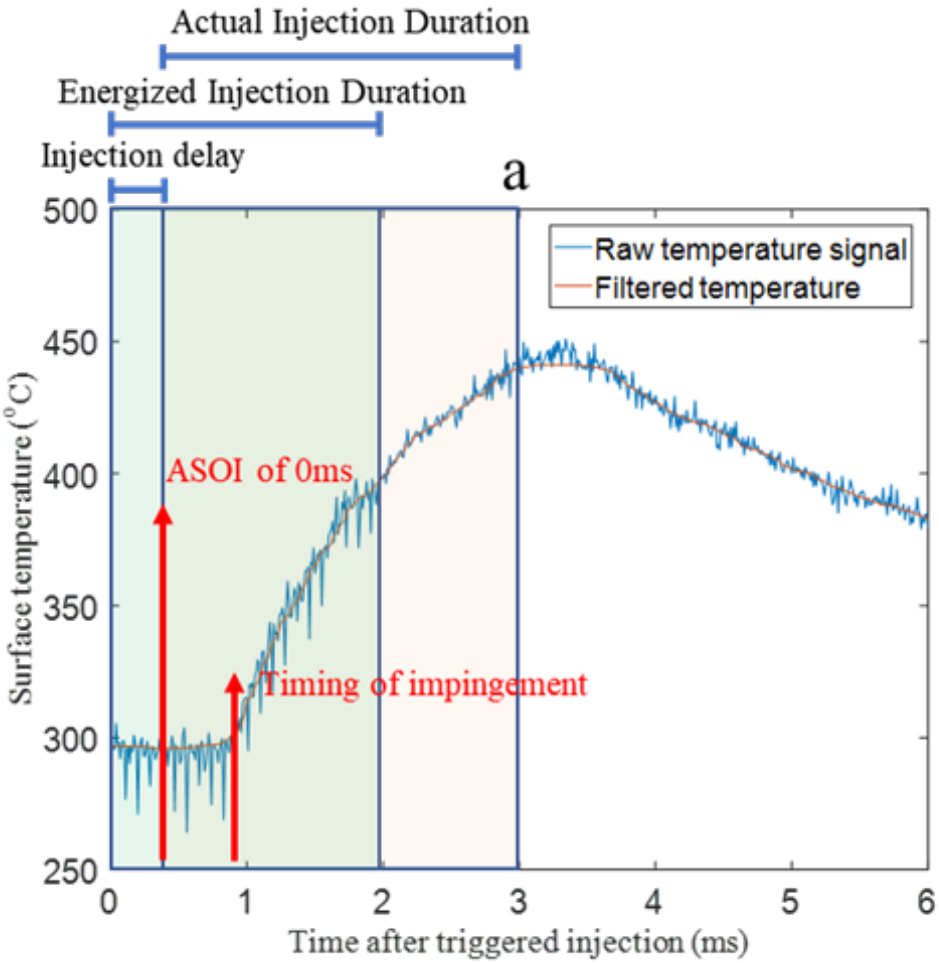

Figure 5.12. Comparison of the raw surface temperature profile with median filtered surface temperature.

After reaching the desired ambient pressure, the injector is triggered to inject the fuel into the chamber. The fuel is injected 0.27 ms later after the trigger signal due to the hydraulic injection delay. The actual injection duration is 2.4 ms which is 0.4 ms longer than the energized injection duration. The following equation is used to calculate the temporal local heat flux:

$$q'' = -k\frac{\Delta T}{d} \tag{5.16}$$

where the k is the thermal conductivity of the stainless steel which is 44.5 W/m*K. ΔT is the temperature difference between the surface and 2 mm below the surface. d is the gap between the surface and embedded thermocouples, which is 2 mm. If the heat flux is positive, the local heat transfer is treated from the wall to the ambient.

However, in some test conditions with the shock of the electrical injection signals, the median filter can't trace the early temperature change after the impingement. Therefore, a Fast-Fourier transform filter is applied to the temperature signals. The details will be provided in section 5.1.7.

5.1.6 Apparent heat release rate calculation

The apparent heat release rate (aHRR) in the constant volume chamber is calculated to identify the combustion phases of impinged combustion by varying the ambient temperature. Based on the assumption of a closed system operating with an ideal gas, the aHRR can be evaluated by Equation (5.17) [2]:

$$\frac{dQ}{dt} = \frac{1}{\gamma - 1} Vol \frac{dP}{dt} \tag{5.17}$$

where the specific heat ratio γ is a constant (1.35) for the mixture used in CV whose volume is fixed at 1.1 L. From Equation 5.17, it could be concluded that the aHRR is proportional to the bulk pressure change in the combustion vessel. Due to the acoustic wave in the vessel, the pressure curve shows an oscillation, and the profile needs to be filtered. The process of filtering pressure is addressed as follows: the pressure drop due to natural cooling is subtracted from the pressure rise because of the combustion. A sample pressure rise due to combustion is shown in Figure 5.13. In addition, the pressure rise is separated into two parts: the premixed portion and the diffusion portion. The separation point is defined as the center of the first rising curve. The pressure rises before and after the

separation point contributes to the aHRR of premixed and diffusion combustion, respectively. A Butter worth filter with a cut-off frequency of 1500 Hz was applied for the diffusion portion.

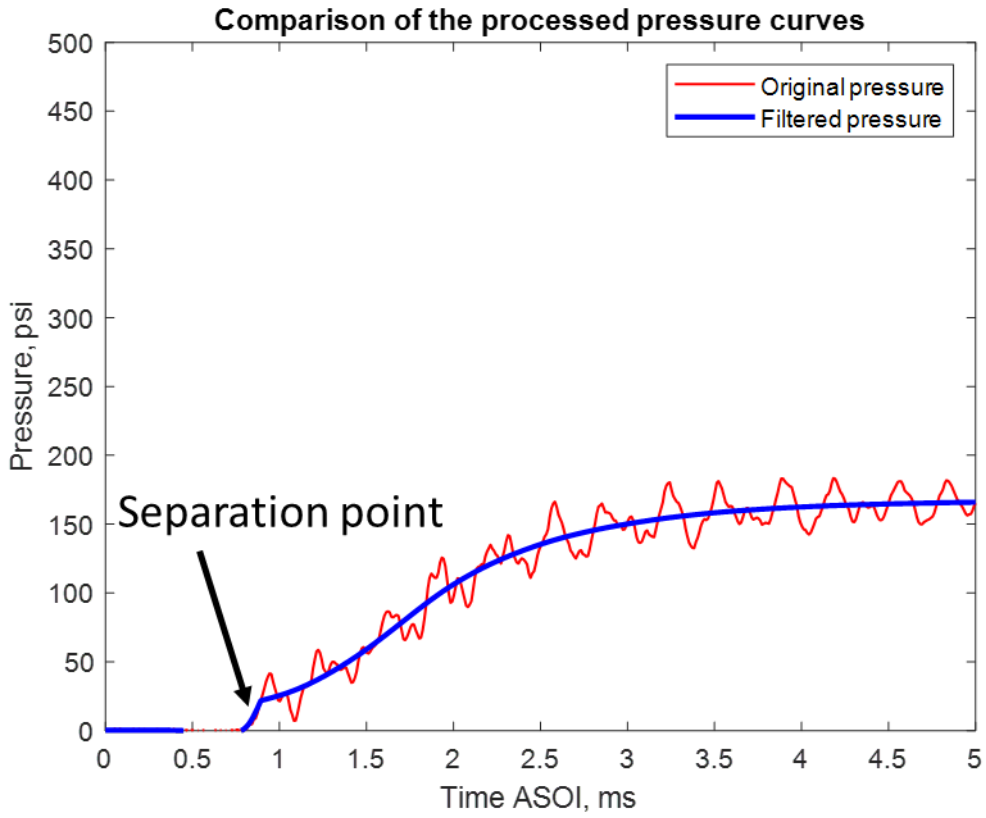

Figure 5.13. Pure pressure rise due to combustion and the filtered pressure.

A typical aHRR profile of diesel spray combustion is shown in Figure 5.14. The overall process is separated into three domains: I: Premixed combustion (constant volume process); II: Diffusion combustion (constant pressure process); III: Late burning. Note that there is an increase of heat release rate at an early stage of region I due to the cool flame effect.

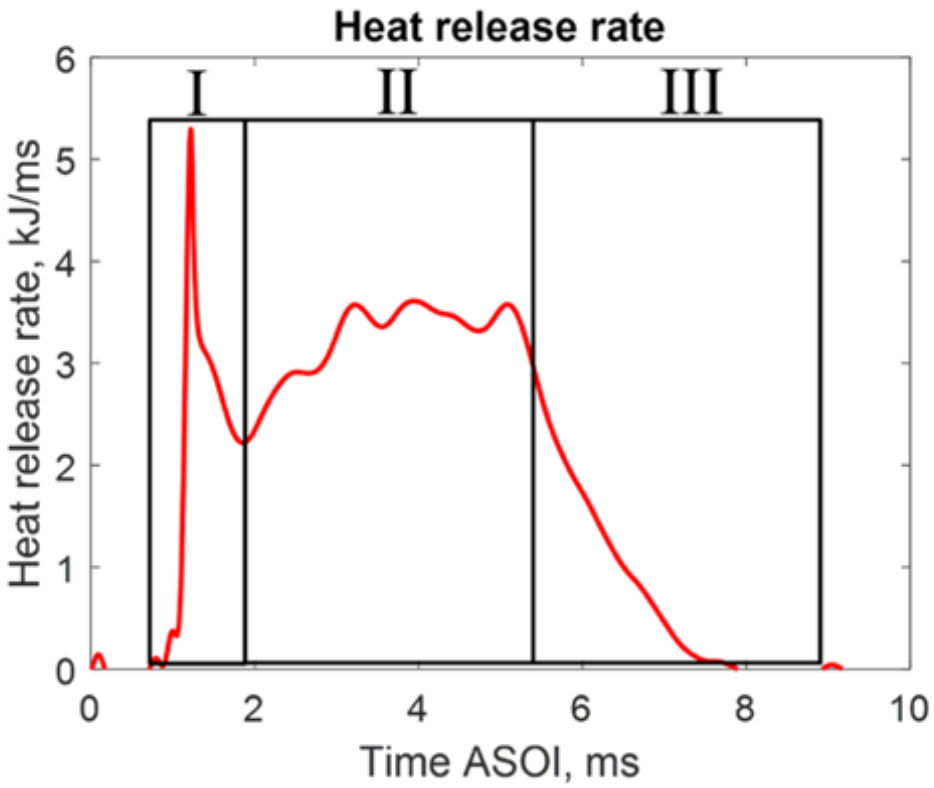

Figure 5.14. The heat release rate of typical free spray diesel combustion.

5.1.7 Fast-Fourier Transform related signal processing

Due to the disturbance of the electrical shock from the injector driver, the temperature profiles acquired from DAQ need to be properly filtered. Initially, a median filter with 100th order is applied to the raw signals in section 5.1.5. However, the median filtered signals can't track the dropping down phase after the impingement during the injection signals. Therefore, a fast Fourier transform (FFT) filter is applied to the original signals [119]. In Figure 5.15, the raw temperature profile, fast Fourier transform filtered, and median filtered profile is overlaid. The start of injection (SOI) is also marked in Figure 5.15. The actual temperature profile during the injection is blocked by the electronic injection signals. The power spectrum of the raw signals is shown in Figure 5.16. A low-pass strategy is adopted, and the cut-off frequency has been set to 500 Hz. In Figure 5.15, it could be seen that the FFT filtered signals could track before injection, during the

injection, and after the injection phases properly. The start of injection is determined by finding the first electrical signal of the injection driver then adding the hydraulic delay of the injector which is ~ 0.27 ms for the LBZ injector.

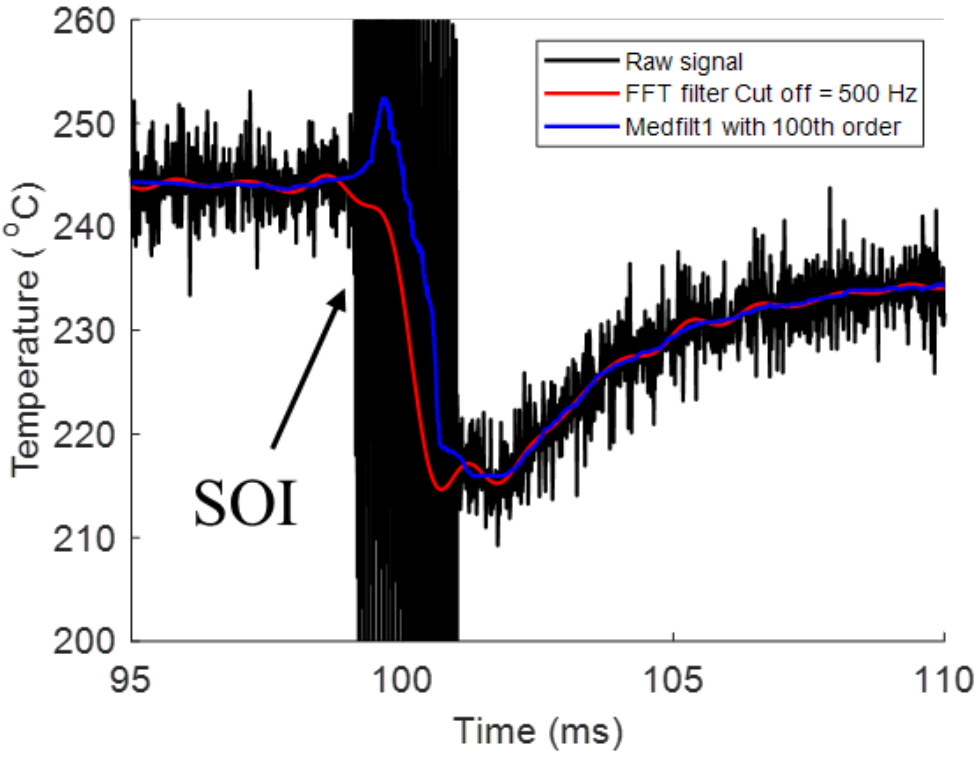

Figure 5.15. Overlaid raw, FFT filtered and 1D median filtered temperature profiles.

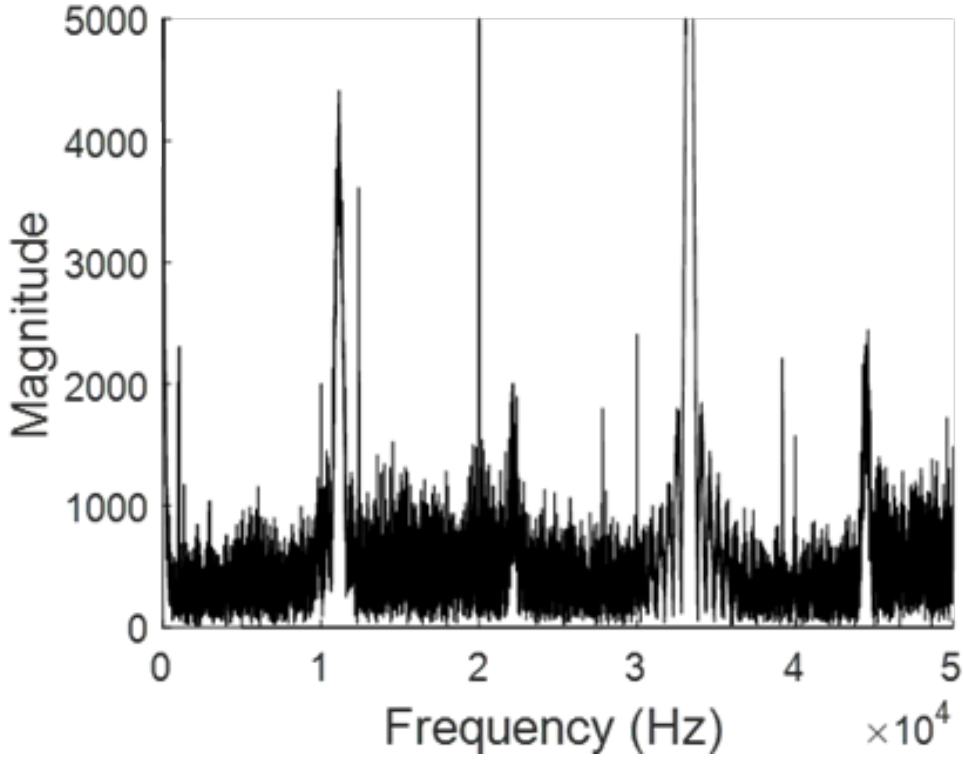

Figure 5.16. The power spectrum of raw temperature signal from FFT.

5.2 Simulation related data processing

In section 5.1, the main methods of data processing for experiments have been introduced. In this section, the data post-processing for simulations will be explained in three different sub-sections: the column data extractions and definitions such as liquid length, ignition delay, etc., from the output files directly generated by the simulations, the virtual natural luminosity calculated from the simulations through using the theory of black radiation of soot and the curvature calculation for spray boundary generated in the simulations.

5.2.1 Data extraction from simulations and definitions

The outcomes from simulations are converted to column format using the built-in tool from CONVERGE© Studio. The data of column format is reconstructed in a 3D domain using the MATLAB scatter interpolant function. The 3D data could also be visualized by an

open-source post-processing software, ParaView. It can quickly build visualizations to analyze data using qualitative and quantitative techniques. ParaView was developed to analyze extremely large datasets using distributed memory computing resources. Especially, it could provide the ability to render the dataset for better visualization. For simulations in reacting conditions, the ignition delay and liquid length are important to verify the outcomes from simulations with experiments. There are two ways to define the ignition delay: light intensity-based, and chamber pressure-based. The ignition delay obtained from the high-speed image is based on the threshold of intensity. A sample temporal maximum intensity is shown in Figure 5.17. The solid black line indicates the instantaneous maximum intensity on log scale in the high-speed image. Once the maximum intensity reaches the steady-state, half of it is defined as the threshold (dashed line). The time at the cross point is defined as the ignition delay.

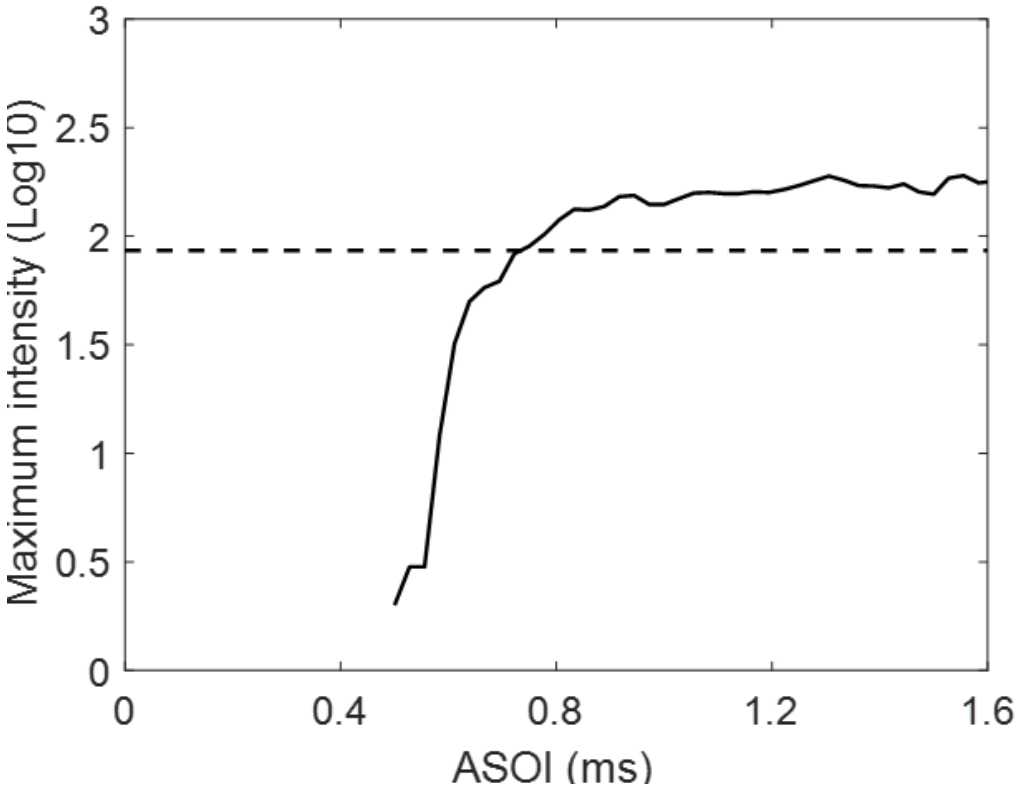

Figure 5.17. A sample of ignition delay determination based on the maximum intensity of the flame.

However, for simulations, it is hard to obtain the natural luminosity directly. Therefore, the ignition delay is determined by the pressure rise due to the combustion. Ignition delay was defined as the time when the mean pressure exceeded the originally filled pressure by 3 kPa, identical to the experiments.

For the liquid length, it is obtained by finding the maximum extent of the spray development in experiments. In the simulation, spray penetration before impingement was defined as the distance between the nozzle tip and the leading edge of the liquid spray encompassing 97% of the fuel mass.

The standards for ignition delay and spray penetration are based on the ECN [81]. Details regarding the comparison between experiments and simulations will be discussed in section 5.3.

5.2.2 Natural luminosity generated by simulations

A method to visualize the soot field from a spray flame in CFD simulations was developed by Hessel et al. and utilized in this study [120]. This method allowed direct comparisons between natural luminosity images and CFD numerical results for the relative brightness of the soot incandescence. The method was based on projecting blackbody radiation from the soot cloud along line-of-sights onto a two-dimensional plane and accounted for the optical characteristics of the imaging system. The length scale of line-of-sight integration in the current study was 0.2 mm/pixel. Higher resolution could not be achieved due to the extremely huge computer memory requirement when processing the CFD column format data.

The details of converting the soot volume fraction to the natural luminosity are provided as follows. The soot volume fraction is the ratio of the mass of soot divided by the volume of the cell to the mass of soot divided by the volume of soot particle. The processing steps are: Firstly, the radiant intensity of a soot particle assuming blackbody radiation is calculated based on the refractive index and temperature of soot particles. Then the soot

emissivity is calculated based on the soot volume fraction and the distance along the line-of-sight direction within a cell. In the current thesis, the direction of line-of-sight is the z-axis which is the vertical direction. Next, the soot transmissivity is calculated by subtracting soot emissivity from 1. Finally, the signals received by the camera sensor are locally calculated by multiplying the soot transmissivity, the radiant intensity, and the spectral response of the camera. After the local calculation, the signals are integrated along the line-of-sight direction.

In a previous study [116], a direct comparison between the experiments and simulations have not been done. This was because that the line-of-sight integrated CFD luminosity images did not share the same luminosity scale with the experimental high-speed images. To facilitate direct comparison, the CFD intensity $I(x,y)_{CFD}$ was scaled with respect to the camera display scale (0-255). Figure 5.18 shows the highest intensity at each timestamp for the experimental results. The calibration point for simulations is chosen at the same time step to match the time of maximum experimental intensity. As can be seen in the figure, the highest intensity is increased with time and it reaches the maximum value at a certain time *t* ASOI, and then stays at a nearly constant value in experiments. Therefore, it is assumed time *t* ASOI is a relatively steady-state and the maximum intensity is the same for both the experiments and simulations at *t* under the same display scale. The scaled flame luminosity $I'(x,y)_{CFD}$ is obtained by using the following equation:

$$I'(x,y)CFD = I(x,y)CFD * [max(I(x,y)EXP)/cal(I(x,y)CFD)]|t \quad (5.18)$$

The $cal(I(x,y)_{CFD})$ and $max(I(x,y)_{EXP})$ are marked with green and red circles in Figure 5.18, respectively. However, this method has limitations because the trends of experiments and simulations are diverse after the calibration point. The maximum intensity of experiments drops but the maximum intensity of simulations continues going up. This scaling process needs to be further modified to fit the trend to match the experimental results.

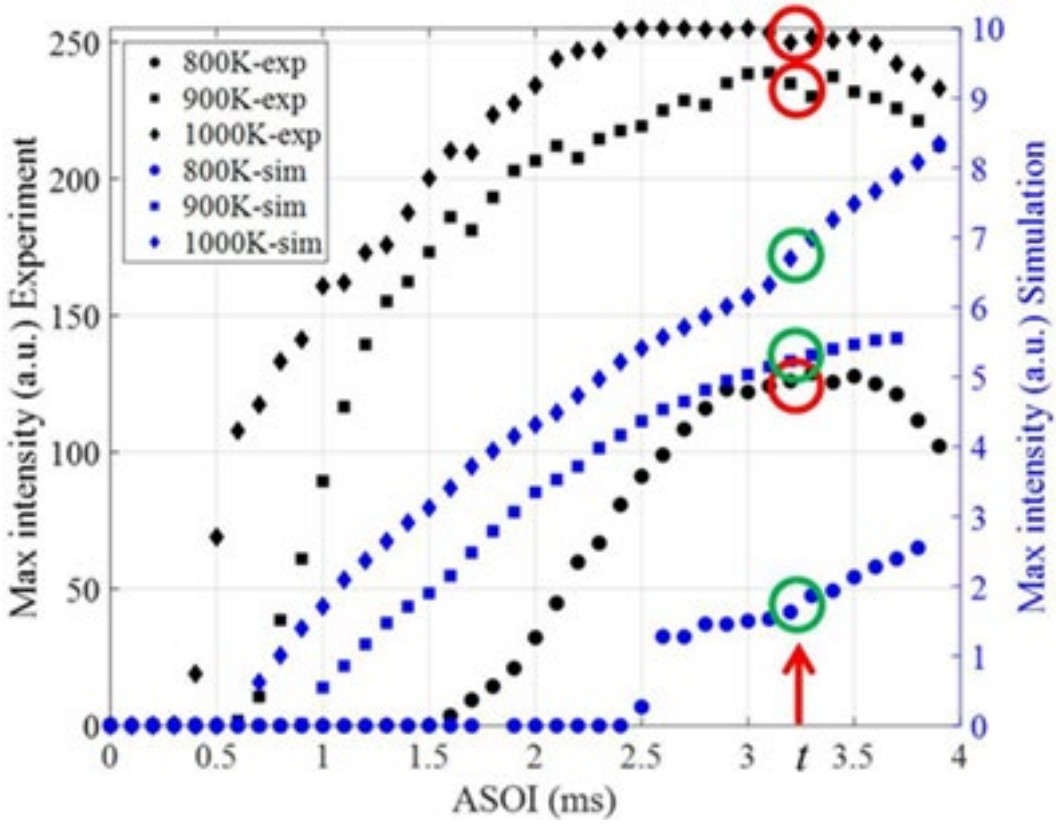

Figure 5.18. Temporal maximum intensity comparison between experiments and simulations. The $cal(I(x,y)_{CFD})$ and $max(I(x,y)_{EXP})$ are marked with green and red circles, respectively.

5.2.3 Curvature calculation for transient turbulent impinging spray boundary

In order to directly compare the curvature distribution with experimental results, LES simulation results were interpolated into a reconstructed domain with a grid resolution of 0.1047 mm. Limited by the computational cost associated with the resolution of the reconstructed data, CFD data analysis was only performed on a plane 1 mm above the impinging plate. The flame front boundary was traced by using the OH radicals contour (instead of natural luminosity in experiments) on the chosen plane. The curvature distribution was characterized as histograms with a bin size of 0.05 mm^{-1} for both experiments and simulations. The calculation of the boundary curvatures follows the method introduced in section 5.1.3. A sample of instantaneous OH contour is shown on the

left of Figure 5.19. By using the boundary tracking method, the binary area of spray occupied region is detected and the boundary is marked together with the binary image. This detection is shown in the middle of Figure 5.19. The curvature profile from one edge of the spray boundary to another is displayed on the right of Figure 5.19.

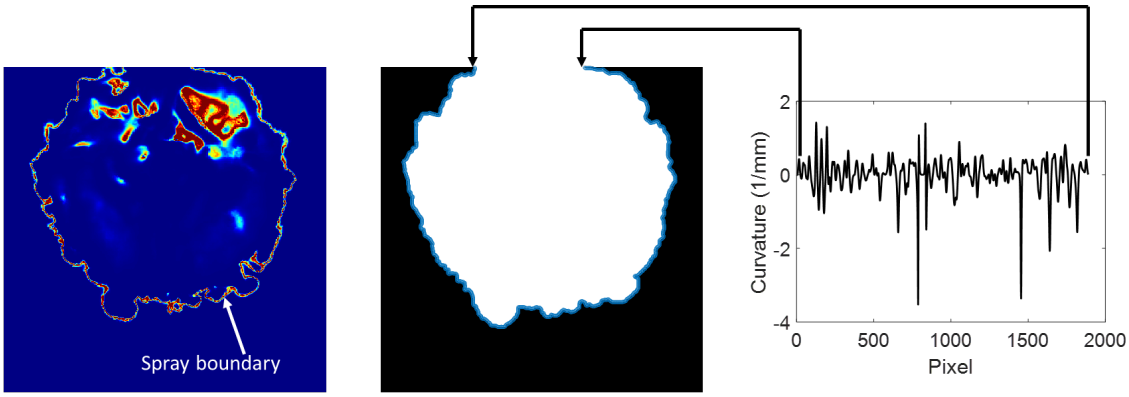

Figure 5.19. Left: Instantaneous OH contour from 900 K flame. Middle: Binary area of spray detected by the boundary tracking method. Right: Curvature profile of the detected boundary.

5.3 Validation of simulations

After the model description and definitions from simulations, the validation of simulations against the experimental results will be discussed in this section. The spray penetration and ignition delay will be compared between RANS, LES, and experimental results. The penetration and ignition delay validations for film cases will be discussed independently. The qualitative flame shape validation will be discussed in Chapter 6.

5.3.1 Validations of spray penetration

Spray penetration is one of the most widely used parameters for model validation. Figure 5.20 shows the temporal liquid penetration comparison between the experiment and the simulation at an ambient temperature of 900 K with 0% O_2 before spray impinging on the wall, at 0.45 ms ASOI.

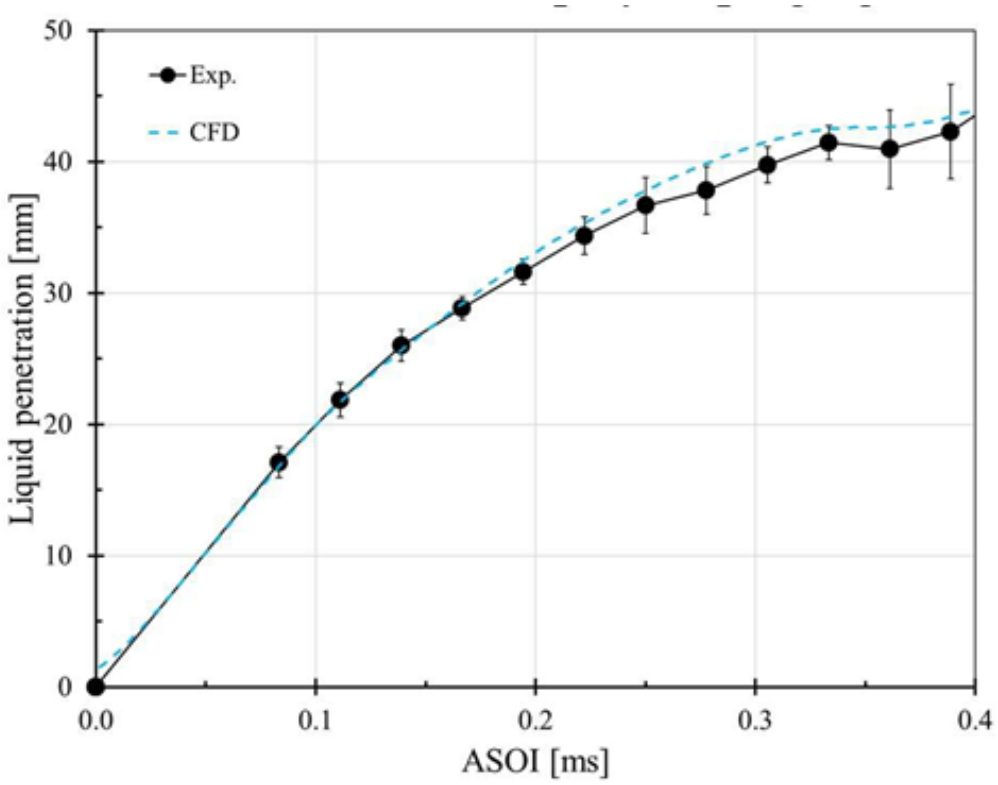

Figure 5.20. Spray liquid length comparison between RANS simulation and experiments. T_{amb} = 900 K, P_{inj} = 1500 bar and 0% O_2.

Figure 5.21 shows that the simulated liquid penetration for LES simulations matches the experimental results well which means the spray momentum is predicted well. The time of spray impingement at the current test condition is ~ 0.45 ms ASOI which is nearly identical between experiments and simulations. From Figure 5.21, it can be seen that the liquid length under T_{amb} of 900 K is close to the traveling distance. Thus, it can be concluded that spray under 900 and 1000 K ambient temperatures will not deposit distinct film but the spray under 800 K will under the impinging distance of 40 mm.

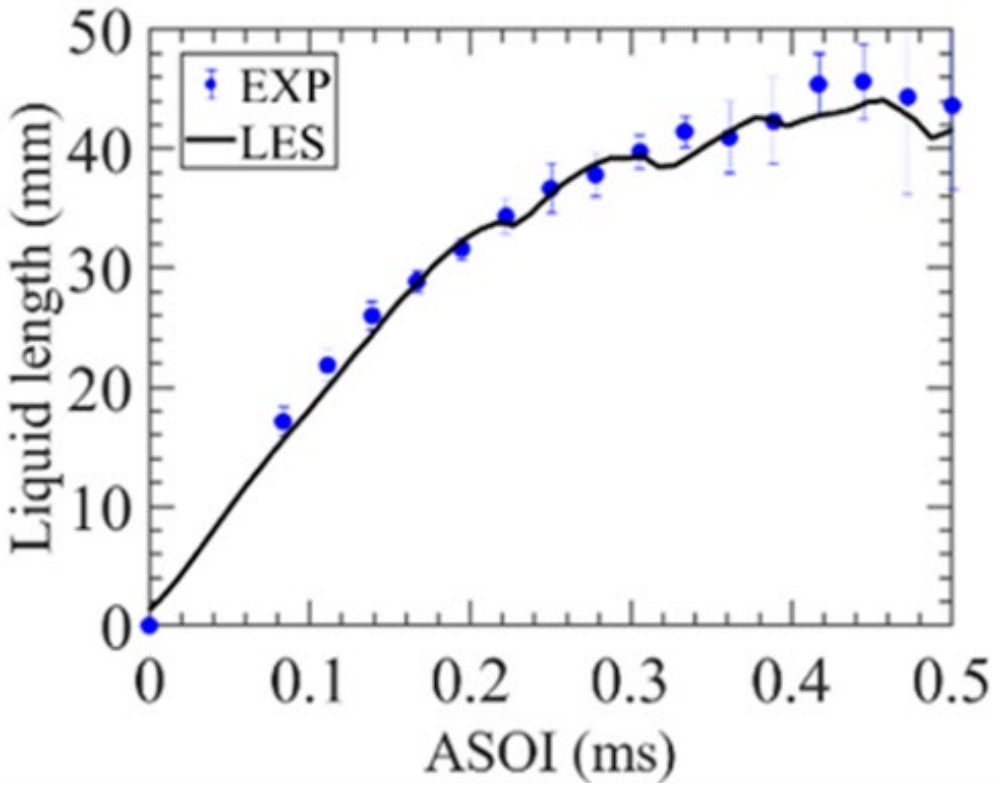

Figure 5.21. Spray liquid length comparison between LES simulation and experiments. T_{amb} = 900 K, P_{inj} = 1500 bar and 0% O_2.

For the film case, spray penetrations at different ambient temperatures and impinging distances were obtained from simulations and their comparisons with experimental data are shown in Figure 5.22. It is noted that the film case applies the RANS turbulence model.

In Figure 5.22, it is observed that the simulation results matched well with the experimental result before 0.2 ms ASOI. After 0.2 ms ASOI, under the same impinging distance, the simulations slightly over-predict the spray penetration. It is noted that the spray penetration is saturated at an impinging distance of 30 mm after 0.2 ms ASOI due to the earlier impingement at a lower impinging distance.

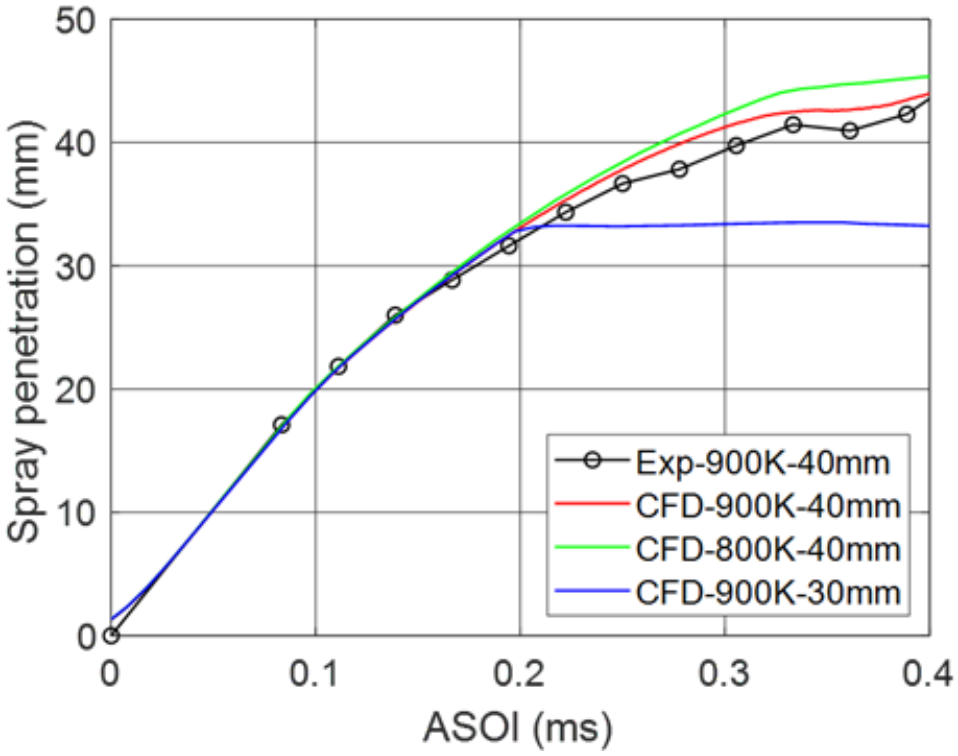

Figure 5.22. Validation of the spray penetration for film case.

5.3.2 Validations of ignition delay

After discussing the spray penetration, the ignition delays from RANS, LES, and film cases will be provided in this section.

Figure 5.23 shows ignition delays at different ambient temperatures both in experiments and simulations. As mentioned in the previous section, ignition delay was obtained based on pressure- rise. The simulated ignition delay matches quite well at 900 K and 1000 K while it is over-predicted at 800 K. In addition, although the ambient temperature varied, the spray or the flame traveled towards the impinging plate with the same initial momentum. Thus, the spray impingement time was maintained the same under three temperature conditions around 0.45 ms, represented with a red solid line in Figure 5.23. It is also interesting to point out that though ignition delays at three ambient temperature cases is all longer than 0.45 ms, the flame luminosity at 900 K and 1000 K can be visualized

even before the impingement [121]. This is likely because the luminosity could be either produced by the cool flame or the other radicals' chemiluminescence.

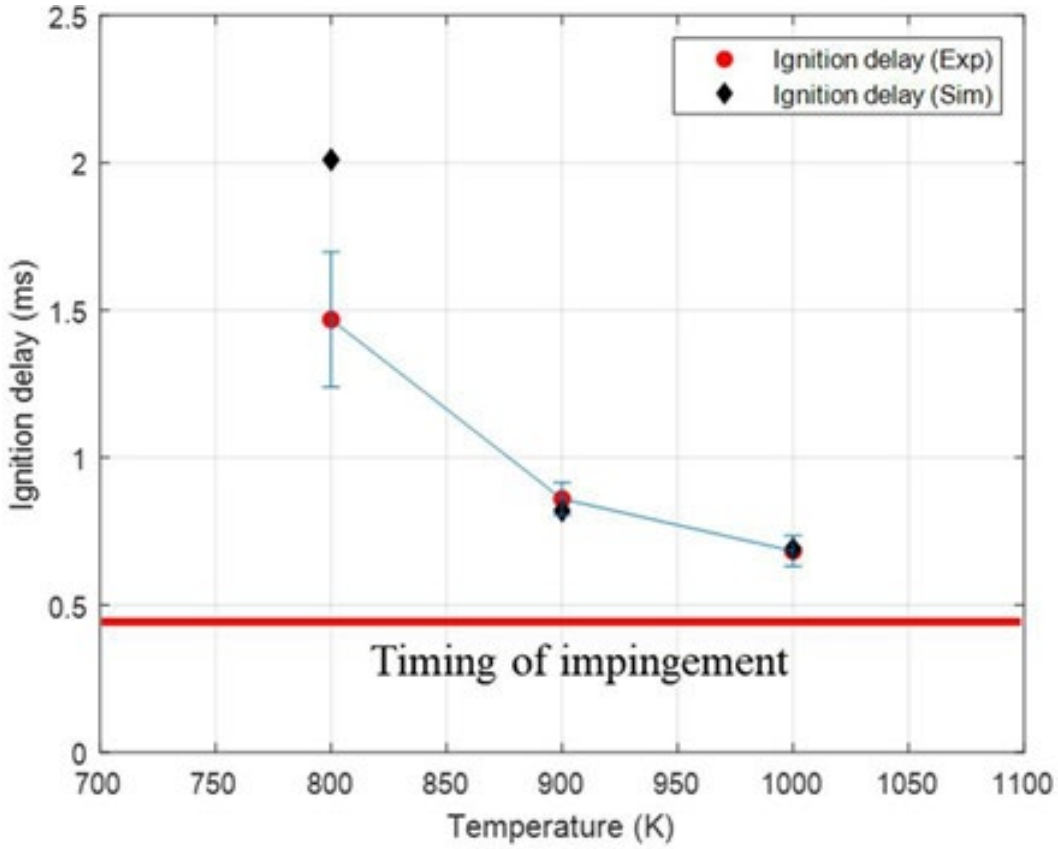

Figure 5.23. Pressure-based ignition delay comparison between RANS simulations and experiments under different ambient temperatures.

Figure 5.24 shows ignition delays comparison for LES simulations at ambient temperatures of 800, 900, and 1000 K with 18% O_2 in both experiments and simulations. Simulation results showed 0.01 ms less variation at 800 and 900 K, and 0.1 ms less variation at 1000 K. The well-matched ignition delays indicate that the auto-ignition behaviors could be predicted well by the simulations. The well-matched ignition delay is also crucial for predicting the correct ignition location and representing the flame development from simulations.

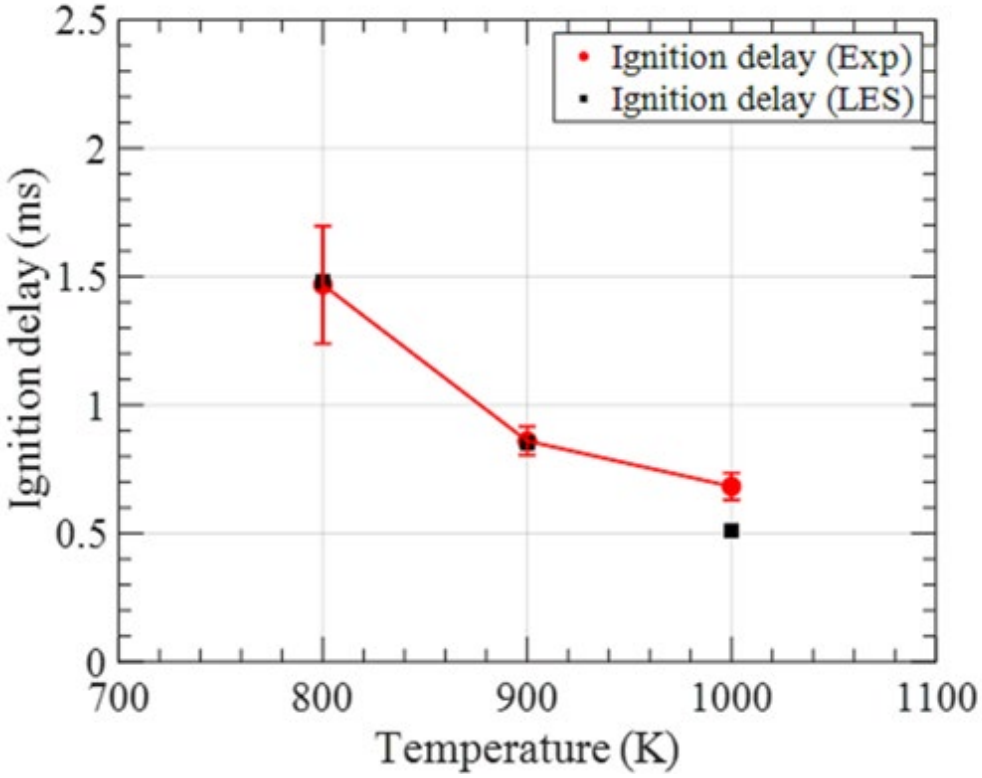

Figure 5.24. Pressure-based ignition delay comparison between LES simulations and experiments under different ambient temperatures.

Validation of ignition delays for film cases is shown in Figure 5.25. From Figure 5.25, it could be observed that the ignition delay matches well under the ambient temperatures of 900 and 1000 K. The impinging distance doesn't have significant effects on the ignition delay under these two ambient temperatures. However, the simulation result at an ambient temperature of 800 K is over-predicted by around 0.5 ms. And shorter impinging distance leads to longer ignition delay at an ambient temperature of 800 K. The outcomes from simulations could do the quantitative comparison for the 900 and 1000 K cases but qualitative comparison for the 800 K case since the ignition delay is over-predicted at 800 K case.

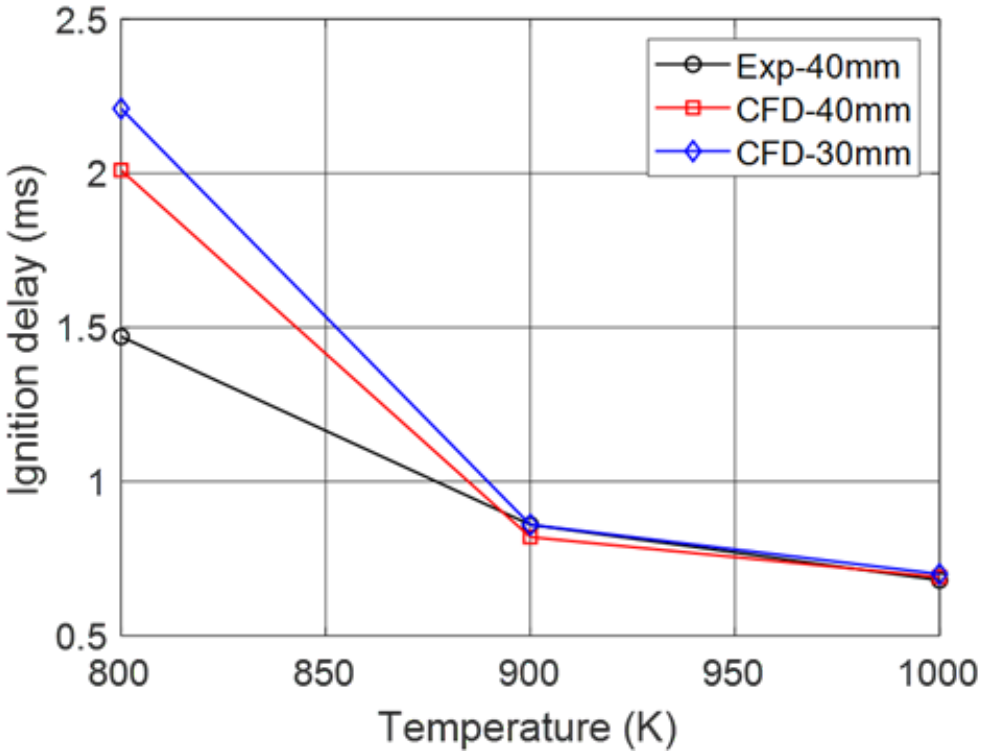

Figure 5.25. Pressure-based ignition delay comparison between RANS (film) simulations and experiments under different ambient temperatures and impinging distances.

6 Macroscopic spray and flame boundary structure and behavior of an impinging diesel spray[3]

In this chapter, the macroscopic impinged spray characteristics under both non-vaporizing conditions and reacting conditions will be discussed. The macroscopic boundary structure includes the distance of the impinged spray from the impinging point, the propagation rate of the spray, and radial intensity distribution from the Mie scattering signals and natural luminosity signals. In the first section, the propagation distance and propagation rate from non-vaporizing conditions are examined. In the second section, the flame front and bulk flame propagation speed are evaluated from reacting conditions. The results from non-vaporizing and reacting conditions are then compared to discuss the effect of reactions on

---

[3] Reprinted with permission from SAE papers 2019-01-0067 and 2019-01-0267 ©2019 SAE International. Reprinted with permission from International Journal of Engine Research (IJER) and the American Society of Mechanical Engineers (ASME). The materials in this chapter were published in the following papers:

- Zhao, Z., Zhu, X., Zhao, L., Naber, J. et al., "Spray-Wall Dynamics of High-Pressure Impinging Combustion," SAE Technical Paper 2019-01-0067, 2019, https://doi.org/10.4271/2019-01-0067.
- Zhao, Z., Zhu, X., Naber, J., and Lee, S., "Impinged Diesel Spray Combustion Evaluation for Indirect Air-Fuel Mixing Processes and Its Comparison with Non-Vaporing Impinging Spray Under Diesel Engine Conditions," SAE Technical Paper 2019-01-0267, 2019, https://doi.org/10.4271/2019-01-0267.
- Zhao, Z, Zhao, L, & Lee, S. "Evaluation of Soot Production Near a Cold Surface for an Impinged Diesel Spray Combustion." Proceedings of the ASME 2020 Internal Combustion Engine Division Fall Technical Conference. ASME 2020 Internal Combustion Engine Division Fall Technical Conference. Virtual, Online. November 4–6, 2020. V001T05A002. ASME. https://doi.org/10.1115/ICEF2020-2938
- Zhao Z, Zhu X, Naber J, Lee S-Y. Assessment of impinged flame structure in high-pressure direct diesel injection. International Journal of Engine Research. 2020;21(2):391-405. doi:10.1177/1468087419859788

the bulk spray propagation. In the last section, the results from CFD simulations are compared against the experimental results to verify the numerical outcomes.

6.1 Time-resolved flame images and validation of flame shape from natural luminosity

Time-resolved side-view images of flame luminosity (with dimensions of 50 mm vertical and 66.5 mm horizontal) are shown in Figure 6.1 to study the dynamics of impinged flame propagation. The injector tip and impinging plate are marked with blue triangles and solid yellow lines, respectively. As shown in the first row of Figure 6.1, the soot is first observed above the plate at around 0.4 ms ASOI at the ambient temperature of 1000 K. At 0.6 ms ASOI, the observed soot region expands towards the impinging plate. At an ambient temperature of 900 K, the location of initially observed soot is closer to the impinging plate than the location at an ambient temperature of 1000 K but still lies above the plate. The appearance of the impinged flame at an ambient temperature of 900 K is comparable with the one at an ambient temperature of 1000 K, but less soot is formed at the upstream. It is also notable that a soot-rich region (the brightest region) is formed at the top of the flame front at these two temperatures. At the ambient temperature of 800 K, the soot is first observed in between 1.7 and 2.2 ms ASOI. When the impinged flame flashes back from the leading edge towards the impinging point, no soot is observed in the backside of the impinging point. At around 3 ms ASOI, there is no soot observed upstream for all three cases due to the end injection.

Based on the previous study [122], the lift-off length of the free spray diesel combustion at an ambient temperature of 1000 K and ambient density of 22.8 kg/m^3 is below 30 mm. And this lift-off length is much shorter compared to the distance between the injector tip and impinging plate in this study (> 40 mm). The behavior of impinged spray combustion resembles the free spray combustion before the impingement. Therefore, the ignition location is above the plate at the ambient temperature of 1000 K in this study. Since the soot is formed near the lift-off length region in free spray combustion, there is a flame

impingement in between 0.6 and 1 ms ASOI which can be seen in the first row of images in Figure 6.1. Similarly, there is also flame impingement observed when the ambient temperature is 900 K. However when the ambient temperature is reduced to 800 K, the lift-off length is much longer, and the flame impingement is no longer visible at this ambient temperature.

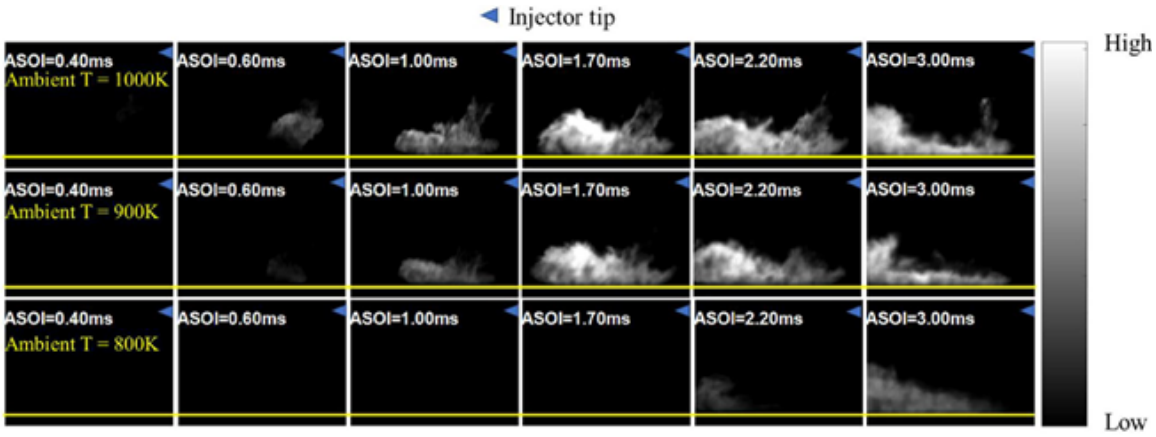

Figure 6.1. A time-resolved flame luminosity development on varying ambient temperature from a side view.

Time-resolved natural luminosity images of the experiments and line-of-sight integrated RANS simulation results from the bottom view are shown in Figure 6.2. It is noted that the line-of-sight soot field is integrated along z-direction in simulations. The impinging point at each condition is marked as a red point in the image. The direction of upstream incoming spray and the direction of flame expansion on the plate is marked with a green solid line and red dashed lines, respectively. The expanding flame is stretched from a circular shape at 1.2 ms ASOI towards an oval shape after 2ms ASOI. The flame luminosity is observed peripheral with respect to the impinging point in the experiments. In the simulation, even the soot luminosity is also peripheral with respect to the impinging point, the region upstream near the impinging point is not occupied by soot and there is no luminosity observed close to the impinging point as well.

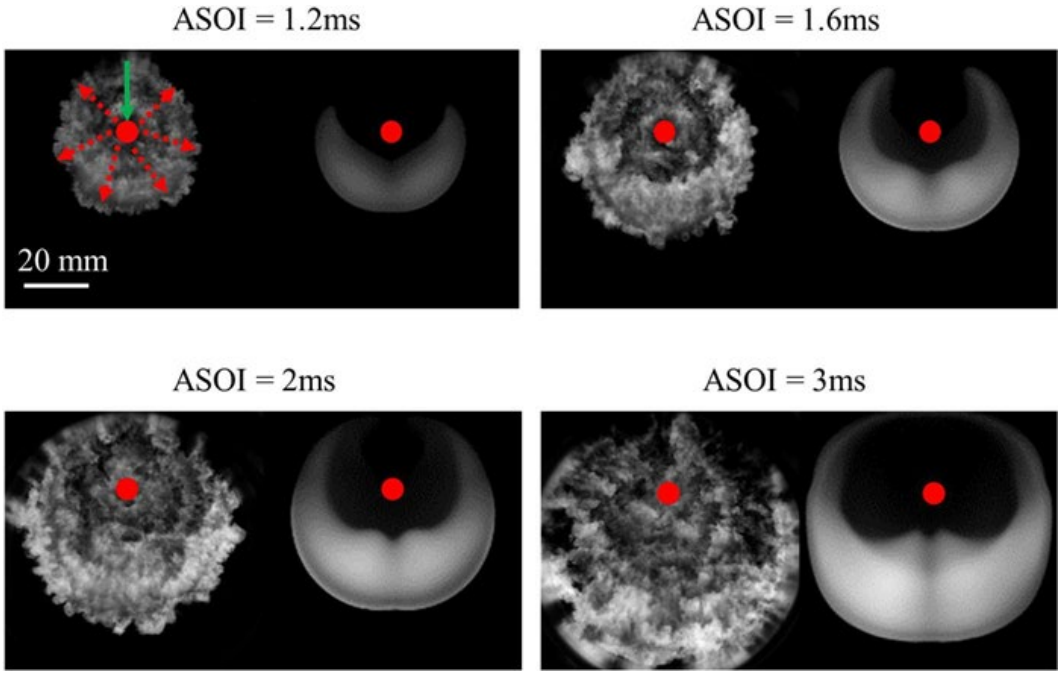

Figure 6.2. Time-resolved natural luminosity images from experiments/line-of-sight luminosity image from simulations, the 900K flame. Left: experiment results; right: simulation results. Impinging point is marked as a red dot. The direction of upstream incoming spray and the direction of flame expansion on the plate is marked with a green solid line and red dashed lines in the very first image, respectively.

Time-resolved natural luminosity images of the experiments and line-of-sight integrated LES simulation results from the bottom view are shown in Figure 6.3. It is noted that the line-of-sight soot field is integrated along z-direction in simulations. The impinging point at each condition is marked as a red point in the image. The direction of upstream incoming spray and the direction of flame expansion on the plate is marked with a green solid line and red dashed lines, respectively. The expanding flame is stretched from a circular shape at 1.2 ms ASOI towards an oval shape after 2 ms ASOI. The flame luminosity is peripherally observed with respect to the impinging point in the experiments. In the simulations, the soot luminosity is also peripherally observed but the region near the impinging point is not occupied by soot and there is nearly no flame luminosity observed close to the impinging point.

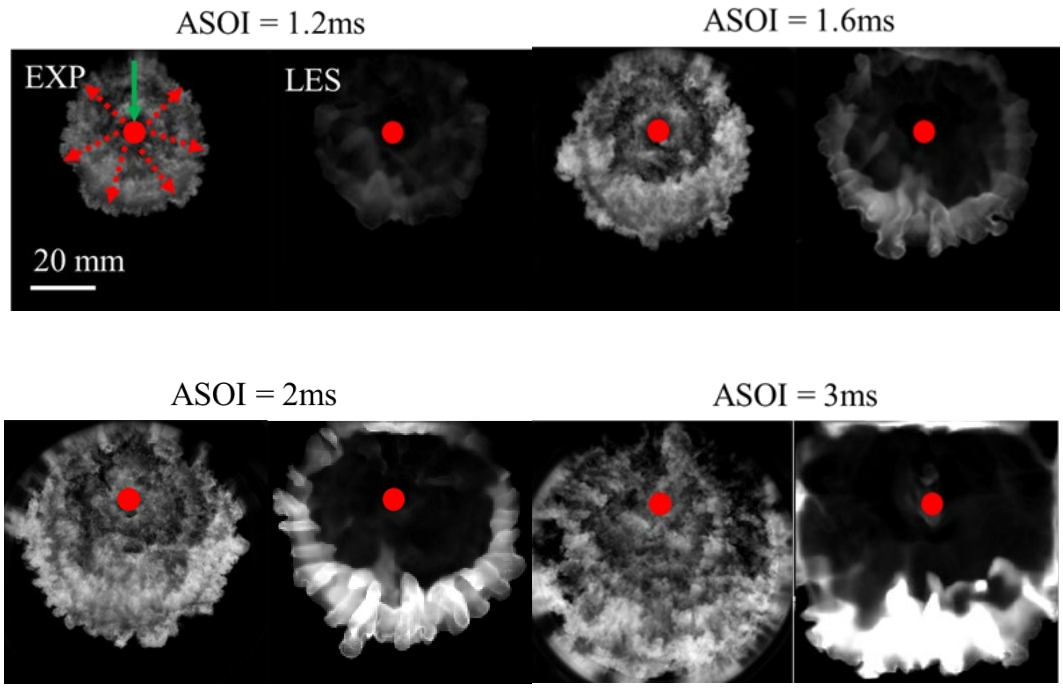

Figure 6.3. Time-resolved natural luminosity images from experiments/line-of-sight LES luminosity image from simulations, the 900 K flame. Left: experiment results; right: numerical results. Impinging point is marked as a red dot. The direction of upstream incoming spray and the direction of flame expansion on the plate is marked with a green solid line and red dashed lines in the very first image, respectively.

6.2 Non-vaporizing spray propagation characteristics after impingement

6.2.1 Spray front distance

The expansion distance for an impinged spray is defined as the distance from the local spray/flame outer boundary to the impinging point. Local expansion distance is used to examine the shape of impinged spray development quantitatively and globally. Four different time marks after starting of impingement (ASI) with an interval of 0.5 ms are chosen from the beginning of the impingement towards the end of injection. The baseline condition (T_{amb} = 423 K, P_{inj} = 1500 bar and ρ_{amb}= 22.8 kg/m^3) for non-vaporizing spray is

shown in Figure 6.4. The expansion distance is obtained radially starting from the spray axis and averaged by 5 repeats. Generally, local expansion distance increases with time at a given circumferential angle but the highest value is always at θ = 180° as most of the spray momentum is distributed along the axial direction after the impingement. The expansion rate which is the time derivative of expansion distance illustrates a decrement along with different ASIs. Except for the axial direction at 180°, most of the radial directions exhibit a deceleration when the time is increased which could be concluded from the more compact profiles. Such a phenomenon indicates that the spray expansion is decelerated due to the shear force acting on the spray from the impinging surface.

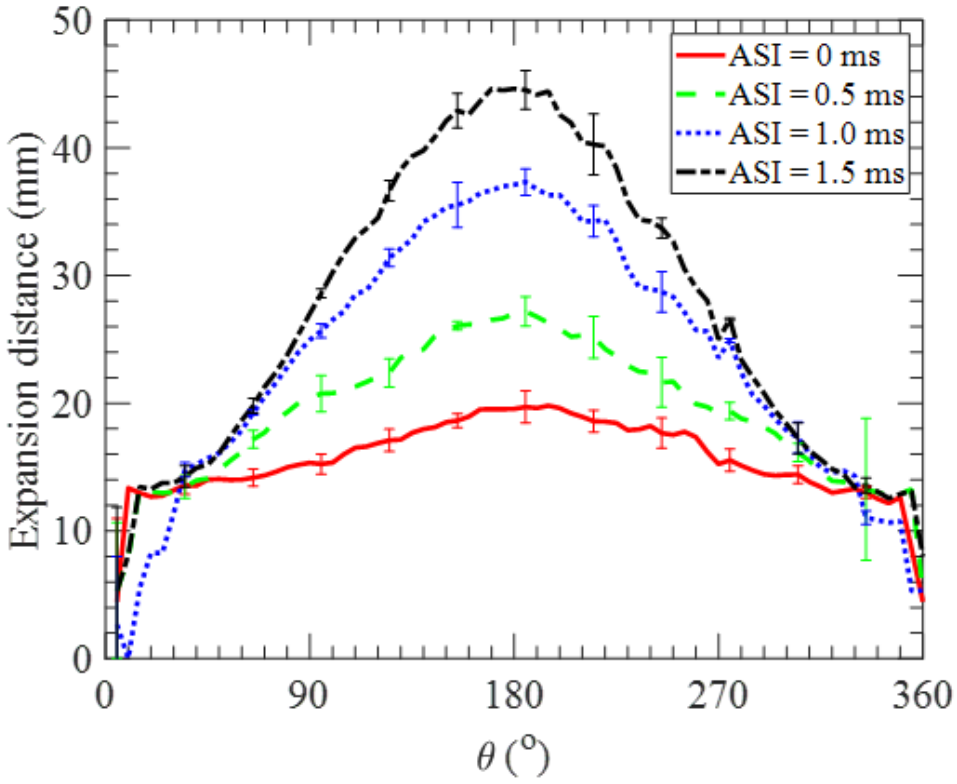

Figure 6.4. Profile of expansion distance of liquid spray expansion along radial directions. Conditions: T_{amb} = 423 K, P_{inj} = 1500 bar and ρ_{amb}= 22.8 kg/m^3.

6.2.2 IRT plots of non-vaporizing diesel spray

In section 6.2.1, the magnitude of the velocity of an expanding spray was obtained but the spray momentum is a combination of local mass and velocity. As mentioned in section 3.3.1, the signals from Mie scattering could represent the qualitative mass distribution of certain liquid droplets. In section 5.1.2, an image processing method called IRT was introduced to process the experimental spray images from the Mie scattering technique. With the help IRT method, the spatial and temporal information of Mie scattering images can be used to exploit qualitative mass distribution. The intensities of Mie scattering are attributed to the incident light angle, droplet size, and intensity of the light source. In the current study, the light source directly illuminates the bottom window of the combustion vessel. Therefore, the local intensities in Mie scattering images are mainly contributed by the number of droplets, i.e., the amount of mass deposited on the plate. Since the charge gas pressure is usually chosen as the adjustable parameter in the engine test instead of injection pressure, the effect of ambient density on the mass distribution will be discussed in this section for a non-vaporizing spray. The effect of ambient density on the local averaged intensity is shown in Figure 6.5, where it can be seen that the averaged intensities are uniformly distributed except in the axial direction which is the region between 150° and 210°. The averaged intensity at axial direction is much higher than other regions at the same time instant. With ambient density increment, averaged intensity also increases, while this increment happens in the axial direction only.

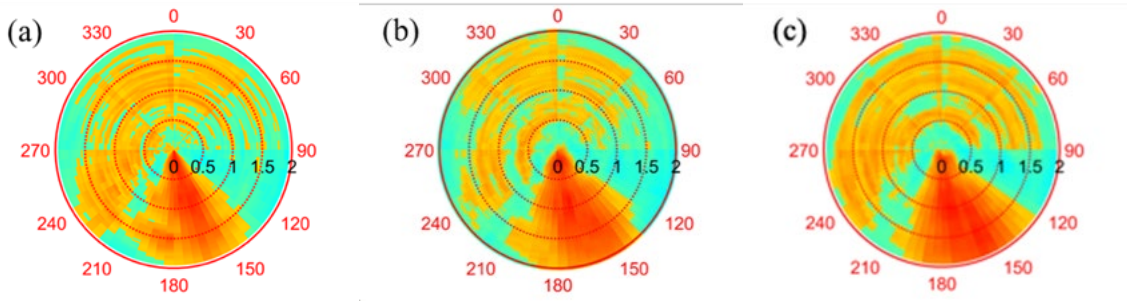

Figure 6.5. Intensity-axial-time under different ambient density (a) 14.8 kg/m^3 (b) 22.8 kg/m^3 (c) 30.0 kg/m^3. Conditions: T_{amb} = 423 K, P_{inj} = 1500 bar. The numbers marked on the dashed circles indicate the ASI time.

6.2.3 Droplet sizing measurement under non-vaporizing conditions

Location	Heater Temp (C)	Amb. Density (kg/m^3)	Inj. Pressure (bar)	Sensor Number	Total # of repeats
1	No	22.8	1500	1-36	5
2	No	22.8	1500	1-36	3
2	No	22.8	1200,1500,1800	16-36	9
2	200	14.8,22.8,30	1200,1500,1800	16-36	15
2	250	14.8,22.8,30	1200,1500,1800	16-36	15
3	No	22.8	1500	1-36	3
3	No	22.8	1500	16-36	3

Figure 6.6. Test conditions for droplet sizing measurement.

The test conditions for droplet sizing measurements are shown in Figure 6.6. The ambient density, injection pressure, and temperature of the impinging plate are varied. The total sensor number is 36. Some of the tests were using sensors number 16-36 to only focus on the smaller size of the droplet. The Sauter Mean Diameter (SMD, D_{32}) results are defined as the diameter of a sphere that has the same volume/surface area ratio as a particle of interest, which is a parameter standing for the average particle size. SMDs show an increase after impingement, as shown in Figure 6.7. The low temperature (135℃) case has the highest SMD value during the whole process. 200℃ case has slightly higher SMD than 250℃ case. The detailed probability density function (PDF) plots of particle size distribution at 5 ms ASOI are compared among three plate temperatures, as shown in Figure 6.8. The PDF shows the particle size distribution at 5 ms ASOI. The center of PDF locates at 54.12 μm, 18.48 μm, and 15.85 μm for 135℃, 200℃, and 250℃, respectively.

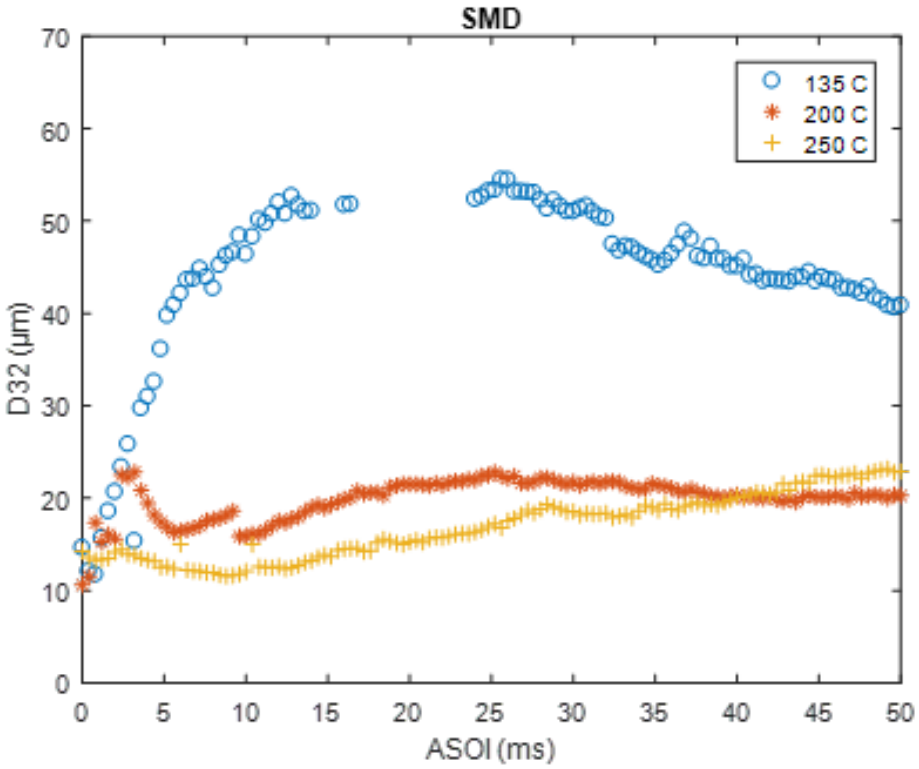

Figure 6.7. Instantaneous SMD for different plate temperatures.

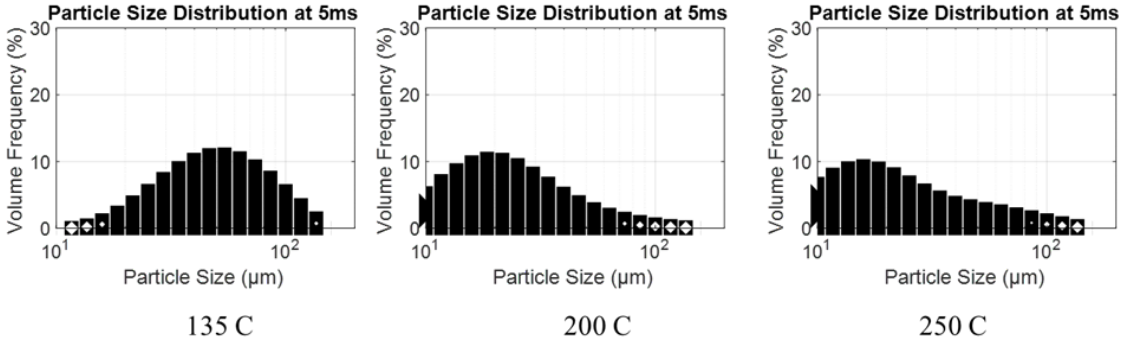

Figure 6.8. Particle size distribution at various plate temperatures.

Droplet sizing measurement was carried out in five different locations and various ambient conditions. Figure 6.9 shows a schematic of the five locations in the experimental setup and the timing that the spray tip reaches the center of each detection location respectively. Baseline condition is ambient density of 22.8 kg/m^3, injection pressure of 1500 bar.

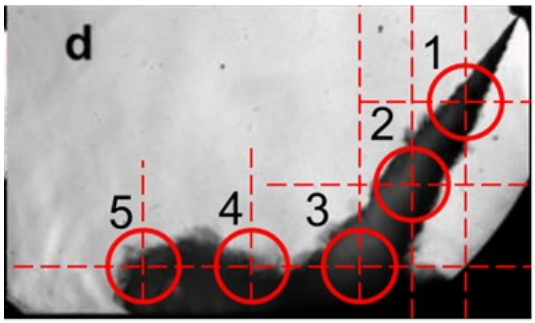

Position	Spray tip reach position center timing
1	0.333ms
2	0.444ms
3	0.667ms
4	1.056ms
5	1.583ms

Figure 6.9. A schematic of droplet sizing measurement.

The SMD (Sauter mean diameter) is the main outcome of the droplet sizing measurement. Figure 6.10 shows the SMD evolution with time at 5 different locations at the baseline condition. Before the end of spray(~2.7ms), location 3 (impinging point) has the largest SMD. After the end of the spray, the SMD at 4 and 5 surpass at 3.

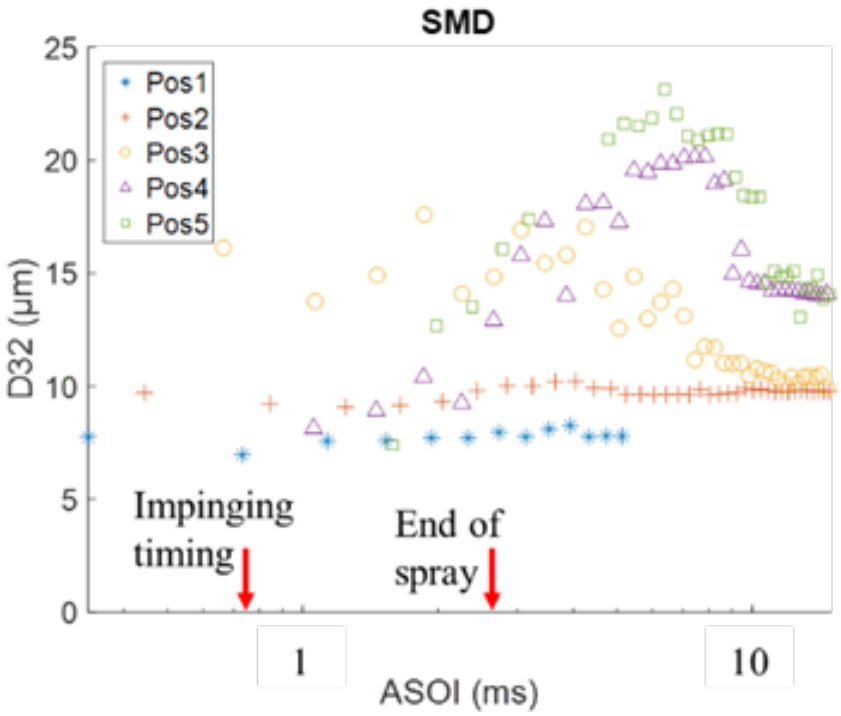

Figure 6.10. Instantaneous SMD at five different locations at the baseline condition.

Figure 6.11 shows the results of the effect of injection pressure and ambient density on SMD evolution. Apparently, the injection pressure does not hold an obvious effect on the SMD. During the late spray, 1500 bar case shows a little bit high SMD than 1200 bar and 1800 bar cases. However, the high ambient density leads to smaller SMD, due to the effect that better air mixing and air entrainment.

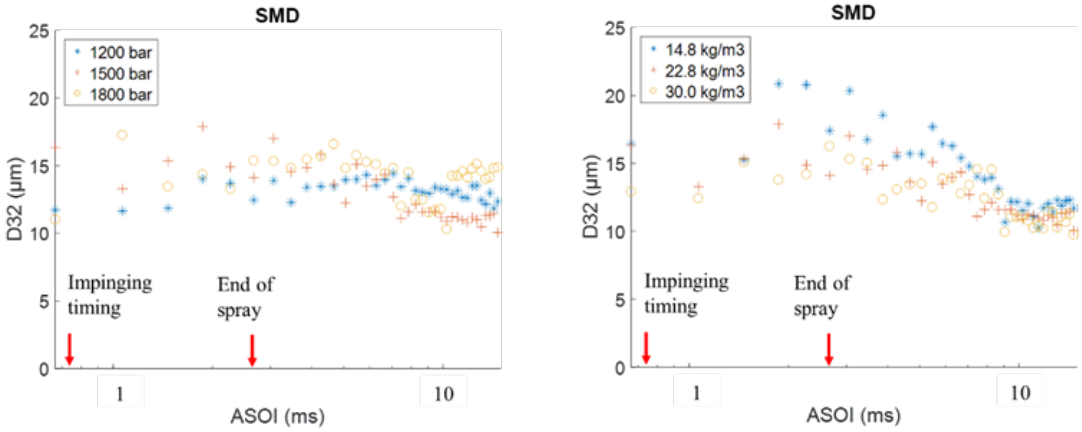

Figure 6.11. Effect of injection pressure and ambient density on SMD.

6.3 Reacting spray propagation characteristics after impingement

6.3.1 Flame front distance and bulk flame propagation rate

In the previous study, the expansion distance at axial and radial directions of the diesel impinged spray was quantified under non-vaporizing conditions [29]. In the current study, the flame expansion is visualized by the soot incandescence. Therefore, the flame front is important to locate the soot regions during the flame expansion. The flame front boundary is obtained to investigate the difference between the behavior of spray expansion and flame expansion.

The local flame front distance at T_{amb} (ambient temperature) of 1000 K is shown in Figure 6.12. The local flame front distances at four different timestamps are chosen to represent the trend of growth of the flame front, starting from 0.8 ms ASOI to 2 ms ASOI with an interval of 0.4 ms. At a given time, the local flame front distance is plotted along with the

sequence of θ. Generally, the local flame front distance increases as the ASOI increases. At 0.8 ms ASOI (~ 0.3 ms after the flame impingement), the local flame front distance shows nearly a flat line with a magnitude of ~10 mm. However, at 1.2 ms ASOI, the local flame front distance at axial direction jumps towards around 25 mm from ~ 10 mm while the distance at two radial directions only increases to around 20 mm. At 1.6 ms ASOI, the local flame front distance keeps increasing but the growth rate in the same period (0.4 ms) at axial direction decreases. At 2 ms ASOI, the flame front distance has a slower rate of growth except for sectors between 0° to 50° and 300° to 360°. Such a phenomenon is due to the fact that the flame reaches the edge of the bottom window after 1.6 ms ASOI. Therefore, the local flame front distance is saturated at around 20 mm in sectors between 0° to 50° and 300° to 360°.

In order to compare the development of the pattern of flame expansion under-reacting cases and liquid fuel expansion under non-vaporizing cases, the ratio of axial flame distance to radial flame distance is obtained from taking the ratio of the flame distance at 180° to the flame distance at 90°. In a previous study [29], the ratio was around 1.4 under non-vaporizing conditions at 2 ms ASOI when the vertical distance between the nozzle tip and the impinging plate was 52 mm, showing an oval shape. When the vertical distance is reduced down to 40 mm, the ratio of axial to radial distance is increased to around 1.6 ~ 1.7 at 2 ms ASOI. The increased ratio of axial distance to radial distance may be due to the higher injection momentum at the shorter distance and combustion process. Such a phenomenon indicates that the shape of flame expansion is stretched, showing a slimmer oval shape along the axial direction. The increased ratio could allow more fuel vapor to accumulate in the axial direction, forming a fuel-rich zone and further producing soot in the subsequent combustion process.

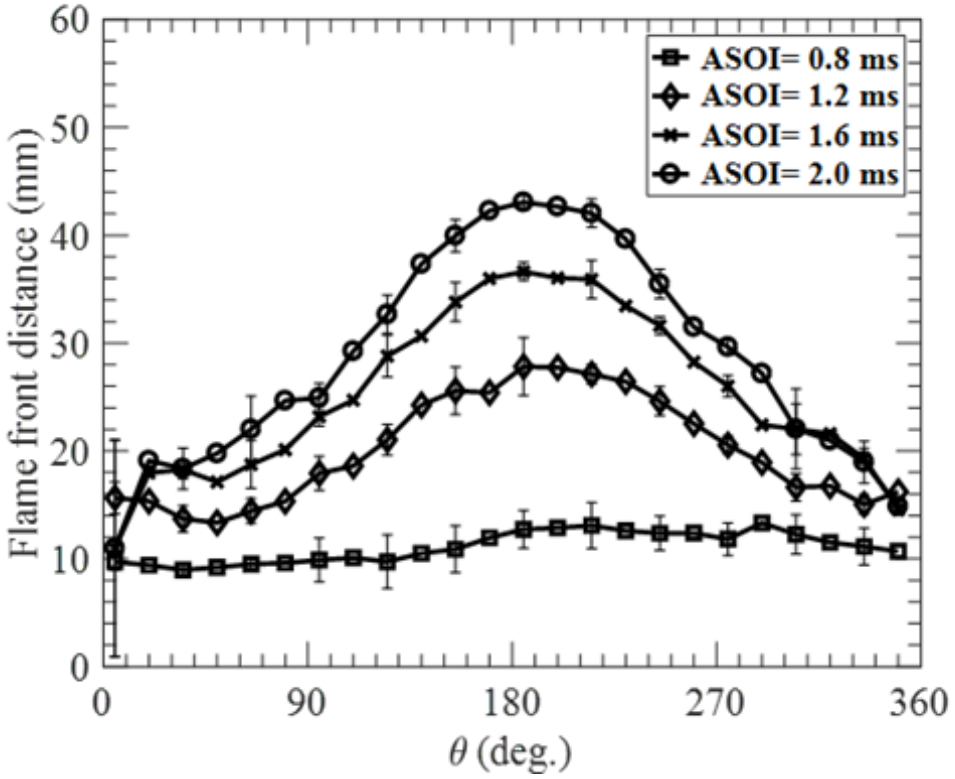

Figure 6.12. Profile of local flame front distance at T_{amb} = 1000K and four different time stamps.

The local flame front distance at T_{amb} of 900 K is shown in Figure 6.13. The profile of local flame front distance shows an asymmetric shape along with the axial direction. The local flame front distance is calculated starting from 1.2 ms ASOI at T_{amb} of 900 K. Compared with results at T_{amb} of 1000 K, the local flame front distance (FFD) is lower at 1.2 ms ASOI at T_{amb} of 900 K but shows a similar magnitude after 1.6 ms ASOI.

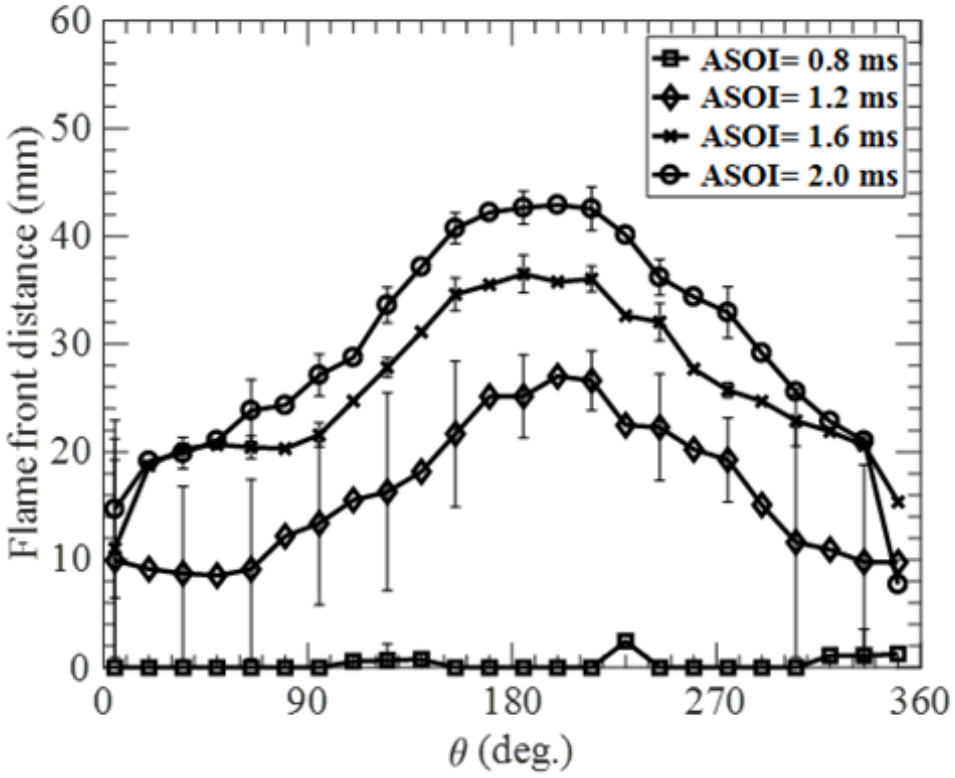

Figure 6.13. Profile of local flame front distance at T_{amb} = 900K and four different time stamps.

The local FFD shows an asymmetric shape, indicating an oval shape of the flame expansion pattern. The ratio of axial to radial distance is increased as the vertical distance between the nozzle tip and impinging plate is reduced. At T_{amb} of 900 K, soot doesn't occupy the impinged spray before 1.6 ms ASOI. The soot area grows to catch the impinged spray outer boundary. Such a phenomenon leads to the fact that flame expansion rate at the early stage of timing after the flame impingement is lower compared with T_{amb} of 1000 K.

In early engine cycles, the injection pressure could significantly affect the quality of the air-fuel mixing process [123]. Higher injection pressure could enhance the air-fuel mixing because it could allow more opportunity for the fuel to mix with air. Unlike a free spray, the momentum of impinged spray is re-distributed after the impingement. There are four stages defined for the expansion rate under non-vaporizing cases after the impingement:

rapid deceleration; slow deceleration; constant expansion rate and expansion termination. If these stages are valid for impinged combustion, the regions which surround the impinging point should have the best quality of air-fuel mixing while the local region near the leading edge of the flame should have the worst quality of air-fuel mixing because the region near the leading edge sits in expansion termination stage. In this section, the effect of ambient temperature on the flame expansion rate is discussed. Local flame expansion rate (FER) is also plotted along the sequence of θ.

The local FER at T_{amb} of 1000 K is shown in Figure 6.14. At 0.8 ms ASOI, the axial direction has the maximum velocity and the profile of the speed shows an asymmetric shape along the axial direction. At 1.2 ms ASOI, the axial direction shows a rapid deceleration while the velocity at other directions slowly decreases. At 1.6 ms AOSI, the flame expansion rate reaches the constant expansion regime, showing a nearly uniform velocity distribution from sectors 50° to 300°. At 2 ms ASOI, the flame front distance is already saturated in the sectors 0° to 90° and 270° to 360°. Therefore, in these sectors, the velocity decreases to nearly 0 m/s. While the magnitude of mean velocity at 2 ms ASOI is slightly lower than the mean velocity at 1.6 ms AOSI, the stage of velocity is still in the constant expansion regime. Therefore, at T_{amb} of 1000 K, the behavior of the flame expansion follows rapid deceleration; slow deceleration, and constant expansion rate.

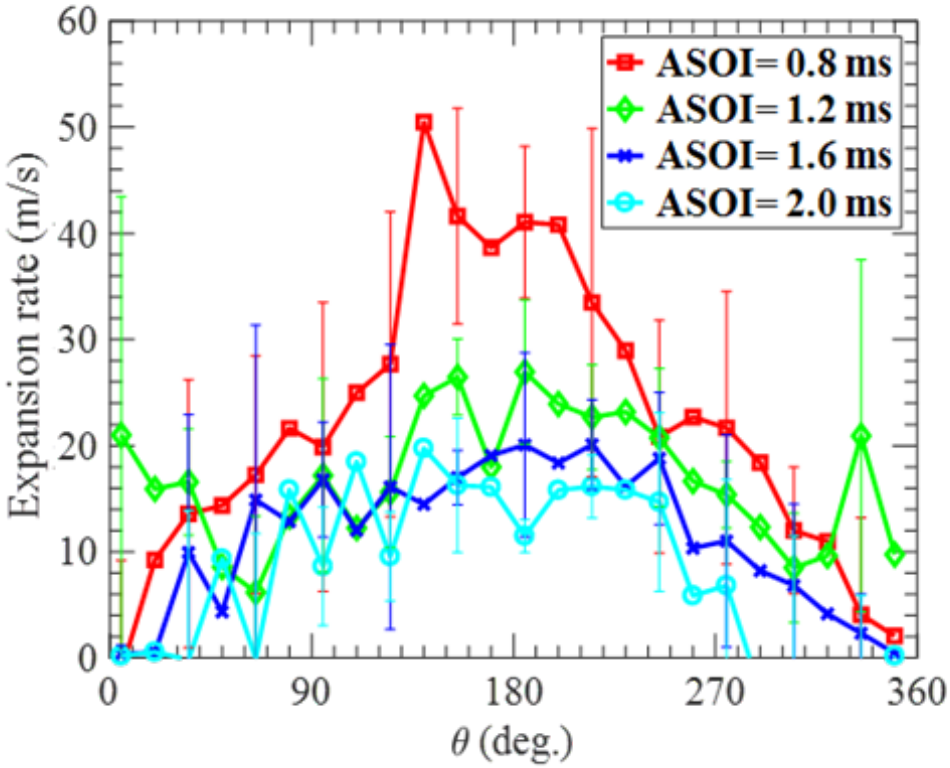

Figure 6.14. Profile of local expansion rate at T_{amb} = 1000K and four different time stamps.

At T_{amb} of 900 K, the flame expansion rate is calculated starting from 1.2 ms ASOI. The profiles are shown in Figure 6.15. The flame expansion reaches the constant expansion regime after 1.6 ms ASOI. Furthermore, the velocity profile at T_{amb} of 900 K matches the velocity profile at T_{amb} of 1000 K. It is found that the ambient temperature doesn't show significant effects on the expansion rate after 1.6 ms ASOI. However, at an ambient temperature of 900 K and 1.2 ms ASOI, the velocity is lower than the one at 1.6 ms ASOI under the same T_{amb}. This is due to the fact that the soot luminosity starts to be visualized at 1 ms ASOI and soot occupied area starts to expand in the impinged spray. The calculated flame expansion rate represents the growth rate of soot occupied area. The overall flame expansion at T_{amb} of 900 K still follows rapid deceleration; slow deceleration and constant expansion rate when soot occupies the impinged spray.

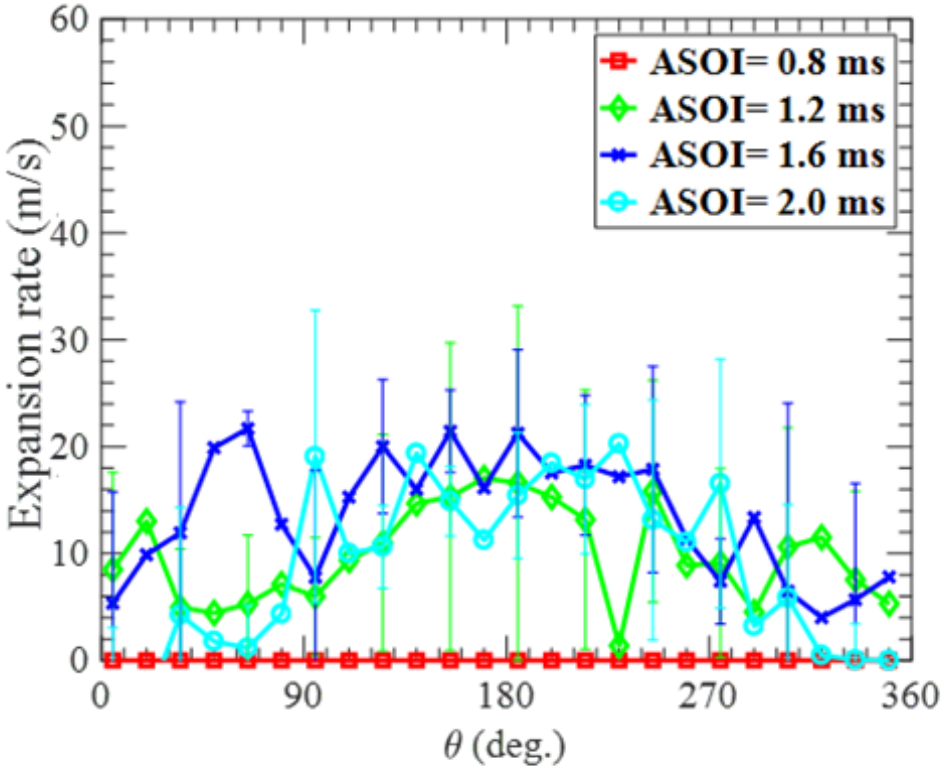

Figure 6.15. Profile of local expansion rate at T_{amb} = 900K and four different time stamps.

6.3.2 Distance distributions of different levels of natural luminosity

In this section, the distance distribution of flame luminosity is evaluated. In the previous section, a fuel-rich zone is assumed to be formed at the leading edge of the axial direction. If this assumption is true, a relatively bright sooting flame should be visualized at the leading edge of the axial direction. Note that there is no intensity threshold for this histogram study. Therefore, very few flame luminosities are observed outside the occupied flame area. The distance distribution at three different timestamps (1.2, 1.6, and 2 ms ASOI) which correspond to the timing of the evaluated FFD and FER are chosen to investigate the temporal distance distribution and its correlation with the FFD and FER.

An additional timestamp (3 ms ASOI) is chosen because it is the timing of the early stage after the end of injection.

The distance distribution of flame luminosity at T_{amb} of 1000 K is shown in Figure 6.16. The distance distribution of flame luminosity at 1.2, 1.6, 2, and 3 ms ASOI is shown in Figure 6.16(a), (b), (c), and (d), respectively. At 1.2 ms ASOI, three intensity groups (0-50, 50-100, 100-150) occupy the flame area and there is no flame luminosity higher than 150 observed at this moment. Most of the flame luminosity sits within the range of 15 mm to 20 mm. At 1.2 ms ASOI, the axial FFD is around 28 mm and the radial FFD is around 20 mm which can be obtained from Figure 6.12. The flame pixels are treated to be located near the leading edge of the axial direction when the distance between the flame pixel and impinging point is larger than radial FFD at a given time. At 1.6 ms ASOI, there are some flame luminosities in the intensity range 150-200 observed between 20 mm and 30 mm. At 2 ms ASOI, the histogram of flame luminosities in the intensity range 150-200 increases. The number of flame luminosities in the intensity range 150-200 is even, radially distributed on the plate between 10 mm and 50 mm. At this moment, the axial and radial FFDs are ~ 43 mm and ~ 25 mm, respectively. At 3 ms ASOI, the combustion phase reaches the late burning, and all fuel is injected into the vessel. There is a deep valley for three intensity groups (0-50, 50-100, 100-150) observed between 40 mm and 50 mm. The other two intensity groups (150-200 and 200-250) claim this region, indicating there is a soot-rich zone formed at the leading edge of the axial direction.

The distance distribution of flame luminosity at T_{amb} of 900 K is shown in Figure 6.17. Before 1.6 ms ASOI, the flame occupied region (calculated from the integration of the flame occupied area) is smaller at T_{amb} of 900 K. The axial direction has a much smaller flame occupied region, showing a sharp decrease in the total counts of flame pixels beyond the distance of 20 mm. Even though the flame is still mainly occupied by that three intensity groups (0-50, 50-100, 100-150), the percentage of each of the three groups is not evenly distributed anymore. At the leading edge of the axial direction, the flame is mainly occupied by the group with the range of intensity 50-100 before 3 ms ASOI. At 3 ms ASOI,

the distribution and flame occupied area are similar between T_{amb} of 1000 K and 900 K but the fuel-rich zone at T_{amb} of 900 K is not as bright as the case of T_{amb} of 1000 K.

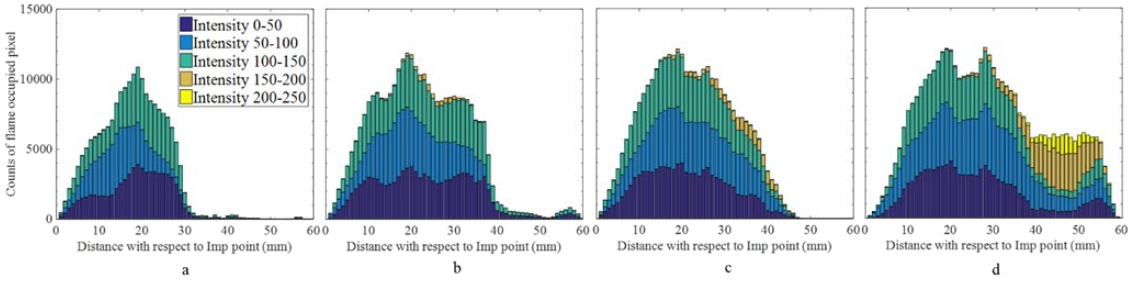

Figure 6.16. Distance distribution of flame luminosity at T_{amb} = 1000 K (a) 1.2 ms ASOI (b) 1.6 ms ASOI (c) 2 ms ASOI and (d) 3 ms ASOI.

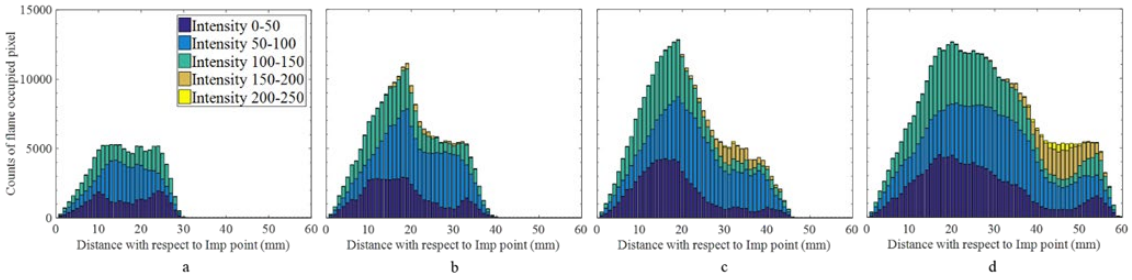

Figure 6.17. Distance distribution of flame luminosity at T_{amb} = 900 K (a) 1.2 ms ASOI (b) 1.6 ms ASOI (c) 2 ms ASOI and (d) 3 ms ASOI.

6.4 Comparison of macroscopic boundary structure between non-vaporizing and reacting spray

6.4.1 Comparison of front boundary and propagation rate

In the previous sections, the local FFD and FER under reacting conditions were evaluated. In the previous study, a conceptual model of non-vaporizing impinged spray was described [31]. In that model, a vortex is formed at the leading edge of the axial direction and there is a stagnation region on the top of the leading edge. The local expansion rate and expansion

distance under non-vaporizing conditions are evaluated and compared with the local FFD and FER to validate that conceptual model for the reaction cases.

The local liquid spray expansion distance at T_{amb} of 423 K is shown in Figure 6.18. Generally, the profile of local expansion distance shows an asymmetric shape along with the axial direction. And it increases along with the ASOI increases. Compared to the local D with the local FFD, the magnitude of distance between 100° and 250° is similar between the non-vaporizing and impinged combustion conditions, indicating the overall expansion/propagation patterns aren't changed due to the different ambient temperature and reactions. However, the fluctuation of the expansion distance is smaller than the reacting conditions. Such a phenomenon is due to the fact that the liquid fuel expansion is not easily perturbed by the ambient air compared with the gaseous phase of vapor fuel, showing a smaller shot-to-shot fluctuation on the expansion boundary under non-vaporizing conditions. Note that there are huge fluctuations of expansion distance near the backside of the impinging point. This is because the reflection on the edge of the bottom fixture affects the local intensity.

The expansion rate at T_{amb} of 423 K is shown in Figure 6.19. Similar to the FER, the axial direction always has the maximum magnitude of the velocity under non-vaporizing conditions. The axial direction also has the maximum deceleration rate. From 0.8 to 1.2 ms ASOI, the axial velocity is reduced from around 55 m/s to 25 m/s while in the radial direction, the velocity is only reduced from around 35 m/s to 15 m/s. After 1.6 ms ASOI, the sharp spike at axial direction is no longer observed. The velocity is similar between 1.6 and 2 ms ASOI and there is no huge difference in temporal velocity distribution from 100° to 250°. At 0.8 ms ASOI, the velocity is higher at non-vaporizing conditions but shows a similar spatial magnitude distribution after 1.2 ms ASOI.

After the comparison between the local expansion distance and flame front distance, the similar magnitude of these two distances shows that the behavior of the flame propagation under reacting conditions follows the same behavior of the spray expansion under non-vaporizing conditions.

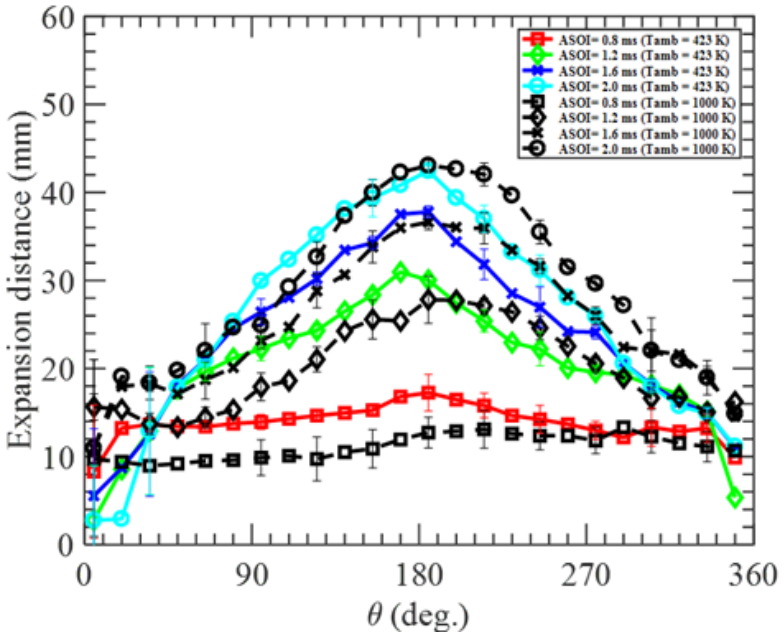

Figure 6.18. Comparison of local expansion distance at T_{amb} = 423K and flame front distance at T_{amb} = 1000 K.

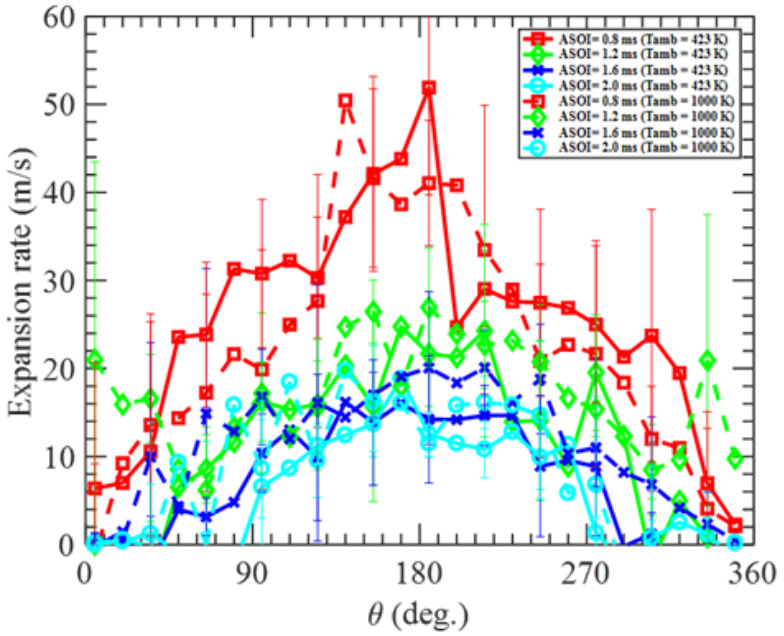

Figure 6.19. Comparison of local expansion rate at T_{amb} = 423K and T_{amb} = 1000 K.

6.5 Macroscopic flame boundary structure

6.5.1 IRT plots of reacting diesel spray

As a result, the effect of ambient temperature on IRT is shown in Figure 6.20(a). From the start of injection to the disappearance of flame, three ASOI times (i.e., 2 ms, 4 ms, and 6 ms) are marked with concentric red circles. The fuel spray is injected at 0° with respect to the impinging point. The timing of the first appearance of observed soot is marked by the green symbols over the entire sector. The time-resolved integration of flame luminosity is shown in Figure 6.20(b) to explain the evolution of overall soot production on the plate. The time-resolved integration of flame luminosity is obtained by adding up the normalized magnitude of 72 sectors at a given time. The red, green, and blue solid lines represent the time-resolved level of soot production at ambient temperatures of 1000 K, 900 K, and 800 K, respectively.

In Figure 6.20(a), the initial soot is observed at around 0.4, 0.8, and 1.8 ms ASOI at an ambient temperature of 1000 K, 900 K, 800 K, respectively. When the ambient temperature is 800 K, there is no soot observed in the regions between 0° to 30° and 330° to 360°, the backside of the impinging point. At an ambient temperature of 900 K, the soot is observed circumferentially with respect to the impinging point. A similar phenomenon is also observed at an ambient temperature of 1000 K with some irregularity. The green markers form a smooth circle at the ambient temperature of 1000 K, showing a consistent timing of the appearance of the first observed soot. While the magnitude of local IRT reduces as the ambient temperature is decreased, the most intensified regions of soot production at individual ambient temperatures are all located in between 150° and 210° after 2 ms ASOI. In Figure 6.20(b), the magnitude of temporal overall soot production is higher as the ambient temperature is increased. The slope of soot production is comparable at an ambient temperature of 1000 K and 900 K before the end of injection (at around 3 ms ASOI), but shows a slower rate of soot production at the ambient temperature of 800 K. After the end of injection, the magnitude of soot production begins to drop at all three ambient

temperatures. After around 3.5 ms ASOI, the soot production shows a sudden decrease at an ambient temperature of 1000 K and 900 K on account of the effect of flame quenching in the radial direction. The fuel spray reaches the vertical distance of 40 mm at 0.5 ms ASOI under the same injection pressure, ambient density, and distance between the injector and impinging plate. Therefore, in this study, the timing of fuel impingement is assumed to be 0.5 ms ASOI.

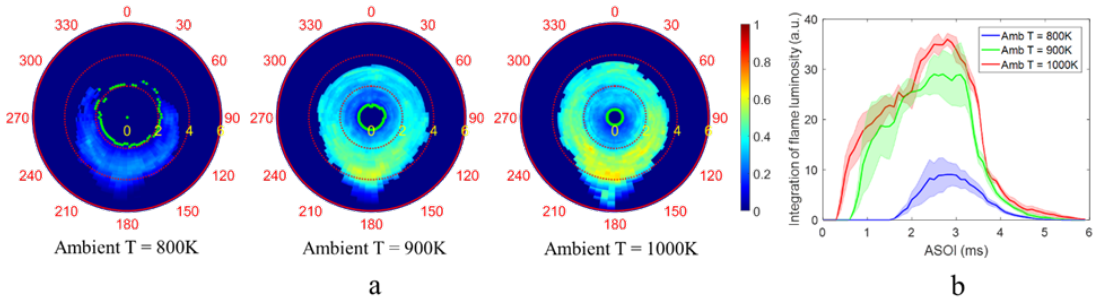

Figure 6.20. Effect of ambient temperature on the integration of flame luminosity (a) IRT results (b) time-resolved integration of flame luminosity.

The IRT results of different oxygen levels are shown in Figure 6.21(a). As can be seen in Figure 6.21(a), the occupied soot region of low oxygen percentage cases is comparable with high oxygen percentage cases while less local soot is formed at a given time. The soot is also observed between 0° to 30° and 330° and 360° at low oxygen percentage, indicating there is flame impingement and soot formation takes place above the plate at low oxygen percentage.

The time-resolved integration of flame luminosity at different ambient oxygen percentages is shown in Figure 6.21(b). The initial soot is observed at a similar time for these two oxygen percentages, showing approximately the same rate of temporal soot production before 0.8 ms ASOI. The temporal soot production at low oxygen percentage is lower than the one at high oxygen percentage in between 0.8 and 3.5 ms ASOI. There are two falling stages of soot production with different slopes. From around 3.5 to 4 ms ASOI, the temporal soot production shows a sharp reduction because of the effect of flame quenching in the radial direction. The second falling stage is mainly caused by the effect of flame

quenching in the axial direction. It is noted that the temporal soot production at low oxygen percentage exceeds the one at high oxygen percentage after around 3.5 ms ASOI when the remaining fuel is consumed after the end of injection.

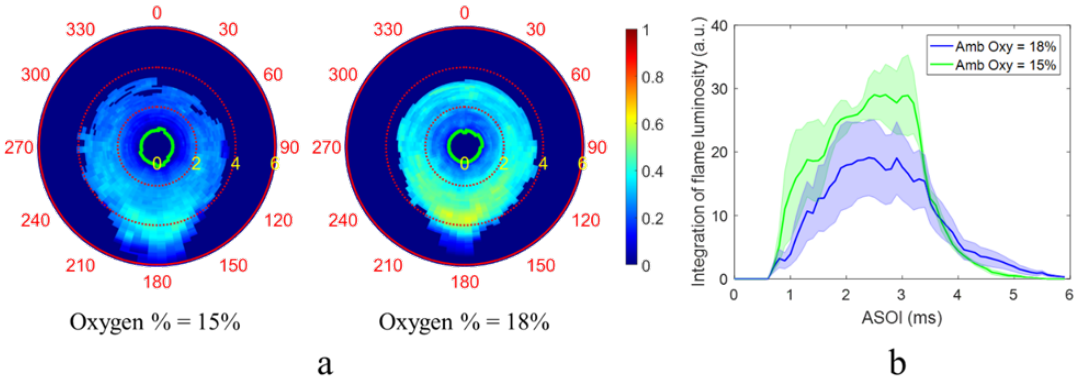

Figure 6.21. Effect of oxygen level on the integration of flame luminosity (a) IRT results (b) time-resolved integration of flame luminosity.

Comparisons of IRT plots between experiments (left) and RANS simulation (right) are shown in Figure 6.22. Three ambient temperatures, 800 K, 900 K, and 1000 K are evaluated and shown from top to bottom. In general, the simulation results follow similar trends with experiments, showing that the relative intensity increases as the ambient temperature increases. The brightest region is observed in between 150° and 210° in both experiments and simulations while there is one peak observed at 180° in the experiments and two peaks observed at 210° and 150° in the simulations. However, the IRT plots from simulation show a wing shape, leaving an open area between 330° to 360° and 0° to 30°. The open area tends to close as the ambient temperature increases. The relative brightness of the 800 K flame is similar between the simulation and the experiment while the other two flames show a more intensive region after 2 ms ASOI. From the side view of experiments, the ignition starts before the impingement at both 900 K and 1000 K flames while far downstream after the impingement at 800 K flame. This phenomenon will lead to radial soot formation on the plate at both 900K and 1000 K flame, experimentally. While in the simulations, the structure of IRT plots of all three cases is similar to the experimental 800 K flame. Thus, if the ignition starts before the impingement, soot will be formed peripheral

with respect to the impinging point after the impingement, looking from the bottom view. However, if the ignition starts after the impingement, soot will be formed mostly downstream but not close to the impinging point as well as the upstream.

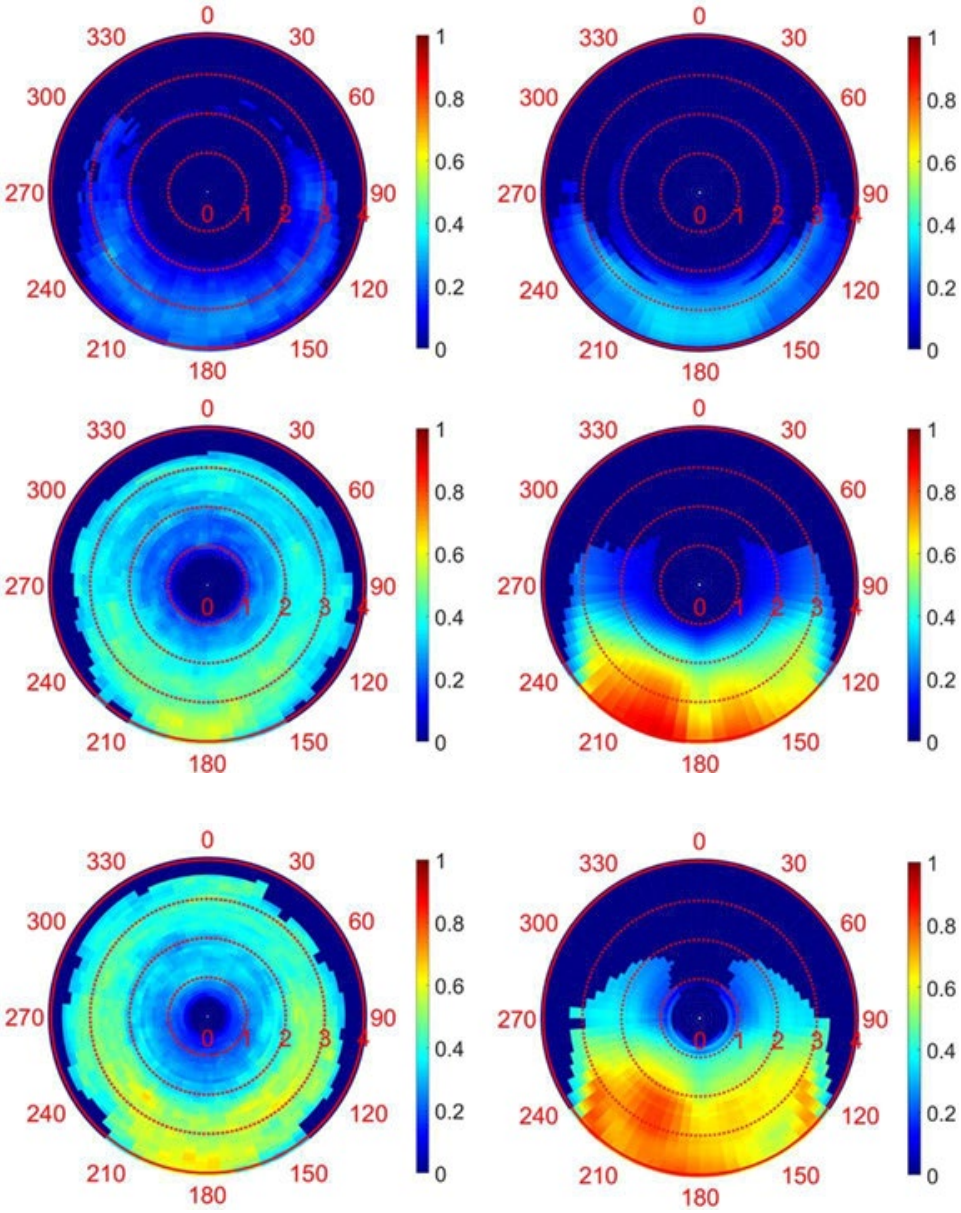

Figure 6.22. IRT plots under different ambient temperatures. Left column: experimental results, right column: RANS simulation results. Ambient temperature of 800 K, 900 K and 1000 K, from top to bottom.

IRT plots of experiments (left) and LES simulations (right) are shown in Figure 6.23. The 900 K and 1000 K flames are evaluated and the results are shown from top to bottom. In general, the numerical results follow similar trends with experiments. Unlike the uniformly distributed intensity in experiments, the intensity in simulations is more intensive and not uniformly distributed in the angular domain. This is because the scaling process is more like a multiplying process without any physical conversion from the outcomes of the interpreted CFD luminosity towards the grayscale of the physical camera. However, even the luminosity distribution is not exactly the same between experiments and simulations, the high-intensity area is observed between 150° and 210° in both experiments and simulations. A more intensive region is shown in the 900 and 1000 K ambient conditions after 2 ms ASOI.

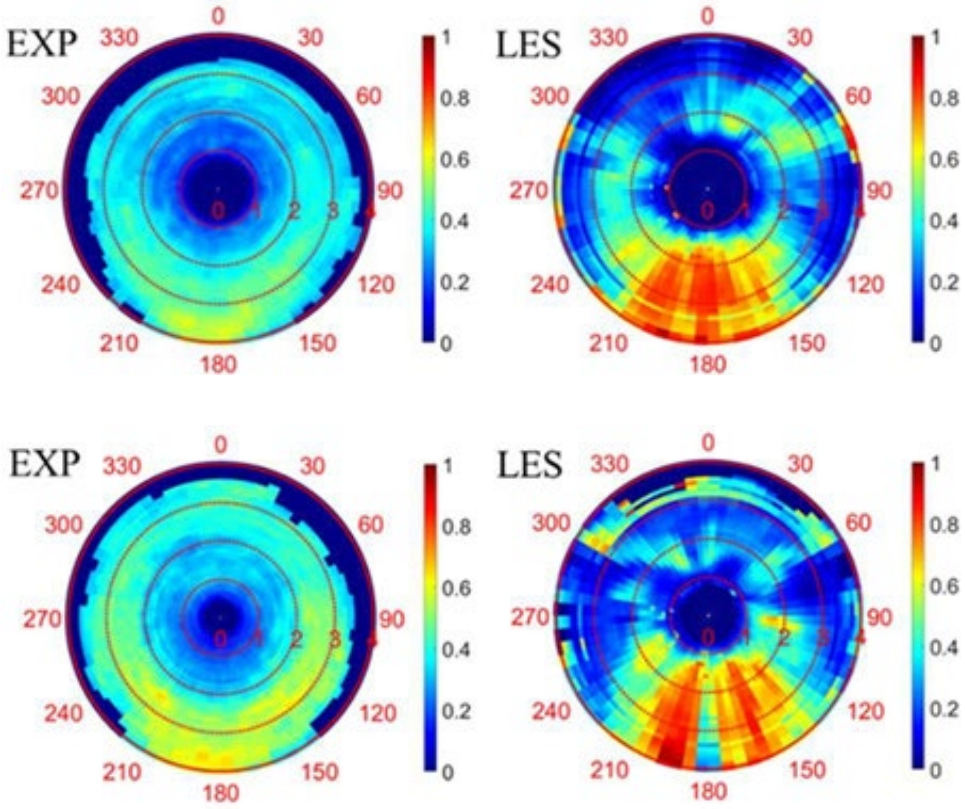

Figure 6.23. IRT plots under different ambient temperatures. Left column: experimental results, right column: LES simulation results. The 900 K and 1000 K flames are shown from top to bottom.

6.5.2 Distance distributions of different levels of intensity from CFD interpretation

The distance between the flame-occupied pixel and the impinging point is calculated and plotted in a stacked bar chart with a bin width of 1 mm in Figure 6.24. Four different time steps listed from left to right, 1.2 ms, 1.6 ms, 2.0 ms, and 3.0 ms ASOI were shown for 900 K flame. The RANS simulation results are shown on the top while the experimental results are shown on the bottom. It is found that the relative highest flame luminosity is located close but behind the leading edge of the flame boundary. With the flame expansion on the impinging plate, the maximum expansion distance from the simulations is increasing which is marked with the solid line.

The summation of all bars should equal the area of flame occupied region. And the discrepancy between the simulation and experiments mainly happens within 0 to 10 mm which is close to the impinging point. This is because the high-speed images captured the luminosity from the bottom view. The luminosity in this region may be caused by the luminosity in the spray cone above the impinging plate. The highest flame expansion distance shows good agreement between the experiments and simulations, as marked by a red line in Figure 6.24. Also, the distributions of pixel distance relative to the impinging point share similar trends between the experimental and simulation result, although, in the simulation result, the region within 30 mm is occupied by relatively low intensity (0-50).

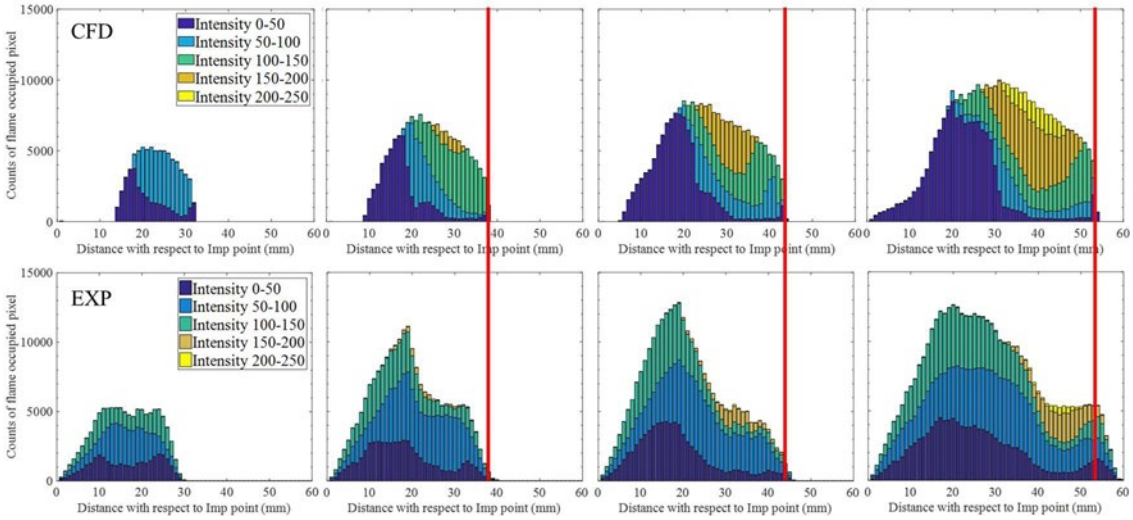

Figure 6.24. Distance distribution of flame luminosity at different ASOI, 1.2 ms, 1.6 ms, 2.0 ms, 3.0 ms, from left to right, 900 K flame, top row: RANS simulation results; bottom row: experimental results.

The distance between the flame-occupied pixel and impinging point is calculated and plotted in a stacked bar chart with a bin width of 1 mm in Figure 6.25 and Figure 6.26. The experimental results are shown on the left and the LES numerical results are shown on the right for both 900 and 1000 K ambient conditions at four different time steps (1.2, 1.6, 2, and 3 ms ASOI) from top to bottom.

The summation of all bars should equal the area of flame occupied region. The discrepancy of the shape of the distribution between the simulations and experiments mainly happens within 0 to ~ 10 mm which is close to the impinging point. This phenomenon could be observed in Figure 6.23. Except for the region between 0 to ~ 10 mm, the shape of the distribution of pixel distance shares similar trends between the experimental and numerical results.

The distance distribution of flame of 900 K ambient condition is shown in Figure 6.25. In numerical results, most of the intensity is lower than 50 at 1.2 ms ASOI. At 1.6 ms ASOI, the quantity of intensity lower than 50 is nearly maintained the same but intensities higher than 50 are started to be observed. At 2 ms ASOI, very high intensities (> 200) are carried

by the spray from ~ 30 to ~ 50 mm. The maximum distance of the experiments is located at ~ 30, ~ 40, ~ 45, and ~ 58 mm at 1.2, 1.6, 2, and 3 ms ASOI, respectively. The high intensities are mainly located in between ~ 40 and ~ 50 mm at 3 ms ASOI in experiments. From the simulations, the maximum distance is located at ~ 35, ~ 45, ~ 50, and ~ 60 mm at 1.2, 1.6, 2, and 3 ms ASOI, respectively. The high intensity from the simulations is mainly located between ~ 35 and ~ 55 mm at 3 ms ASOI. By comparing the locations of high intensity (> 150) and maximum distance at each time step, it is then concluded that the relative high flame luminosity is located close but behind the leading edge of the flame boundary.

The distance distribution of flame of 1000 K ambient condition is shown in Figure 6.26. In both experiments and simulations, the quantity of 0-50, 50-100, and 100-150 are nearly the same along with the axial distance before 1.6 ms ASOI. At 2 ms ASOI, the high intensity (> 150) starts to be observed in the experiments. At 3 ms ASOI, high intensity is observed between ~ 40 and ~ 55 mm near the leading edge of the flame. In numerical results, the percentage of low intensity is (< 50) increased significantly in between the region between the ~ 10 and ~ 40 mm. Intensities higher than 150 start to vanish after 2 ms ASOI, making a low intensity (< 50) dominate the intensity distribution. Similar to the experimental results, high intensity (> 150) is also observed near the leading edge of the flame in the simulations.

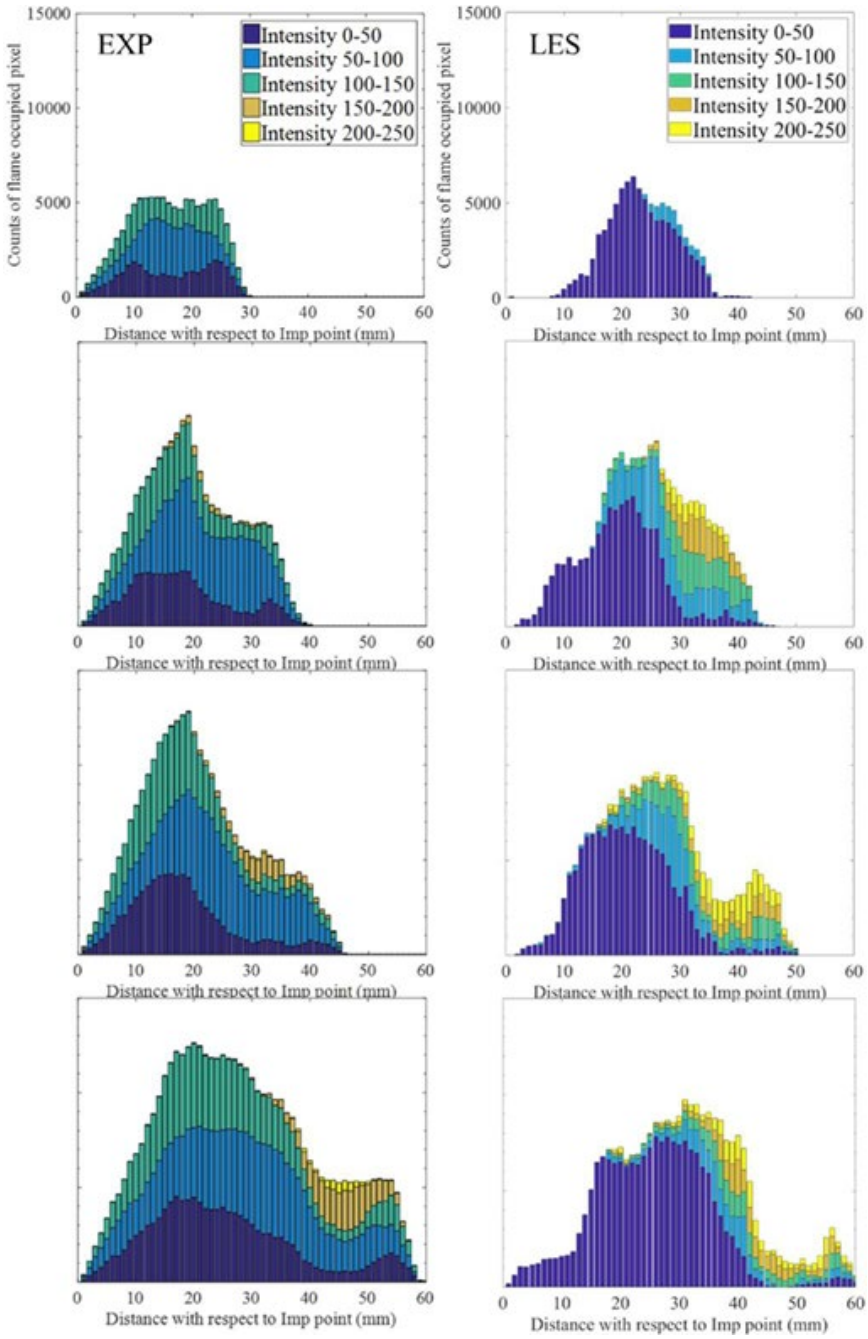

Figure 6.25. Distance distribution of flame luminosity at different ASOIs, 1.2, 1.6, 2, and 3 ms, from top to bottom, the 900 K flame, left: experimental results; right: LES simulation results.

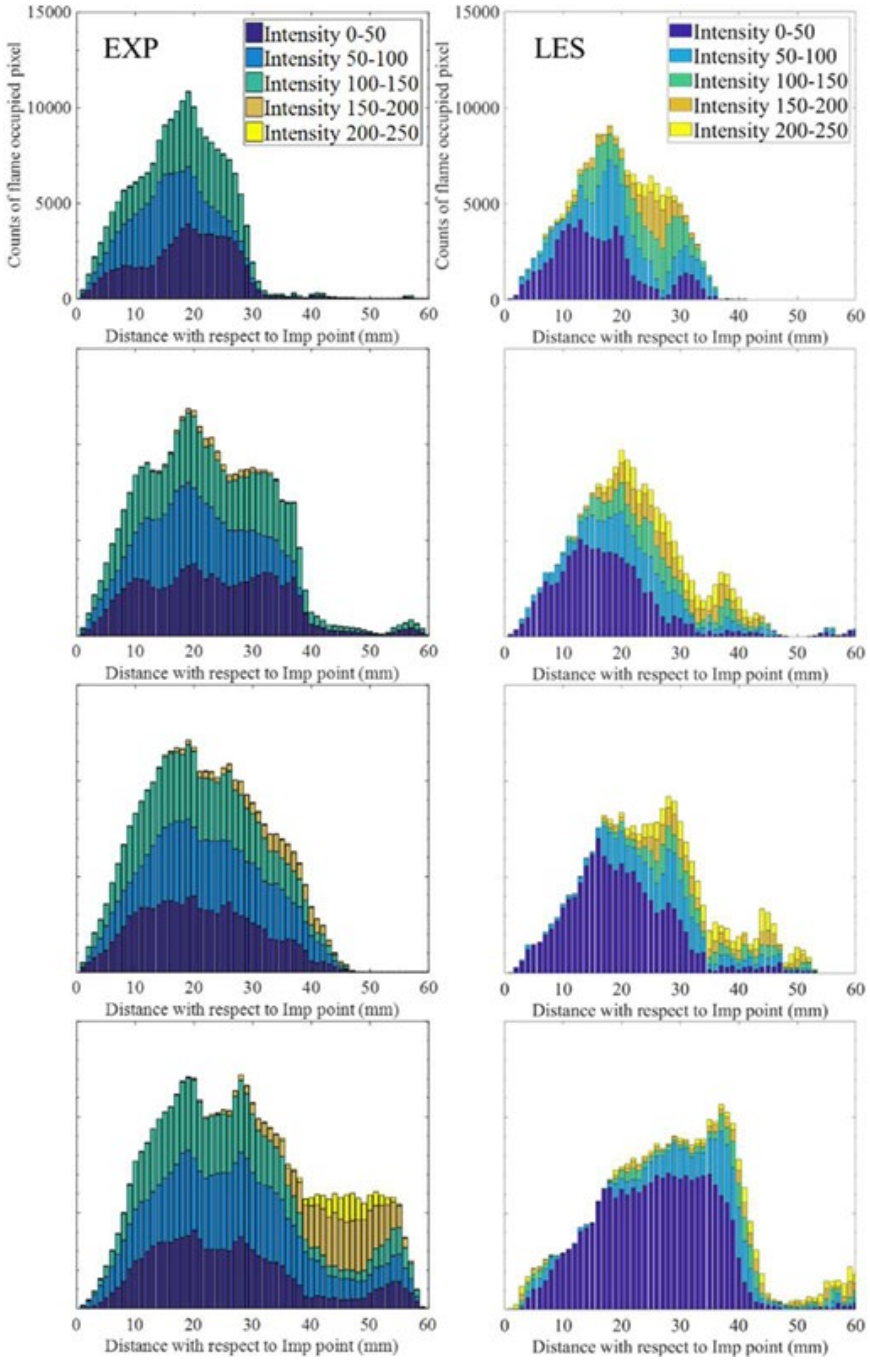

Figure 6.26. Distance distributions of flame luminosity at different ASOIs, 1.2, 1.6, 2.0, 3.0 ms, from top to bottom, the 1000 K flame, left: experimental results; right: LES simulation results.

7 Microscopic spray and flame boundary structure and behavior of an impinging diesel spray[4]

7.1 Experimental results

7.1.1 Curvature distribution of a non-vaporizing impinging spray

In order to quantify local characteristics of the expanding impinged spray boundary, curvature distribution (or histogram) of the boundaries is present in Figure 7.1. Positive curvature indicates a convex shape of spray expansion while negative curvature refers to a concave shape of spray expansion. Zero curvature indicates flatness. The summation of the counts of curvatures equals total pixels along the boundary at a given time. Since total pixels on the boundary increase, because the perimeter of the boundary increases along with time, the summation of counts of curvature is increasing. The absolute magnitude of

---

[4] Reprinted with permission from SAE papers 2019-01-0267 ©2019 SAE International. Reprinted with permission from International Journal of Engine Research (IJER) and the American Society of Mechanical Engineers (ASME). The materials in this chapter were published in the following papers:

- Zhao, Z., Zhu, X., Naber, J., and Lee, S., "Impinged Diesel Spray Combustion Evaluation for Indirect Air-Fuel Mixing Processes and Its Comparison with Non-Vaporing Impinging Spray Under Diesel Engine Conditions," SAE Technical Paper 2019-01-0267, 2019, https://doi.org/10.4271/2019-01-0267.

- Zhao, Z, Zhao, L, & Lee, S. "Evaluation of Soot Production Near a Cold Surface for an Impinged Diesel Spray Combustion." Proceedings of the ASME 2020 Internal Combustion Engine Division Fall Technical Conference. ASME 2020 Internal Combustion Engine Division Fall Technical Conference. Virtual, Online. November 4–6, 2020. V001T05A002. ASME. https://doi.org/10.1115/ICEF2020-2938

- Zhao Z, Zhu X, Naber J, Lee S-Y. Assessment of impinged flame structure in high-pressure direct diesel injection. International Journal of Engine Research. 2020;21(2):391-405. doi:10.1177/1468087419859788

curvature mostly falls in between 0 and 0.5 mm^{-1} (relatively flat region) nevertheless very few highly wrinkled shapes are observed (absolute magnitude of curvature is greater than 0.5 mm^{-1} but counts are lower than 20). The boundary of spray expansion becomes more wrinkled just after the spray impingement when comparing the curvature distribution between 0 and 0.5 ms ASI.

Standard deviation is used to describe the dispersion degree of distribution. In the current study, the curvature distribution is symmetric along curvature (at 0 mm^{-1}) which means the mean value is near 0 mm^{-1}. A larger standard deviation of curvature distribution represents boundary more wrinkled compared to the boundary which has a smaller standard deviation of curvature distribution. At 1 ms ASI, the standard deviation is 0.34 mm^{-1}, and the mean value is 0.026 mm^{-1}. At 1.5 ms ASI, the standard deviation is 0.3 $mm^{-1,}$ and the mean value is 0.02 mm^{-1} under non-vaporizing conditions. Such a phenomenon can be observed by comparing the curvature distribution between Figure 7.1(b-d). While the number of boundary pixels grows significantly, most of the local curvature starts to remain in the same region that curvature equals zero. A high peak of ~ zero curvature is observed as growing, indicating the overall boundary of spray expansion under non-vaporizing conditions becomes smoother along with time. After the spray impingement, the outmost boundary initially becomes wrinkled due to the splash and rebound phenomenon but smooth at a later expansion. During the expansion, the momentum of droplets is dissipating while most of the impinged fuel is still in the liquid phase at T_{amb} = 423 K. The air perturbation may not be strong enough to make the boundary highly wrinkled. Therefore, very few relatively large magnitudes of curvature are observed (absolute magnitude of curvature > 0.5 mm^{-1}).

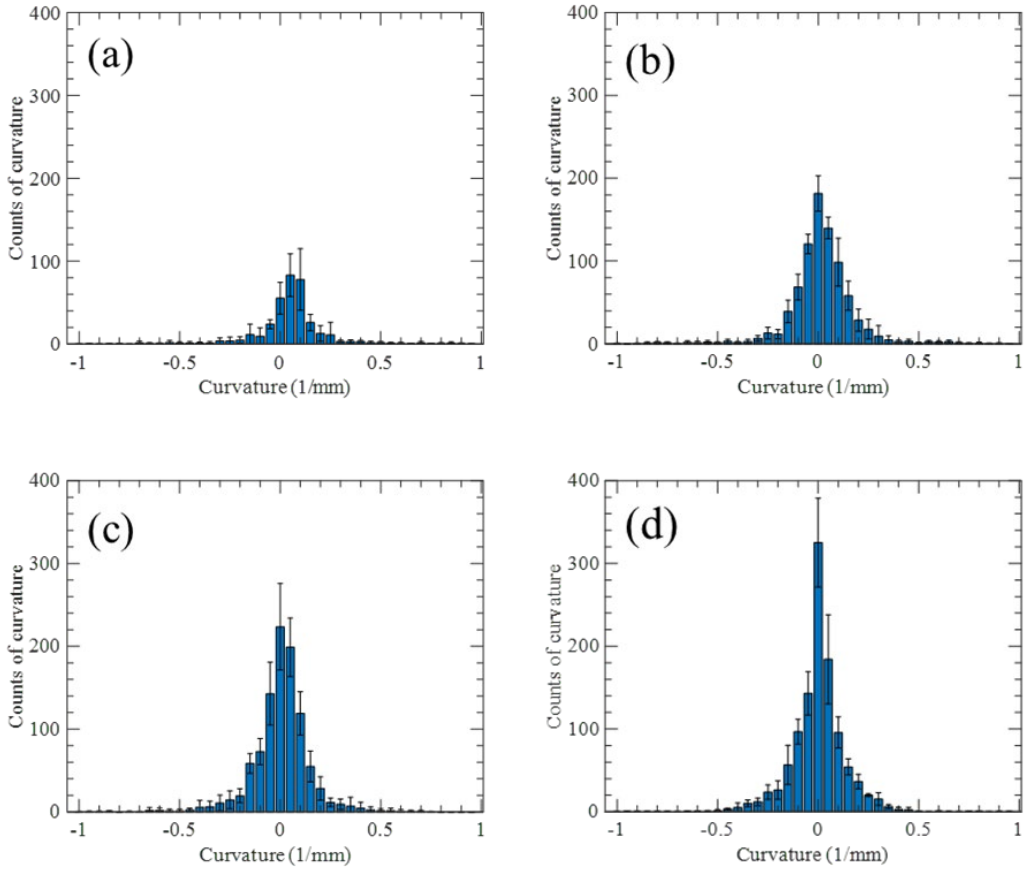

Figure 7.1. Local curvature distribution development (a) ASI = 0 ms (b) ASI = 0.5 ms (c) ASI = 1 ms (d) ASI = 1.5 ms. Conditions: T_{amb} = 423 K, P_{inj} = 1500 bar and ρ_{amb}= 22.8 kg/m^3.

7.1.2 State-relationship between local curvature and intensity of Mie scattering

It is postulated that wrinkled boundary may result from the strength of air entrainment and spray momentum. Stronger air entrainment suppresses the spray expansion, leading to a concave shape of the boundary. The dissipation rate of the impinged spray momentum would be slower in a region with weaker air suppression, leading to form a convex shape of the boundary. The concave region may accumulate more droplets than the convex region because the movement of droplets in the concave region is limited. The scatter plot between integrated intensity at a given boundary pixel and its curvature is shown in Figure 7.2.

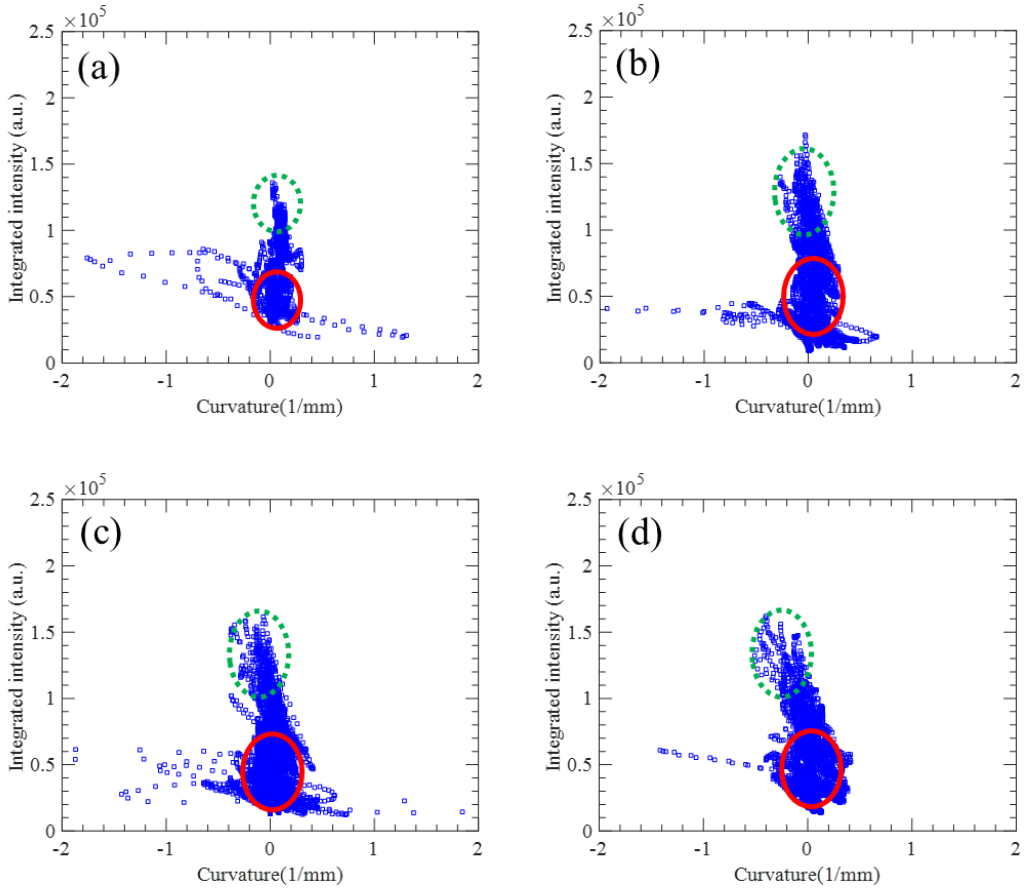

Figure 7.2. Curvature correlation with neighbor integrated Mie scattering intensity (a) ASI = 0 ms (b) ASI = 0.5 ms (c) ASI = 1 ms (d) ASI = 1.5 ms. Conditions: T_{amb} = 423 K, P_{inj} = 1500 bar and ρ_{amb} = 22.8 kg/m^3. The scatters obtained from θ = 0° and θ = 180 ° are shown in the red circle and green circle, respectively.

Two regions are marked with red circles and green dashed circles. The red region is mainly occupied by the boundary pixels near θ = 0° with low magnitude integrated intensity while the green region is mainly occupied by the boundary pixels near θ = 180° with high magnitude of integrated intensity. In Figure 7.2, most scatters reside symmetrically, vertically along the curvature (at 0 mm^{-1}) where the local outmost boundary is relatively flat. Under non-vaporizing conditions, the shape of spray expansion is mainly controlled by spray momentum because the momentum flux of the liquid phase is much higher than the vapor phase and air perturbation is not strong enough to significantly change the shape of the spray expansion. The effect of air entrainment on liquid spray expansion can be

negligible. However, if the ambient temperature is raised enough to fully vaporize the fuel before impingement, it is expected the shape of spray expansion is mainly controlled by both spray momentum and air entrainment.

7.1.3 Curvature distribution of a reacting impinging spray

The curvature of the flame outmost boundary is calculated to investigate the effect of air entrainment on the shape of flame expansion. The snapshots of curvature distribution at the different ASI times are shown in Figure 7.3 for the 900 K flame. As expected, the flame outmost boundary demonstrates a more wrinkled structure than the liquid spray expansion boundary. The majority of curvature magnitude resides in between -1.0 to 1.0 mm^{-1}. At 0.5 ms ASI, the curvature profile shows an asymmetric shape along zero curvature. Unlike the curvature distribution of non-vaporizing conditions as seen in Figure 7.1, the range of absolute value of curvature under reacting conditions stretches from -2 to 2 mm^{-1}, creating very fine flame wrinkles. The standard deviation of the curvature distribution is 0.4 mm^{-1} at 1 ms ASI and it increases to 0.7 mm^{-1} at 1.5 ms ASI. This indicates that the outmost flame boundary becomes more wrinkled with time. As time progresses, the concave region is continuously suppressed and the convex region keeps expanding, making the boundary more stretched. Compared with the standard deviation at 1.5 ms ASI which is 0.3 mm^{-1} under non-vaporizing conditions, the flame boundary is obviously much more wrinkled after the impingement than that under the non-vaporizing conditions. At 1 ms ASI, the curvature distribution is comparable with the curvature distribution at 0.5 ms ASI except for the zero curvature. Note that this curvature distribution information provides only the degree of wrinkling not the fluctuation amplitude of wrinkles. As time progresses, the counts of curvature are nearly the same at a given curvature except for the zero curvature.

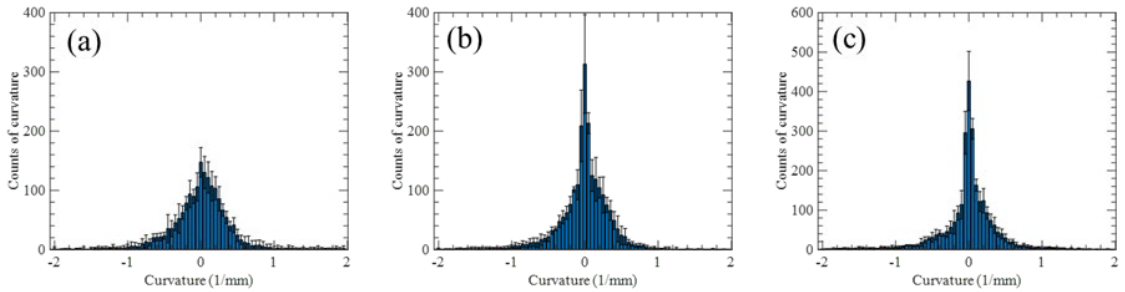

Figure 7.3. Curvature distribution of flame outmost boundary (a) ASI = 0.5 ms, (b) ASI = 1 ms, and (c) ASI = 1.5 ms. Conditions: T_{amb} = 900 K, P_{inj} = 1500 bar, and ρ_{amb} = 22.8 kg/m^3.

The curvature of flame outmost boundary at T_{amb} = 1000 K shown in Figure 7.4 is also evaluated to investigate the effect of ambient temperature on the local flame expansion structure. Compared with the curvature distribution at T_{amb} = 423 K, high curvatures (absolute value of curvature > 1 mm^{-1}) are also observed. Compared with the curvature distribution at T_{amb} = 900 K as shown in Figure 7.3, a temporally similar curvature distribution can be seen, and therefore, the effect of ambient temperature on the flame expansion boundary is insignificant, as long as the flame development is identical. The global structure of flame expansion is found to be similar to the structure of spray expansion under non-vaporizing conditions due to the identical spray momentum distribution after the impingement, while the local structure of flame outmost expansion boundary, i.e., the degree of wrinkling, is significantly modified by the strength of air entrainment.

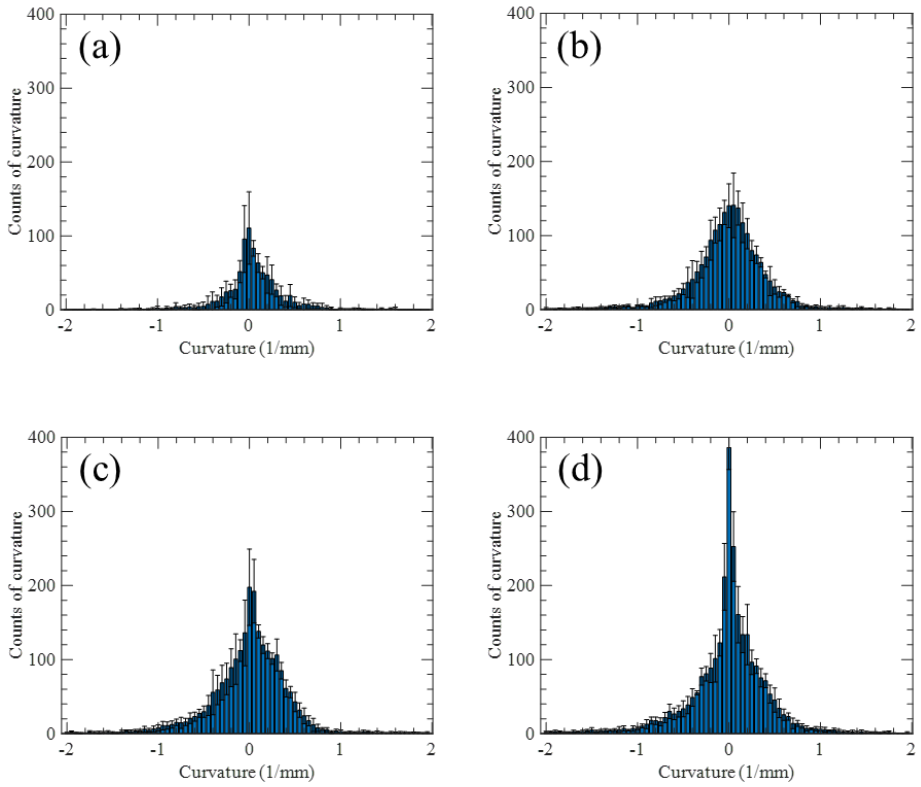

Figure 7.4. Curvature distribution of flame outmost boundary at (a) ASI = 0 ms, (b) ASI = 0.5 ms, (c) ASI = 1 ms, and (d) ASI = 1.5 ms. Conditions: T_{amb} = 1000 K, P_{inj} = 1500 bar and ρ_{amb} = 22.8 kg/m^3.

7.1.4 State-relationship between local curvature and intensity of natural luminosity

With the visual inspection of expanding impinged flame, there exists a coherent pattern on the flame boundary and the near-field flame luminosity (intensity). Here, the correlation is calculated on the curvature along the impinged flame boundary by integrating the luminosities in a square region with 2 mm-length which is determined by the sensitivity analysis in the vicinity of the boundary. Unlike non-vaporizing cases, the scatter plot in Figure 7.5 illustrates coherent distribution from the high integrated intensity (relative high soot production) at the negative curvature (concave) to the low integrated intensity (relative low soot production) at the positive curvature (convex). This correlation is obviously seen as an inverted “S”-shape, which is marked with a red solid line, with time, as seen in Figure

7.5. During the flame expansion on the plate, soot tends to be formed near the concave shape of the flame boundary where the flame expansion is greatly suppressed. With continuous fuel injection, more fuel vapor is possibly accumulated in concave regions and it may lack the opportunity to mix with ambient air. While in the convex region, i.e., positive curvature, the magnitude of integration of soot luminosity becomes smaller, showing much less soot formed near the flame boundary. In the convex region, the outmost flame appears to exceed the current boundary, yielding more opportunity for the vapor fuel to mix with the ambient air and thus further prohibit soot formation in that region. This inverted S-shape is a new finding of the state relationship at the solid-liquid-gas interface flame propagation.

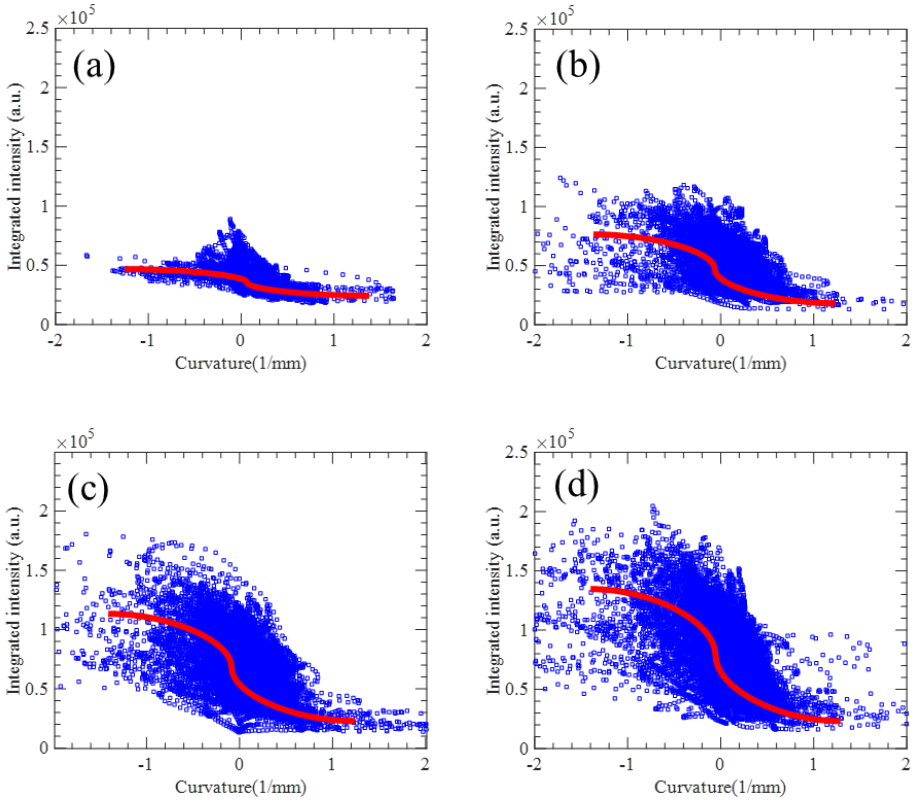

Figure 7.5. Curvature correlation with neighbor integrated soot luminosity (a) ASI = 0 ms, (b) ASI = 0.5 ms, (c) ASI = 1 ms, and (d) ASI = 1.5 ms. Conditions: T_{amb} = 1000 K, P_{inj} = 1500 bar and ρ_{amb} = 22.8 kg/m^3.

7.1.5 Mechanism of flame boundary formation after impingement

From the curvature distributions at different ASIs, the positive and negative curvatures are almost distributed evenly along the flame boundary. By analyzing the curvature profiles along the flame boundary, the quantity of the peaks could be found at the given ASI time. Due to the radial propagation of the flame on the impinging plate, a method that transfers curvature profile to the angular domain was used. Detailed information on this re-sampling-based method is provided in [124]. Figure 7.6 shows the power spectrum results from the 900 K flame. The power spectrum is colored by the normalized amplitude at a given ASI. The *x*-axis is the degrees per peak after the transformation (for example, 40 degrees per peak indicates it could be found a peak on the flame boundary rotating every 40 degrees). By dividing the degrees per peak, the quantity of convex and concave on the flame could be found. The power spectrum generated from the curvature profile represents the characteristics of the peak on the flame boundary along with ASI. From Figure 7.6, it is observed that there is an intensive band between 15 and 40 degrees per peak. An intensive band seating indicates that the peaks are distributed evenly along the flame boundary. The single band is nearly unchanged along with ASI. However, the boundary is not purely formed with certain degrees per peak. There are also some parts that show higher degrees per peak than 40 after 1.7 ms ASI which indicates there is a violent fluctuation on the flame boundary.

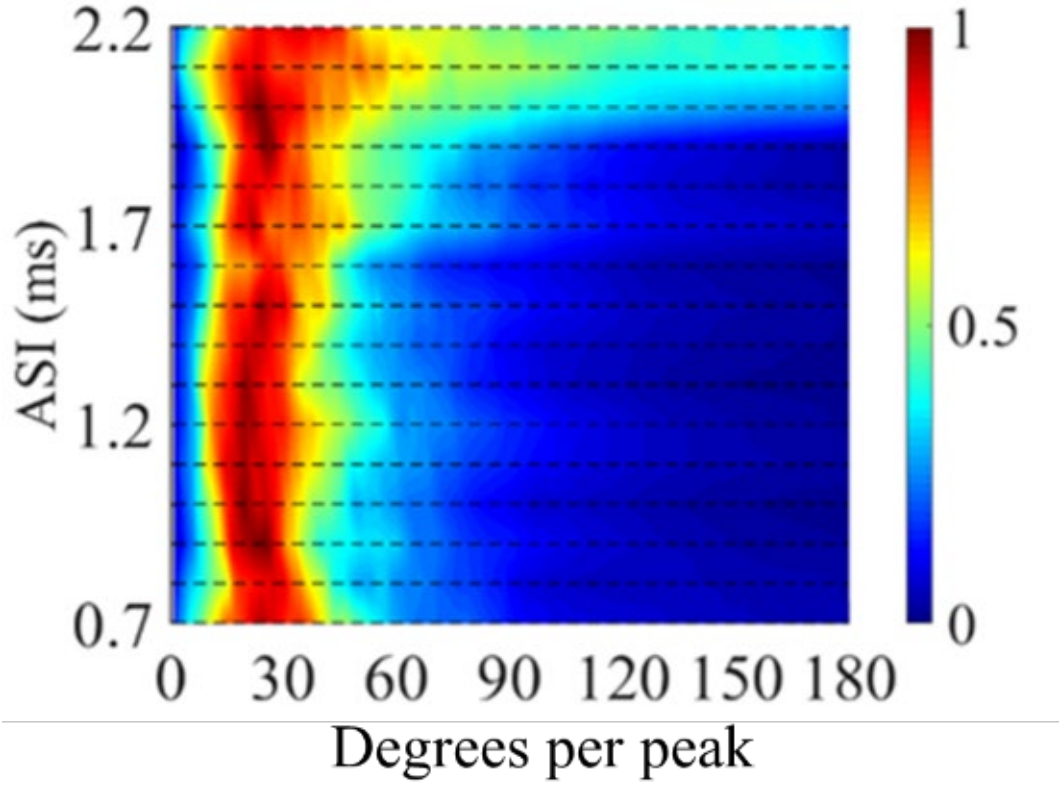

Figure 7.6. Normalized power spectrum of the curvature profile for the 900 K flame.

Figure 7.7 shows the power spectrums of the curvature profile of the 1000 K flame at each ASI. A single peak is observed near 30 degrees per peak in the power spectrum of both 900 and 1000 K flames. However, compared to the spectrum of the 900 K flame, the intensive band is narrower which indicates the flame boundary is more stable. Echoing the curvature distribution from Figure 7.3 and Figure 7.4, the microscopic flame structure is comparable and even the fluctuation behavior of the flame front is similar under ambient temperature 900 and 1000 K. Due to the fact that the combustion characteristics are different under 900 and 1000 K ambient conditions, the spray momentum could be the main factor that affects the macroscopic flame structure in terms of propagation rate, flame front distance, curvature magnitude of the flame front as well as the distribution of curvatures along the boundary.

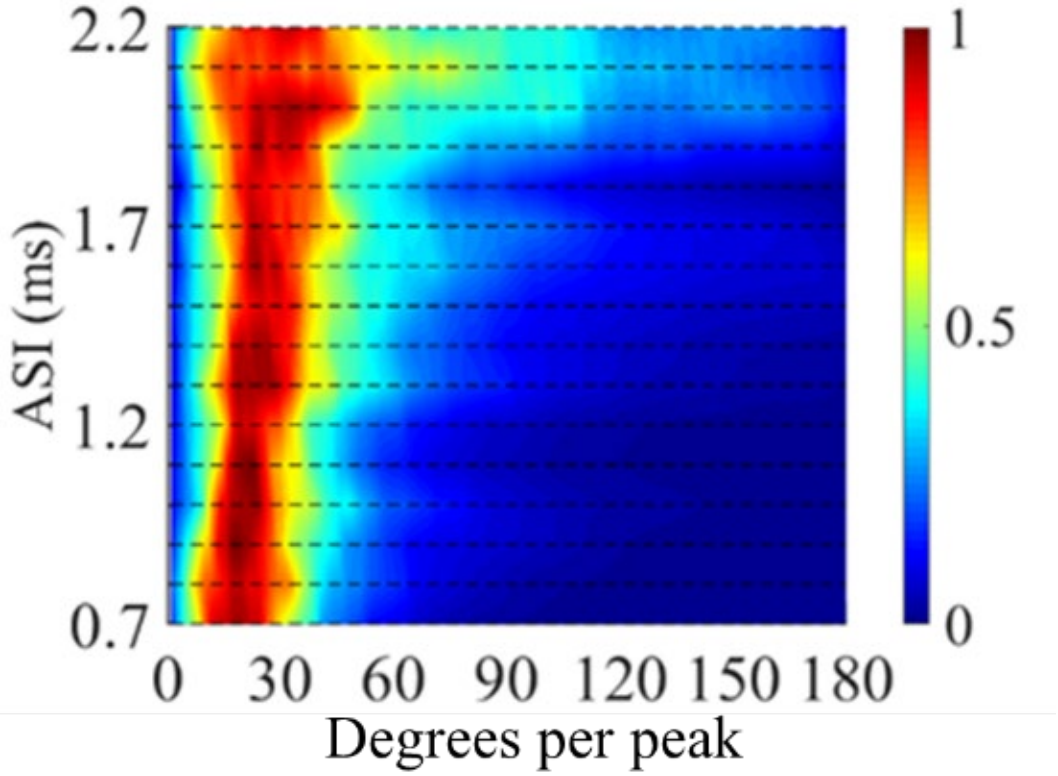

Figure 7.7. Normalized power spectrum of the curvature profile for the 1000 K flame.

7.2 Simulation results

7.2.1 Curvature distribution from simulations

The curvature of the flame boundary is one of the parameters that could be used to evaluate the turbulence intensity and quality of mixing along the flame boundary. The precision of the curvature calculation depends on the grid resolution of the images or the cell size of the simulations. Therefore, simulation column-format results were interpolated into a reconstructed 3D domain with a fixed size for all cells with a resolution of 0.1047 mm/cell to match the pixel resolution of experimental high-speed images. The curvature of flame boundary in simulations was performed on a horizontal plane ~ 1 mm (~ 10 cells height) above the impinging plate. However, the curvatures obtained from experiments were traced

by the projected flame looking from the bottom. The flame boundary in simulations was traced through the OH radicals' contour (instead of natural luminosity in experiments) on the chosen plane. Curvatures of the flame boundary were calculated according to ref [118]. The curvature distributions were characterized as histograms with a bin size of 0.05 mm^{-1} for both experiments and simulations.

Figure 7.8 shows the comparison of curvature distribution at 0.5 and 1.0 ms ASI of the 900 K flame. Boundary pixels having higher absolute curvatures than 2 mm^{-1} were binned into -2 mm^{-1} and 2 mm^{-1}, respectively. These high curvature pixels have relatively small quantities (~ 1% of all evaluated pixels) so they would not affect the global shape of the distributions. Generally, symmetric distribution with respect to zero curvature (flat flame boundary) at the center and rapidly decaying in both negative and positive directions are observed in both experiments and simulations. The mean value and standard deviation of the curvature profile for the 900 K flame at both 0.5 and 1.0 ms ASI are close to the experimental results (~ 7% deviation). It is noted that the sharp spikes of zero curvature of experiments at 1 ms ASI are due to the smooth boundary blocked by the view of the impinging plate which could be seen in Figure 5.19(middle).

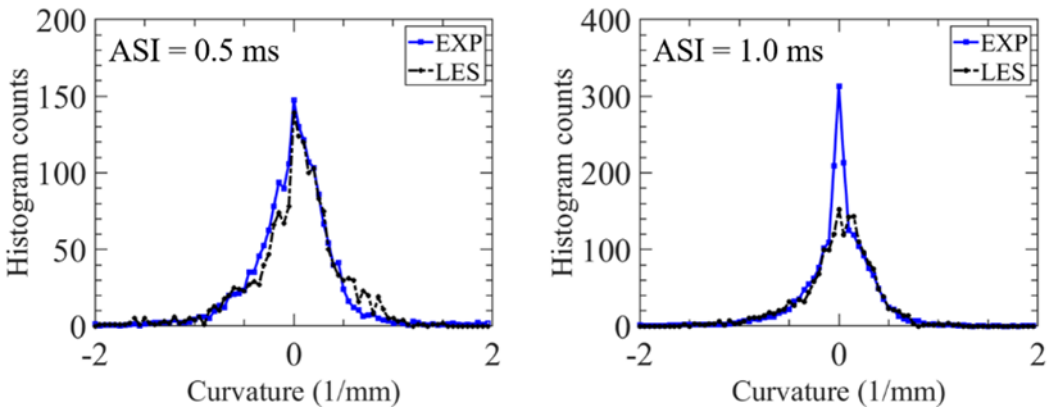

Figure 7.8. Curvature distributions of the 900 K flame.

Figure 7.9 shows a comparison of the curvature distributions between experiments and simulations of the 1000 K flame at 0.5 and 1.0 ms ASI. Simulation results agreed with experimental results. From 0.5 to 1.0 ms ASI, the mean curvature value changes from

0.02 mm^{-1} to 0.01 mm^{-1}, and the standard deviation increases from 0.38 mm^{-1} to 0.66 mm^{-1}. A similar trend of curvature distribution is observed in both 900 and 1000 K flames in simulations.

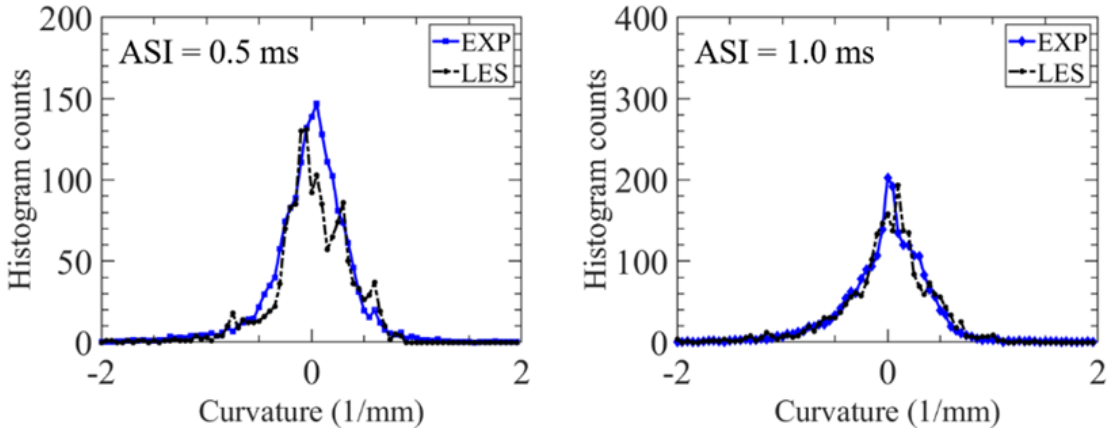

Figure 7.9. Curvature distribution of the 1000 K flame.

7.2.2 Vertical temperature and soot distributions at different heights above the impinging plate

As the flame is propagating on the plate, the maximum expansion distance is getting increased. A normalized distance is required to represent the locations of the corresponding intensive soot regions at different time steps. It is the ratio of the flame location to the distance of the leading edge. The normalized distance of 0 and 100% represents a location at the impinging point and the leading edge of the flame, respectively.

Figure 7.10 demonstrates the definition of the normalized distance and a cut view of the impinged flame of 900 K ambient condition. The impinging point is marked as a red dot and two scales, 50 and 100% are marked with black lines. The chosen plane is aligned with the spray axis with a thickness of 0.2 mm.

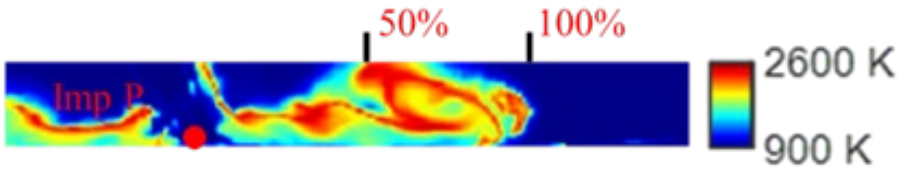

Figure 7.10. Definition of the normalized distance between the impinging point and leading edge.

After the ignition delay, residence time affects the soot formation of diesel spray combustion. As the ignition delays are unlike for various ambient temperature conditions, the ASOI is inappropriate for evaluating the soot formation. Hence a new time scale called AID (after the ignition delay) is used to maintain the residence time of soot. AID represents the difference between ASOI and ignition delay. 0.5, 1 and 1.5 ms AID are the three various timesteps used in ambient 900 and 1000 K conditions.

Figure 7.11 shows the temperature and soot mass fraction of the the 900 K flame in a given cross-section together at each time step. At the ambient 900 K condition, the profiles for temperature (black) and soot mass fraction (red) vs. the height from the impinging surface at different normalized distances (50 to 80%) are represented in Figure 7.11. The temperature is ranged from 900 to 2600 K and the soot mass fraction is ranged from 0 to $2*10^{-3}$.

The profiles show that temperature and soot mass fraction are changed in the layer near the impinging surface. The starting point which is located at the one-cell height (0.125 mm) above the impinging surface is marked as ‘close to plate’ (C to plate) in Figure 7.11. At 0.5 ms AID and a normalized distance of 0%, the temperature profile has one peak at ~ 8 mm height. The peak of the temperature indicates the upper flame boundary. As the height lowers, the temperature is decreased because fuel occupies the region near the impinging point. At the normalized distance of 50%, two peaks on the temperature profile are observed at different heights such as ~ 8 and ~ 3.7 mm. The higher peak indicates the flame boundary while the lower peak indicates the boundary between the high-temperature region and soot formation region in the flame. Below the lower peak soot mass fraction is

increased and temperature is decreased. The temperature and soot mass fraction profiles are similar at a normalized distance of 60 and 70% compared to 50% whereas at a normalized distance of 80% different trends are observed near the impinging surface. Both temperature and soot mass fraction are decreased below ~1.5 mm.

For normalized distances of 50, 60, and 70%, the results at 1 ms AID shows a similar trend as 0.5 ms AID for soot mass fraction less than 2 mm height, i.e., soot mass fraction is increased as the temperature is decreased near the impinging plate. Whereas at 80% soot mass fraction is ~0 below 2 mm height but observed temperature between 0.5 and 5 mm is ~2200 K then is decreased below 0.5 mm.

All normalized distances show a similar trend below 2 mm height at 1.5 ms AID, i.e., soot mass fraction is increased, and temperature is decreased. From the color map of soot mass fraction, a dense core of soot is observed at the top of the leading edge of the flame and a layer of soot is observed just above the plate.

Figure 7.12 shows the temperature and soot mass fraction of the 1000 K flame in each cross-section. The profiles for temperature (black) and soot mass fraction (red) vs. the height from the impinging surface at different normalized distances (50 to 80%) are represented in Figure 7.12. At 0.5 ms AID, the region near the impinging point is mainly occupied by the fuel. Thus, the temperature at a normalized distance of 0% near the same point is much lower than the flame temperature. From the soot mass fraction map, a dense core of soot is observed near the leading edge of the flame between the normalized distance of 60 and 80%. At all normalized distances, the soot mass fraction is increased, and temperature is decreased below 2 mm height.

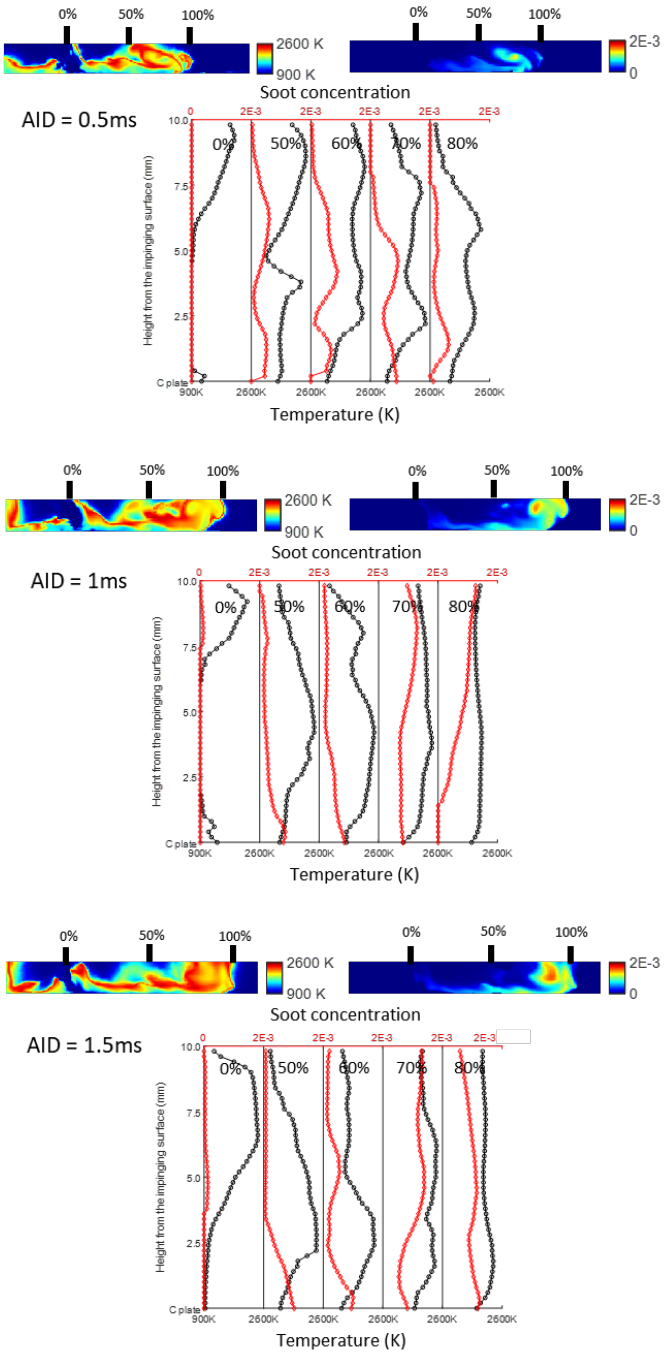

Figure 7.11. Temperature, soot mass fraction map, and profiles near the impinging plate. From top to bottom: AID = 0.5, 1.0 and 1.5 ms, the 900 K flame. *C plate = close to the impinging plate.

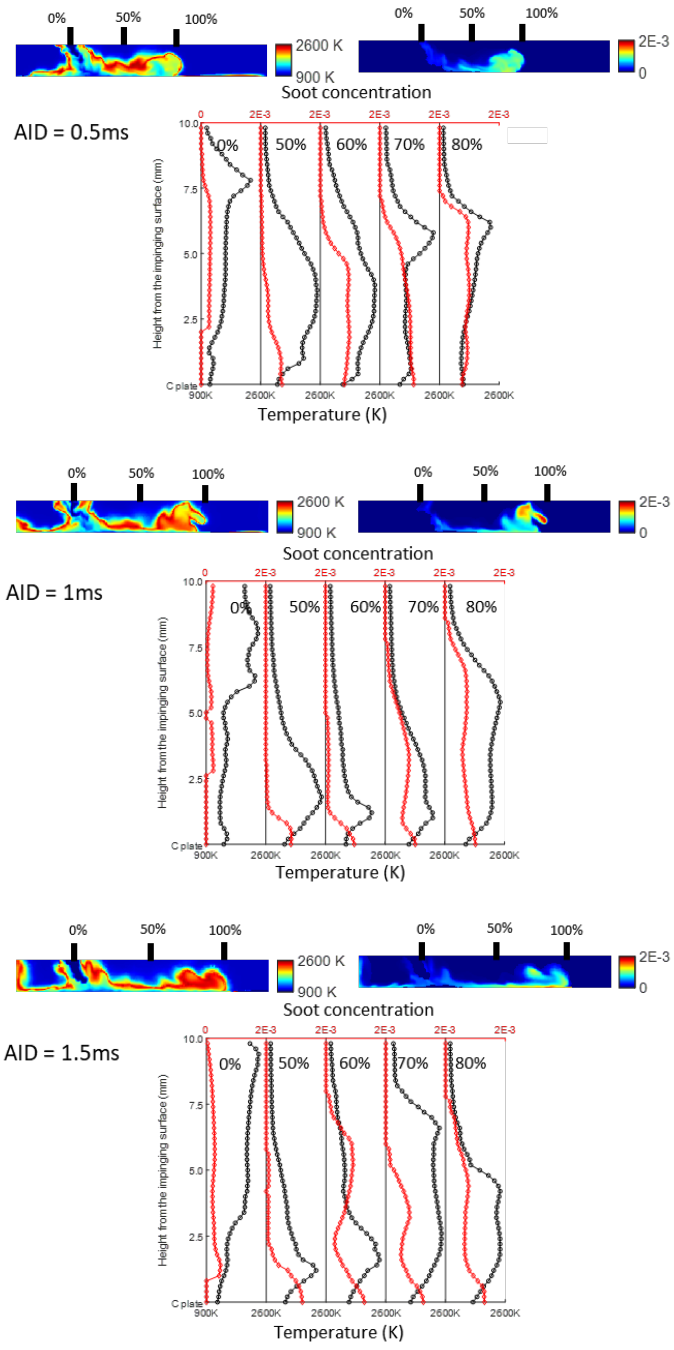

Figure 7.12. Temperature, soot mass fraction map, and profiles near the impinging plate. From top to bottom: AID = 0.5, 1.0 and 1.5ms, the 1000 K flame.

At 1 ms AID, below 1.5 mm height soot mass fraction near the impinging surface is increased as the temperature is decreased. From the soot mass fraction map, relatively

dense soot regions are observed between normalized distances 60 and 80%. One dense soot core is above the plate and a soot layer is also found near the impinging plate. At 1.5 ms AID, soot mass fraction is increased and temperature is decreased below 2 mm height at all normalized distances. The soot core at the top of the leading edge vanishes and a denser soot layer is located near the impinging plate.

From Figure 7.11 and Figure 7.12, the soot mass fraction is generally increased near the impinging surface. From the temperature map, a relatively low-temperature layer is found close to the impinging surface at all three temp steps, attributed to the heat transfer between the plate and flame. The temperature in the layer is mostly seated in the temperature range of soot formation. Therefore, the soot is observed near the impinging surface. Also, ambient gas is hard to entrain to the region close to the wall which will lead to worse soot oxidation.

When the flame propagates on a plate, the soot layer which is formed near the impinging plate is accumulated and moving with the leading edge of the flame. This is due to continuous fuel deposited on the wall and worse soot oxidation because of lack of air entrainment to the wall. From the soot mass fraction map of all three timesteps, the soot layer starts to be formed after the impingement and the soot mass fraction in the soot layer is increased when the residence time of soot is increased.

8 Thermal characteristics of an impinging diesel spray[5]

In this Chapter, the apparent heat release rate from the reacting conditions and the heat flux of an impinging diesel spray is discussed. The heat transfer coefficients obtained from the heat flux are also calculated to define the heat transfer regimes with respect to the distance from the impinging region. The heat transfer coefficients were obtained from non-vaporizing conditions.

8.1 The apparent heat release rate of an impinging diesel spray

The effect of ambient temperature on heat release rate is shown in Figure 8.1. Red, green, and blue solid curves show the heat release rate at ambient temperatures of 1000 K, 900 K, and 800 K, respectively. The transparent color band represents the uncertainty among 5 repeats. The timing of vapor fuel impingement (t_{vimp}) and flame impingement (t_{fimp}) are marked with black arrows in Figure 8.1.

---

[5] Reprinted with permission from SAE papers 2019-01-0067 and 2019-01-0267 ©2019 SAE International. Reprinted with permission from International Journal of Engine Research (IJER). The materials in this chapter were published in the following papers:

- Zhao, Z., Zhu, X., Zhao, L., Naber, J. et al., "Spray-Wall Dynamics of High-Pressure Impinging Combustion," SAE Technical Paper 2019-01-0067, 2019, https://doi.org/10.4271/2019-01-0067.
- Zhao, Z., Zhu, X., Naber, J., and Lee, S., "Impinged Diesel Spray Combustion Evaluation for Indirect Air-Fuel Mixing Processes and Its Comparison with Non-Vaporing Impinging Spray Under Diesel Engine Conditions," SAE Technical Paper 2019-01-0267, 2019, https://doi.org/10.4271/2019-01-0267.
- Zhao Z, Zhu X, Naber J, Lee S-Y. Assessment of impinged flame structure in high-pressure direct diesel injection. International Journal of Engine Research. 2020;21(2):391-405. doi:10.1177/1468087419859788

At the ambient temperature of 1000 K, a sharp spike due to premixed combustion is observed. A lower magnitude of temporal aHRR as compared to the premixed portion is observed, after around 1 ms ASOI. At the ambient temperature of 900 K, the premixed portion is still notable, but the duration of the premixed portion is extended. There is also a large shot-to-shot variation of the magnitude of aHRR in the premixed phase compared to an ambient temperature of 1000 K. As seen in the second row of Figure 6.1, the flame is formed very near to the plate at an ambient temperature of 900 K. This shot-to-shot variation could be possible because of the fluctuation of flame impact on the impinging plate. Even though the duration of the premixed combustion portion is different at ambient temperatures of 900 K and 1000 K, the temporal magnitude of aHRR of these two ambient temperatures is the same with each other after around the 1.7 ms ASOI. At an ambient temperature of 800 K, the discrete premixed and diffusion portions are no longer notable. As can be seen in the third row of Figure 6.1, the flame is observed after 1.7 ms ASOI and far at the front side of the impinging point. The aHRR starts to increase after around 1.5 ms ASOI and this delayed ignition gives more time for fuel to vaporize and mix with the air. The trend of the apparent heat release rate at an ambient temperature of 800 K resembles the trend of low-temperature premixed combustion in the previous study [125]. The combustion phase at an ambient temperature of 800 K is more like premixed combustion.

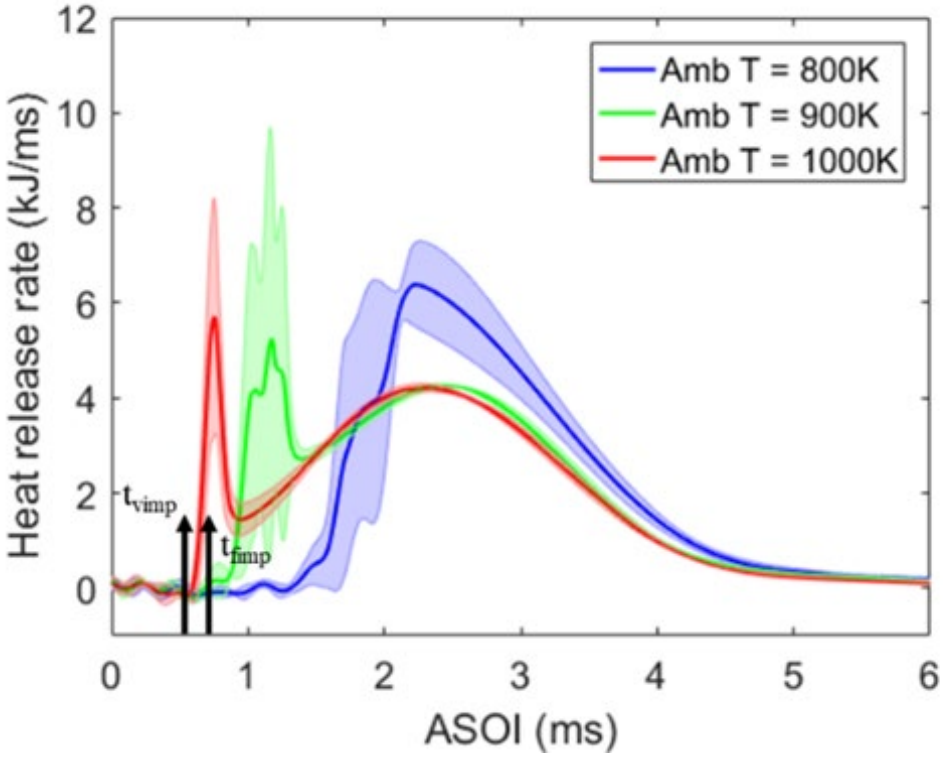

Figure 8.1. Effect of ambient temperature on the apparent heat release rate.

8.2 Heat flux of an impinging diesel spray

During the flame propagation on the plate, there is heat loss from the flame to the impinging plate. The local heat transfer at a given location is considered affected by flame temperature. Therefore, three heat probes are lined along with the axial direction to investigate the effect of spray impingement on the local heat transfer. The local heat flux at different temperatures and locations is discussed in this section.

The heat flux at locations A, B, and C at an ambient temperature of 1000 K is shown in Figure 8.2. After the start of injection but before spray impingement, there is heat transfer from ambient air to the plate because of the temperature difference (T_{amb} of 900 K and 1000 K, the plate temperature is heated up from 423 K to 523 K in heat flux measurements). The heat flux data were analyzed with the subtraction of the pre-burn heat loss. The temporal heat flux reaches the maximum at around 3 ms AOSI. Location B has the

maximum temporal heat flux while location A has the minimum temporal values of heat flux. Since the flame firstly impinges on the plate and then propagates radially, the heat flux at location B starts to increase first and the direct impingement makes the heat flux maximum at location B.

At T_{amb} of 900 K, the magnitude of heat flux at location A is similar to the one at T_{amb} of 1000 K. The profiles of the 900 K flame are shown in Figure 8.3. However, the temporal magnitude at location B is different from the magnitude at location B at T_{amb} of 1000 K. Note that Nusselt number is a function of Reynolds number and Prandtl number. In this study, Prandtl number doesn't change. In Figure 6.14 and Figure 6.15, after 1.2 ms ASOI, the expansion rate is similar between the ambient temperatures of 900 K and 1000 K. Therefore, Reynolds number is comparable in these two cases, which leads the Nusselt number similar and therefore, the convective heat transfer coefficient is nearly the same under T_{amb} of 900 K and 1000 K. Since the heat flux is calculated by using convective heat transfer coefficient and temperature difference between the flame and cold surface, high flame temperature could lead to high local heat flux. Therefore, heat flux at location B under T_{amb} of 900 K is lower than the one under T_{amb} of 1000 K because the flame temperature is lower at T_{amb} of 900 K than T_{amb} of 1000 K [135]. Therefore, the temporal magnitude of the heat flux near the impinging point is mainly controlled by the flame temperature because of the direct impingement. At location C, the magnitude of heat flux at T_{amb} of 900 K is higher than the heat flux at T_{amb} of 1000 K. The flame expansion rate is higher at location C under T_{amb} of 900 K which is FER at θ of 360°. With the same Prandtl number but a higher Reynolds number because of a higher flame expansion rate at location C at T_{amb} of 900 K compared with the FER at location C and T_{amb} of 1000 K, the local Nusselt number is higher, and local convective heat transfer coefficient is higher at location C and T_{amb} of 900 K, leading to higher heat flux compared to it at T_{amb} of 1000 K.

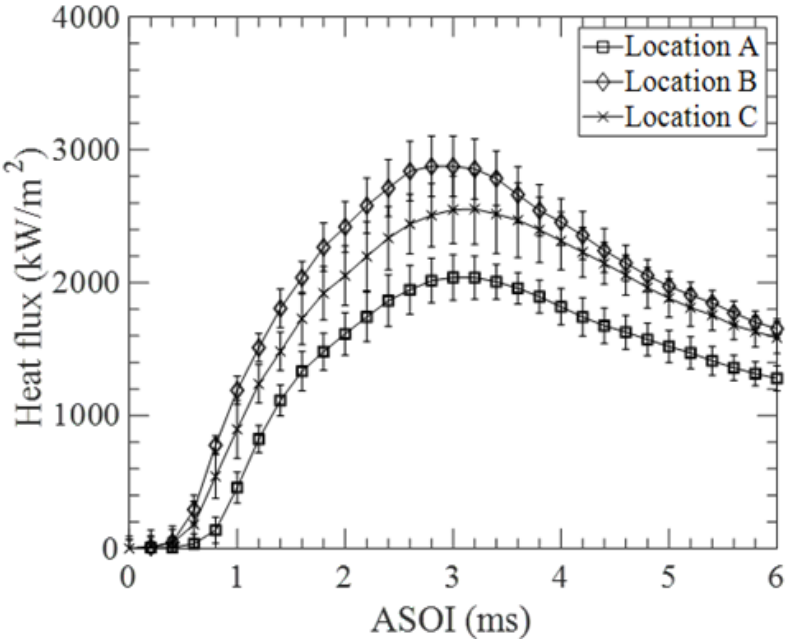

Figure 8.2. Profile of local heat flux at three different locations and T_{amb} = 1000 K.

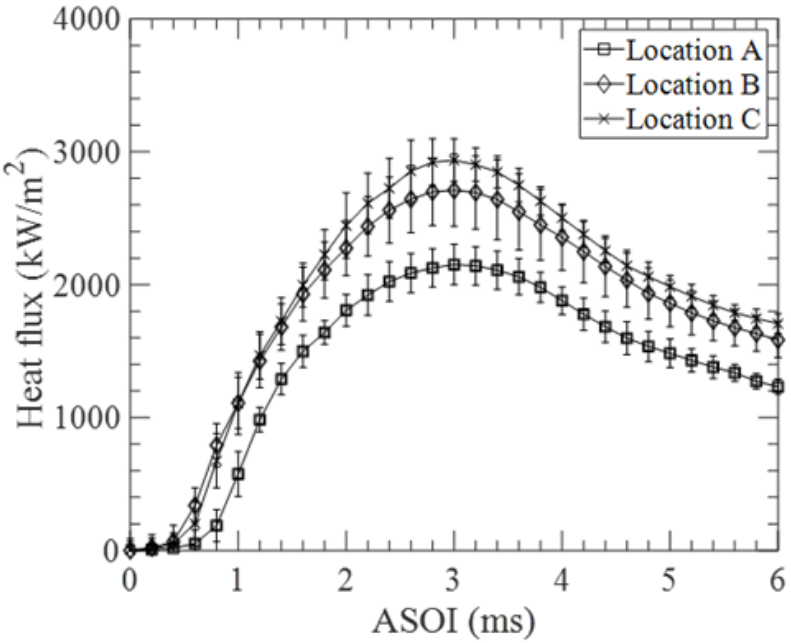

Figure 8.3. Profile of local heat flux at three different locations and T_{amb} = 900 K.

The temporal heat flux at the three locations under different ambient temperatures is shown in Figure 8.4. The local convective heat transfer can be determined by the product of the convective heat transfer coefficient and the temperature difference between the bottom surface and impinging flame. The flame development is quite different at T_{amb} = 800 K compared to the other two temperatures. The 800 K flame developed after impingement while the other two ambient temperature flames began just around the impingement time (900 K flame) or even before the impingement (1000 K flame). The auto-ignition at T_{amb} = 800 K happens at farthest downstream and recesses back towards the impinging point. As can be seen in Figure 8.4, the temporal rate of heat flux of 800 K flame is much lower than the other two conditions. There are possibly two reasons: The convective heat transfer, which is mainly induced by the bulk motion of the flame, is lower under 800 K flame because of lower adiabatic flame temperature. In spite of the temperature difference between surface and combustion gas, radiation of soot particles is another source of local heat flux [136]. The soot production of 800 K flame is found much lower than the other two conditions. Thus, the radiative heat transfer is also lower under 800 K flame. These two factors make the temporal rate of heat flux under 800 K flame near half to other two flames at location A and C and 1/3 at location B.

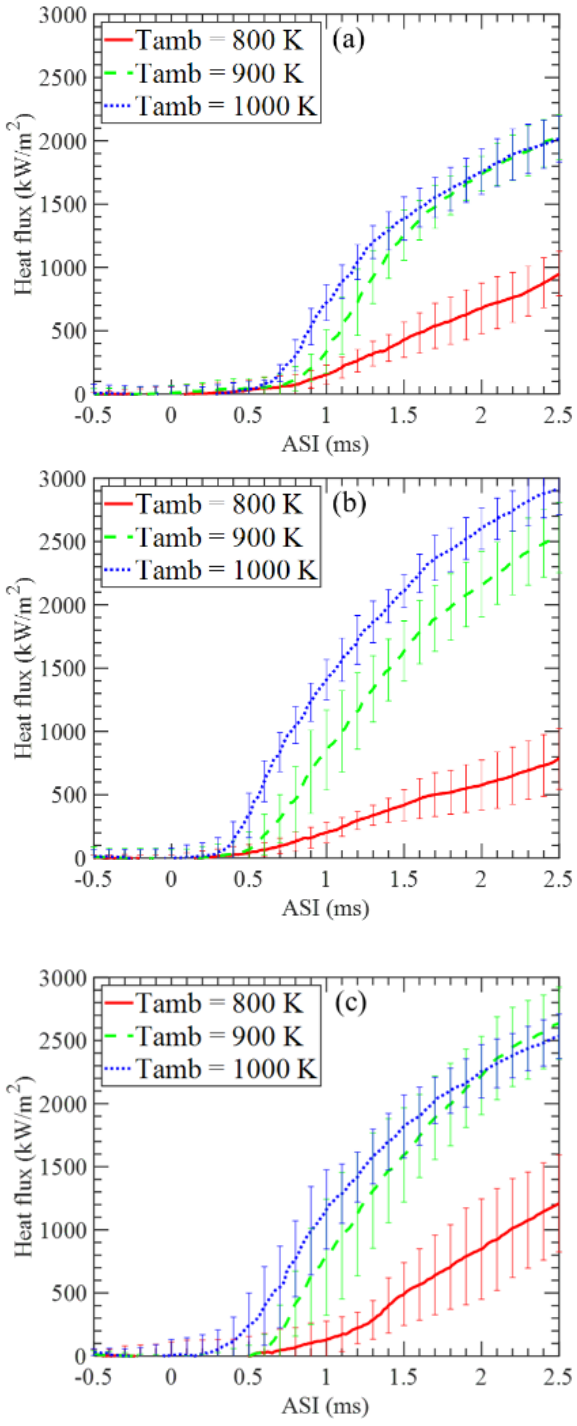

Figure 8.4. Local heat flux at different locations (a) Location A, (b) Location B, and (c) Location C. Conditions: P_{inj} = 1500 bar and ρ_{amb} = 22.8 kg/m^3, 18% O_2.

9 Soot formation in an impinging diesel spray

9.1 The mechanism of soot formation in an impinging spray

According to the observations from ref [121], it is noted that ignition location and soot growth varies among different ambient temperatures. When the test condition has a certain combination (for my cases, P_{inj} of 1500 bar, vertical impinging distance of 40 mm with an impinging angle of 60°, ρ_{amb} of 22.8 kg/m^3, and T_{amb} of 800 K with ultra-low sulfur diesel as the fuel), the high-temperature reaction zones (where OH are formed) are mainly found at the boundary of the impinged part of the spray. From natural luminosity images, the flame propagation direction of the 800 K flame is also different from the 900 and 1000 K flames. A schematic describing such a phenomenon is shown in Figure 9.1 for the flame development of 800 and 1000 K flames from the start of ignition to the timing when the flame is developed. The main spray is rendered with black which is shown in Figure 9.1(a). The darkness of the spray indicates the relative equivalence ratio. A higher equivalence ratio is presented with a darker color. The volume-rendered 3D temperature distributions in the spray are shown in Figure 9.1(b) to (e) with false colors for 800 K (bottom row) and 1000 K (top row) flames.

After the start of injection, when the ignition location is found in the free part of the spray in Figure 9.1(b), the high-temperature region is initiated from the free part of the spray, following the spray momentum and subsequently catching the spray front and covering the whole spray as shown in Figure 9.1(c). However, for the 800 K flame from Figure 9.1(d) to (e), the initial ignition is found at the edge of the expanding spray. The high-temperature region is propagating countering the direction of spray momentum. Such a different flame development behavior may lead to different temperature gradients and mixing behaviors. As the soot formation is strongly related to the temperature and local equivalence ratio, the temperature, equivalence ratio, and soot quantity near the wall among 800 K, 900 K, and 1000 K flames will be discussed and compared detailed in the latter sections.

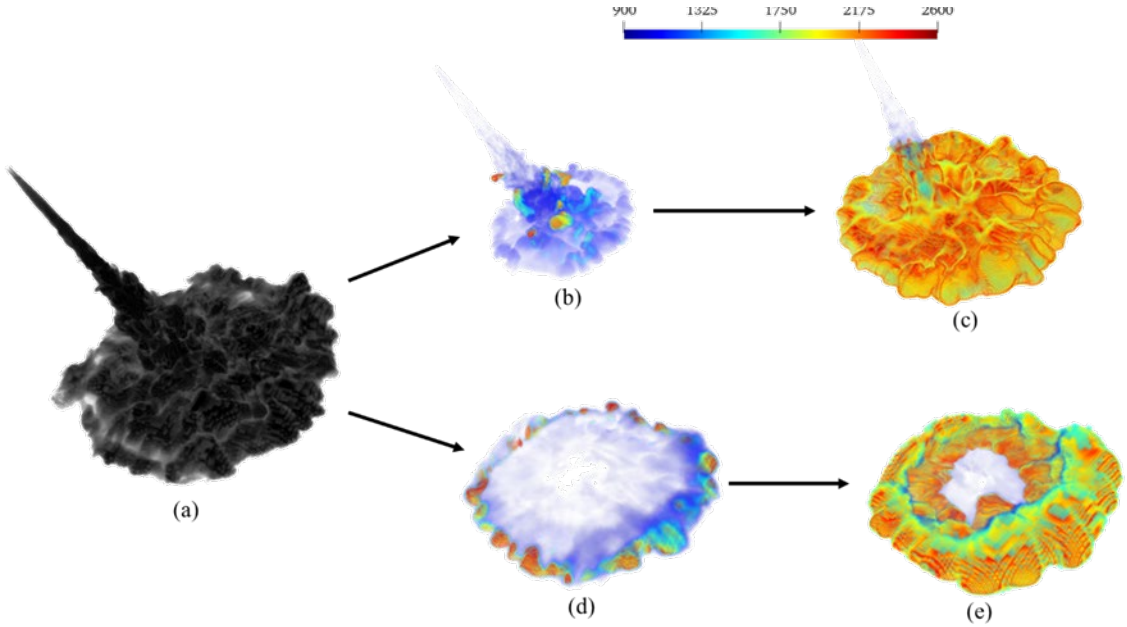

Figure 9.1. Schematic of different types of flame development (volume-rendered from simulations). (a) The fuel-air mixture. Instantaneous distribution of iso-surfaces of the temperature of (b) 1 ms ASOI of the 1000 K flame, (c) 1.5 ms ASOI of the 1000 K flame, (d) 2 ms ASOI of the 800 K flame, (e) 2.5 ms ASOI of the 800 K flame.

A qualitative comparison of the experimental flame and LES generated flame is shown in Figure 9.2. As the natural luminosity is a representative of local soot radiation which is a function of local temperature and soot volume fraction, the temperature and soot mass fraction from simulations are presented in Figure 9.2 for the comparison. The experimental flame was combined by two high-speed images, from the side and bottom view, obtained from two individual combustion events but the same operating condition. The temperature and soot mass fraction distributions from simulations are volume-rendered with false color. By visually comparing the shape of the flame and the luminosity of the flame, the wrinkles of the flame boundary are qualitatively comparable between experiments and simulations. From the natural luminosity images, the most luminous region is found at the leading edge of the flame within the vortex region. Meanwhile, at the same location, the soot mass fraction is relatively high from the simulation results. The visual comparison could confirm

the flame development is globally predictable from LES simulation in terms of soot formation and flame structure.

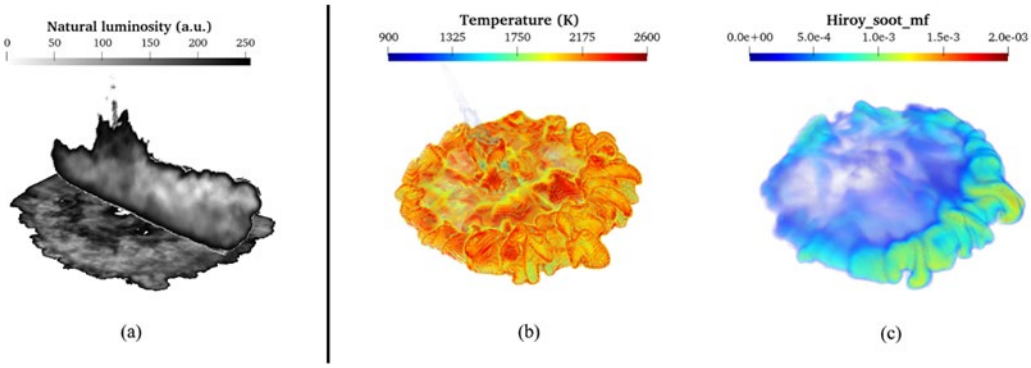

Figure 9.2. Comparison of flame shape between experiments and simulations. (a) Natural luminosity images from bottom view and side view. (b) Instantaneous distribution of iso-surfaces of temperature. (c) Instantaneous distribution of iso-surfaces of soot mass fraction. The left-hand side and right-hand side of the solid line represent the experimental and numerical results, respectively.

The ignition location of the 800 K flame was found at the edge of the expanding spray while the ignition location was found at the free spray part above the plate for the 1000 K flame. The ignition location of the 900 K flame was found close to the impinging region near the wall. To separate flame behaviors by ignition location, the 900 K flame is chosen as a reference for comparing different flame development behaviors. For better spatially visualization of the flame, especially the region near the wall, the soot mass fraction, temperature, and equivalence ratio are volume-rendered through the open-source Paraview program [137].

Firstly, the temporal soot mass fraction, temperature, and equivalence distributions of the 900 K flame are shown in Figure 9.3. The starting time is selected as 1 ms ASOI which is just after the ignition delay of the 900 K flame. The ending time is 2.5 ms ASOI which is around the actual end of injection. At 1 ms ASOI, high equivalence ratios are in the free spray and low equivalence ratios are found in the expanding spray. The splash of parcels in the impinged spray and larger contact surface area benefits the air-fuel mixing process,

resulting in lower equivalence ratios in the expanding spray. Meanwhile, the flame with high temperature starts to propagate along the surface of the expanding spray. Low soot mass fractions are found inside the flame. Although soot starts to be formed, the short residence time leads to low soot mass fraction and sparse distribution in the flame. The low soot mass fraction here indicates the presence of soot initiation at an early stage after the ignition delay.

At 1.5 ms ASOI, while the free spray still shows high equivalence ratios, the leading edge of the expanding spray shows a relatively higher equivalence ratio than 1 ms ASOI. It is due to the fuel accumulation where the impinging spray waves propagate near the impinging surface. Meanwhile, high soot mass fractions start to be observed at the same locations of high equivalence ratio regions. Low soot mass fractions are found near the impinging region, indicating that the soot is initiated near the impinging region for the 900 K flame. At 1.5 ms ASOI, the spray further expands on the plate and the leading edge of the spray starts to roll up following the direction of the vortex generated by the spray impingement. Furthermore, soot is continuously formed at the leading edge where both the equivalence ratio and temperature favor the soot condition. After the end of injection, both free spray and expanding spray show less fuel-rich and subsequently less soot formed at the leading edge of the spray compared to 2 ms ASOI.

To summarize, when the ignition location is in the free spray, the flame is developing along the surface of the spray and propagates along with the spray momentum. When the incoming fuel is going to burn, there is not enough time for it to mix with the air as the fuel is soon contacting the reaction zones. Therefore, fuel-rich zones near the wall are immediately consumed by the flame and lack the opportunity for air entrainment at the bottom of the spray.

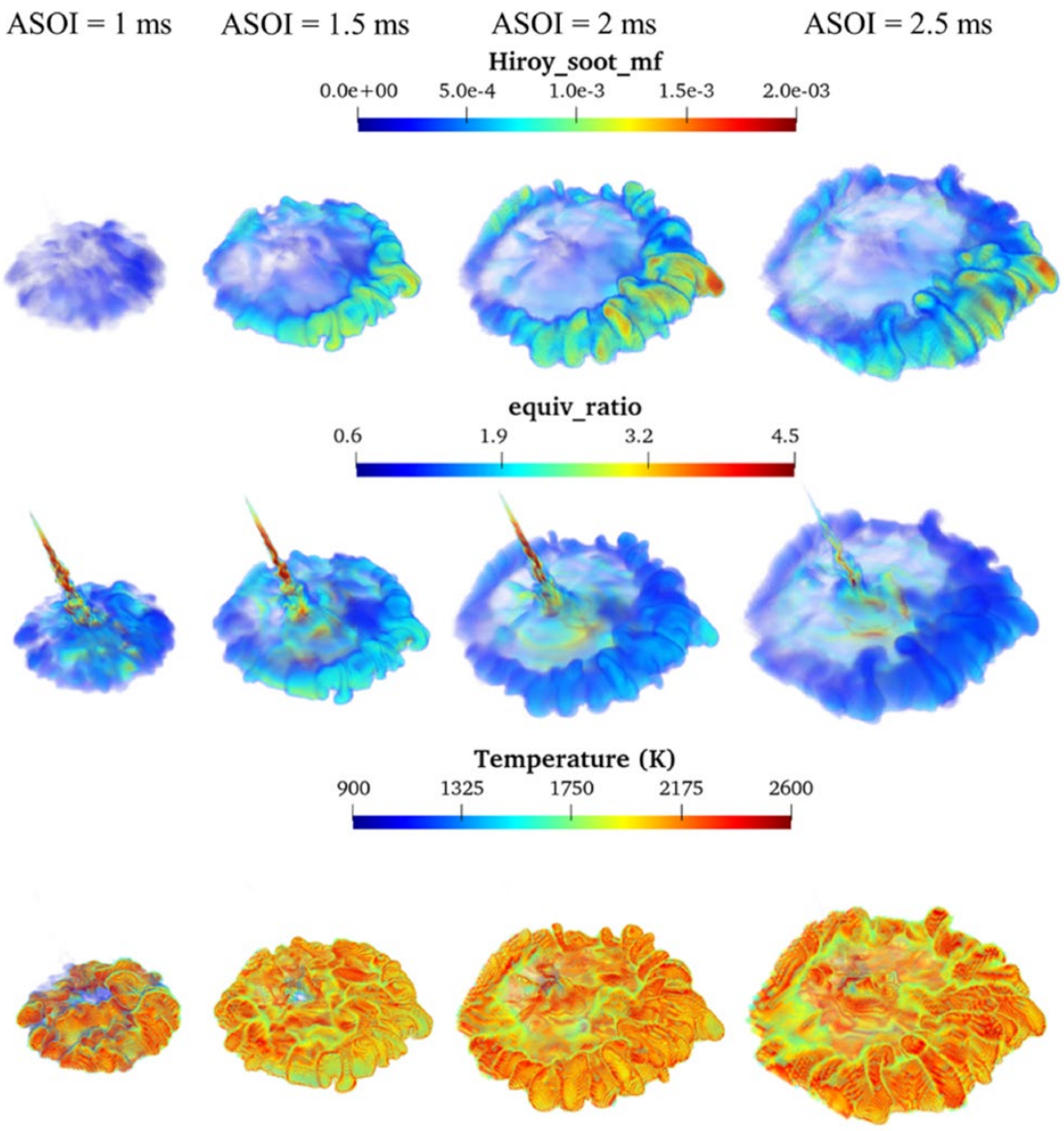

Figure 9.3. Flame development of the 900 K flame. Instantaneous distribution of iso-surfaces of soot mass fraction, equivalence ratio, and temperature are shown from top to the bottom. Four ASOIs, from 1 to 2.5 ms are chosen.

When the ambient temperature is increased to 1000 K, the ignition location is elevated towards the nozzle, but the flame is still propagating along the direction of spray momentum. The volume-rendered soot mass fraction of 900 and 1000 K flames are shown in Figure 9.4 for comparison. From Figure 9.4, the spray shape where the equivalence ratio

is richer than 0.6 is similar between the 900 K and 1000 K flames, e.g., qualitatively comparable spray area. Most soot is formed at the leading edge of the spray in both the 900 K and 1000 K flames. However, the 1000 K flame has a globally local higher soot mass fraction. A higher ambient temperature shortens the ignition delay as well as the lift-off length, giving a smaller area of air entrainment upstream. It is noted that the high soot mass fraction spots at the left of the 1000 K flame at 2.5 ms ASOI are due to the flame contact with the sidewall.

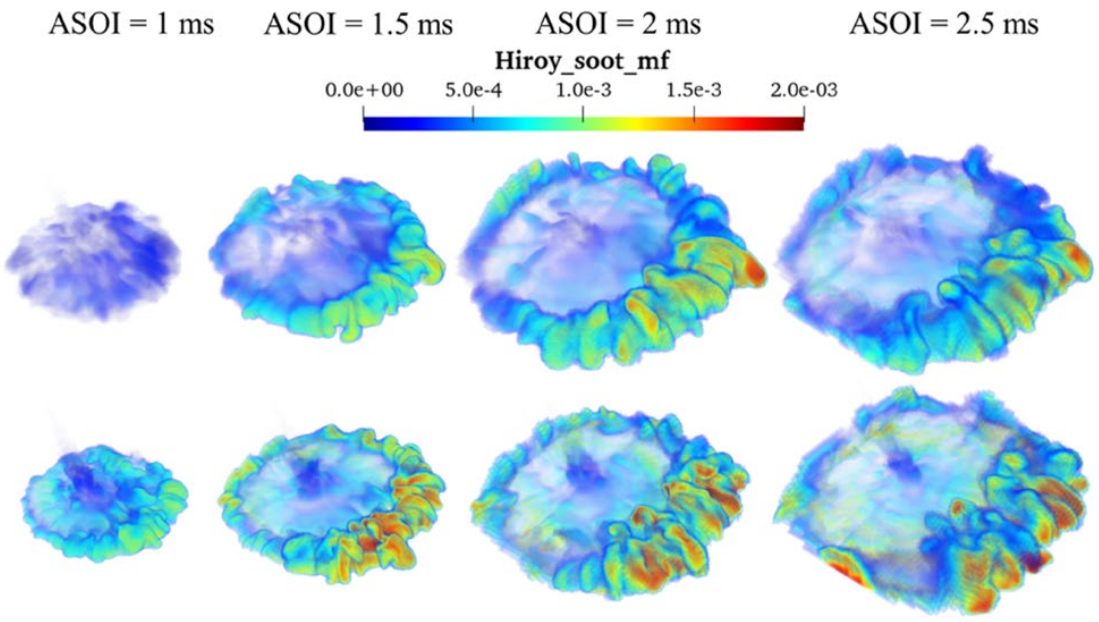

Figure 9.4. Comparison of the instantaneous distribution of iso-surfaces of soot mass fraction between the 900 K (top row) and 1000 K (bottom row) flames. Four ASOIs, from 1 to 2.5 ms are chosen.

For the 800 K flame, the behavior of flame development is quite different from the 900 and 1000 K flames and it is shown in Figure 9.5. The flame with a high temperature (> 2200 K) starts to be formed nearly 0.5 ms after the ignition delay. Besides, the ignition location is not found at the free spray part rather than the edge of the expanding impinged spray. The flame propagation and spray expanding directions are marked with red and black arrows in the temperature distributions at 2 ms ASOI. Due to a longer mixing time, the equivalence

ratio in the part of the spray that is before the impingement is globally decreased compared to the 900 K flame as there is more air entrained into the spray. Also, the mixing quality could also be affected by the ignition delay [60]. The air entrainment rate is reduced due to the ignition and hot gas expansion inside spray gives hardness to the air entrainment as well. Not only the equivalence ratio at the leading edge of the impinged spray is reduced, but the equivalence ratio at the free spray is also reduced from above 4 at the 900 K flame to less than 3 at the 800 K flame. As the time is increased to the end of the injection, the flame is propagating from the leading edge to the impinging region which could be seen from the temperature distribution at 2.5 ms ASOI. Meanwhile, the soot mass fraction is significantly reduced compared to the 900 and 1000 K flames, and nearly no soot formed near the impinging region. The void region near the impinging point is due to the existence of the film. The film leads to quenching and blocks the soot formation in film occupied region, but it still contributes to soot formation above the film [11]. Another evidence for soot-blocked-by-film is that only the 800 K flame deposits distinct film and there is nearly no soot formed in the impinging region. After 3.5 ms ASOI, the flame starts to dissipate, and the soot mass fraction is globally reduced.

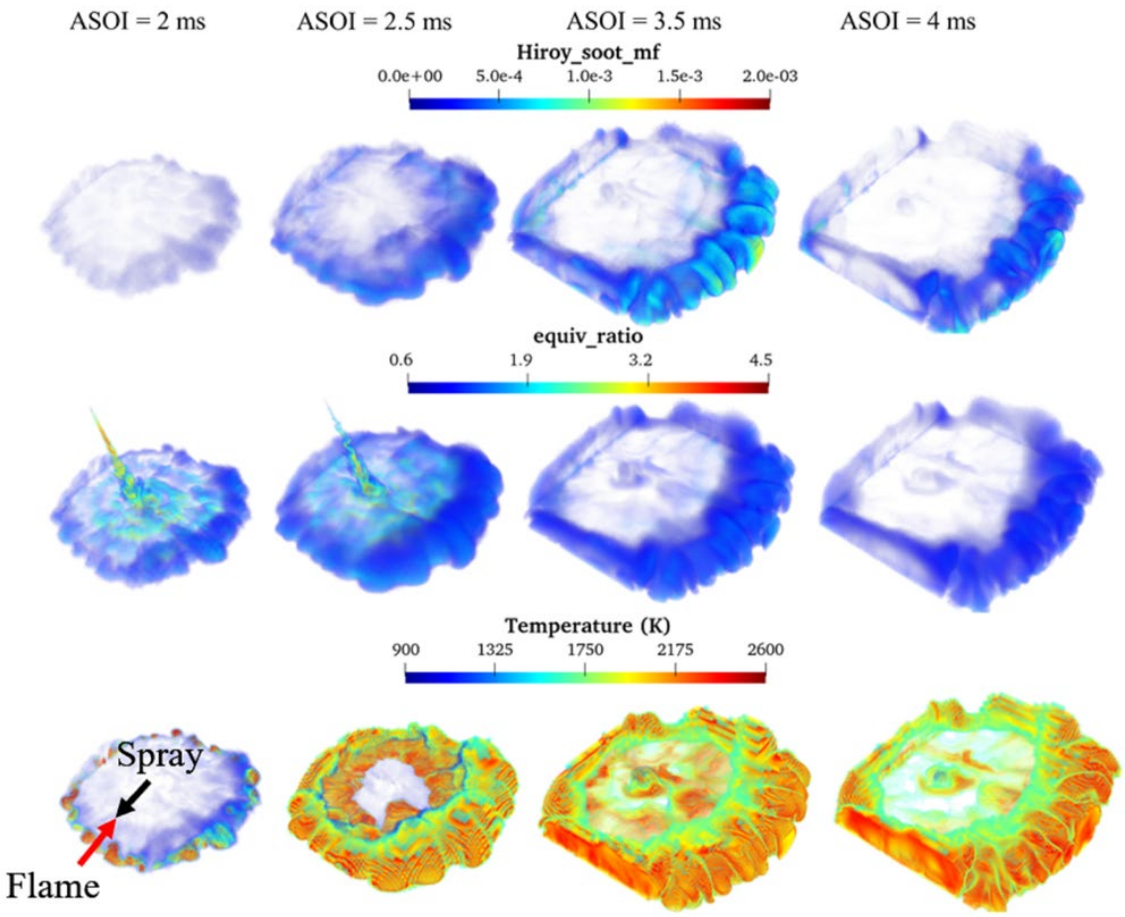

Figure 9.5. Flame development of the 800 K flame. Instantaneous distribution of iso-surfaces of soot mass fraction, equivalence ratio, and temperature are shown from top to the bottom. Due to the longer ignition delay, four ASOIs are shifted to 2 to 4 ms.

In Figure 9.6, a cut view of the 900 K flame at the centerline of the spray axis, 1.5 ms ASOI, is presented to show the spatial distributions of cool flame, soot, and OH radicals. The fuel-air mixture, formaldehyde (CH_2O), soot precursor (Acetylene (C_2H_2)), OH radicals, and soot are combined to show the progress of mixing, auto-ignition, soot precursor formation, soot accumulation, and soot oxidation. Initially, after the injection, the spray experiences a mixing process with ambient gas to form a fuel-air mixture. After the ignition delay, cool flame indicator CH_2O is formed at the tip of the fuel-air mixture near the impinging location. The CH_2O significantly accumulates in the near-wall region and an abrupt increase in the concentration of CH_2O was also observed [138]. C_2H_2 is

formed in the post-impingement part of the spray and is mainly found near the wall. At bottom of the leading edge of the spray, the combination of soot precursor and relative low soot is found. Carried by the vortex at the leading edge of the spray and experiencing longer soot residence time, the combination of soot precursor and initial soot (low soot mass) becomes mature soot that has relative high soot mass in the core of the vortex at the leading edge of the spray. When the mature soot is continuously lifted by the vortex, it touches the soot oxidation layer where the OH radicals are formed and start to be oxidized. The oxidation layer is thicker at the top of the vortex where the counter-flow exists.

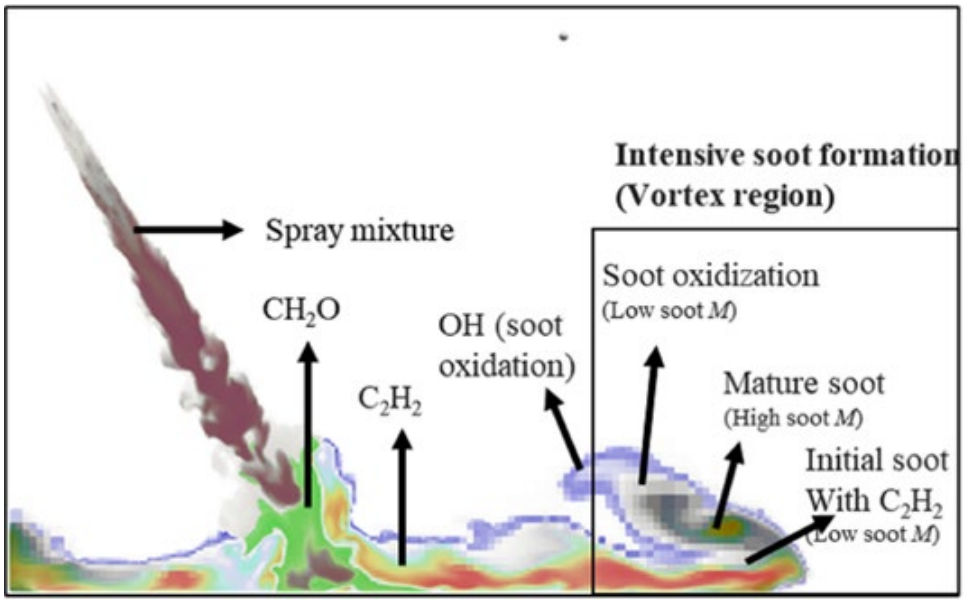

Figure 9.6. A schematic of fuel-air mixture, CH_2O, C_2H_2, soot, and OH formed in an impinging flame.

Due to the oblique impingement, the mass of the spray is not distributed radially uniform. Thus, the tendency of soot formation may be varied in different radial locations. From Figure 9.6, the vortex region is defined as the front side of the impinged spray and the impinged spray axially behind the impinging point is defined as the backside of the spray. To compare the difference of soot mass fraction at the front and backside of the spray, a horizontal plane at 1 mm above the wall is chosen for analysis in Figure 9.7. Soot mass fraction is shown with a range of 0 to 0.002. The void regions found in the spray are those

regions that have an equivalence ratio lower than 0.6. In Figure 9.7(a), a line with an arrow indicates the centerline of the spray axis and the cross point of the arrow line with a perpendicular line indicates the location of the impinging point. The main spray is then horizontally divided into the back and front parts with respect to the perpendicular line. The back and front sides of the spray are shown in Figure 9.7(b) and (c), respectively. Through visual observation, the front side shows a relatively average higher soot mass fraction than the back side. Meanwhile, the soot mass fraction near the leading edge of the spray is significantly higher than the backside and impinging region of the spray.

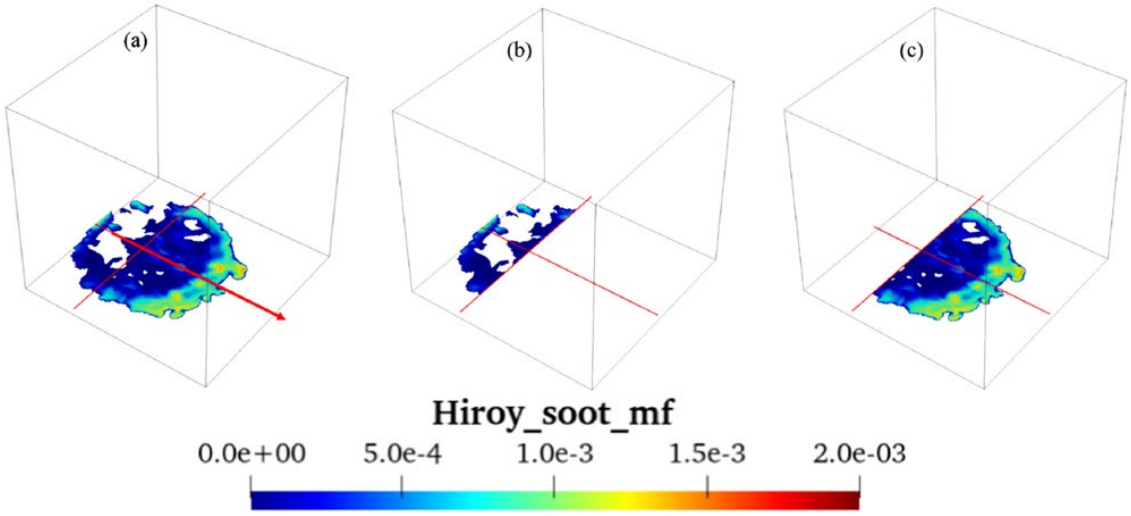

Figure 9.7. Differences of soot formation at the front and back sides of the impinging point.

From the Hiroyasu soot model, soot mass fraction is acquired from the outputs of the simulations. The absolute soot mass is then calculated by multiplying the total cell mass with the soot mass fraction. Then the total soot mass at the front side of the spray is summed up with all analyzed cells. In order to distinguish the differences of total soot mass between the front and back sides, the total soot mass of the front side of the spray and the whole plane from four different heights is obtained and compared in Figure 9.8. The soot mass formed on the backside of the spray could be obtained by subtracting the soot mass on the front side from the whole plane. The temporal total soot mass on different heights is shown with black, red, green, and blue lines. By comparing the soot mass between the whole plane

and front side, it is noticeable that the soot mass at 5 and 7 mm is nearly overlaid between solid and dashed lines which means the soot formed at the backside could be neglected. Thus, for soot formation-oriented analysis, only the front side of the spray will be discussed in the remaining sections.

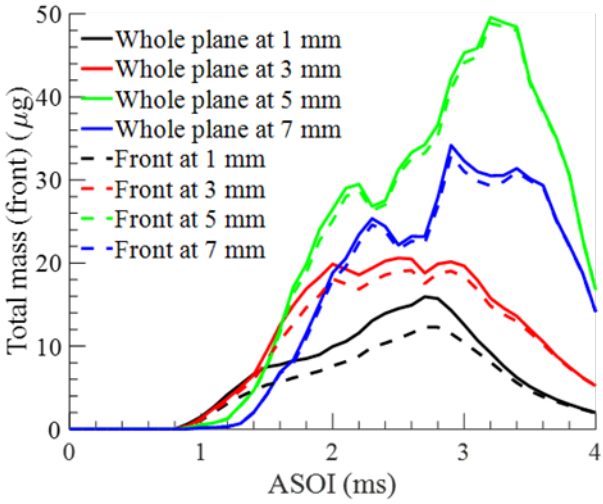

Figure 9.8. Instantaneous total soot mass on different heights for the 900 K flame.

Two factors are affecting the absolute soot mass which is the total mass of cell and soot mass fraction. The total cell mass, soot mass fraction, and absolute total soot mass at four different heights for the 900 K flame are shown in Figure 9.9 to present the progress of soot formation after the ignition delay. In Figure 9.9(a), when the spray is propagating after the impingement, the mass at 1- and 3-mm heights firstly increases as the fuel is mixed with the ambient air. After ~ 1.2 ms ASOI, the mass at 5- and 7-mm heights start to increase, and it shows a higher slope than 1 and 3 mm after 1.5 ms ASOI. This phenomenon is attributed to the vortex formed at the leading edge that carries the fuel-air mixture from the near-wall region to a higher altitude. After the end of the injection, the cell mass starts to decrease at 1- and 3-mm heights but 5- and 7- mm heights are keeping increasing due to the existence of the vortex. The cell mass is reduced after ~ 3.5 ms ASOI at 5 and 7 mm when the vortex is dissipated.

Soot mass fraction is another factor influencing the absolute soot mass. In Figure 9.9(b), the average soot mass fraction at 1, 3, 5, and 7 mm are shown. After the ignition delay, the average soot mass fraction at four heights is initially increased simultaneously. However, it is diverged after 1 ms ASOI and increased faster if closer to the wall before ~ 1.3 ms ASOI. After ~ 1.3 ms ASOI, both the cell mass and average soot mass fraction at 5- and 7-mm height are increasing faster and they exceed 1 and 3 mm height. At 1- and 3-mm heights after 1.3 ms ASOI, the slope of the average soot mass fraction profile becomes smaller until the fraction reaches the maximum at the end of injection. Meanwhile, at 5- and 7- mm heights, after the rising phase, the average soot mass fraction reaches a plateau and drops due to the end of the injection. However, it increases again and drops after ~ 3.3 ms ASOI. As attributed by the higher cell mass and soot mass fraction, the absolute total soot mass is initially higher in the near-wall region before ~ 1.3 ms ASOI. After dropping for a short period, due to the huge cell mass increase, the soot mass also significantly increases at 5- and 7- mm heights while the average soot mass fraction is not changing dramatically.

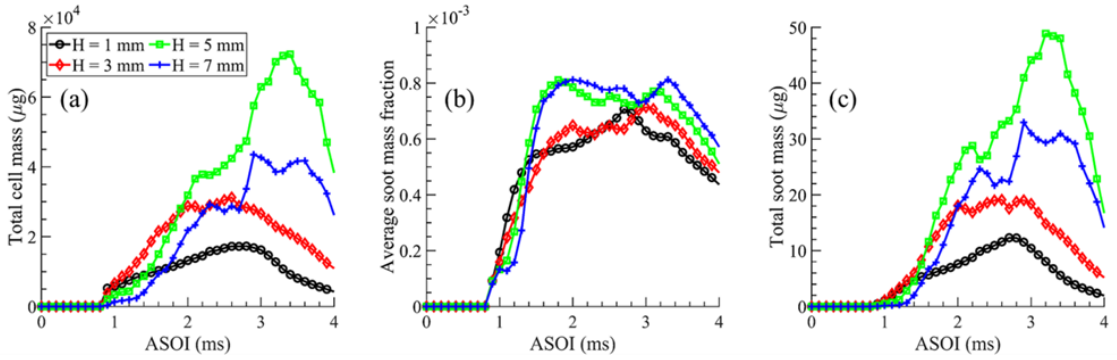

Figure 9.9. Instantaneous soot mass fractions and absolute soot mass at different heights for the 900 K flame. (a) Total cell mass. (b) Average soot mass fraction. (c) Total soot mass.

From Figure 9.6, soot precursor is mainly formed in the near-wall region, and soot is formed in the vortex region which is between 3 and 7- mm in height. Thus, for comparison of soot formation in three different flames, the average mass fraction of soot and soot precursors for the 800 K, 900 K, and 1000 K flames are shown in Figure 9.10. For better

visualization, the soot mass fraction is multiplied by a factor of 10. In the 800 K flame, after the ignition delay, soot precursor is significantly higher at 1 mm compared to the other three heights. Even after the end of injection and all the fuel is injected in the domain, the soot mass fraction is remained at a low level compared to the 900 and 1000 K flames. For the 900 K flame, only the mass fraction of the soot precursor will be discussed. At 1- and 3-mm heights, the mass fraction of the soot precursor firstly reaches a plateau and then decreases while at the other two heights, it drops after ~ 1 ms AOSI and recovers after ~ 1.3 ms ASOI. It is found that the mass fraction of the precursor is always higher at 1 mm which means the precursor is mainly formed in the near-wall region. For the 1000 K flame, the trends are similar to the 900 K flame, but the magnitude of soot and precursor mass fraction is higher.

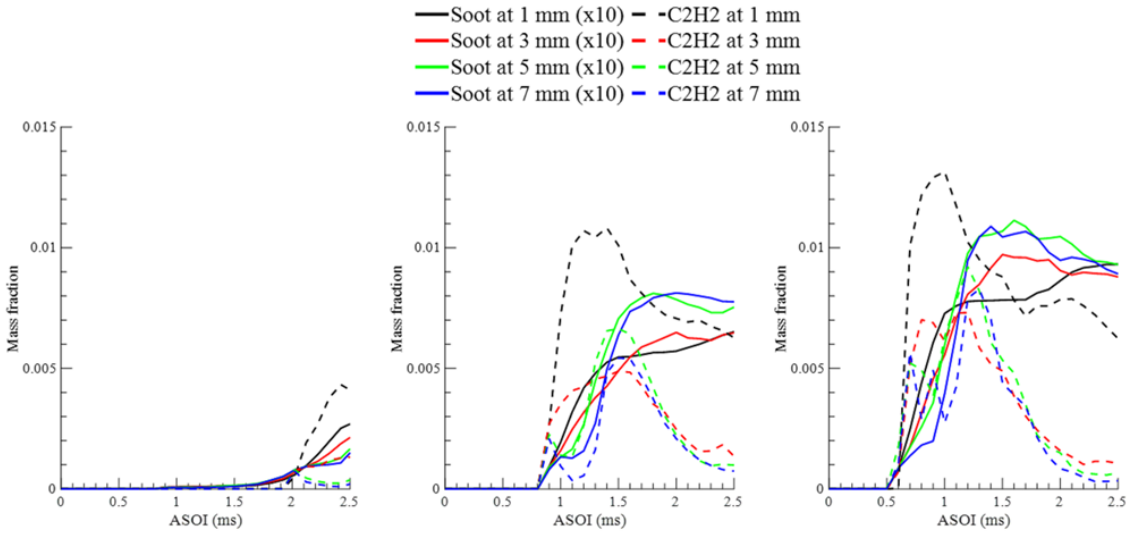

Figure 9.10. Instantaneous soot and soot precursor mass fractions for 800 K, 900 K, and 1000 K flames, from left to right, respectively. Soot mass fraction is multiplied by a factor of 10 to make a better comparison with precursor mass fraction.

9.2 Relationship between quantity of soot and local temperature

After discussing the curvature of the flame boundary, it is found that local curvature is correlated with local qualitative soot quantity [55]. The soot formation is affected by local

flame temperature and equivalence ratio. From LES simulations, the temperature and soot quantity are non-uniform at different heights above the plate. The results at six different heights, i.e., 1, 2, 4, 6, 8, and 10 mm above the plate which is ranging from close to the wall to far above the wall are presented. The temperature distributions are only presented where the soot is intensively formed. The grid size of the interpolated data is 0.2 mm which indicates that the distribution is shown within the height ± 0.1 mm. Three AIDs, 0.5, 1, and 1.5 ms are adopted to investigate the flame development at different heights.

The contours of temperature and soot mass fraction of the 900 K flame at 0.5 ms AID are shown in Figure 9.11 from left to right, respectively at the heights of 1, 2, 4, 6, 8, and 10 mm are shown from top to bottom. The occupied area of soot is decreased as the height is away from the impinging surface. At a height of 1 mm, the area of soot formation nearly occupies the whole downstream region. A relatively low-temperature band is found at the leading edge of the flame where there is intensively soot formation. At the close-by wall, soot also occupied the region near the impinging point, but the mass fraction is relatively low. As the height is increased to 2 mm, the occupied soot and mass fraction nearly maintain the same as the area of the height of 1 mm. At a height of 4 mm, the thickness of the soot band is increased but its perimeter is decreased. At a height of 6 mm, the soot formation at two sides vanishes and soot is only formed nearby the leading edge of the flame. At heights of 8 and 10 mm, the area of soot formation shrinks because there is not too much spray over the height of 10 mm.

In Figure 9.11, it could be observed that soot is intensively formed at a temperature below 1800 K. However, low-level soot concentration is also presented close to the wall in high-temperature regions. In order to quantify the correlation of temperature and soot formation at different heights, the scattering plots which show the local temperature and soot mass fraction in each cell are shown in Figure 9.12. A 2-D histcount function is used to obtain the scatter density at a certain temperature and soot mass fraction. The bin sizes of temperature and soot mass fraction are 10 K and $4*10^{-5}$, respectively. At the height of 1 mm, the shape of the distribution is displayed as a triangle. An intensive band is observed

between the temperature of 1600 and 2200 K. At the height of 2 mm, the shape of the distribution is also displayed as a triangle shape. The intensive band is shifted to the boundary of the top right part. At the height of 4 mm, the shape of the distribution becomes a combined relationship with two arms, one on the bottom, the other one with a ~ 45 degrees angle. It is defined these two arms as dependent region and independent region, respectively. In the dependent region, soot formation is increased as the temperature is decreased where the soot and temperature have a dependency. In the independent region, the soot formation is nearly unchanged even the temperature is ranged low from 1300 K and up to 2400 K. As the height is increased, the intensive band is shifted towards the dependent region. Looking at the contour of the soot mass fraction, the soot formation near the impinging point has vanished above the height of 4 mm. In meantime, the scatters in between the independent and dependent regions are vanished when the height is above 4 mm. Thus, it can be addressed that the scatters in between the two arms are caused by the soot formed near the impinging point. At the height of 6 and 8 mm, the shape of the distribution is similar to it at a height of 4 mm.

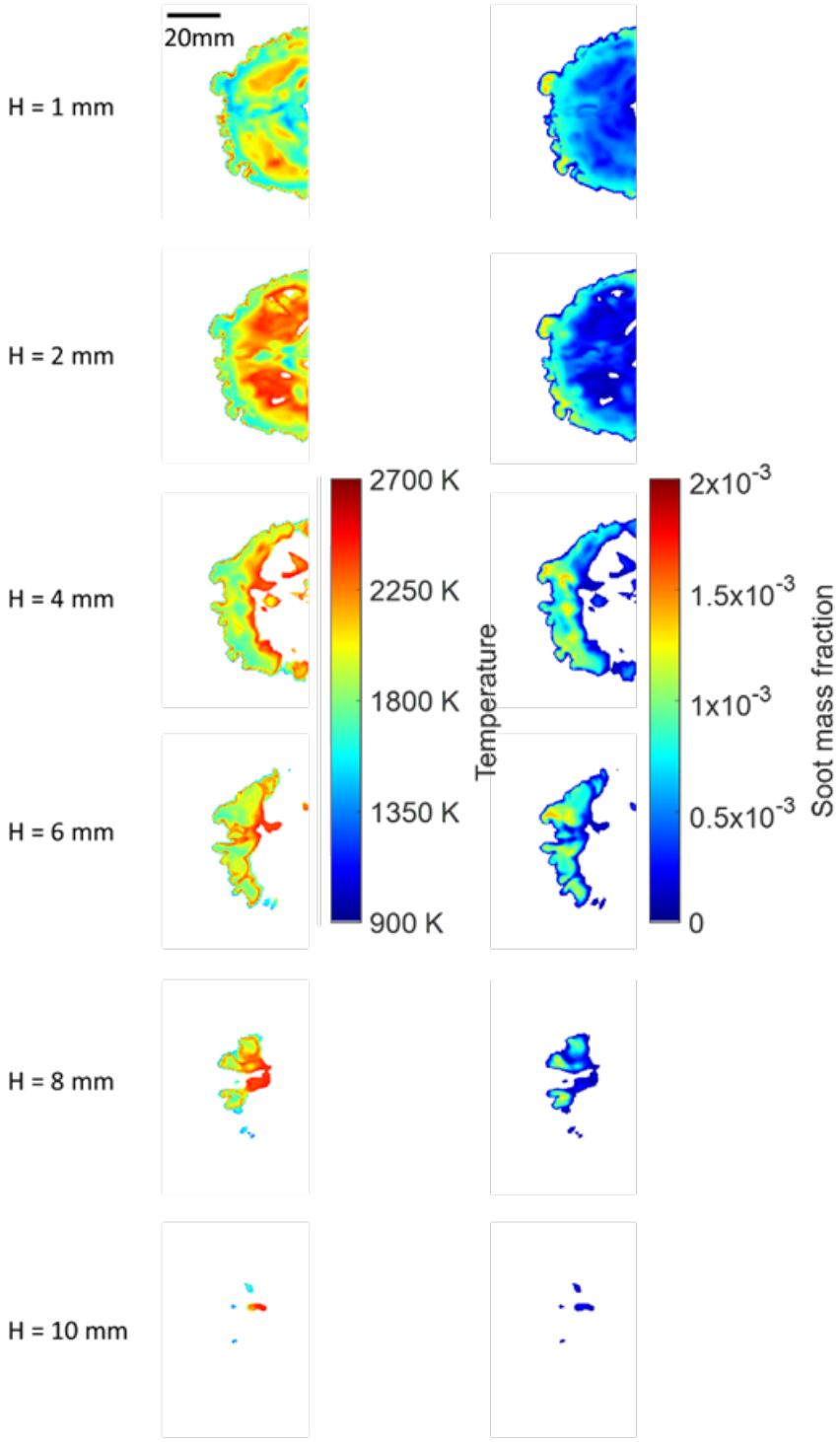

Figure 9.11. The contours of temperature and soot mass fraction at different heights above the plate, AID = 0.5 ms, the 900 K flame.

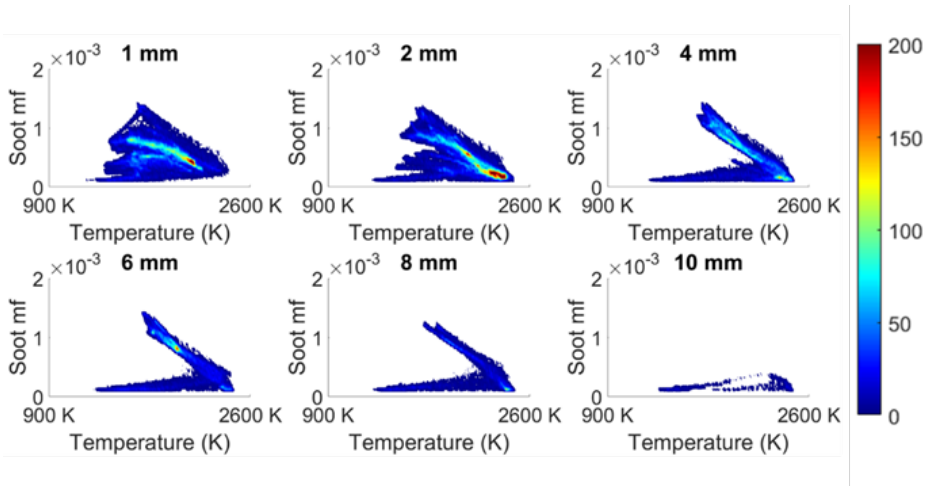

Figure 9.12. The correlation of soot mass fraction and temperature at different heights above the impinging plate, AID = 0.5ms, the 900 K flame.

From Figure 9.11 and Figure 9.12, it could be observed that the soot and temperature are similar between the height of 1 to 2 mm, 4 to 6 mm, and 8 to 10 mm, individually. Hence, the current thesis will only present the results of the height of 1, 4, and 8 mm for the representatives of three different levels of height, close to the wall (below 2 mm), medium height (2-8 mm), and far above the wall (above 8 mm). The distributions of temperature and soot mass fraction as well as the scattering plots of the 900 K flame at 1 ms AID are shown in Figure 9.13 from left to right, respectively. At a height of 1 mm, the area of soot formation nearly occupies the whole downstream region. A relatively low-temperature band is found at the leading edge of the flame. Dense soot cores are found close to the leading edge of the flame. At the height close to the wall, soot is also observed near the impinging point, but the soot mass fraction is relatively low. At the medium height, the area of soot formation maintains the same near the leading edge of the flame but the soot formation near the impinging point is disappeared. The area of dense soot cores is increased as the height is increased. At a height of 8 mm, the soot is only formed axially near the leading edge of the flame.

From the scattering plots, the area of the soot-occupied region is decreased as the height is increased. At a height of 1 mm, the shape of the distribution is also displayed as a triangle.

At a height of 4 mm, the shape of distribution also becomes a two-arms type. The intensive band is shifted towards the dependent region. Compared with the distribution of height of 1, 4, and 8 mm, the scatters in between the two regions are vanished which is attributed to the disappearance of soot formation near the impinging point. The slope of the dependent region is increased compared to the slope of 0.5 ms AID. The higher slope indicates that the same soot mass fraction location would have a higher temperature in the dependent region.

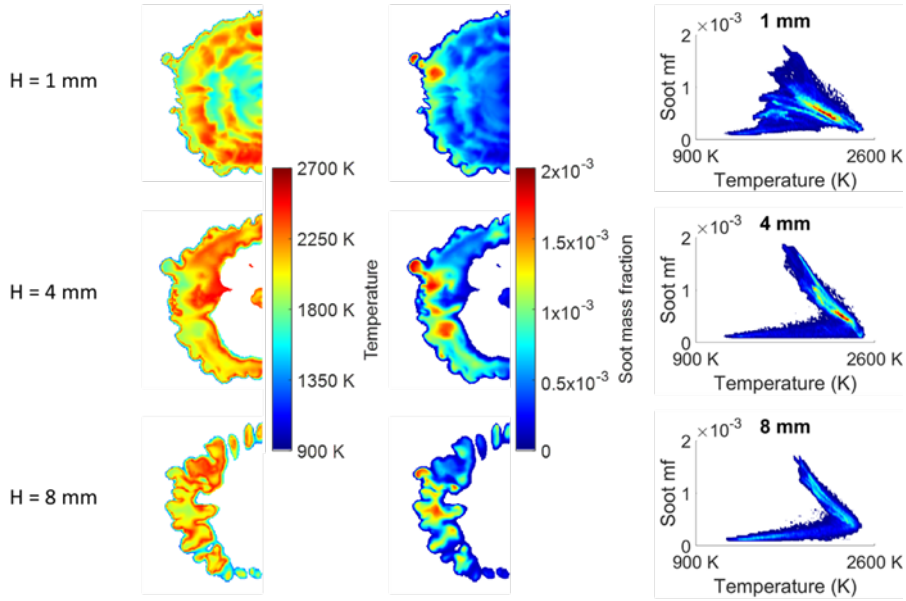

Figure 9.13. The contours of temperature and soot mass fraction at different heights above the plate, AID = 1 ms, the 900 K flame.

The distributions of temperature and soot mass fraction of the 900 K flame at 1.5 ms AID are shown in Figure 9.14 from left to right, respectively. The low-temperature band near the leading edge of the flame is much thicker than the band of 0.5 and 1 ms AID. At the medium height, the area of soot formation is smaller than the area of the height of 1 mm. Dense soot regions start to be observed near the leading edge of the flame at the downstream region. Dense soot regions are nearly at the same spatial location, but the area is decreased far above the plate. The scattering plots between temperature and soot mass

fraction are also shown in Figure 9.14 in the third column. The trend of the scatters is similar compared to the trend of 0.5 and 1 ms AID. However, there are more scatters sitting in the independent regions. From the flame development, it could be observed that the area of soot formation is increased as the height is decreased. More soot will be formed close to the wall especially near the impinging region.

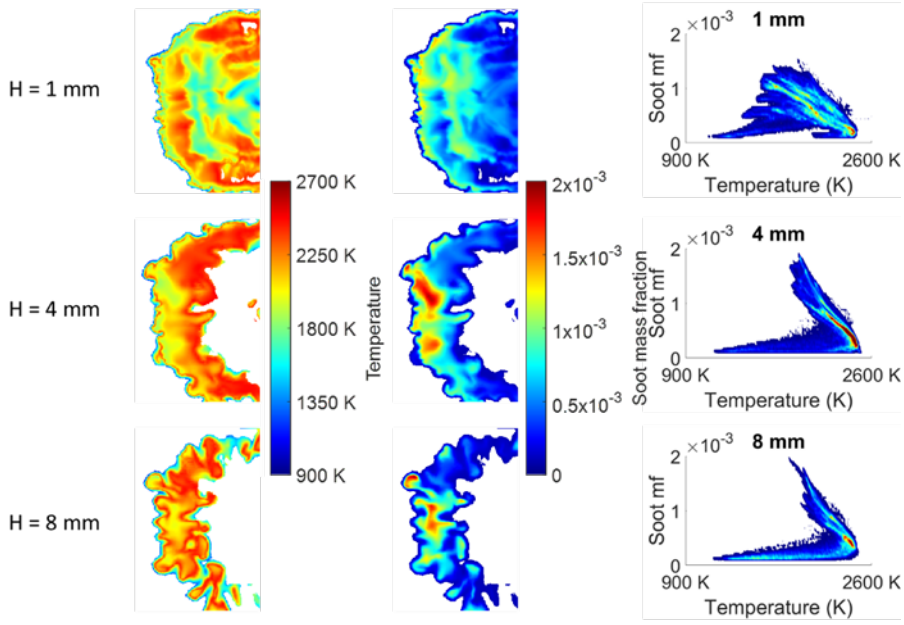

Figure 9.14. The contours of temperature and soot mass fraction at different heights above the plate, AID = 1.5 ms, the 900 K flame.

The distributions of temperature and soot mass fraction of the 1000 K flame at 0.5 ms AID are shown in Figure 9.15 from left to right, respectively. It is noted that the 0.5 ms AID of 1000 K flame is ~ 0.3 ms earlier than the 0.5 ms AID of 900 K flame. Only two heights are chosen at 0.5 ms AID as there is no spray far above the plate at this time. At a height of 1 mm, the area of soot formation nearly occupies the whole downstream region. Compared to the results of the flame of 900 K at 0.5 ms AID, the soot is more uniformly distributed along with the plate instead of intensively forming near the leading edge. At the medium height, the area of the flame shrinks faster than the flame of 900 K ambient condition and

this is because that the flame is just developed after the impingement at a temperature of 1000 K ambient condition. The scattering plots between temperature and soot mass fraction are shown in Figure 9.15, third column. The area of the soot-occupied region is decreased as the height is increased. The intensive band is observed close to the plate but disappeared at medium height. The distribution is also shifted from a triangle shape to a dependent-independent shape as the height is increased.

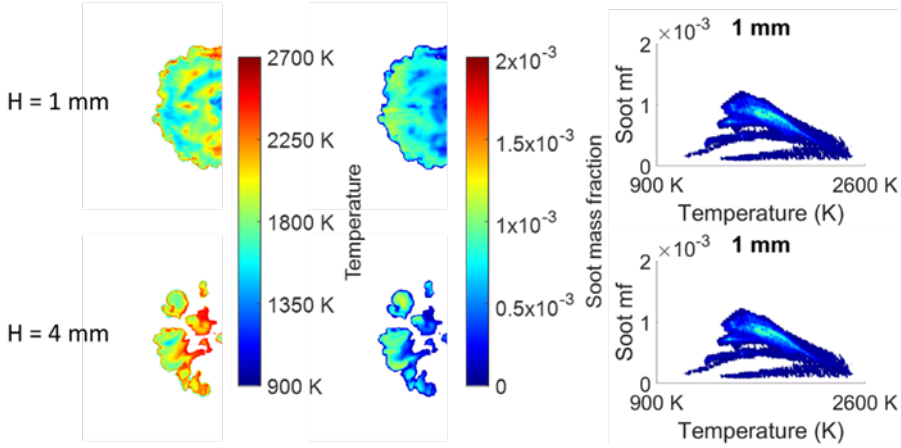

Figure 9.15. The contours of temperature and soot mass fraction at different heights above the plate, AID = 0.5 ms, the 1000 K flame.

The distributions of temperature and soot mass fraction of the 1000 K flame at 1 ms AID are shown in Figure 9.16 from left to right, respectively. As flame propagates on the plate, the soot tends to be formed from the inside of the flame to the leading edge of the flame. At the medium height, high soot mass fraction cores are observed near the leading edge of the flame. The area of soot occupied region shrinks further but the dense soot cores are still visible far above the plate. The scattering plots between temperature and soot mass fraction are shown in Figure 9.16, right. Unlike the previous scattering plots, the intensive band is not dense as it of the 900 K flame. However, the trend is similar to it of the 900 K flame.

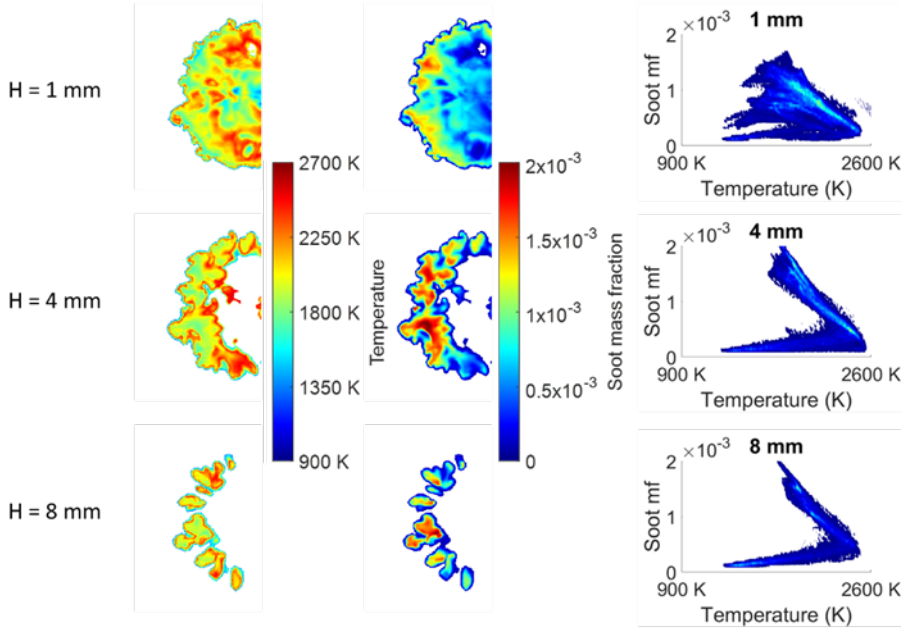

Figure 9.16. The contours of temperature and soot mass fraction at different heights above the plate, AID = 1 ms, the 1000 K flame.

The distributions of temperature and soot mass fraction of 1000 K flame at 1.5 ms AID are shown in Figure 9.17 from left to right, respectively. At close to the wall, the area of soot formation nearly occupies the whole flame region. The low-temperature band is no longer uniformly distributed along the flame boundary. Dense soot cores are observed at the concave regions of the leading edge of the flame. Soot is also observed near the impinging point. At the medium height, denser soot cores are observed which have higher soot mass fraction than the flame of 900 K ambient conditions. At far above the plate, only the dense soot cores are left. The scattering plots between temperature and soot mass fraction are shown in Figure 9.17. The soot mass fraction is extended higher, and the slope of the dependent region is further increased. The higher slope indicates that high soot mass region is going to be formed at relatively high temperatures.

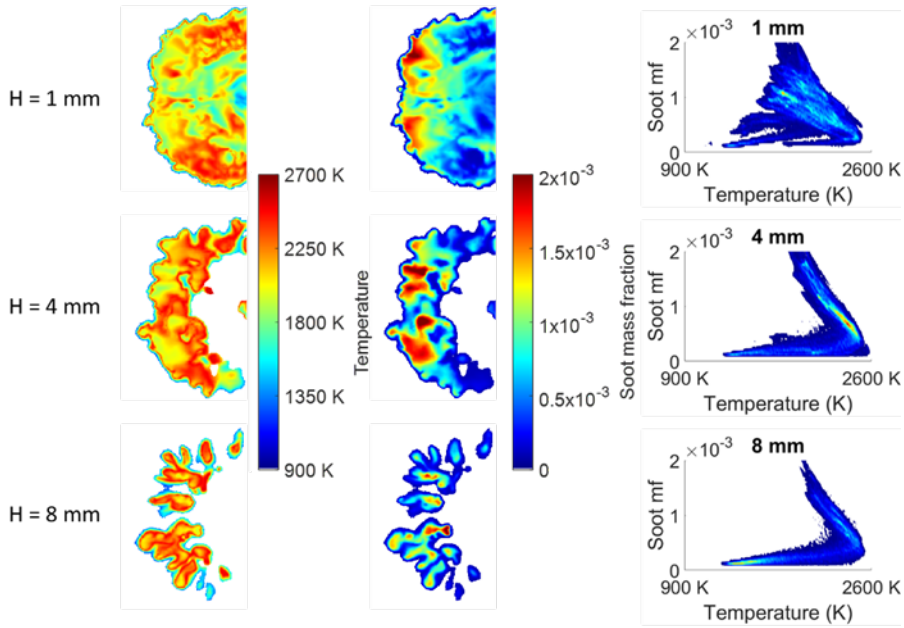

Figure 9.17. The contours of temperature and soot mass fraction at different heights above the plate, AID = 1.5 ms, the 1000 K flame.

From the visualization of the distributions of soot mass fraction and temperature, it could be observed that the temperature and soot quantity have a strong relationship. The high quantity of soot mass is mainly formed at the relatively low-temperature region which is between 1400 and 2000 K. When the height is close to the impinging plate, soot is formed in the whole flame. Dense soot cores start to be observed near the leading edge of the flame. As the height is increased, the soot near the impinging point is disappeared and the area of dense soot cores is increased. After a certain height, e.g., 4 mm, the area of soot formation shrinks compared to the soot formation close to the wall.

9.3 Relationship between quantity of soot and local equivalence ratio

Figure 9.18 shows a scatter plot of the average soot mass versus curvature on the chosen plane for 900 K flame. The plane is 1 mm above the wall. Most scatters reside in the region between -1 mm^{-1} and 1 mm^{-1} where the average soot mass is lower than $0.5*10^{-5}$ µg at

0.5 ms ASI. The highest average soot mass is around $1*10^{-5}$ µg. The minimum average soot mass is close to 0 at 0.5 ms ASI. The relatively small amount of soot mass is because the 0.5 ms ASI is very close to the ignition time (~ 0.36 ms ASI) and soot is not formed at large quantities just after the ignition timing. At the high positive curvature side, the average soot mass is very low which is below $0.1*10^{-5}$ µg. At the high negative curvature side, although some scatter have very low soot mass, scatters with relatively high soot mass ($> 0.5*10^{-5}$ µg) are observed. As time increases to 1.0 ms ASI, the total amount of soot increases significantly. The maximum average soot mass is above $6*10^{-5}$ µg and the minimum average soot mass is around $0.5*10^{-5}$ µg at 1.0 ms ASI.

To investigate the effect of air entrainment on curvature, the scatters in Figure 9.18 are colored by the corresponding local average equivalence ratio. The equivalence ratio is decreased at the flame front where the fuel is consumed. The average equivalence ratio was obtained similarly as the average soot mass, only with a larger square window size of 16 mm^2, to obtain reasonable information. At 0.5 ms ASI, fuel-rich scatters (equivalence ratios > 2) are observed in the concave segments. The scatters located at the left top corner have an equivalence ratio higher than 1.5, producing higher soot mass. The scatters located at the right bottom corner have an equivalence ratio lower than 1.5. At 1.0 ms ASI, the scatters show an inverse 'T' distribution. In the region between ~ 0.5 mm^{-1} and 0.5 mm^{-1}, fuel richer scatters produce a larger quantity of soot mass. In concave segments, scatters with a high equivalence ratio larger than 2 are observed where curvature < -1 mm^{-1}. In convex segments, scatters have a relatively small equivalence ratio around 1 where curvature > 1 mm^{-1}.

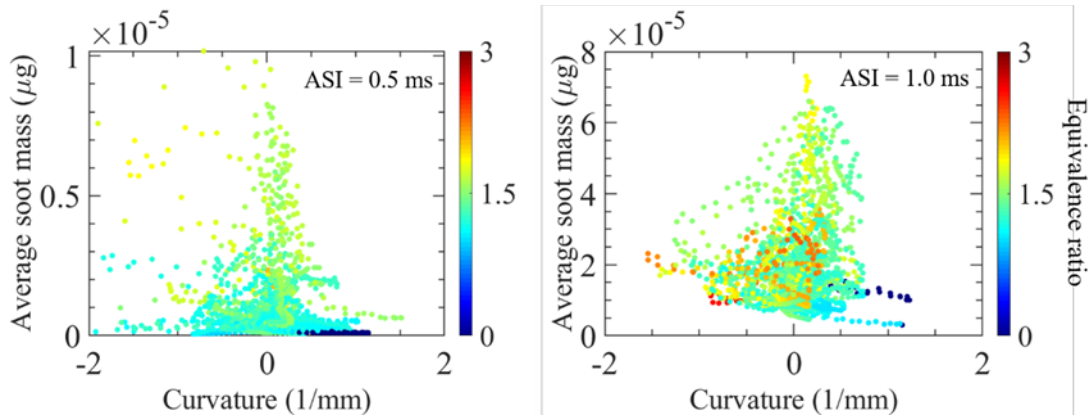

Figure 9.18. Curvature-soot relationship for the 900 K flame.

Figure 9.19 shows scatters of the average soot mass versus curvatures on the chosen plane for 1000 K flame. At 0.5 ms ASI, the maximum average soot mass is around $1.1*10^{-4}$ µg and the minimum average soot mass is around $2*10^{-5}$ µg. At 0.5 ms ASI, by comparing the soot mass between concave and convex segments, it is found that relatively high soot mass is produced in concave segments. At 1.0 ms ASI, the scatter cloud is mainly distributed symmetrically along zero curvature. The distribution of the scatters shows an inverse 'T' pattern. The soot mass production in concave and convex segments is equalized at 1.0 ms ASI.

The scatters in Figure 9.19 are also colored by the corresponding local equivalence ratio. Unlike the scatters under 900 K ambient, scatters with a high equivalence ratio (~3) are observed at 0.5 ms ASI. The reason could be that the vaporization of fuel is enhanced at 1000 K, but the entrained air is still nearly the same quantity without additionally introduced turbulence. More vaporized fuel will increase the local equivalence ratio. Most scatters with a high equivalence ratio are observed near-zero curvature, however, the scatters in concave segments show a higher equivalence ratio compared to that in convex segments. At 1.0 ms ASI, the overall equivalence ratio decreases because of more entrained air during the flame propagation attributed to a larger contact area between ambient and flame.

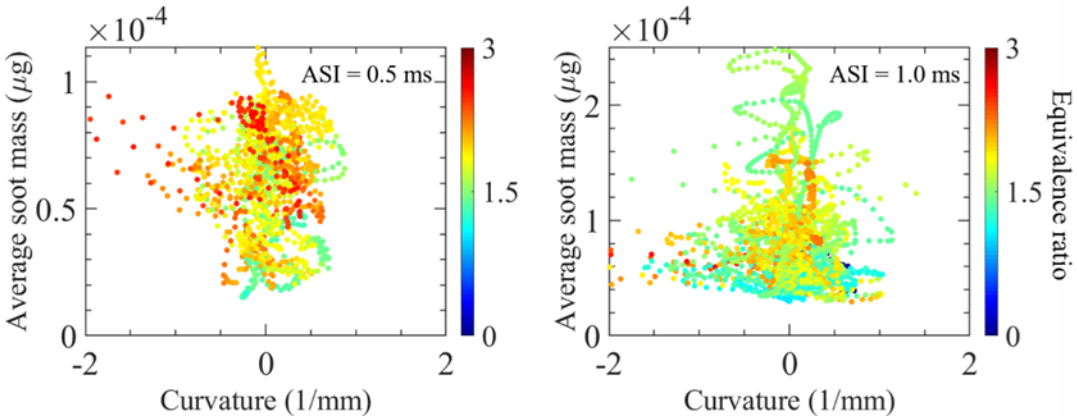

Figure 9.19. Curvature-soot relationship for the 1000 K flame.

10 Film formation on an impinging surface and its relationship with impinging diesel spray combustion[6]

10.1 Film evaporation process without reaction

10.1.1 Film evaporation comparison

The film evaporation test is based on the duration when the film is fully vaporized. From section 3.3.1, a specific optical setup for the vaporization test was adopted and the schematic of the setup is shown in Figure 10.1.

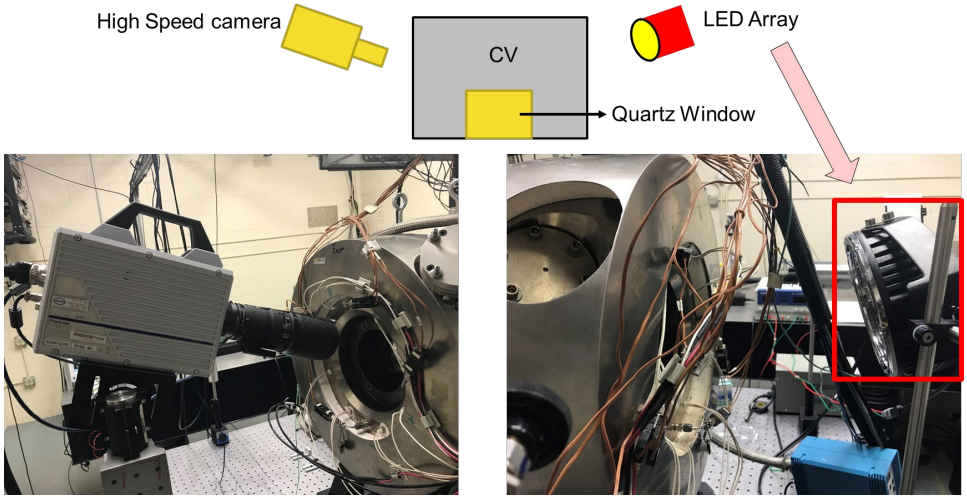

Figure 10.1. Schematic of the optical setup for film vaporization tests.

[6] Reprinted with permission from SAE papers 2021-01-0543 ©2021 SAE International. The materials in this chapter were published in the following paper:

- Zhao, Z., Zhu, X., Zhao, L., Tang, M. et al., "A Numerical Study for the Effect of Liquid Film on Soot Formation of Impinged Spray Combustion," SAE Technical Paper 2021-01-0543, 2021, https://doi.org/10.4271/2021-01-0543.

During the spray impingement on the surface, a liquid film mark will remain on the plate which can be tracked through the boundary tracking method in section 5.1.1. However, the camera looking from the side view (in Figure 10.1) could benefit the precision of boundary tracking by getting rid of the reflection from the bottom view. A diffuser was mounted in front of the LED to provide a uniform light source. A sample of the film area obtained from the side view is shown in Figure 10.2. Due to the tilted angle of the camera, the scale of the x and y-axis is different. Therefore, a 10 mm scale is shown on the background-subtracted film image for both the x and y-axis. From this technique, the film thickness and subsequent film mass can't be quantified but the film area could be obtained. The film area is valuable for quantitatively analyzing the film residence time during the spray event.

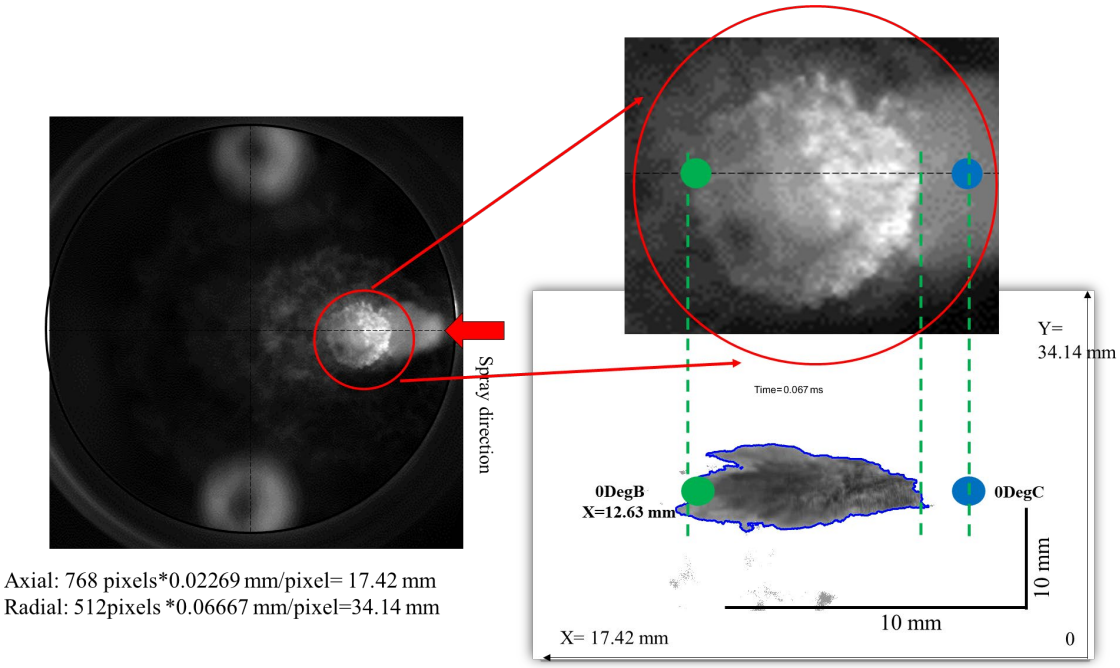

Figure 10.2. A schematic of film area calculation from a tilted side view.

A sample of instantaneous film area is shown in Figure 10.3. The evaporation time is defined as the time between point A when the film shows the maximum area and point B when the film area is decreased to 10% of the maximum area. As can be seen in Figure 10.3, the film area is decreased exponentially, and a exponential curve fitting is applied. The constant and exponential coefficient are 283.6 and -1.8, respectively.

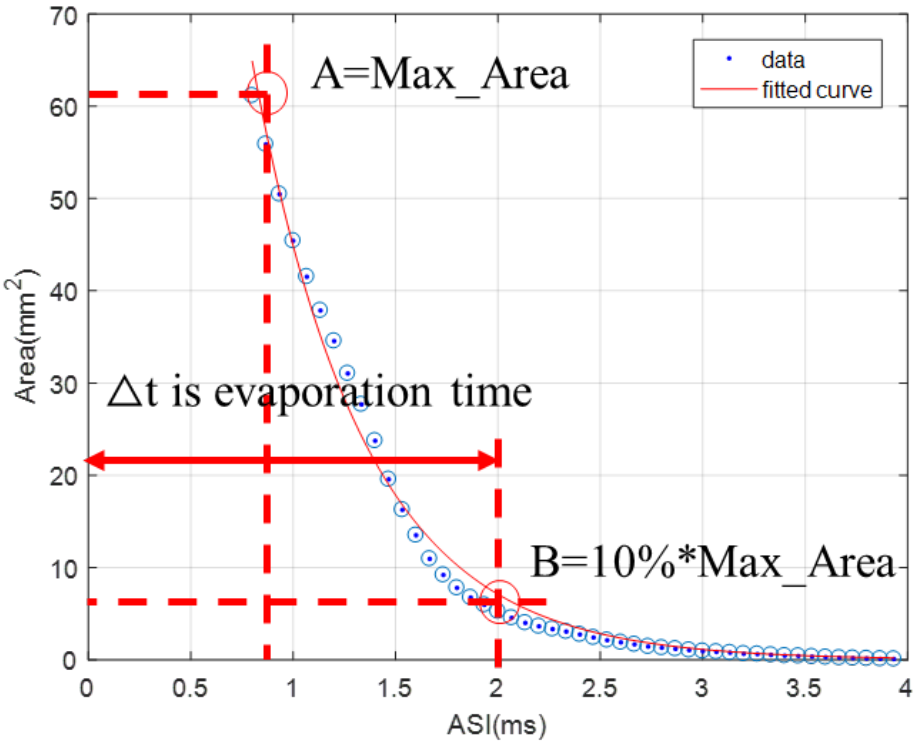

Figure 10.3. A sample of instantaneous film area from the baseline condition.

After that, the effect of ambient density and injection pressure on the vaporization time is shown in Figure 10.4 and Figure 10.5. As the ambient density and injection pressure is increased, the evaporation time is decreased. By increasing the ambient density from 14.8 to 30 kg/m^3, the evaporation time is only reduced ~ 0.3 ms. However, when the injection pressure is increased from 600 to 1200 bar, the evaporation time is reduced to half. Interestingly, it is noted that the mechanism of the film deposition is varied under different ambient densities and injection pressures. Increasing the ambient density and lowering the injection pressure both increases the spray momentum, but the evaporation time is oppositely changed. Under different ambient densities, although the spray momentum is increased but the evaporation time is increased. Under different injection pressures, the evaporation time is increased when the spray momentum is reduced. Therefore, the spray momentum is not the only factor that affect the evaporation time. The film evaporation also takes into account the fuel atomization, mixing, splash and rebound phenomenon.

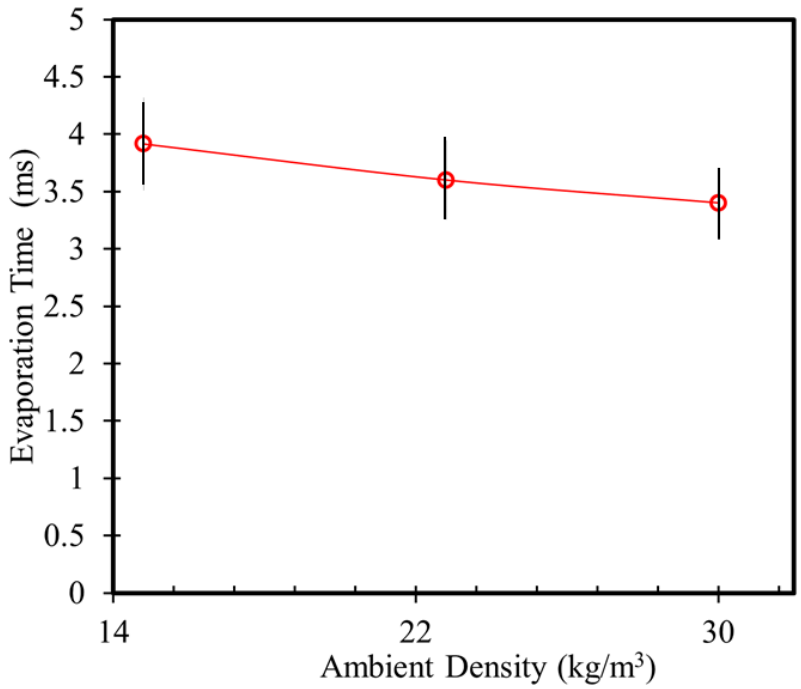

Figure 10.4. The effect of ambient density on the evaporation time of the liquid film.

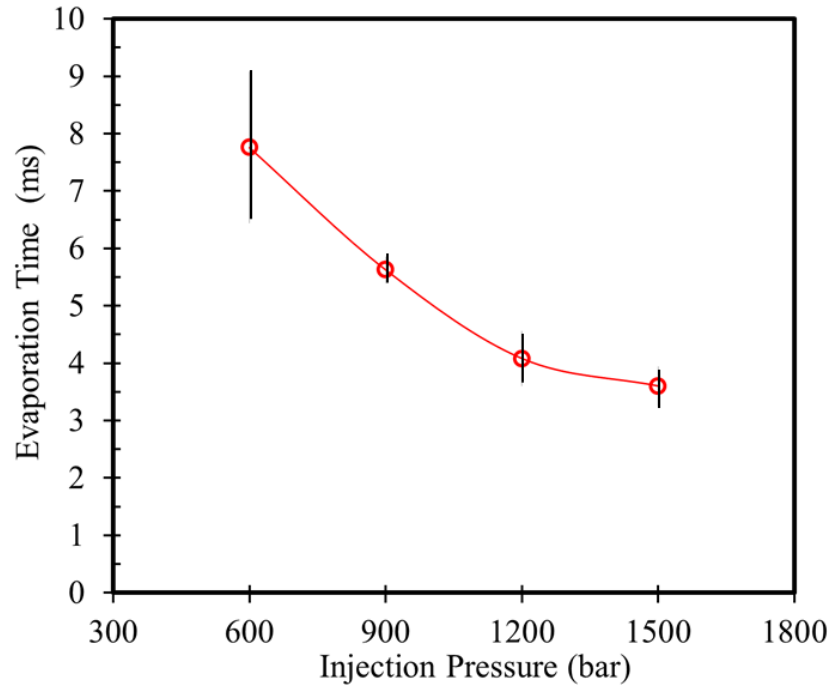

Figure 10.5. The effect of injection pressure on the evaporation time of the liquid film.

10.1.2 Film thickness on a roughened surface

After the calibration for the RIM technique, the single-hole injector with a nozzle diameter of 200 μm was mounted on the combustion vessel and the distance between the injector tip and rough plate is ~ 33.65 mm. N-heptane as the liquid fuel was injected on the rough flat surface at various ambient and injection conditions. The ambient temperature is 423 K which is the same as the rough surface temperature, and the fuel temperature is 363 K. All other test conditions are the same as the single-hole injector test conditions. Film thickness is calculated based on the above calibration result and a small area (2*2 mm^2) near the impinging point is selected for film thickness calculation. The film thickness at each condition is averaged from five repeats.

The effects of ambient density and injection pressure on film thickness as a function of impinging time are shown in Figure 10.6 and Figure 10.7. The actual fuel injection is terminated at 2.5 ms ASOI and the mist which hinders the signal capturing exists until 4.6 ms. Therefore, data is analyzed after 4.6 ms until the complete vaporization of film. The complete film vaporization occurs under 20 ms ASOI. Generally, the film thickness decreases with ambient density and injection pressure and the thickness range is from 0.5 to 1.2 μm.

For the film thickness measurements, each test is based on at least 3 repeats. Film mass, film area and averaged film thickness are all decrease after the end of impinging due to the evaporation. However, all the film properties are showing some extended decreases. As shown in Figure 10.6, the film properties increase with a decrease of ambient density due to the fact that higher ambient density causes enhanced fuel atomization and air entrainment.

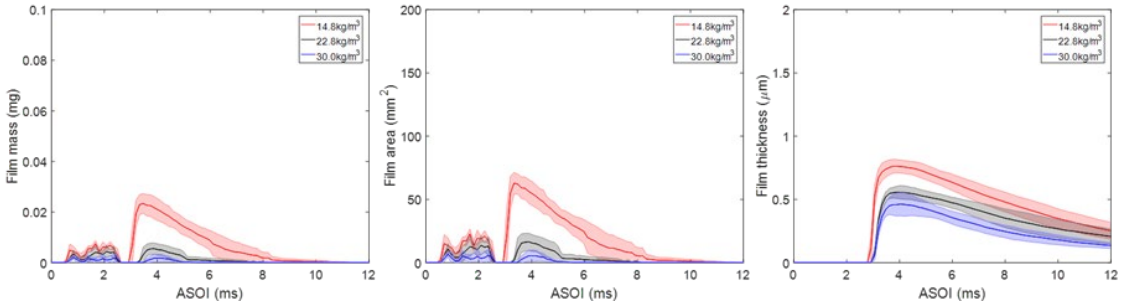

Figure 10.6. Effect of ambient density on film properties: film mass, film area, and film thickness.

As shown in Figure 10.7, The film properties increase with a decrease of injection pressure because higher injection pressure causes enhanced fuel atomization and air entrainment. Relatively lower spray momentum makes the liquid easier to wet the wall and become a film.

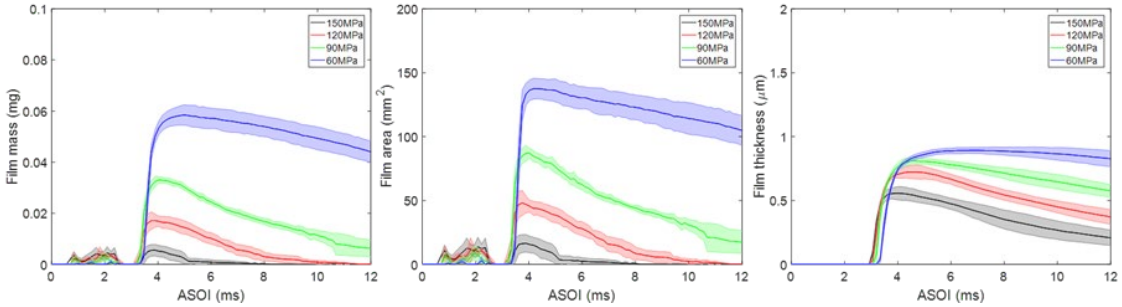

Figure 10.7. Effect of injection pressure on film properties: film mass, film area, and film thickness.

10.2 Film formation from simulations and its impact on flame and soot formation

10.2.1 Film area and thickness of different ambient temperatures

The global deposited film mass and formed soot mass could not present the local intensive regions of film and soot formation of an impinging spray. Two local parameters, film thickness and soot mass fraction, could indicate where the film is relatively thicker or

thinner and soot is intensively formed. Hence, local distributions of film thickness, temperature and soot mass fraction close to the impinging surface will be discussed in the following sections.

The film thickness at different time stamps and ambient temperatures are shown in Figure 10.8. A 20 mm- length scale, location of the impinging point, and the spray expansion directions after the impingement are presented in Figure 10.8, the 800 K case at 1ms ASOI. For the 800 K case, the film is observed after the impingement and it is not fully vaporized before 4 ms ASOI, i.e., the end of simulation time. From Figure 10.8, the film is observed radially around the impinging point but mainly formed in the downstream direction. Before the end of injection, there is an intensive spot at the impinging point which could be seen at 1 and 2 ms ASOI at an ambient temperature of 800 K. After the end of the injection, the intensive spot is evaporated but the downstream film is still observed which shows several intensive film rings radially. The distribution is similar, but the film thickness is reduced at 4 ms ASOI compared to it at 3 ms ASOI. For the 900 K case, the shape of the distribution is similar to it at 1 ms ASOI at 800 K. The intensive spot is also observed near the impinging point and a single intensive ring is formed at the leading edge of the film region. As time is increased, the intensive ring becomes several rings, showing a pattern of different waves after the impingement. However, the local film thickness and overall film area are lower at the 900 K case compared to the 800 K case. For the 1000 K case, the film is only clearly observed at 0.4 ms ASOI which is just after the impingement. The film is soon fully vaporized due to shorter ignition delay and higher ambient temperature. Thus, the film is barely observed at 0.8 and 1 ms ASOI.

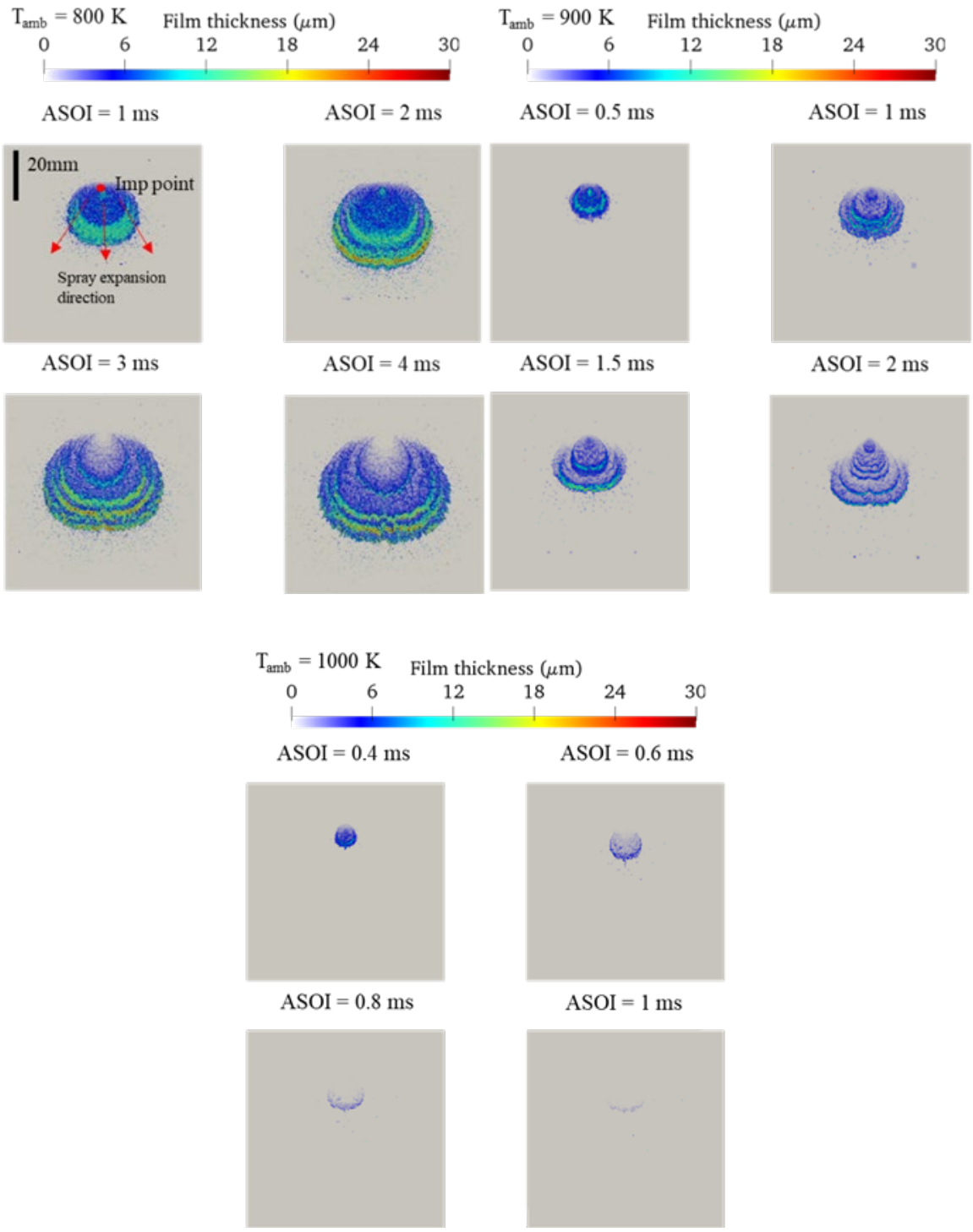

Figure 10.8. Film thickness distributions on the impinging plate. Test conditions: P_{inj} = 1500 bar, ρ_{amb} = 22.8 kg/m^3, O_2 = 18%, impinging distance = 30 mm.

The temperature distributions are shown in Figure 10.9. The target plane is chosen 0.25 mm (one minimum cell height) above the impinging surface. By comparing the film thickness in Figure 10.8 and temperature distributions at 3 and 4 ms ASOI for the 800 K case, a temperature transition region is found between the film leading edge and flame initiation region. The temperature in the transition region is reduced due to film evaporation.

Two wings of high-temperature cores are merged into one region with a low temperature in the middle and a high temperature at the two sides. The boundary of the high-temperature region is smooth before the evaporation of the film. At 2.5 ms ASOI, the liquid film is evaporating so that a non-smooth boundary in the transition region (perturbed region in Figure 10.9) is observed. The temperature is decreased because the film vaporization obtains the heat from the high-temperature spray. At 3 ms ASOI, the film is fully evaporated, and the boundary of the high-temperature region becomes smooth again. For the 1000 K case, the temperature distributions show the recession, but the film effect is not significant on the temperature distribution because the film is already fully evaporated before 1 ms ASOI. However, even the film is fully evaporated after 1 ms ASOI, the film region is too rich to burn, leading to a low-temperature region observed near the original film region at 2 ms ASOI for the 1000 K case.

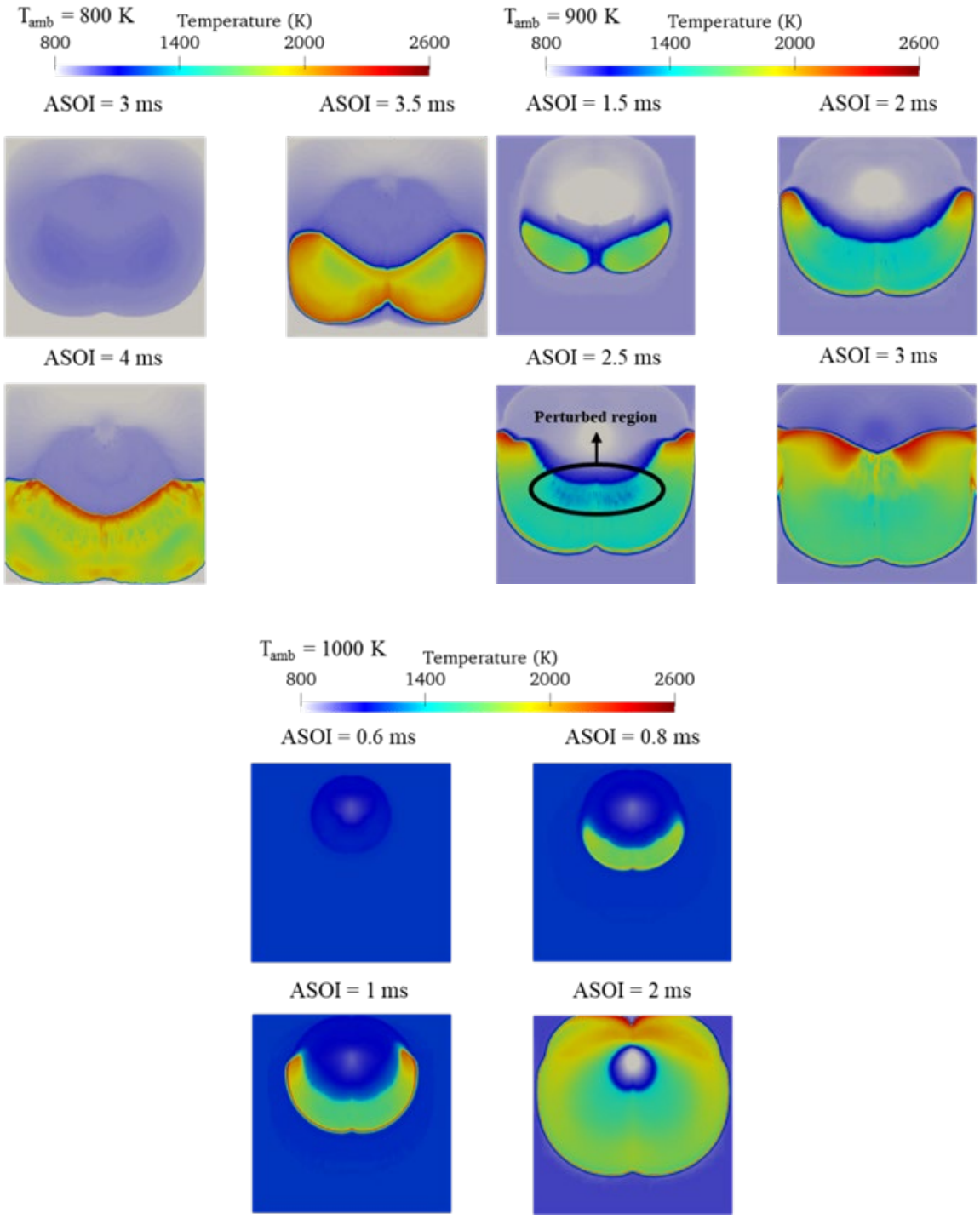

Figure 10.9. Temperature distributions on the impinging plate. Test conditions: P_{inj} = 1500 bar, ρ_{amb} = 22.8 kg/m^3, O_2 = 18%, impinging distance = 30 mm.

After discussing film thickness distributions, the distributions of soot mass fraction are discussed. The soot mass fractions which are 0.25 mm above the impinging surface are shown in Figure 10.10. It is noted that the scale of soot mass fraction of 800 K is lower than other temperatures. By comparing the temperatures in Figure 10.9 and soot distributions, the soot is formed in the medium temperature range which is ~ between 1400 to 2000 K. All cases show the intensive soot region in the downstream with a wing shape. As time is increased, the soot occupied region is propagating from the leading edge of the flame back to the impinging point side. However, the film region slows the soot growth back to the impinging point region, forming a transition region between the soot-occupied region and film leading edge. Compared to the distribution at 3.5 and 4 ms ASOI of the 800 K case, the location of soot formation near to the plate is nearly the same and there is no soot formed near the impinging point. This is because the impinging region is occupied by the liquid film, and it is too rich to burn. For the 900 K case, the pattern observed from the 800 K case is still observed. Due to less film deposition and faster film evaporation, the soot region starts to grow back to the impinging point at 3 ms ASOI. This is clearly seen at 3 ms ASOI where the boundary of the soot region is not uniform and perturbed by the film evaporation in the transition region. For the 1000 K case, the film is nearly totally evaporated after 0.6 ms ASOI. Due to the unburnt fuel near the film region, soot is not observed near the impinging region.

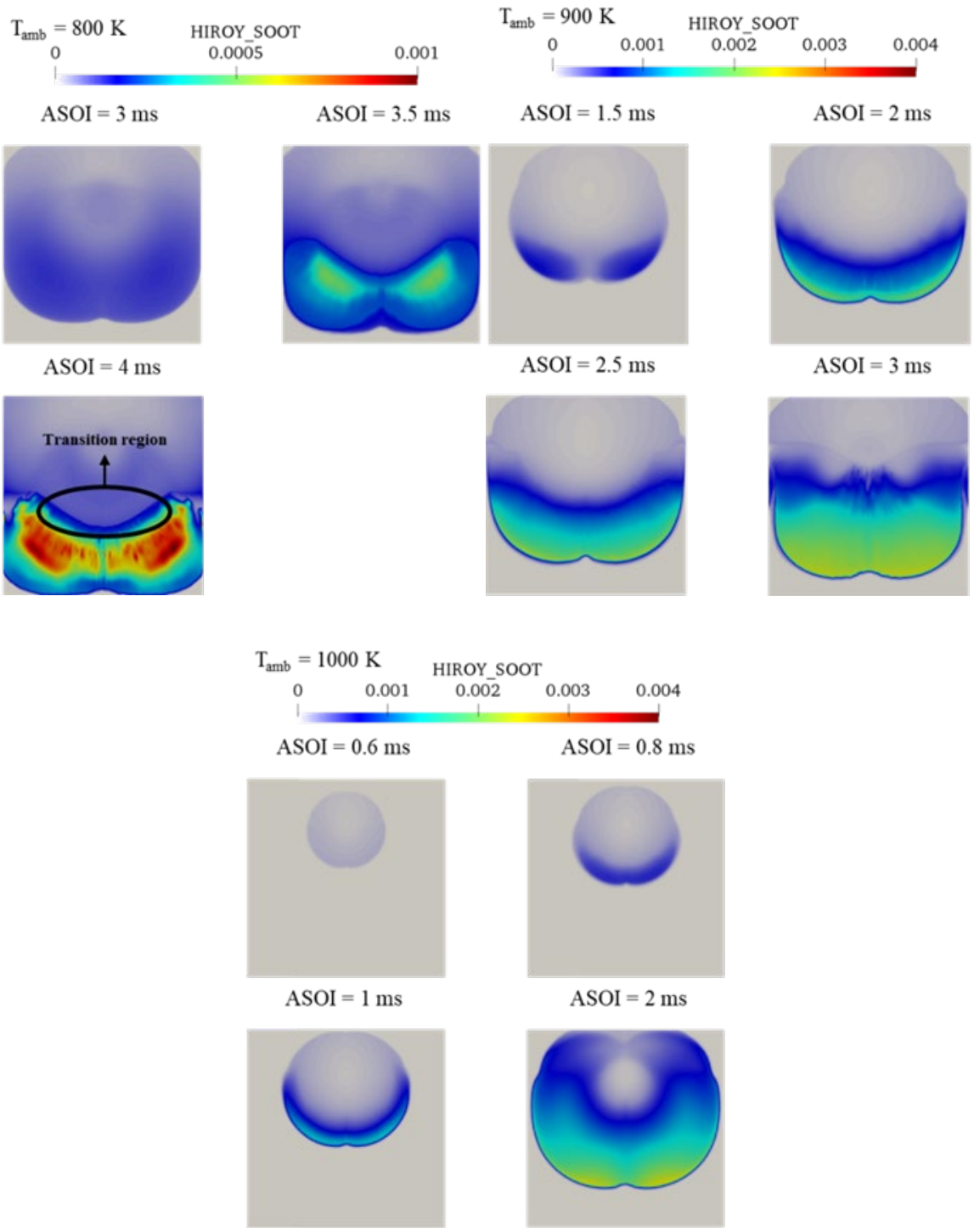

Figure 10.10. Soot mass fraction distributions on the impinging plate. Test conditions: P_{inj} = 1500 bar, ρ_{amb} = 22.8 kg/m^3, O_2 = 18%, impinging distance = 30 mm.

10.2.2 Film area and thickness of different impinging distances

Two different impinging distances are used to discuss the effect of the impinging distance on film deposition and soot formation. The deposited film mass and formed soot mass in the chamber at 30- and 40-mm impinging distances for the 800 K case are shown in Figure 10.11. As can be seen in the film mass profiles, the deposited film mass is significantly reduced when the impinging distance is increased to 40 mm. The reason is that a longer impinging distance will reduce the opportunity of liquid spray contact on the impinging surface, especially when the liquid length is close to the impinging distance. However, meanwhile, the formed soot in the chamber is increased when the impinging distance is higher. This is because the film is fully vaporized in the chamber and involved in flame. The fuel mass in the chamber could be calculated by subtracting the film mass from the total injected mass. By comparing the ratio of formed soot and fuel mass in the chamber, a longer impinging distance leads to a higher ratio of vapor fuel, subsequently higher soot production.

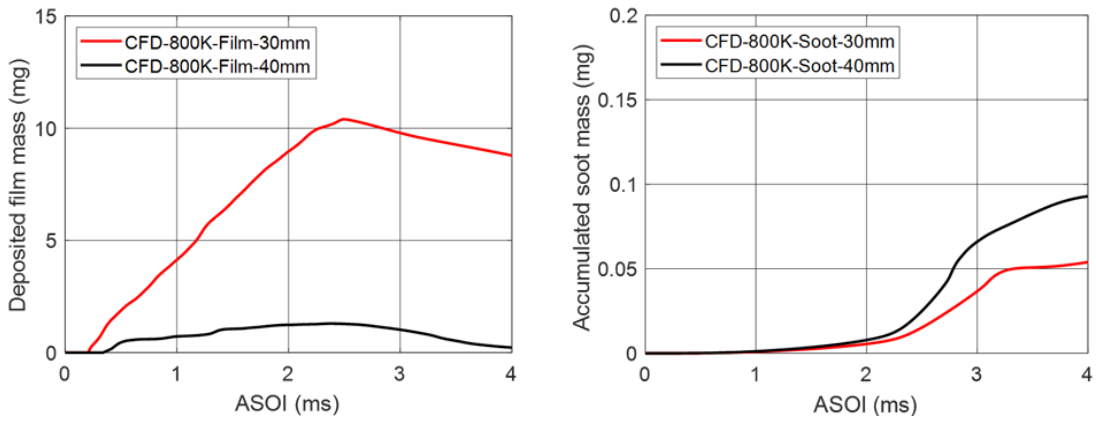

Figure 10.11. Total deposited film and formed soot mass at different impinging distance. Test conditions: P_{inj} = 1500 bar, ρ_{amb} = 22.8 kg/m^3, O_2 = 18%, T_{amb} = 800 K.

The film thickness distributions at 40 mm impinging distance under 800 K is shown in Figure 10.12. Film thicknesses at four timestamps, 1, 1.5, 2, and 2.5 ms ASOI are shown to explain the film deposition when the impinging distance is longer. At 1 ms ASOI, the film thickness is nearly evenly distributed around the impinging point. The intensive spot

near the impinging point observed from the 30 mm impinging distance case no longer exists. At 2 ms ASOI, even the intensive spot is still not observed, but a relatively thicker ring is observed at the film leading edge because of the continuous film deposition from different impinging waves. However, the single ring shows local thinner film thickness, compared to the 30 mm impinging distance case. After 2 ms ASOI, the local film thickness is also reduced due to the film evaporation.

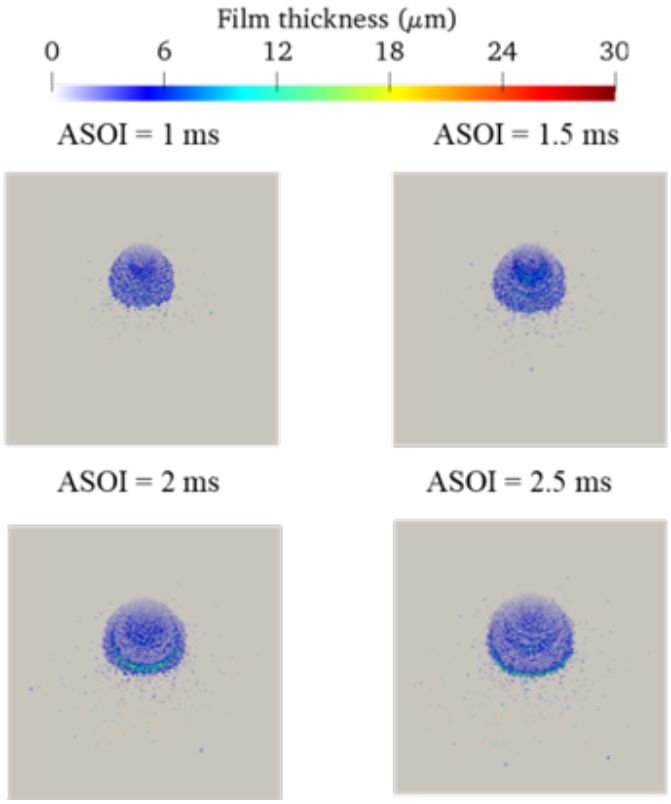

Figure 10.12. Film thickness distributions on the impinging distance at impinging distance of 40 mm. Test conditions: P_{inj} = 1500 bar, ρ_{amb} = 22.8 kg/m^3, O_2 = 18%, T_{amb} = 800 K.

10.2.3 Film area and thickness of different oxygen concentration

From previous sections, it is concluded that higher ambient temperature and longer impinging distance could directly reduce the deposited film mass. Higher ambient temperature could not only directly promote the film evaporation but also shorter the

ignition delay, subsequently enhancing the film evaporation through the film-flame interaction. To discuss the effect of the ignition delay individually on the film evaporation, the ambient temperature is maintained at 900 K case but the oxygen level is increased to 21% to shorter the ignition delay. Therefore, the ambient temperature won't affect the film evaporation before the ignition delay and the effect of ignition delay could be discussed independently.

The deposited film mass and formed soot mass in the chamber at different oxygen levels are shown in Figure 10.13. As can be seen in the film mass profiles, the deposited film mass between 18% and 21% O_2 cases is nearly the same before the ignition delay. This is because the ambient temperature is the same, leading to a similar film evaporation rate before the ignition delay. The film mass starts to be generally reduced after ~ 1.5 ms ASOI. The profile shape is also nearly the same between different oxygen levels. The peaks and valleys are also matched at the same time with the rate of injection. 21% O_2 case has higher soot production between 1 to 3 ms ASOI but lower soot production after ~ 3 ms ASOI. This could be because the oxidation is stronger in a 21% O_2 environment after the end of the injection.

The film thickness distributions of different oxygen levels are shown in Figure 10.14. The same time stamps are used to make a direct comparison of film thickness between 18% and 21% oxygen cases. Echoing the film thickness of 18% O_2 in Figure 10.8, the shape of film thickness distribution is almost identical between 18% and 21% O_2 cases before 1 ms ASOI with the same ambient temperature, 900 K. After the ignition delay, early formed flame and higher temperature from 21% O_2 environment leads to local lower film thickness at the same given time. This could be observed from film thickness distribution at 1.5 and 2 ms ASOI.

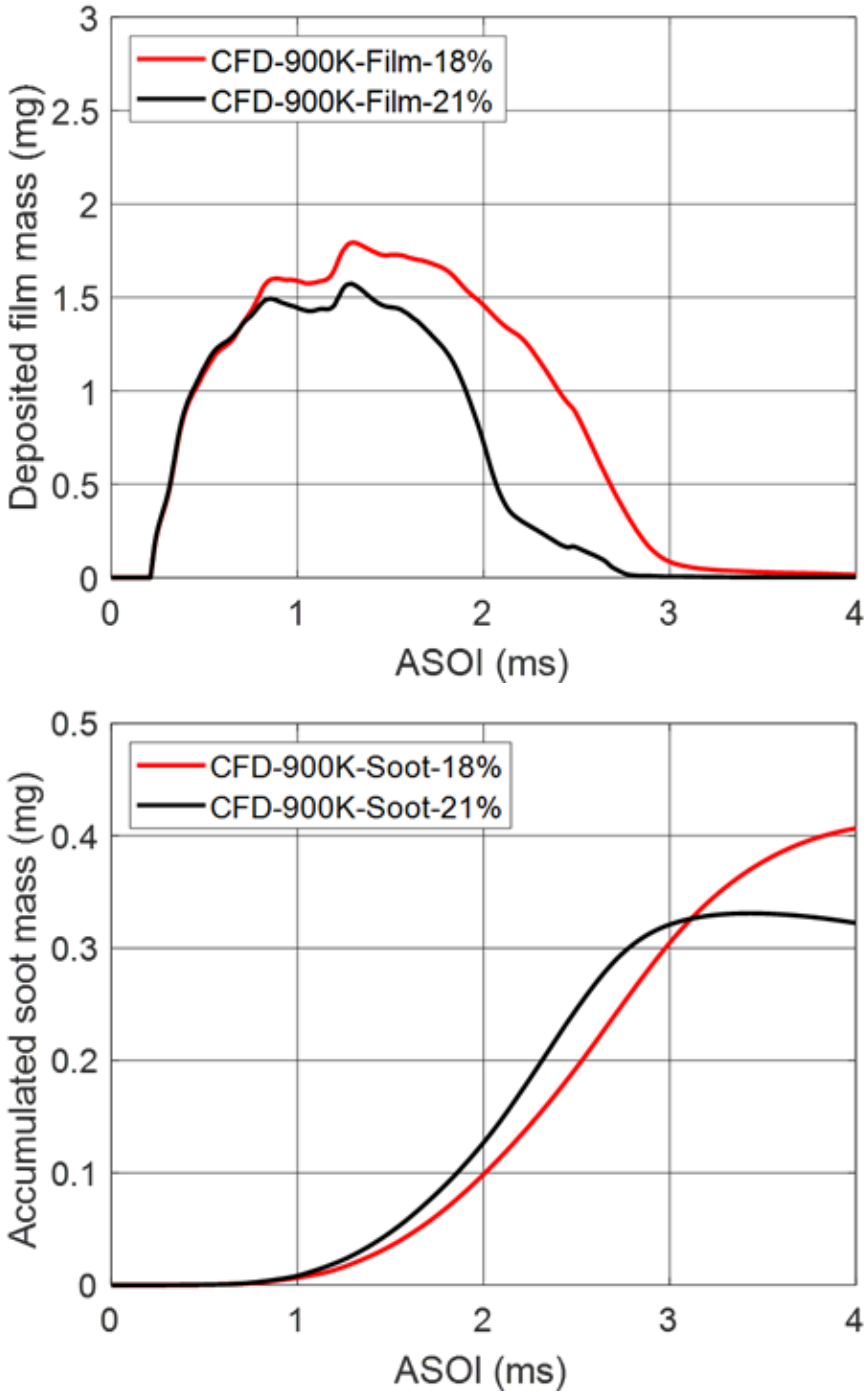

Figure 10.13. Total deposited film and formed soot mass at different oxygen concentration. Test conditions: P_{inj} = 1500 bar, ρ_{amb} = 22.8 kg/m^3, T_{amb} = 900 K, impinging distance = 30 mm.

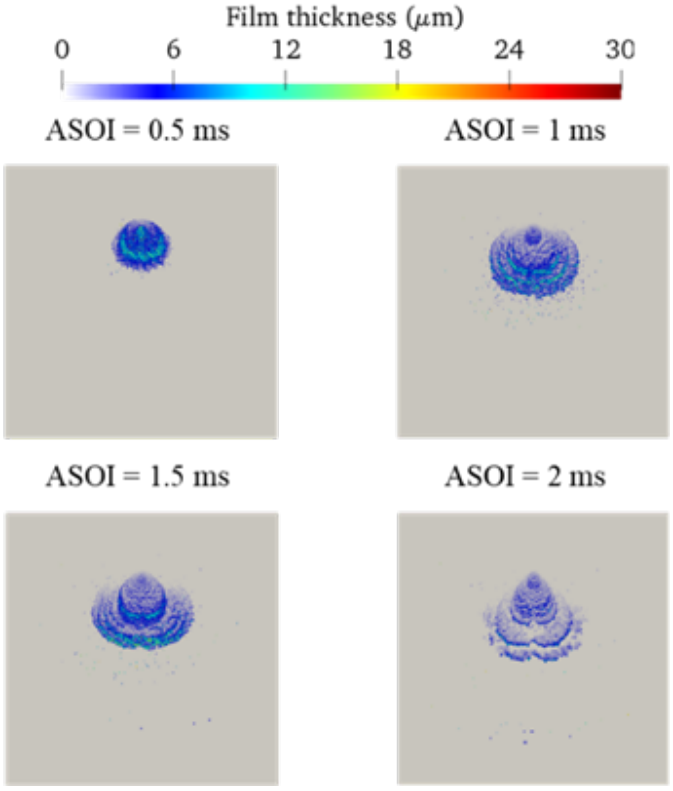

Figure 10.14. Film thickness distributions on the impinging distance at 21% oxygen concentration. Test conditions: P_{inj} = 1500 bar, ρ_{amb} = 22.8 kg/m^3, T_{amb} = 900 K, impinging distance = 30 mm.

10.2.4 Impact of film formation on impinging diesel spray combustion

After validating the spray and the combustion models, the effects of ambient temperatures on the film deposition and soot formation are presented. The profiles of deposited film mass on the plate under different ambient temperatures are shown in Figure 10.15. The profile of total injected fuel mass is also shown in the same figure for comparison. The total injected fuel mass is saturated after ~ 2.4 ms ASOI as the actual injection is ~ 2.4 ms. After 0.2 ms ASOI, the spray impinges on the plate and the liquid film starts to be deposited at an impinging distance of 30 mm. The rate of total film mass is a combination of the rate of film deposition and film evaporation. If the film deposition is faster than its evaporation, the deposited film mass is increased. Under different ambient temperatures, the film mass

at a given ASOI is always higher at a lower ambient temperature. At a high ambient temperature such as 1000 K, the deposited film mass is a very small amount which is lower than ~1% of the total injected fuel mass. At an ambient temperature of 800 K, the deposited film mass keeps increasing until 2.5 ms ASOI and starts to be reduced afterward. It is observed that the film starts to evaporate immediately after the ignition delay in the 800 K case. However, for the 900 K case, film evaporation starts 0.6 ms later after the ignition delay. This is because that the spray is still impinging to deposit the film when the ignition starts at 900 K case while the spray is almost ended when the ignition starts at 800 K case. Thus, it is concluded that the film deposition takes the domination over the film evaporation when the spray is still coming which makes the film evaporation less effective on the deposited film mass before the end of the injection. At the ambient temperature of 1000 K, the ignition delay is further reduced and there is much less opportunity for film deposition as the fuel spray is vaporized and ignited immediately after the start of the injection.

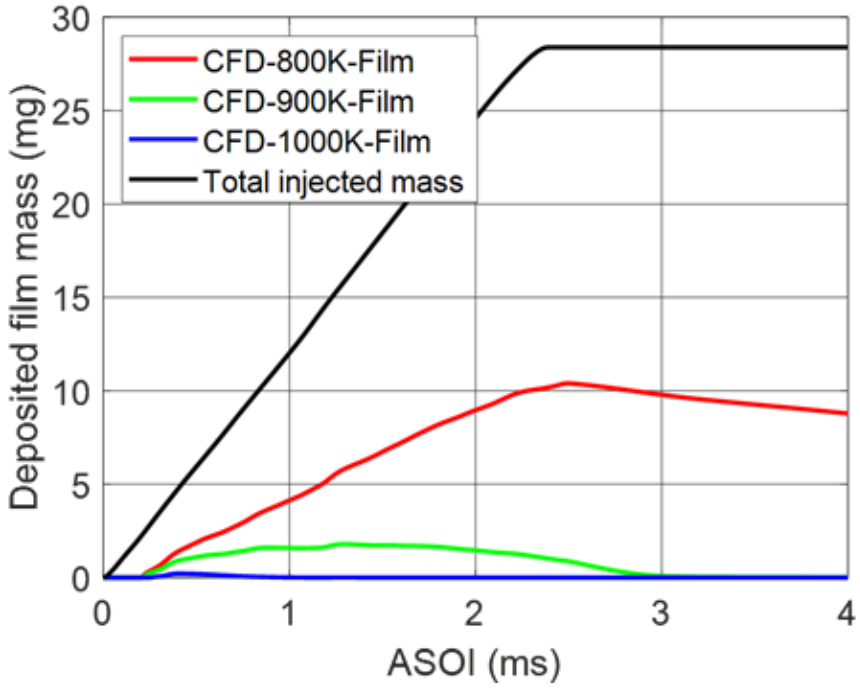

Figure 10.15. Total deposited film mass on the plate. Test conditions: P_{inj} = 1500 bar, ρ_{amb} = 22.8 kg/m^3, O_2 = 18%, impinging distance = 30 mm.

After discussing the deposited film mass at different ambient temperatures, the total soot mass formed in the simulation domain is compared between different ambient temperatures. The results of soot outcomes at different ambient temperatures are shown in Figure 10.16. After the ignition delay, higher ambient temperature leads to higher soot production in the chamber. For the 1000 K case, it is noted that faster soot oxidation than soot formation is observed after ~ 3 ms ASOI as the total soot mass is reduced. However, the profile at an ambient temperature of 800 K shows a different trend because the ignition delay is close to the end of the injection. The late combustion process was not influenced by the spray process for the 800 K case. Soot quantity is nearly unchanged after ~ 3.2 ms ASOI.

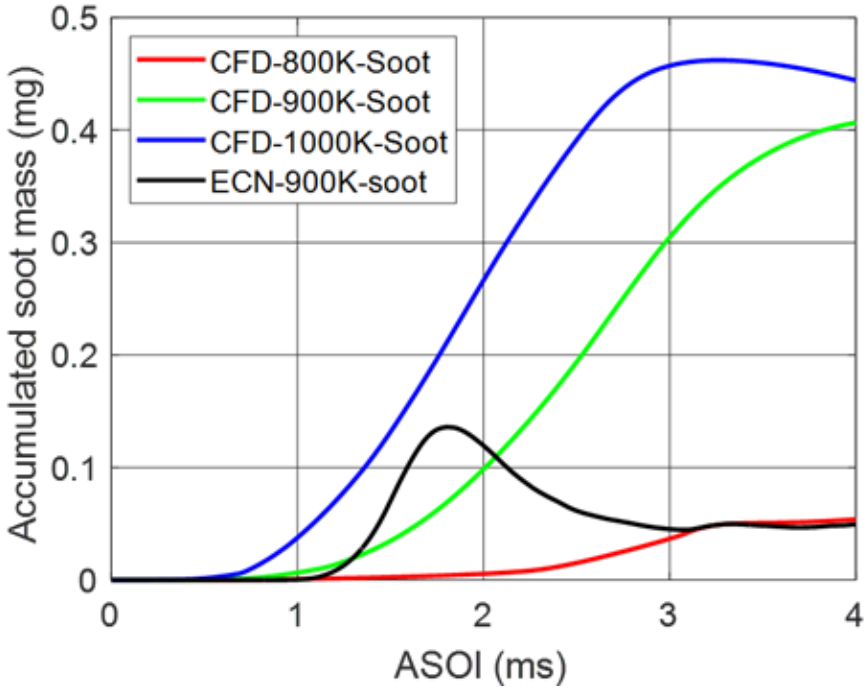

Figure 10.16. Total formed soot mass in the simulated domain. Test conditions: P_{inj} = 1500 bar, ρ_{amb} = 22.8 kg/m^3, O_2 = 18%, impinging distance = 30 mm.

In order to compare the soot formation between an impinging spray and a free spray, soot profile of a free spray from the ECN database [81] with the same nozzle size (200 µm), injection pressure (1500 bar), ambient temperature (900 K) and density (22.8 kg/m^3) but

different oxygen level (15%) and n-dodecane as the fuel was adopted. Due to different oxygen levels and different injection specs, only a qualitative comparison will be performed. After the flame initiation, soot starts to be formed for both experiments and simulations. However, the trend of total soot mass is different between ECN results and simulations. In ECN results, soot mass firstly increases then decreases to a steady state. In the simulations, soot mass is keeping increasing but shows a slower formation rate than ECN results between 1.2 to 2 ms ASOI. This is because the amount of vaporized fuel of the impinging case is reduced due to the film deposition and thus less fuel is involved in the flame. After ~ 1.5 ms ASOI, the film in the impinging spray starts to be evaporated and more fuel is vaporized to involve in the flame. In order to present the relation between film deposition and soot formation, the profiles of film deposition rate and soot formation rate of the 900 K case from simulations are shown in Figure 10.17. The positive and negative film deposition rates indicate film deposition and evaporation, respectively. Globally the film deposition rate is decreased and shifted from film deposition to film evaporation while the soot formation rate is always increased before ~ 2.6 ms ASOI. The film evaporation rate and soot formation rate are matching the maximum at ~ 2.6 ms ASOI. This could confirm that when more fuel is vaporized from the film into vapor to lead to local fuel-rich zones, the soot formation rate is increased. After ~ 2.6 ms ASOI, the injection is ended and thus both film evaporation rate and soot formation rate are reduced because there is no fuel coming anymore.

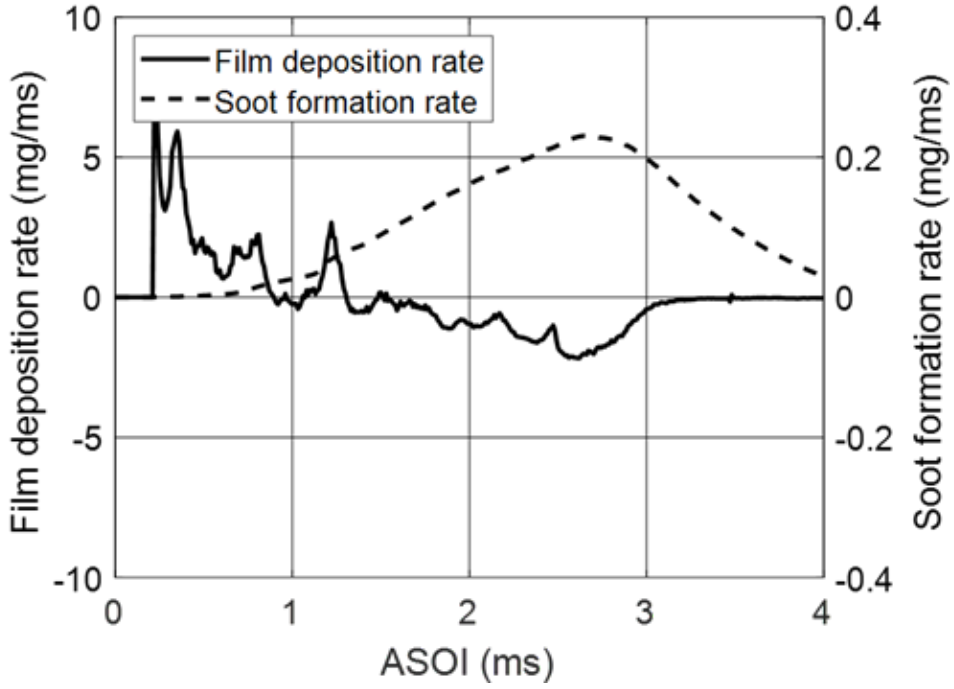

Figure 10.17. The rates of film deposition and soot formation from simulations. Test conditions: P_{inj} = 1500 bar, ρ_{amb} = 22.8 kg/m^3, O_2 = 18%, impinging distance = 30 mm, T_{amb} = 900 K.

11 Conclusion and future work

11.1 Main findings

In the current study, the characteristics of a diesel impinging spray are evaluated from both non-vaporizing and reacting conditions under various parameters such as injection pressure, ambient density, ambient composition, and impinging distances. Furthermore, the soot formation in an impinging spray is evaluated in both experiments and simulations. The experimental work was done in a constant volume combustion chamber at Michigan Technological University with various optical diagnostics. For the numerical study, a commercial CFD software CONVERGE© is used to simulate the spray and combustion behavior for an impinging spray. Both RANS and LES turbulence models are applied for different purposes. The results identify the global spray and flame structure of an impinging spray, the boundary structure of the flame with local soot, the heat loss during the spray-wall interaction, film formation, and its interaction with flame. The conclusions which can be derived from the present work are summarized as follows:

11.1.1 Macroscopic flame structure

- As the ambient temperature is increased, flame luminosity is observed before the impingement and further above the plate, i.e., 900 K and 1000 K. For the high-temperature conditions, the flames appear before the impingement and impact on the plate with radially spreading. However, the flame at 800 K appears at the front side, far away from the impinging point, and recess towards the impinging point.

- The flame expansion rate is governed by the spray momentum (injection pressure and ambient density). The low ambient temperature only reduces the flame expansion rate at the early stage of combustion after spray impingement. On contrary, the ambient temperature doesn't show significant effects on flame expansion rate in a later stage of combustion.

- At T_{amb} of 1000 K and 900 K, the flame expansion rate follows the stages after the impingement similarly defined from the non-vaporizing conditions: 1) rapid deceleration; 2) slow deceleration; 3) constant expansion rate.

- Due to the increased ratio of axial to the radial flame front, fuel vapor is possible to be transported towards the top of the leading edge of the axial direction, generating a soot-rich zone during the combustion event. A very intensive soot region is observed at the leading edge of the axial direction.

- With the help of the IRT method, the most intensive soot luminosity region and Mie scattering signal region are located along the impinged spray axial direction. Comparing the IRT plots for the non-vaporizing and reacting conditions, the most intensive soot region is formed in the axial direction which is mainly due to the fuel accumulation in the axial direction, forming a fuel-rich zone. Local temporal outmost boundaries of flame are found to have wrinkles attributed to air entrainment.

- Lowering oxygen percentage reduces the temporal soot generation before the end of injection. However, soot generation becomes high at low oxygen percentage when the left-over fuel is consumed after the end of injection.

11.1.2 Microscopic flame structure

- The profiles of curvature distribution are nearly similar after the impingement for both non-vaporizing and reacting conditions. However, the hot combustion gas is easier, compared to the liquid fuel, to be entrained by ambient gas, making the increment of wrinkles in reacting conditions. The correlation of the boundary curvature and near-field soot formation demonstrates an inverted ‘S’ shape distribution with time. More soot is formed in concave regions while less soot is formed in convex regions.

- From the analysis of impinged flame front curvature, the two evaluated ambient temperatures (900 K and 1000 K) show the unnoticeable influences on the curvature distribution, implicitly the same level of flame-air mixing rate. This indicates, to some extent, a similar level of induced turbulence via flame impacting.

- LES simulation results showed good agreements in global spray combustion characteristics, such as liquid length and ignition delay, as well as the transient local spray/flame structure after the impingement by comparing the curvature distribution of the flame boundary. These findings indicate that the spray models could well predict the propagation behavior after the impingement.

- From the curvature profiles, the curvatures of concave and convex regions are nearly paired with each other. As the ambient temperature is increased, a more violent flame makes the flame boundary more wrinkled.

11.1.3 The apparent heat release rate and heat flux

- From the analysis of heat release rate, lowering ambient temperature delays the auto-ignition, allowing more time for fuel to vaporize and mix with air, leading to the extended duration of premixed combustion.

- Peak heat flux is observed near the impinging point and the difference of local heat flux is mainly due to the difference between flame and surface temperatures when the flame development is identical. However, local heat flux is much lower attributed to the soot radiation when there is much less soot formed at lower temperature flame.

11.1.4 Soot formation in an impinging spray

- With the current arrangement of the injection, more fuel would like to be dumped towards the front side of the impinging point, which will lead to higher soot mass fraction at the leading edge compared to the impinging region.

- The oxidation close to the wall is weaker than the top surface as the ambient gas is hard to entrain to pass the flame to the wall side. Also, the temperature is reduced and seated into the range of soot formation due to the heat transfer from the flame to the wall.

- As the residence time was increased, it was observed that the soot near the impinging plate and leading-edge is continuously accumulated.

- From the wall to the ambient, total soot mass on a horizontal plane is increased to the maximum then decreased. Soot is initially formed near the wall and carried by the vortex at the leading edge to an upper altitude. When the soot is moved near the oxidation layer, the total soot mass is reduced due to soot oxidation.

- The soot precursor is mainly formed near the wall and converted to soot at the leading edge. After the end of the injection, the soot mass near the wall is reduced as there is no supply for the fuel-air mixture. However, the remaining fuel in the chamber is carried by the vortex and continuously forms soot at higher heights.

11.1.5 Film formation and its interaction with flame

- Under the same impinging distance, higher ambient temperature leads to a thinner film. The relation between the film mass and ambient temperature is not linear. The film mass under an ambient temperature of 800 K is nearly 40% to 50% of the injected fuel mass while the film mass is only ~10% and 1% of the total injected mass under an ambient temperature of 900 K and 1000 K, respectively.

- The film deposition rate is globally decreased before the end of the injection. Along with the decreased film deposition, the soot formation rate is globally increased before the end of the injection. According to the distributions of temperature, the temperature near the film region shows a lower value due to the film evaporation into the flame. A temperature transition region is observed between the flame and film leading edge where the temperature is relatively low.

- Different impinging distances lead to different film patterns on the impinging surface. Under 30 mm impinging distance, the film shows a waving pattern with high film thickness at the leading edge of the film. An intensive film spot is also observed near the impinging point under 30 mm impinging distance. 40 mm impinging distance could significantly reduce the global film mass and local film thickness compared to the 30 mm impinging distance case. The intensive film spot near the impinging point no longer exists. Only a single ring with high film thickness is observed at the leading edge of the film under 40 mm impinging distance.

- Under the same ambient temperature but with different oxygen levels, the film formation and evaporation are nearly identical before the ignition delay. Due to the high oxygen level, 21% oxygen case shows an early ignition delay. The higher flame temperature generated by a high oxygen level environment leads to lower global film mass and local film thickness.

11.2 Future work

The remaining goals for the current study are:

- The surface curvature in the 3D domain will be obtained and the soot oxidation rate along the surface will be correlated with the surface curvature.
- The film-flame interaction for diesel spray will be experimentally investigated. A specific optical technology may be developed to capture the film, flame simultaneously and the quantitative measurement for the film thickness can be achieved.
- The low-temperature combustion mechanism which considers the quenching effect when the flame touches the hard surface will be developed.

Based on future work, the current thesis will be an indicator for the direction of further investigation for diesel impinging spray with combustion.

12 Reference List

[1] EIA (Energy Information Administration), U.S. energy flow, U.S. Energy Inf. Adm. (2017) 1–234. https://www.eia.gov/totalenergy/data/monthly/pdf/flow/total_energy.pdf%0Ahttp://large.stanford.edu/courses/2018/ph241/green1/docs/doe-eia-0035-2018-4.pdf.

[2] J.B. Heywood, Internal combustion engine fundamentals, McGraw-Hill Education, 2018.

[3] A.S. Cheng, B.T. Fisher, G.C. Martin, C.J. Mueller, Effects of fuel volatility on early direct-injection, low-temperature combustion in an optical diesel engine, Energy & Fuels. 24 (2010) 1538–1551.

[4] H. Huang, C. Zhou, Q. Liu, Q. Wang, X. Wang, An experimental study on the combustion and emission characteristics of a diesel engine under low temperature combustion of diesel/gasoline/n-butanol blends, Appl. Energy. 170 (2016) 219–231.

[5] M.P.B. Musculus, J.E. Dec, D.R. Tree, D. Daly, D. Langer, T.W. Ryan III, A.C. Matheaus, Effects of water-fuel emulsions on spray and combustion processes in a heavy-duty DI diesel engine, SAE Trans. (2002) 2736–2756.

[6] D.L. Siebers, Liquid-phase fuel penetration in diesel sprays, SAE Trans. (1998) 1205–1227.

[7] J.E. Dec, A conceptual model of DL diesel combustion based on laser-sheet imaging, SAE Trans. (1997) 1319–1348.

[8] L. Andreassi, S. Ubertini, L. Allocca, Experimental and numerical analysis of high pressure diesel spray–wall interaction, Int. J. Multiph. Flow. 33 (2007) 742–765.

[9] M.C. Drake, T.D. Fansler, A.S. Solomon, G.A. Szekely Jr, Piston fuel films as a

source of smoke and hydrocarbon emissions from a wall-controlled spark-ignited direct-injection engine, SAE Trans. (2003) 762–783.

[10] N. Jüngst, S.A. Kaiser, Visualization of soot formation from evaporating fuel films by laser-induced fluorescence and incandescence, Proc. Combust. Inst. 38 (2021) 1089–1097. https://doi.org/https://doi.org/10.1016/j.proci.2020.06.076.

[11] M.A. Shahbaz, N. Jüngst, R. Grzeszik, S.A. Kaiser, Endoscopic fuel film, chemiluminescence, and soot incandescence imaging in a direct-injection spark-ignition engine, Proc. Combust. Inst. 38 (2021) 6213–6220. https://doi.org/10.1016/j.proci.2020.09.004.

[12] L. Zhao, Z. Zhao, X. Zhu, N. Ahuja, J. Naber, S.-Y. Lee, High pressure impinging spray film formation characteristics, SAE Technical Paper, 2018.

[13] D. Maligne, G. Bruneaux, Time-resolved fuel film thickness measurement for direct injection SI engines using refractive index matching, SAE Technical Paper, 2011.

[14] Y. Li, X. Li, W. Cao, Z. Shi, Y. Bo, H. Wu, Acting mechanism of low ambient temperature on wall-impinging diesel spray ignition at an extensive range, Fuel. 304 (2021) 121344.

[15] M.P.B. Musculus, P.C. Miles, L.M. Pickett, Conceptual models for partially premixed low-temperature diesel combustion, Prog. Energy Combust. Sci. 39 (2013) 246–283.

[16] H.S. Fridriksson, M. Tuner, O. Andersson, B. Sunden, H. Persson, M. Ljungqvist, Effect of piston bowl shape and swirl ratio on engine heat transfer in a light-duty diesel engine, SAE Technical Paper, 2014.

[17] S.A. Skeen, J. Manin, L.M. Pickett, Simultaneous formaldehyde PLIF and high-speed schlieren imaging for ignition visualization in high-pressure spray flames,

Proc. Combust. Inst. 35 (2015) 3167–3174.

[18] K. Cung, A. Moiz, J. Johnson, S.-Y. Lee, C.-B. Kweon, A. Montanaro, Spray–combustion interaction mechanism of multiple-injection under diesel engine conditions, Proc. Combust. Inst. 35 (2015) 3061–3068.

[19] P.M. Lillo, L.M. Pickett, H. Persson, O. Andersson, S. Kook, Diesel spray ignition detection and spatial/temporal correction, SAE Int. J. Engines. 5 (2012) 1330–1346.

[20] L.M. Pickett, C.L. Genzale, G. Bruneaux, L.-M. Malbec, L. Hermant, C. Christiansen, J. Schramm, Comparison of diesel spray combustion in different high-temperature, high-pressure facilities, SAE Int. J. Engines. 3 (2010) 156–181.

[21] L.M. Pickett, J. Manin, C.L. Genzale, D.L. Siebers, M.P.B. Musculus, C.A. Idicheria, Relationship between diesel fuel spray vapor penetration/dispersion and local fuel mixture fraction, SAE Int. J. Engines. 4 (2011) 764–799.

[22] L.M. Pickett, S. Kook, T.C. Williams, Visualization of diesel spray penetration, cool-flame, ignition, high-temperature combustion, and soot formation using high-speed imaging, SAE Int. J. Engines. 2 (2009) 439–459.

[23] Ö.O. Taşkiran, M. Ergeneman, Experimental study on diesel spray characteristics and autoignition process, J. Combust. 2011 (2011).

[24] S.L. Wei, W.Q. Long, L.Y. Feng, B.G. Du, X.Y. Leng, Study of spray impingement and a squish combustion system for diesel engines, Proc. Inst. Mech. Eng. Part D J. Automob. Eng. 224 (2010) 117–124.

[25] J. Egermann, M. Taschek, A. Leipertz, Spray/wall interaction influences on the Diesel engine mixture formation process investigated by spontaneous Raman scattering, Proc. Combust. Inst. 29 (2002) 617–623.

[26] Y. Zama, Y. Odawara, T. Furuhata, Experimental investigation on velocity inside a diesel spray after impingement on a wall, Fuel. 203 (2017) 757–763.

[27] M. Ogura, X.F. Bao, Characteristics of Combustion and Exhaust Gas and Fuel Consumption In DI Diesel Engine Using Ringed Impingement Wall Head, SAE Technical Paper, 2001.

[28] X. Cheng, L. Chen, G. Hong, F. Yan, S. Dong, Modeling study of soot formation and oxidation in DI diesel engine using an improved soot model, Appl. Therm. Eng. 62 (2014) 303–312.

[29] X. Zhu, L. Zhao, Z. Zhao, N. Ahuja, J. Naber, S.-Y. Lee, An experimental study of diesel spray impingement on a flat plate: effects of injection conditions, in: Ilass Eur. 28th Eur. Conf. Liq. At. Spray Syst., Editorial Universitat Politècnica de València, 2017: pp. 208–215.

[30] H. Yu, X. Liang, G. Shu, Y. Wang, H. Zhang, Experimental investigation on spray-wall impingement characteristics of n-butanol/diesel blended fuels, Fuel. 182 (2016) 248–258.

[31] L. Zhao, R. Torelli, X. Zhu, R. Scarcelli, S. Som, H. Schmidt, J. Naber, S.-Y. Lee, An experimental and numerical study of diesel spray impingement on a flat plate, SAE Int. J. Fuels Lubr. 10 (2017) 407–422.

[32] Y. Ma, S. Huang, R. Huang, Y. Zhang, S. Xu, Spray and evaporation characteristics of n-pentanol–diesel blends in a constant volume chamber, Energy Convers. Manag. 130 (2016) 240–251.

[33] A.J. Torregrosa, V. Bermúdez, P. Olmeda, O. Fygueroa, Experimental assessment for instantaneous temperature and heat flux measurements under diesel motored engine conditions, Energy Convers. Manag. 54 (2012) 57–66.

[34] J. Wang, H. Fu, Y. Hu, Y. Cai, K. Chen, Experiment investigation on the effects of

air assisted SCR spray impingement on wall temperature evolution, Energy. 204 (2020) 117943.

[35] Y. Hou, Y. Tao, X. Huai, Y. Zou, D. Sun, Numerical simulation of multi-nozzle spray cooling heat transfer, Int. J. Therm. Sci. 125 (2018) 81–88.

[36] Z.-F. Zhou, S.H.M. Murad, J.-M. Tian, J. Camm, R. Stone, Experimental investigation on heat transfer of n-pentane spray impingement on piston surface, Appl. Therm. Eng. 138 (2018) 197–206.

[37] Z.-F. Zhou, L. Liang, S.H.M. Murad, J. Camm, M. Davy, Investigation of fuel volatility on the heat transfer dynamics on piston surface due to the pulsed spray impingement, Int. J. Heat Mass Transf. 170 (2021) 121008.

[38] U. Mathis, M. Mohr, R. Kaegi, A. Bertola, K. Boulouchos, Influence of diesel engine combustion parameters on primary soot particle diameter, Environ. Sci. Technol. 39 (2005) 1887–1892.

[39] W. Park, S. Park, R.D. Reitz, E. Kurtz, The effect of oxygenated fuel properties on diesel spray combustion and soot formation, Combust. Flame. 180 (2017) 276–283.

[40] M. Frenklach, Reaction mechanism of soot formation in flames, Phys. Chem. Chem. Phys. 4 (2002) 2028–2037.

[41] U.S. Jyothi, K.V.K. Reddy, Experimental Study on Hydrogen Enriched Diesel Engine with Varied Piston Bowl Geometry for Emission Reduction, J. Mech. Eng. 6 (2015) 16.

[42] X. Wang, Z. Huang, W. Zhang, O.A. Kuti, K. Nishida, Effects of ultra-high injection pressure and micro-hole nozzle on flame structure and soot formation of impinging diesel spray, Appl. Energy. 88 (2011) 1620–1628.

[43] A. Jain, A.P. Singh, A.K. Agarwal, Effect of fuel injection parameters on combustion stability and emissions of a mineral diesel fueled partially premixed charge compression ignition (PCCI) engine, Appl. Energy. 190 (2017) 658–669.

[44] A.P. Singh, A.K. Agarwal, Partially homogenous charge compression ignition engine development for low volatility fuels, Energy & Fuels. 31 (2017) 3164–3181.

[45] X.-B. Cheng, Y.-Y. Hu, F.-Q. Yan, L. Chen, S.-J. Dong, Investigation of the combustion and emission characteristics of partially premixed compression ignition in a heavy-duty diesel engine, Proc. Inst. Mech. Eng. Part D J. Automob. Eng. 228 (2014) 784–798.

[46] L. Zhao, N. Ahuja, X. Zhu, Z. Zhao, S.-Y. Lee, Splashing criterion and topological features of a single droplet impinging on the flat plate, SAE Int. J. Engines. 11 (2018).

[47] W. Du, Q. Zhang, Z. Zhang, J. Lou, W. Bao, Effects of injection pressure on ignition and combustion characteristics of impinging diesel spray, Appl. Energy. 226 (2018) 1163–1168.

[48] G. Bruneaux, Combustion structure of free and wall-impinging diesel jets by simultaneous laser-induced fluorescence of formaldehyde, poly-aromatic hydrocarbons, and hydroxides, Int. J. Engine Res. 9 (2008) 249–265.

[49] A.L. Pillai, R. Kai, T. Murata, T. Ikedo, R. Masuda, R. Kurose, Numerical analysis of heat transfer characteristics of spray flames impinging on a wall under CI engine-like conditions, Combust. Flame. (2021) 111615. https://doi.org/https://doi.org/10.1016/j.combustflame.2021.111615.

[50] H. Kawanabe, J. Komae, T. Ishiyama, Analysis of flow and heat transfer during the impingement of a diesel spray on a wall using large eddy simulation, Int. J. Engine Res. 20 (2019) 758–764.

[51] J. Moussou, G. Pilla, J. Sotton, M. Bellenoue, F. Rabeau, High-frequency wall heat flux measurement during wall impingement of a diffusion flame, Int. J. Engine Res. 22 (2021) 847–855.

[52] R. Mahmud, T. Kurisu, K. Nishida, Y. Ogata, J. Kanzaki, O. Akgol, Effects of injection pressure and impingement distance on flat-wall impinging spray flame and its heat flux under diesel engine-like condition, Adv. Mech. Eng. 11 (2019) 1687814019862910.

[53] Z. Zhang, F. Liu, Y. An, H. Gao, W. Du, Y. Gao, J. Lou, Effect of wall surface temperature on ignition and combustion characteristics of diesel fuel spray impingement, Appl. Therm. Eng. 137 (2018) 47–53.

[54] D. Mohaddes, P. Boettcher, M. Ihme, Hot surface ignition of a wall-impinging fuel spray: Modeling and analysis using large-eddy simulation, Combust. Flame. 228 (2021) 443–456. https://doi.org/https://doi.org/10.1016/j.combustflame.2021.02.025.

[55] Z. Zhao, X. Zhu, J. Naber, S.-Y. Lee, Assessment of impinged flame structure in high-pressure direct diesel injection, Int. J. Engine Res. 21 (2020) 391–405.

[56] T. Kitamura, T. Ito, J. Senda, H. Fujimoto, Mechanism of smokeless diesel combustion with oxygenated fuels based on the dependence of the equivalence ration and temperature on soot particle formation, Int. J. Engine Res. 3 (2002) 223–248.

[57] K. Li, K. Nishida, Y. Ogata, B. Shi, Effect of flat-wall impingement on diesel spray combustion, Proc. Inst. Mech. Eng. Part D J. Automob. Eng. 229 (2015) 535–549.

[58] I.M.R. Fattah, H.L. Yip, Z. Jiang, A.C.Y. Yuen, W. Yang, P.R. Medwell, S. Kook, G.H. Yeoh, Q.N. Chan, Effects of flame-plane wall impingement on diesel combustion and soot processes, Fuel. 255 (2019) 115726.

[59] F. Liu, Z. Yang, Y. Li, H. Wu, Experimental study on the combustion characteristics of impinging diesel spray at low temperature environment, Appl. Therm. Eng. 148 (2019) 1233–1245.

[60] M. Pucilowski, M. Jangi, H. Fatehi, K.M. Pang, X.-S. Bai, LES study of diesel flame/wall interaction and mixing mechanisms at different wall distances, Proc. Combust. Inst. 38 (2021) 5597–5604. https://doi.org/https://doi.org/10.1016/j.proci.2020.05.056.

[61] H. Jiang, T. Li, Y. Wang, P. He, B. Wang, The evolution of soot morphology and nanostructure along axial direction in diesel spray jet flames, Combust. Flame. 199 (2019) 204–212. https://doi.org/https://doi.org/10.1016/j.combustflame.2018.10.030.

[62] D. Kim, S. Kook, R. Kusakari, K. Shinohara, K. Iijima, T. Aizawa, Soot particles in piston-top pool fires and exhaust at 5 and 15 MPa injection pressure in a gasoline direct-injection engine, Proc. Combust. Inst. 38 (2021) 5761–5768. https://doi.org/https://doi.org/10.1016/j.proci.2020.05.034.

[63] L. Rao, Y. Zhang, S. Kook, K.S. Kim, C.-B. Kweon, Morphology and internal structure of soot particles under the influence of jet–swirl and jet–jet interactions in a diesel combustion environment, Combust. Flame. 214 (2020) 25–36. https://doi.org/https://doi.org/10.1016/j.combustflame.2019.12.017.

[64] Y. Zhang, D. Kim, L. Rao, S. Kook, K.S. Kim, C.-B. Kweon, In-flame soot particle structure on the up- and down-swirl side of a wall-interacting jet in a small-bore diesel engine, Proc. Combust. Inst. 37 (2019) 4847–4855. https://doi.org/https://doi.org/10.1016/j.proci.2018.07.104.

[65] M.K. Le, Y. Zhang, R. Zhang, L. Rao, S. Kook, Q.N. Chan, E.R. Hawkes, Effect of jet–jet interactions on soot formation in a small-bore diesel engine, Proc. Combust. Inst. 36 (2017) 3559–3566.

https://doi.org/https://doi.org/10.1016/j.proci.2016.07.025.

[66] H. Cho, K. Min, Measurement of liquid fuel film distribution on the cylinder liner of a spark ignition engine using the laser-induced fluorescence technique, Meas. Sci. Technol. 14 (2003) 975.

[67] H. Luo, K. Nishida, Y. Ogata, Evaporation characteristics of fuel adhesion on the wall after spray impingement under different conditions through RIM measurement system, Fuel. 258 (2019) 116163.

[68] Y. Liu, Y. Pei, R. Guo, C. Wang, B. Xu, Investigation of the liquid fuel film from GDI spray impingement on a heated surface with the laser induced fluorescence technique, Fuel. 250 (2019) 211–217.

[69] H. Luo, K. Nishida, S. Uchitomi, Y. Ogata, W. Zhang, T. Fujikawa, Effect of temperature on fuel adhesion under spray-wall impingement condition, Fuel. 234 (2018) 56–65.

[70] A. Saito, K. Kawamura, Behavior of fuel film on a wall at fuel spray impinging, Int. J. Fluid Mech. Res. 24 (1997).

[71] J. Senda, M. Ohnishi, T. Takahashi, H. Fujimoto, A. Utsunomiya, M. Wakatabe, Measurement and modeling on wall wetted fuel film profile and mixture preparation in intake port of SI engine, SAE Trans. (1999) 1083–1098.

[72] F. Schulz, W. Samenfink, J. Schmidt, F. Beyrau, Systematic LIF fuel wall film investigation, Fuel. 172 (2016) 284–292.

[73] B. Yang, J. Ghandhi, Measurement of diesel spray impingement and fuel film characteristics using refractive index matching method, SAE Technical Paper, 2007.

[74] E.P. K.J. Richards, P.K. Senecal, CONVERGE 2.4 manual, n.d.

[75] M. Tao, P. Zhao, B. VanDerWege, C. Iyer, H. Ge, Further study on wall film effects and flame quenching under engine thermodynamic conditions, Combust. Flame. 216 (2020) 100–110. https://doi.org/https://doi.org/10.1016/j.combustflame.2020.02.022.

[76] D. Piazzullo, M. Costa, L. Allocca, A. Montanaro, V. Rocco, A 3D CFD simulation of GDI sprays accounting for heat transfer effects on wallfilm formation, SAE Int. J. Engines. 10 (2017) 2166–2175.

[77] X. Li, H. Pan, X. Dong, D. Hung, M. Xu, Spray impingement wall film breakup by wave entrainment, Proc. Combust. Inst. 37 (2019) 3287–3294.

[78] S.H. Lee, G.H. Ko, H.S. Ryou, K.B. Hong, Development and application of a new spray impingement model considering film formation in a diesel engine, KSME Int. J. 15 (2001) 951–961.

[79] H. Pan, D. Xiao, D. Hung, M. Xu, X. Li, Experimental investigations of wall jet droplet impact on spray impingement fuel film formation, Fuel. 241 (2019) 33–41.

[80] E. Stevens, R. Steeper, Piston wetting in an optical DISI engine: fuel films, pool fires, and soot generation, SAE Trans. (2001) 1287–1294.

[81] Engine Combustion Network, (n.d.). https://ecn.sandia.gov/.

[82] Y.-D. Liu, M. Jia, M.-Z. Xie, B. Pang, Enhancement on a skeletal kinetic model for primary reference fuel oxidation by using a semidecoupling methodology, Energy & Fuels. 26 (2012) 7069–7083.

[83] G. Mie, Beiträge zur Optik trüber Medien, speziell kolloidaler Metallösungen, Ann. Phys. 330 (1908) 377–445.

[84] Lord Rayleigh, XXXIV. On the transmission of light through an atmosphere containing small particles in suspension, and on the origin of the blue of the sky,

London, Edinburgh, Dublin Philos. Mag. J. Sci. 47 (1899) 375–384.

[85] G.S. Settles, E.E. Covert, Schlieren and shadowgraph techniques: Visualizing phenomena in transport media, Appl. Mech. Rev. 55 (2002) B76–B77.

[86] J. Menser, F. Schneider, T. Dreier, S.A. Kaiser, Multi-pulse shadowgraphic RGB illumination and detection for flow tracking, Exp. Fluids. 59 (2018) 1–11.

[87] G.R.S. Avinash, C. Kavitha, B. Ashok, R. Vignesh, V. Venkat, V. Karthickeyan, Study of diesel fuel multiple injection characteristics using shadow-graphic imaging technique with CRDI system in constant volume chamber, Fuel. 279 (2020) 118436.

[88] J.E. Dec, Soot distribution in a DI diesel engine using 2-D imaging of laser-induced incandescence, elastic scattering, and flame luminosity, SAE Technical Paper, 1992.

[89] C.J. Mueller, G.C. Martin, Effects of oxygenated compounds on combustion and soot evolution in a DI diesel engine: broadband natural luminosity imaging, SAE Trans. (2002) 518–537.

[90] J. O'Connor, M. Musculus, In-cylinder mechanisms of soot reduction by close-coupled post-injections as revealed by imaging of soot luminosity and planar laser-induced soot incandescence in a heavy-duty diesel engine, SAE Int. J. Engines. 7 (2014) 673–693.

[91] K. Cho, L. Zhao, M. Ameen, Y. Zhang, Y. Pei, W. Moore, M. Sellnau, Understanding fuel stratification effects on partially premixed compression ignition (PPCI) combustion and emissions behaviors, SAE Technical Paper, 2019.

[92] S. Som, G. D'Errico, D. Longman, T. Lucchini, Comparison and standardization of numerical approaches for the prediction of non-reacting and reacting diesel sprays, SAE Technical Paper, 2012.

[93] P.K. Senecal, E. Pomraning, K.J. Richards, S. Som, Grid-convergent spray models for internal combustion engine computational fluid dynamics simulations, J. Energy Resour. Technol. 136 (2014).

[94] L. Zhao, R. Torelli, X. Zhu, J. Naber, S.-Y. Lee, S. Som, R. Scarcelli, M. Raessi, Evaluation of diesel spray-wall interaction and morphology around impingement location, SAE Technical Paper, 2018.

[95] L. Zhao, A.A. Moiz, S. Som, N. Fogla, M. Bybee, S. Wahiduzzaman, M. Mirzaeian, F. Millo, J. Kodavasal, Examining the role of flame topologies and in-cylinder flow fields on cyclic variability in spark-ignited engines using large-eddy simulation, Int. J. Engine Res. 19 (2018) 886–904.

[96] S. Som, Z. Wang, Y. Pei, P.K. Senecal, E. Pomraning, LES of Vaporizing Gasoline Sprays Considering Multi-injection Averaging And Grid-convergent Mesh Resolution, in: Intern. Combust. Engine Div. Fall Tech. Conf., American Society of Mechanical Engineers, 2015: p. V002T06A002.

[97] H. Hiroyasu, T. Kadota, Models for combustion and formation of nitric oxide and soot in direct injection diesel engines, SAE Trans. (1976) 513–526.

[98] J. Nagle, Oxidation of carbon between 1000-2000°C, in: Proc. Fifth Carbon Conf. London, England, 1962, 1962.

[99] R.D. Reitz, F. V Bracco, Mechanism of atomization of a liquid jet, Phys. Fluids. 25 (1982) 1730–1742.

[100] D. Kuhnke, Spray/wall interaction modelling by dimensionless data analysis, Shaker, 2004.

[101] P.J. O'Rourke, A.A. Amsden, A spray/wall interaction submodel for the KIVA-3 wall film model, SAE Trans. (2000) 281–298.

[102] A.A. Amsden, P.J. O'Rourke, T.D. Butler, KIVA-II: A computer program for chemically reactive flows with sprays, Los Alamos National Lab.(LANL), Los Alamos, NM (United States), 1989.

[103] C.H. Chiang, M.S. Raju, W.A. Sirignano, Numerical analysis of convecting, vaporizing fuel droplet with variable properties, Int. J. Heat Mass Transf. 35 (1992) 1307–1324.

[104] Q. Chen, Comparison of different k-ε models for indoor air flow computations, Numer. Heat Transf. Part B Fundam. 28 (1995) 353–369.

[105] Z. Han, R.D. Reitz, Turbulence modeling of internal combustion engines using RNG κ-ε models, Combust. Sci. Technol. 106 (1995) 267–295.

[106] D.C. Wilcox, Turbulence modeling for CFD, DCW industries La Canada, CA, 1998.

[107] E. Roohi, A.P. Zahiri, M. Passandideh-Fard, Numerical simulation of cavitation around a two-dimensional hydrofoil using VOF method and LES turbulence model, Appl. Math. Model. 37 (2013) 6469–6488.

[108] P.K. Senecal, E. Pomraning, K.J. Richards, S. Som, An investigation of grid convergence for spray simulations using an LES turbulence model, SAE Technical Paper, 2013.

[109] E.D. Pomraning, Development of large eddy simulation turbulence models, The University of Wisconsin-Madison, 2000.

[110] M.P. Halstead, L.J. Kirsch, C.P. Quinn, The autoignition of hydrocarbon fuels at high temperatures and pressures—fitting of a mathematical model, Combust. Flame. 30 (1977) 45–60.

[111] J. Xin, D. Montgomery, Z. Han, R.D. Reitz, Multidimensional modeling of

combustion for a six-mode emissions test cycle on a DI diesel engine, (1997).

[112] J. Abraham, F. V Bracco, R.D. Reitz, Comparisons of computed and measured premixed charge engine combustion, Combust. Flame. 60 (1985) 309–322.

[113] O. Colin, A. Benkenida, The 3-zones extended coherent flame model (ECFM3Z) for computing premixed/diffusion combustion, Oil Gas Sci. Technol. 59 (2004) 593–609.

[114] N. Otsu, A threshold selection method from gray-level histograms, IEEE Trans. Syst. Man. Cybern. 9 (1979) 62–66.

[115] X. Zhu, High Injection Pressure Dme Ignition and Combustion Processes: Experiment and Simulation, (2019).

[116] M. Tang, Spray and Combustion Studies of High Reactivity Gasoline in Comparison to Diesel under Advanced Compression Ignition Engine Conditions, (2018).

[117] F. Mokhtarian, A. Mackworth, Scale-based description and recognition of planar curves and two-dimensional shapes, IEEE Trans. Pattern Anal. Mach. Intell. (1986) 34–43.

[118] A.E. Bayley, Y. Hardalupas, A.M.K.P. Taylor, Local curvature measurements of a lean, partially premixed swirl-stabilised flame, Exp. Fluids. 52 (2012) 963–983.

[119] M. Frigo, S.G. Johnson, FFTW: An adaptive software architecture for the FFT, in: Proc. 1998 IEEE Int. Conf. Acoust. Speech Signal Process. ICASSP'98 (Cat. No. 98CH36181), IEEE, 1998: pp. 1381–1384.

[120] R. Hessel, Z. Yue, R. Reitz, M. Musculus, J. O'Connor, Guidelines for interpreting soot luminosity imaging, SAE Int. J. Engines. 10 (2017) 1174–1192.

[121] Z. Zhao, X. Zhu, L. Zhao, J. Naber, S.-Y. Lee, Spray-wall dynamics of high-

pressure impinging combustion, SAE Technical Paper, 2019.

[122] D. Siebers, B. Higgins, Flame lift-off on direct-injection diesel sprays under quiescent conditions, SAE Trans. (2001) 400–421.

[123] S. Han, J. Kim, C. Bae, Effect of air–fuel mixing quality on characteristics of conventional and low temperature diesel combustion, Appl. Energy. 119 (2014) 454–466.

[124] J.R. Blough, D.L. Brown, H. Vold, The time variant discrete Fourier transform as an order tracking method, SAE Trans. (1997) 3037–3045.

[125] S. Kimura, O. Aoki, Y. Kitahara, E. Aiyoshizawa, Ultra-clean combustion technology combining a low-temperature and premixed combustion concept for meeting future emission standards, Sae Trans. (2001) 239–246.

[126] R. Dou, Z. Wen, G. Zhou, Heat transfer characteristics of water spray impinging on high temperature stainless steel plate with finite thickness, Int. J. Heat Mass Transf. 90 (2015) 376–387. https://doi.org/https://doi.org/10.1016/j.ijheatmasstransfer.2015.06.079.

[127] Y. Liao, R. Furrer, P. Dimopoulos Eggenschwiler, K. Boulouchos, Experimental investigation of the heat transfer characteristics of spray/wall interaction in diesel selective catalytic reduction systems, Fuel. 190 (2017) 163–173. https://doi.org/https://doi.org/10.1016/j.fuel.2016.11.035.

[128] T. IKEDO, K. Inagaki, Y. Nomura, U. Reiko, H. OYAGI, Proposal of Wall Heat Transfer Coefficient Applicable to Spray-wall Interaction Process in Diesel Engines (Second Report: Improvement of Diesel Combustion Simulator UniDES by the Proposed Wall Heat Transfer Coefficient), SAE Technical Paper, 2019.

[129] J.R. Rybicki, I. Mudawar, Single-phase and two-phase cooling characteristics of upward-facing and downward-facing sprays, Int. J. Heat Mass Transf. 49 (2006)

5–16.

[130] D. Xiao, S. Qiu, D. Hung, X. Li, K. Nishida, M. Xu, Evaporation and condensation of flash boiling sprays impinging on a cold surface, Fuel. 287 (2021) 119423.

[131] D.W. Stanton, C.J. Rutland, Multi-dimensional modeling of thin liquid films and spray-wall interactions resulting from impinging sprays, Int. J. Heat Mass Transf. 41 (1998) 3037–3054.

[132] J.H. Lienhard, Heat transfer in flat-plate boundary layers: a correlation for laminar, transitional, and turbulent flow, J. Heat Transfer. 142 (2020).

[133] S. Pawar, D.K. Patel, The Impingement Heat Transfer Data of Inclined Jet in Cooling Applications: A Review, J. Therm. Sci. 29 (2020) 1–12.

[134] J.D. Naber, D.L. Siebers, Effects of gas density and vaporization on penetration and dispersion of diesel sprays, SAE Trans. (1996) 82–111.

[135] L.M. Pickett, Low flame temperature limits for mixing-controlled Diesel combustion, Proc. Combust. Inst. 30 (2005) 2727–2735.

[136] R.S. Wolf, W.K. Cheng, Heat transfer characteristics of impinging diesel sprays, SAE Technical Paper, 1989.

[137] K. Moreland, L. Avila, L.A. Fisk, Parallel unstructured volume rendering in paraview, in: Vis. Data Anal. 2007, International Society for Optics and Photonics, 2007: p. 64950F.

[138] M. Lee, Y. Fan, Y. Ju, Y. Suzuki, Ignition characteristics of premixed cool flames on a heated wall, Combust. Flame. 231 (2021) 111476. https://doi.org/https://doi.org/10.1016/j.combustflame.2021.111476.

[139] A.O. Ojo, D. Escofet-Martin, J. Collins, G. Falconetti, B. Peterson, Experimental investigation of thermal boundary layers and associated heat loss for transient

engine-relevant processes using HRCARS and phosphor thermometry, Combust. Flame. 233 (2021) 111567. https://doi.org/https://doi.org/10.1016/j.combustflame.2021.111567.

A MATLAB programs for data processing introduced in Chapter 5

A.1 Boundary tracking

```
% DOE BOTTOMVIEW DATA ANALYSIS
% MADE BY ZHIHAO JULY 2017
clear all
close all
%% CONDITION SETUP
SOI = 28;          % START OF INJECTION
EOA = 118;          % END OF ANALYSIS
ntotal = EOA;     % TOTAL NUMBERS OF IMAGES TO BE PROCESSED
scale = 0.177;   % SCALE UNIT 'MM/PIXEL'
% scale = 0.1047;   % SCALE UNIT 'MM/PIXEL'
freq = 36000;       % IMAGE ACQUSITION FREQUENCY/FRAME RATE
% freq = 10000;       % IMAGE ACQUSITION FREQUENCY/FRAME RATE
nx = 384;      % IMAGE SIZE X AXIS UNIT 'PIXEL'
ny = 368;      % IMAGE SIZE Y AXIS UNIT 'PIXEL'
% nx = 704;      % IMAGE SIZE X AXIS UNIT 'PIXEL'
% ny = 704;      % IMAGE SIZE Y AXIS UNIT 'PIXEL'
numberToExtract = 1; % DETERMINE HOW MANY AREA TO KEEP, GENERALLY
THE NUMBER IS 1
impingingtime = 30; % THE FRAME OF IMPINGEMENT
boundary_matrix = zeros(nx,ny);
numberToExtract = 1;
%%
dir_raw = 'E:\CV\DOE\DOE 2017 March'; % DIRECTORY OF THE IMAGE
YYYYMMDD = '20170330';
HHMM = '2202';
writerObj = VideoWriter('Bottomview.avi');
writerObj.FrameRate = 3;
open(writerObj);
column = 190;
row = 87;
% column = 357;
% row = 184;
angle = 1*2*pi/360;
angle1 = 5;
b = 500;
ave_radii = 0;
%% READ BACKGROUND IMAGE
```

```
for i=1:1% CHOOSE THE FIRST IMAGE AS THE BACKGROUND
if i < 10
    fullFileName1 = [dir_raw '/' YYYYMMDD '/' HHMM '/' HHMM '00000' num2str(i)
'.bmp'];
   elseif i < 100
    fullFileName1 = [dir_raw '/' YYYYMMDD '/' HHMM '/' HHMM '0000' num2str(i)
'.bmp'];
   elseif i < 1000
    fullFileName1 = [dir_raw '/' YYYYMMDD '/' HHMM '/' HHMM '000' num2str(i)
'.bmp'];
end
Background = imread(fullFileName1); % READING THE BACKGROUND
end
cd([dir_raw '\' YYYYMMDD '\' HHMM]) % CHANGE THE WORKING DIRECTORY
TO THE TARGE FOLDER
%
for i = SOI:EOA % READ IMAGE AFTER THE START OF INJECTION
if i < 10
    fullFileName = [dir_raw '/' YYYYMMDD '/' HHMM '/' HHMM '00000' num2str(i)
'.bmp'];
   elseif i < 100
    fullFileName = [dir_raw '/' YYYYMMDD '/' HHMM '/' HHMM '0000' num2str(i)
'.bmp'];
   elseif i < 1000
    fullFileName = [dir_raw '/' YYYYMMDD '/' HHMM '/' HHMM '000' num2str(i)
'.bmp'];
end
grayimage = imread(fullFileName); % ORIGINAL IMAGE
grayimage = grayimage - Background;
grayimage(grayimage<10) = 0;
grayimage = double(grayimage);
grayimage1 = imgaussfilt(grayimage,2);
grayimage1 = medfilt2(grayimage1,[5 5]);

[filteredimage,estDoS] = imnlmfilt(grayimage);
sigma = estDoS;
thresh = 0.17; % 1800bar
W = gradientweight(grayimage,sigma,'RollOffFactor',4,'WeightCutoff',0.005);
sample = W;
[BINARY,D] = imsegfmm(sample,column,row,thresh);
B = bwboundaries(BINARY);
stats = regionprops(BINARY, 'orientation','area','Extrema','centroid');
 area=[stats.Area].*scale.*scale;
if isempty(area) == 1
```

```
    area = 0;
end
area_time(i,1) = area;

for k = 1:1
  boundary = B{k};
end
figure(1);
imshow(grayimage,[0 255]);
hold on
plot(boundary(:,2),boundary(:,1),'r');
hold on
end
```

A.2 Curvature verification and calculation

```
clear all
close all
%%
image = zeros(765,765);
maskSize = 201;  %
R = (maskSize-1)/2
t_r = (maskSize-1)/2 ;
[x,y] = meshgrid((1-maskSize)/2:maskSize/2,(1-maskSize)/2:maskSize/2);
[t,r] = cart2pol(x,y);
t(r>t_r) = nan;
r(r>t_r) = nan;
[xn,yn] = cart2pol(t,r);
mask = ~isnan(xn);
scale = 0.1047;
theo_curv = 1/(maskSize*scale/2);
middle1 = 383;
middle2 = 383;
column = 383;
row = 383;
image(middle1-R:middle1+R,middle2-R:middle2+R) = image(middle1-
R:middle1+R,middle2-R:middle2+R)+double(mask);
figure(1);
imshow(image);
   B = bwboundaries(image);
   for k = 1:length(B)
     boundary = B{k};
   end
```

```
  starting_point = find(boundary(:,2) == column,1,'first');
  boundary_modified(1:length(boundary)-starting_point+1,2) =
boundary(starting_point:end,2);
  boundary_modified(length(boundary)-starting_point+2:length(boundary),2) =
boundary(1:starting_point-1,2);
  boundary_modified(1:length(boundary)-starting_point+1,1) =
boundary(starting_point:end,1);
  boundary_modified(length(boundary)-starting_point+2:length(boundary),1) =
boundary(1:starting_point-1,1);

  oneD_distance = ((boundary_modified(:,2)-column).^2 + (boundary_modified(:,1)-
row).^2).^0.5;


  abs_oneD = oneD_distance.*scale;
  x_axe = (1:length(boundary_modified(:,1)))';
  y_axe = (1:length(boundary_modified(:,2)))';
  coeff_x = polyfit(x_axe,boundary_modified(:,2),10);
  coeff_y = polyfit(y_axe,boundary_modified(:,1),10);
  [xData, yData] = prepareCurveData(x_axe, boundary_modified(:,2));
  [xData1, yData1] = prepareCurveData(y_axe, boundary_modified(:,1));
  [xData2, yData2] = prepareCurveData(y_axe, oneD_distance);
   % Set up fittype and options.
  ft = fittype( 'smoothingspline' );
  opts = fitoptions( 'Method', 'SmoothingSpline' );
  opts.SmoothingParam = 0.0001;

   % Fit model to data.
  [fitresult, gof] = fit( xData, yData, ft, opts );
  [fitresult1, gof1] = fit( xData1, yData1, ft, opts );
  [fitresult2, gof2] = fit( xData2, yData2, ft, opts );
  polyvalue = feval(fitresult,x_axe).*scale;
  polyvalue1 = feval(fitresult1,y_axe).*scale;
  oneD_distance_poly = feval(fitresult2,y_axe);
  deriv = gradient(oneD_distance_poly,0.1); % 1st deriv
  sec_deriv = gradient(deriv,0.1); % 2nd deriv

  curvature = curv_calc(boundary_modified,polyvalue,polyvalue1,scale);
  figure(2);
  plot(curvature,'-k','LineWidth',2);
  hold on
  theo_y = ones(1,length(curvature)).*theo_curv;
  plot(theo_y,'--k','LineWidth',2);
```

```
  hold on
  xlabel('Pixel','FontSize',20);
  ylabel('Curvature (1/mm)','FontSize',20);
  legend({'Calculated curvature','Theoretical curvature'},'FontSize',20,'Location','south');


function curvature = curv_calc(boundary_modified,polyvalue,polyvalue1,scale)
  for L = 2:length(boundary_modified)-1
  x = 0:704;
%    curvature(:,l) = LineCurvature2D(bound_peak(:,:,l));
  para_t_left = -((polyvalue(L-1,1)-polyvalue(L,1)).^2+(polyvalue1(L-1,1)-
polyvalue1(L,1)).^2).^0.5;
  para_t_right = ((polyvalue(L+1,1)-polyvalue(L,1)).^2+(polyvalue1(L+1,1)-
polyvalue1(L,1)).^2).^0.5;
  para_t = 0;
  para = [para_t_left para_t para_t_right]';
  coef(:,L) = polyfit(para,[polyvalue(L-1,1) polyvalue(L,1) polyvalue(L+1,1)]',2); %x
curve fit
  coefy(:,L) = polyfit(para,[polyvalue1(L-1,1) polyvalue1(L,1) polyvalue1(L+1,1)]',2);
%y curve fit
  x_singleprime(L,1) = coef(2,L);
  x_doubleprime(L,1) = 2*coef(1,L);
  y_singleprime(L,1) = coefy(2,L);
  y_doubleprime(L,1) = 2*coefy(1,L);
  curvature(L,:) = (x_singleprime(L,1).*y_doubleprime(L,1)-
y_singleprime(L,1).*x_doubleprime(L,1))/((x_singleprime(L,1).^2+y_singleprime(L,1).^
2).^1.5);
  x1 = boundary_modified(L-1,2);
  x2 = boundary_modified(L+1,2);
  y1 = boundary_modified(L-1,1);
  y2 = boundary_modified(L+1,1);
  x_mid = boundary_modified(L,2);
  y_mid = boundary_modified(L,1);
  a(L,1) = (y1-y2)/(x1-x2);
  b(L,1) = y1-(a(L,1).*x1);
  mid_point_x(L,1) = (x1+x2)/2;
  mid_point_y(L,1) = (y1+y2)/2;
  a2(L,1) = -1./a(L,1);
  b2(L,1) = y_mid-x_mid.*a2(L,1);
  y = a2(L,1).*x+b2(L,1);
  y_prime = a(L,1).*x+b(L,1);
  R(L,1) = abs(1./(curvature(L,1).*scale));
  length_scale_x(L,1) = sqrt(R(L,1).^2./(1+a2(L,1).^2));
  if L < round(length(boundary_modified)/2)
```

```
    if a2(L,1) > 0 && curvature(L,1) > 0
    x_cen(L,1) = boundary_modified(L,2)+length_scale_x(L,1);
    y_cen(L,1) = boundary_modified(L,1)+a2(L,1).*length_scale_x(L,1);
    else if a2(L,1) > 0 && curvature(L,1) < 0
    x_cen(L,1) = boundary_modified(L,2)-length_scale_x(L,1);
    y_cen(L,1) = boundary_modified(L,1)-a2(L,1).*length_scale_x(L,1);
    else if a2(L,1) < 0 && curvature(L,1) > 0
    x_cen(L,1) = boundary_modified(L,2)-length_scale_x(L,1);
    y_cen(L,1) = boundary_modified(L,1)-a2(L,1).*length_scale_x(L,1);
    else if a2(L,1) < 0 && curvature(L,1) < 0
    x_cen(L,1) = boundary_modified(L,2)+length_scale_x(L,1);
    y_cen(L,1) = boundary_modified(L,1)+a2(L,1).*length_scale_x(L,1);
    end
    end
    end
    end
    end
    if L>=round(length(boundary_modified)/2)
    if a2(L,1) > 0 && curvature(L,1) > 0
    x_cen(L,1) = boundary_modified(L,2)-length_scale_x(L,1);
    y_cen(L,1) = boundary_modified(L,1)-a2(L,1).*length_scale_x(L,1);
    else if a2(L,1) > 0 && curvature(L,1) < 0
    x_cen(L,1) = boundary_modified(L,2)+length_scale_x(L,1);
    y_cen(L,1) = boundary_modified(L,1)+a2(L,1).*length_scale_x(L,1);
    else if a2(L,1) < 0 && curvature(L,1) > 0
    x_cen(L,1) = boundary_modified(L,2)+length_scale_x(L,1);
    y_cen(L,1) = boundary_modified(L,1)+a2(L,1).*length_scale_x(L,1);
    else if a2(L,1) < 0 && curvature(L,1) < 0
    x_cen(L,1) = boundary_modified(L,2)-length_scale_x(L,1);
    y_cen(L,1) = boundary_modified(L,1)-a2(L,1).*length_scale_x(L,1);
    end
    end
    end
    end
    end

    clear para_t_left para_t_right para_t para pos pos1
    end
end
```

A.3 Apparent heat release rate

```
%%%%%%%%%%%%%%%%%%%%%%%%%%%%%%%%%%%%%%%%%%%%%%%%%
%%%%%%%%%%%%%%%%%%%%%%%%%%%%%%%
% Demo code to filter the noise in the raw pressure data for further %
% analysis to obtain heat-release rate and ignition delays.          %
% Zhihao Zhao                                         %
%%%%%%%%%%%%%%%%%%%%%%%%%%%%%%%%%%%%%%%%%%%%%%%%%
%%%%%%%%%%%%%%%%%%%%%%%%%%%%%%%

clear all;
close all;
clc;

% Initialization of the parameters
yyyymmdd       = 20200726;
hhmm           = 1948;
Freq           = 100000;
gamma_gas = 1.35;
MW = 29.1;
hydrodelay_UHS  = 0.25;    % unit: ms; hydraulic delay of the injector.
oxygenlevel     = 0.21;
separation_pt   = 50134;   % 1st separation point
filter_pt1      = 50001;   % starting point for data filtering
filter_pt2      = 51501;   % ending point for data filtering
Temperature_test= 900;     % unit: K
speed_sound = (gamma_gas*8314*Temperature_test/MW)^0.5; % Speed of sound
Pressure_test   = 61;      % unit: bar
F_cutoff1       = 1500;    % cutoff frequency for the 1st butterworth filter, for the 2nd part
of the pressure curve
F_cutoff2       = 5000;    % cutoff frequency for the 2nd butterworth filter, for the
assembled and spline interpolated pressure curve
F_cutoff_fir    = 5000;    % cutoff frequency for the FIR filter
filter_order1   = 5;       % order of the 1st butterworth filter, for the 2nd part of the
pressure curve
filter_order2   = 1;       % order of the 2nd butterworth filter, for the assembled and spline
interpolated pressure curve
ftr_fir_order   = 50;      % order of the FIR filter
Upsample_freq   = 1e7;     % frequency for upsampling after two-part data smoothing
load(strcat('F:\CV\2020 JD spray impingement\JDpressure\', num2str(yyyymmdd), '\',
num2str(hhmm), '\TestFileData.mat'));

% Speed of sound correction for pressure trace delay
```

```
Liquid_length = 24; % Unit mm 24 @ 900 k 24kg/m3 16 @ 1050 k 33kg/m3
Nozzle_vertical_distance = 50.65; % Unit mm
Distance = (((101.3-Liquid_length*sin(pi/10))^2 + (Nozzle_vertical_distance-
Liquid_length*cos(pi/10))^2) + Nozzle_vertical_distance^2)^0.5;
lag_sound = Distance/speed_sound;


% Finding SOI
SOI = min(find(Injection == max(Injection)));
Time_original = 1/Freq:1/Freq:size(Time, 1)/Freq;
Time_original = Time_original';

% Pressure subtraction: exponential decay, select the right range of data to perform data
fitting
Pressure_original = Pressure;
P_fit_range = Pressure(SOI-10000:SOI);
T_fit_range = Time_original(SOI-10000:SOI);

% Curve fitting for pressure subtraction
P_log_range = log(P_fit_range);
p = polyfit(T_fit_range, P_log_range, 1);
y = polyval(p, T_fit_range);
yresid = P_log_range - y;
SSresid = sum(yresid.^2);
SStotal = (length(y)-1) * var(y);
rsq = 1 - SSresid/SStotal;

% Pressure subtraction to determine the pressure rise due to spray combustion
P_sub = Pressure(SOI-50000:SOI+30000);
T_sub = Time_original(SOI-50000:SOI+30000);
T_sub_plot = Time_original(SOI-50000:SOI+30000)-Time_original(SOI);
P_fit = exp(p(1)*T_sub+p(2));
P_diff = P_sub-P_fit;

% Create two filters
[c1, d1] = butter(filter_order1, F_cutoff1/(100000/2)); % Butterworth filter for the 2nd
part of the pressure curve.
[c2, d2] = butter(filter_order2, F_cutoff2/(Upsample_freq/2)); % Butterworth for the
assembled and spline interpolated pressure curve.

% Smoothing the pressure by two different portions
Pressure_1 = P_diff(filter_pt1:separation_pt );
Pressure_2 = P_diff(separation_pt :filter_pt2);
Pressure_1_flip = flipdim(Pressure_1, 1);
```

```
Pressure_1_flipsub = Pressure_1_flip(1)-(Pressure_1_flip-Pressure_1_flip(1));
Pressure_1_assemble = [Pressure_1' Pressure_1_flipsub(2:end)'];
Pressure_2_flip = flipdim(Pressure_2, 1);
Pressure_2_flipsub = Pressure_2_flip(end)-(Pressure_2_flip-Pressure_2_flip(end));
Pressure_2_assemble = [Pressure_2_flipsub' Pressure_2(2:end)'];
Time_1_assemble = T_sub_plot(filter_pt1:(2*separation_pt -filter_pt1));
ftr_fir = fir1(ftr_fir_order, F_cutoff_fir/(100000/2), 'low');
Pressure_1_filt = filtfilt(ftr_fir, 1, Pressure_1_assemble);
Pressure_2_filt = filtfilt(c1, d1, Pressure_2_assemble);

% Assembling the two smoothed curves
mid_pt_P1 = (size(Pressure_1_filt, 1)+1)/2;
mid_pt_P2 = (size(Pressure_2_filt, 1)+1)/2;
Pressure_separation = [Pressure_1_filt((mid_pt_P1-2):mid_pt_P1)'
Pressure_2_filt(mid_pt_P2:(mid_pt_P2+1))'];
Pressure_filt = [Pressure_1_filt(1:mid_pt_P1)' Pressure_2_filt((mid_pt_P2+1):end)'];

% Spline interpolation along the entire pressure curve
Time_filt = T_sub_plot(filter_pt1:filter_pt2);
Time_smoothed = T_sub_plot(filter_pt1):(1/Upsample_freq):T_sub_plot(filter_pt2);
Pressure_hi = spline(Time_filt, Pressure_filt, Time_smoothed);
Pressure_smoothed = filtfilt(c2, d2, Pressure_hi);

% time vector corrections
Time_unfilt_correct = T_sub_plot*1000-hydrodelay_UHS-lag_sound ; % unit: ms
Time_filt_correct = Time_filt*1000-hydrodelay_UHS-lag_sound ;   % unit: ms
Time_smoothed_correct = Time_smoothed*1000-hydrodelay_UHS-lag_sound ;   % unit:
ms
% Plotting
fig = figure;
plot(Time_unfilt_correct, P_diff, '-r', 'LineWidth', 1);
hold on;
plot(Time_filt_correct, Pressure_filt, '-b', 'LineWidth', 2);
hold on;
% plot(Time_smoothed_correct, Pressure_smoothed, '-k', 'LineWidth', 3);
xlim([0 5]);
ylim([0 500]);
xlabel('Time ASOI, ms');
ylabel('Pressure, psi');
legend( 'Original pressure', 'Filtered pressure', 'Location', 'northeast')
title('Comparison of the processed pressure curves');

gamma = 1.35;   % assumption
V = 1.1;        % unit: L
```

```
deltaT = 0.001; % unit: ms
dQ = (1/(gamma-1))*V* diff(Pressure_smoothed)/deltaT*6894.76/10000; % unit: Mega
Watt, dQ/dt = L*psi/sec = (6894.76 psi/Pa * 0.001 m3/L)/(0.001 sec)
T_hrr = Time_smoothed_correct(1:(end-1));
start_index = find(abs(T_hrr-0)<0.0001,1,'first');
start_index2 = find(abs(Time_filt_correct-0)<0.01,1,'first');
% T_hrr = T_hrr';
P_ignd = Pressure_filt(start_index2:start_index2 + 500);
T_ignd = Time_filt_correct(start_index2:start_index2 + 500);
T_save = T_hrr(start_index:start_index + 50000)';
dQ_save = dQ(start_index:start_index + 50000)';
% dQ = dQ';
figure;
plot(T_save, dQ_save, 'r-', 'LineWidth', 2);
xlim([0 5]);
ylim([-10 60]);
xlabel('Time ASOI, ms');
ylabel('Heat release rate, kJ/ms');
title('Heat release rate');
%%
Ignition_delay_P = T_ignd(find(P_ignd>0.435,1,'first'));
```

B Copyright documentation

B.1 SAE response for copyright

Michigan Tech

Zhihao Zhao <zhizhao@mtu.edu>

Copyright permission request for a dissertation

copyright <copyright@sae.org> Wed, Oct 20, 2021 at 11:19 AM
To: Zhihao Zhao <zhizhao@mtu.edu>

Dear Zhihao,

Thank you for reaching out to SAE International with your inquiry. SAE authors are permitted to republish graphics, charts, figures and other content they created for SAE publication in additional papers that they are a named author on, as long as a full reference to the original published SAE source is included, and © SAE International appears next to any reproduced content. We do not require authors to obtain written documentation for those permission requests, as long as they meet the above criteria.

Please feel free to reach out if you have any additional questions.

Regards,

Brandon Joy | Intellectual Property Associate

SAE International

SAE.org | facebook | instagram | linkedin | twitter

[Quoted text hidden]

B.2 ASME response for copyright

Michigan Tech

Zhihao Zhao <zhizhao@mtu.edu>

Copyright permission for a dissertation

Beth Darchi <DarchiB@asme.org> Thu, Oct 21, 2021 at 9:43 AM
To: Zhihao Zhao <zhizhao@mtu.edu>

Dear Mr. Zhao,

It is our pleasure to grant you permission to use **all or any part of** the following ASME paper "Evaluation of Soot Production Near a Cold Surface for an Impinged Diesel Spray Combustion," by Zhihao Zhao, Le Zhao, Seong-Young Lee, Paper No: ICEF2020-2938, cited in your letter for inclusion in a Ph.D. dissertation to be published by Michigan Tech Univ.

Permission is granted for the specific use as stated herein and does not permit further use of the materials without proper authorization. Proper attribution must be made to the author(s) of the materials. **Please note**: if any or all of the figures and/or Tables are of another source, permission should be granted from that outside source or include the reference of the original source. ASME does not grant permission for outside source material that may be referenced in the ASME works.

As is customary, we request that you ensure full acknowledgment of this material, the author(s), source and ASME as original publisher.

Many thanks for your interest in ASME publications.

Sincerely,

Beth Darchi

Publishing Administrator

ASME

2 Park Avenue

New York, NY 10016-5990

From: Zhihao Zhao <zhizhao@mtu.edu>
Sent: Monday, October 18, 2021 11:15 PM

B.3 International journal of engine research reuse policy

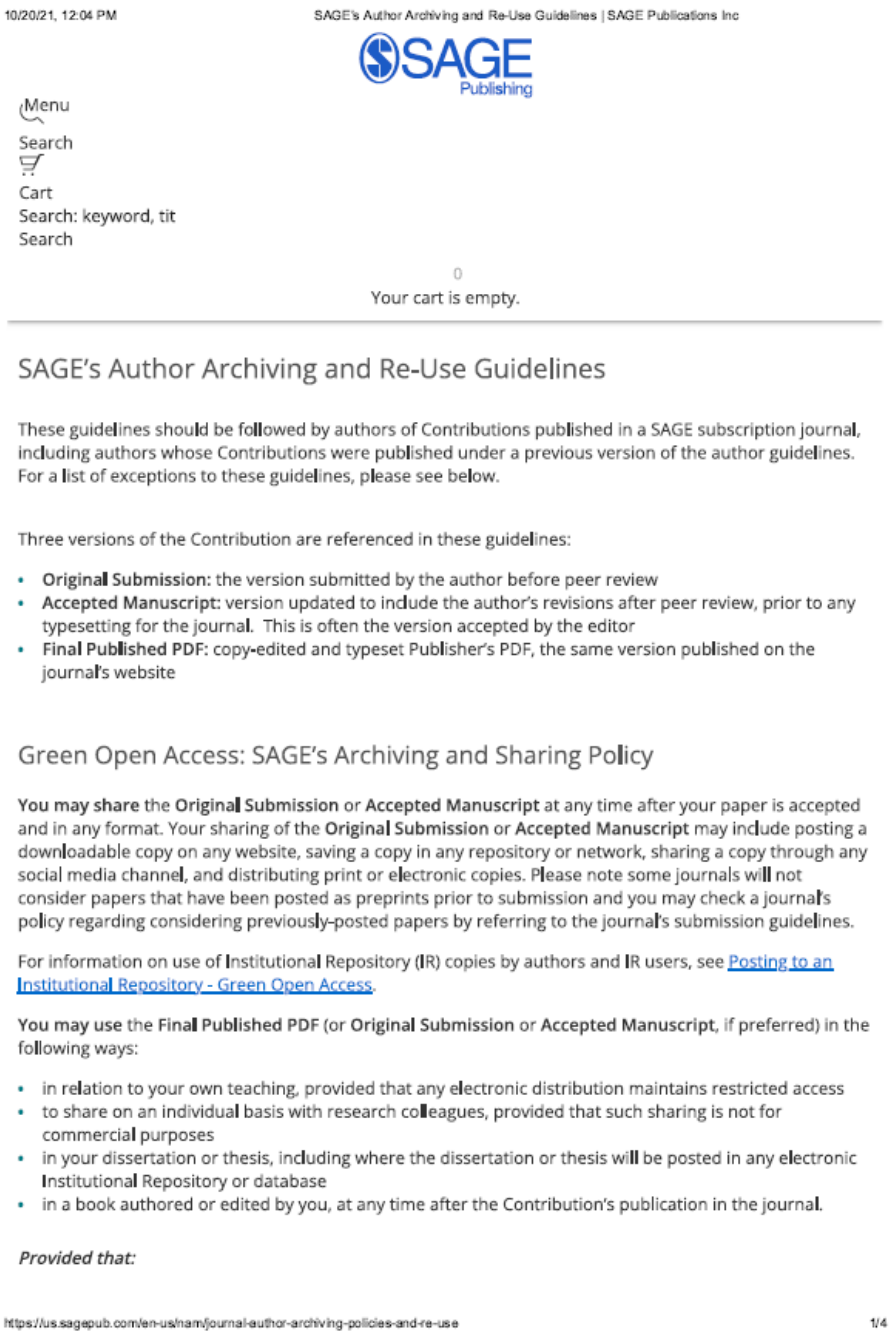

10/20/21, 12:04 PM SAGE's Author Archiving and Re-Use Guidelines | SAGE Publications Inc

Menu
Search
Cart
Search: keyword, tit
Search

0
Your cart is empty.

SAGE's Author Archiving and Re-Use Guidelines

These guidelines should be followed by authors of Contributions published in a SAGE subscription journal, including authors whose Contributions were published under a previous version of the author guidelines. For a list of exceptions to these guidelines, please see below.

Three versions of the Contribution are referenced in these guidelines:

- **Original Submission:** the version submitted by the author before peer review
- **Accepted Manuscript:** version updated to include the author's revisions after peer review, prior to any typesetting for the journal. This is often the version accepted by the editor
- **Final Published PDF:** copy-edited and typeset Publisher's PDF, the same version published on the journal's website

Green Open Access: SAGE's Archiving and Sharing Policy

You may share the **Original Submission** or **Accepted Manuscript** at any time after your paper is accepted and in any format. Your sharing of the **Original Submission** or **Accepted Manuscript** may include posting a downloadable copy on any website, saving a copy in any repository or network, sharing a copy through any social media channel, and distributing print or electronic copies. Please note some journals will not consider papers that have been posted as preprints prior to submission and you may check a journal's policy regarding considering previously-posted papers by referring to the journal's submission guidelines.

For information on use of Institutional Repository (IR) copies by authors and IR users, see Posting to an Institutional Repository - Green Open Access.

You may use the **Final Published PDF** (or **Original Submission** or **Accepted Manuscript**, if preferred) in the following ways:

- in relation to your own teaching, provided that any electronic distribution maintains restricted access
- to share on an individual basis with research colleagues, provided that such sharing is not for commercial purposes
- in your dissertation or thesis, including where the dissertation or thesis will be posted in any electronic Institutional Repository or database
- in a book authored or edited by you, at any time after the Contribution's publication in the journal.

Provided that:

https://us.sagepub.com/en-us/nam/journal-author-archiving-policies-and-re-use 1/4

- Access to the Original Submission and Accepted Manuscript is provided at no charge.
- Any re-use terms for users of websites and repositories (where your **Original Submission** or **Accepted Manuscript** are posted) are restricted to non-commercial and no derivative uses.
- You may not post the **Final Published PDF** on any unrestricted website or repository without permission from SAGE.
- You may not republish or translate any version of your Contribution in another journal without prior permission from SAGE.
- The journal as the original publication of your Contribution is appropriately credited by including the full citation information each time your Contribution, or excerpts, are further distributed or re-used:
  - After your Contribution has been accepted for publication and until it is assigned a DOI, please include a statement that your Contribution has been accepted for publication in the journal.
  - Once full citation information for your Contribution is available, please include this with your posted Contribution, in a format similar to the following:
    Author(s), Contribution Title, Journal Title (Journal Volume Number and Issue Number) pp. xx-xx. Copyright © [year] (Copyright Holder). DOI: [DOI number].

Journal Exceptions

Exceptions to this Author Re-Use policy: The following journals have a different author re-use policy in place. The re-use terms for these journals are stated in the Contributor Agreement used by the Journal.

If you have questions regarding the following titles, contact the permissions team through our SAGE Permissions Portal.

- *California Management Review*
- *Journal of Dental Research*
- *JDR Clinical & Translational Research*
- *Acta Radiologica* (from January 2018)
- *Index on Censorship*
- *Pain News*
- *Political Insight*
- *Recherche et Applications en Marketing*

Related Information

Authors of Contributions published as SAGE Choice or in a Gold Open Access journal should reference Reusing Open Access and SAGE Choice Content. For a list of SAGE's Gold Open Access journals, please see Gold Open Access journals.

Authors of Contributions published under a Creative Commons license may re-use their work under the terms of the Creative Commons license attached to their Contributions and additionally have all rights to re-use their work stated above.

For information about requesting permission for content published in SAGE journals, see Process for Requesting Permission.

For information about author copies, see Author e-prints policy.

If you are submitting a manuscript to a SAGE journal and wish to include previously published materials within the manuscript, visit our Author Gateway Copyright and Permissions FAQs.